The Anatomy and Microcirculation of the Intervertebral Disc

Submitted by Rachel Melanie Palfrey, to the University of Exeter as a thesis for the degree of Doctor of Philosophy in Physics, July 2013

This thesis is available for Library use on the understanding that it is copyright material and that no quotation from the thesis may be published without proper acknowledgement.

I certify that all material in this thesis which is not my own work has been identified and that no material has previously been submitted and approved for the award of a degree by this or any other University.

(Signature)..

Abstract

Low back pain is a costly financial and loss of productivity societal issue. Although its aetiology is unclear, it has been associated with the intervertebral disc and its degeneration which has been thought to be caused in part by poor nutrition. In this thesis the caudal disc of skeletally mature equines is utilised as an animal model. Techniques such as x-ray, light imaging, histology and magnetic resonance imaging were employed to investigate the vascular and structural anatomy of the disc and its surroundings and the uptake of tracers within the disc tissue.

A detailed study of the anatomy revealed similarities with the human lumbar disc. The equine caudal disc consists of two distinct structural areas; a nucleus and annulus. The surrounding vascularisation is similar; a main anteriorly positioned artery, the median caudal artery splits and encircles the centre of the vertebral body providing nutrition to the vertebral body. Smaller vessels anastomose over the surface of the vertebral body. Within the vertebral body the vessels end in capillary terminations at the edge of the vertebral cartilage endplate. As in human lumbar discs these terminations were seen to vary along the endplate with shape and density; the capillaries are densest and larger in the area next to the nucleus. The cartilage endplate itself was found to have a variable width; of between 0.16 mm and 0.33 mm being widest at the nucleus. The annulus was seen to consist of lamellar rings which had high collagen content. A marked difference between equines and humans found was the number and width of lamellae present; equines were found to have on average 5 lamellae with a width range of 140 10 1110 microns. The shape of the discs was also found to be different with equines having almost circular caudal discs

which have a concave superior and inferior surface. The nucleus of the disc, unlike current literature was found to have local order.

An important contribution to knowledge which this thesis has made is data collected on diffusion time and partition coefficient for transport of contrast agents in many regions within the disc. Diffusion was found to be fastest with the neutral ring-shaped molecule Gadovist and slowest in the positive ion, manganese. Partition coefficients between the tracers were also found to vary. The highest partition coefficient was 6 in the central nucleus with manganese and the lowest was 0.5 with Magnevist at 0.5 in the nucleus area.

This information will be useful in aiding drug delivery clinically and performing contrast enhanced imaging for pathology detection.

Contents

Figures

11

14

16

Tables

Equations

1 Introduction

1.1 Introduction

In this thesis the anatomy of the equine intervertebral disc and its associated vascularisation will be examined using a variety of imaging techniques such as x-ray, magnetic resonance, light microscopy and histology. The diffusion of several magnetic resonance sensitive contrast agents within the equine intervertebral disc is investigated. Diffusion within the intervertebral disc can then be contextualised with regards to the intervertebral disc anatomy and its implication for transport of nutrients in the intervertebral disc evaluated.

In this chapter the current knowledge of the intervertebral disc anatomy and vascularisation is discussed. Theories relating to the nutrition and biomechanics of the intervertebral disc and its implications for degeneration are highlighted. Current clinical imaging techniques will also be explored.

1.2 The intervertebral disc

The intervertebral disc is a unique structure that performs many diverse roles. A review by Urban and Roberts (Urban & Roberts, 2003) described the intervertebral disc associated with the lumbar vertebrae as approximately 7 to 10mm thick and 40mm in diameter anterior to posterior in humans. These are the largest intervertebral discs within the spine with cervical intervertebral discs being thinner and smaller. A physiological function of the intervertebral disc is the separation of two vertebral bodies (Bogduk, 2001). Simply resting one vertebra on top of another could make a joint. This would allow gliding

movements, however, not the subtle flexion, extension and lateral bending required for a full range of movement (Bogduk, 2001).

The intervertebral disc is a structure, which is strong but also ultimately deformable, allowing flexibility (Bogduk, 2001). The intervertebral disc is cartilaginous in structure. Remarkably, it shows degeneration as a result of age earlier than any other connective tissue (Urban & Roberts, 2003).

70% of the world's population suffer from low back pain as detailed in a review by Freemont (Freemont, 2001). The aetiology of low back pain is shrouded in mystery, however, the intervertebral disc and its deterioration has been associated with it (Cassinelli, et al., 2001). In fact, by the age of 49, 97% of lumbar intervertebral discs show some degeneration (Miller, et al., 1988) and 10% of back pain sufferers become disabled (Urban & Roberts, 2003). As a society, this becomes a costly burden in terms of health care, days lost at work and benefits (Urban & Roberts, 2003)

Confusion arises, as there is often no clear diagnosis of back pain. There is also difficulty in distinguishing between natural ageing and pathological disorders, particularly in terms of the intervertebral disc (Urban & Roberts, 2003). The possibility of slowing this process of degeneration or even reversing it would benefit disc sufferers (Freemont, 2001).

1.3 Anatomy

1.3.1 Components of the intervertebral disc

On a macroscopic scale, the intervertebral disc is divided into three distinct areas; the vertebral endplate, the annulus fibrosus and the nucleus pulposus as described in a review by Urban & Winlove (Urban & Winlove, 2007).

The vertebral endplate is made of cartilage. It separates the actual disc from the vertebral bodies both superiorly and inferiorly (Urban & Winlove, 2007). The vertebral endplate undergoes many natural changes with maturity. In infancy it is the epiphyseal growth plate for the vertebral bodies. It is thick and makes up a large proportion of the disc. (Urban & Winlove, 2007). The endplate fully covers the ends of the vertebral bodies (Bogduk, 2001). There are small blood vessels only while the epiphyseal plate is present (Urban & Winlove, 2007). There is consistency amongst current literature that as we mature the endplate loses its vascular nature (Urban & Winlove, 2007). A layer of subchondral bone forms between the vertebral endplate and vertebral body (Bogduk, 2001); the ring apophysis ossifies at the margins leading to the outer annular fibres inserting directly into the vertebral body (Bogduk, 2001). By maturity the endplate is less than 1mm thick (Urban & Winlove, 2007).

The type of cartilage within the vertebral endplate is hyaline cartilage. The collagen fibres run parallel to the vertebral bodies and continue into the disc, (Urban & Roberts, 2003). This type of cartilage has small populations of the matrix producing cells called chondrocytes; these are embedded in an amorphous ground substance, mainly proteoglycans and water, reinforced by collagen fibres (Young & Heath, 2000). The endplate also contains proteoglycan macromolecules. There is a greater concentration of proteoglycans and water over the area of the endplate that covers the nucleus (Bogduk, 2001).

The annulus fibrosus consists of two regions; the outer and inner which is described in the review by Cassinelli et al. (Cassinelli, et al., 2001). The outer annulus is dense and highly orientated (Cassinelli, et al., 2001); it contains

predominantly type I collagen giving tensile strength (Eyre & Muir, 1976). The inner annulus has a less dense structure and is not as well organised, (Cassinelli, et al., 2001); it is mainly made of type II collagen, with some type I fibrils; forming a more isotropic network, with proteoglycans and associated water giving compressive strength (Eyre & Muir, 1976). The collagen of the annulus is arranged in 15 to 20 concentric rings or lamellae (Urban, 1990). The lamellae are made up of bundles of fine fibrils that are about 0.1 to 0.2 microns in diameter (Urban, 1990). The lamellae have a thickness of 200 to 400 microns, with the outer anterior lamellae being thicker (Inoue & Takeda, 1975). The collagen bundles are angled to the vertebral bodies between 40°and 70°, alternating in direction between successive bundles (Happey, 1980). Thus, a cross-woven structure is formed (Hukins, 1984).

The annulus fibrosus in adulthood is 70% to 80% water (Patel, 2005). Collagen makes up about 50% to 60% of the dry weight of the annulus fibrosus (Adams, et al., 1977). Like the vertebral endplate, the annulus contains proteoglycans, about 20% W/V (Beard & Stevens, 1980). The proteoglycans form a gel that binds the water between the collagen fibre spaces (Buckwalter, et al., 1985). Of these proteoglycans more than half form large aggregate molecules called aggrecan; aggregates are further explained in section 1.3.2. It has been noted that the inner annulus has a different composition to the outer annulus: there is more collagen and less proteoglycans and water in the outer annulus; there also appears to be some variability between anterior and posterior annulus with the concentration of proteoglycans and water being higher anteriorly (Best, et al., 1994). Cell type has also been seen to vary across the annulus; fibroblast cells occur towards the outer annulus and chondrocyte type cells towards the nucleus (Maroudas, et al., 1975) (Urban & Maroudas, 1980). These cells have

the important role of synthesising the collagen and proteoglycan gel of the annulus; they are located between the collagen fibres and lamellae (Maroudas, et al., 1975) (Urban & Maroudas, 1980). The shape of these cells vary with the cells being more oval proximal to the nucleus. Towards the outer annulus the cells become elongated and run parallel to the collagen fibres (Urban & Roberts, 2003). Also present within the annulus are elastin fibres, which make up 10% W/V of the annulus fibrosus (Johnson, et al., 1985). They have an orientation that is oblique or vertical between lamellae. They are present in greater numbers at the point where the annulus attaches to the vertebral end plate (Johnson, et al., 1982)

The nucleus pulposus in humans is very different in structure from the annulus. The nucleus also contains collagen fibrils. However, these fibrils are finer, being about 20.5 nm. They are also randomly arranged, forming a loose irregular meshwork (Urban, 1990) (Inoue & Takeda, 1975). The collagens along with a small population of cells sit in a semi-fluid matrix containing a variety of proteoglycans (Fawcett & Jensh, 2002). Similarly to the annulus, the nucleus has also been found to be well hydrated. However, when compared to the annulus water makes up a greater proportion of its composition, at around 70 to 90% depending on age (Beard & Stevens, 1980). Collagen only accounts for 15 to 20% of nuclear dry weight (Bushell, et al., 1977). The type of collagen found is also different to the annulus, being type III around the cells and type II in the intercellular matrix (Bogduk, 2001). Proteoglycans made up the greatest proportion of the dry weight of the nucleus at 65%. Half of the proteoglycans in the annulus is aggregated. In the nucleus the majority are in the form of aggrecan monomers with about 25% forming aggregates (Urban & Maroudas, 1980). Within the nucleus it has been found that elastin fibres are present which

are highly ordered in a radial fashion (Urban & Roberts, 2003). These fibres are about 150 microns in length (Urban & Roberts, 2003). The cells of the nucleus responsible for producing the matrix are chondrocyte in nature with a low density of approximately 5000/mm³ (Urban & Roberts, 2003).

The intervertebral disc also contains other minor but vital components. There are a number of small leucine-rich proteoglycans, including decorin, biglycan, fibromodulin and lumican (Brown, et al., 2012) (Sivan, et al., 2013). These are important in repairing the matrix and in homeostasis (Heinegard & Oldberg, 1989) (Grodzinsky & Urban, 1995). They aid fibril formation and prevent mineralisation along the collagen fibres (Heinegard & Oldberg, 1989). Other well dispersed proteins include fibronectin, cartilage matrix protein and cartilage oligomeric matrix protein; they have various functions including interactions with proteoglycans and collagen (Heinegard & Oldberg, 1989). Enzymes such as collagenase, gelatinase and stromelysin have also been found to be present. These enzymes are responsible for destroying old matrix components to produce fresh matrix. They work in conjunction with activators and inhibitors, which control their activity to produce a balance of destruction and production of matrix (Kuettner, 1994).

1.3.2 Molecular structure

The structure of the major components such as collagen and proteoglycans are important in their function.

The fundamental unit of collagen is tropocollagen. It consists of three disulphide bonded polypeptide chains arranged in a helical fashion (Bogduk, 2001). These tropocollagen molecules are 300nm long and 1.5nm wide (Stockwell, 1979). The tropocollagen chains assemble with regular lateral spacing dictated by

cross-links formed between amino acids to form a fibril. In many tissues there is a hierarchical arrangement where fibrils are assembled to form fibres (Bogduk, 2001). Stockwell, 1979, noted that the fibres range in diameter from 5nm to 200nm.

The other major component of intervertebral discs is the proteoglycan molecule; in general proteoglycans consist of a core protein about 100nm to 300nm in length (Urban, 1990), although small proteoglycans such as biglycan and decorin can be less than 10 nm in size (Weber, et al., 1996). To this core protein, glycosaminoglycan side chains are attached (Urban, 1990). The side chains are covalently bound to the core protein and may be chondroitin sulphate, dermatan sulphate, keratan sulphate, heparan sulphate or heparin (Hardingham & Fosang, 1992). Proteoglycans are classified according to the type of glycosaminoglycan chains which they consist of and their molecular weight. Aggrecan is the major proteoglycan found in the intervertebral disc. The most common side chain occurring in aggrecan is chondroitin sulphate; however, it does also contain some keratan sulphate (Hardingham & Fosang, 1992). Each aggrecan contains approximately 100 chondroitin sulphate chains and up to 60 keratan sulphate chains as noted in a review by Kiani et al (Kiani, et al., 2002). As stated previously aggrecan is found as large molecular aggregates. The aggregation is mediated by a globular domain in the protein's core which can bind to a chain of hyaluronic acid, stabilised by a link protein whose mass is relatively small (Hardingham & Fosang, 1992).

The volume enclosed by a proteoglycan molecule into which it can attract water is known as its domain. This water binding capacity of the proteoglycan molecule depends loosely on its size and physical shape (White, et al., 1968).

Water is imbibed due to a large osmotic swelling pressure created due to the negatively charged glycosaminoglycan chains attracting mobile ions such as Na^+; this creates a difference in ionic concentration between the disc tissue and surrounding soft tissue (Kiani, et al., 2002). Aggrecan is immobile in terms of being able to redistribute itself and an imbalance occurs amongst the freely diffusible anions and cations; water is drawn in causing the aggrecan rich matrix to swell and expand (Kiani, et al., 2002). In fact, those proteoglycans containing chondroitin sulphate have both sulphate and carboxyl radicals, giving them twice the water binding capacity compared to proteoglycans containing keratan sulphate; this only has sulphate radicals. The ability of proteoglycans to retain water is therefore mostly proportional to its density of chondroitin sulphate (Urban & Maroudas, 1980). As proteoglycan concentration is greater in the nucleus the highest fixed charge density is found there. In fact it can reach 0.25 milli equivalent/g (Urban & Maroudas, 1979).

1.3.3 Anatomy of the horse spine

This thesis will employ the equine tail as a model system. Therefore the anatomy of the equine spine will be briefly reviewed. The equine spine is split into cervical (7 vertebrae), thoracic (18 vertebrae), lumbar (6 vertebrae), sacrum (5 vertebrae) and caudal (Budras, 2001). The caudal or coccygeal spine gives structure to the tail and normally consists of approximately 18-20 vertebrae (Budras, 2001). The cervical, thoracic and lumbar vertebrae are similar in shape to their human counterpart, with prominent transverse and spinous processes. The last few vertebrae in the caudal spine are different in shape being thin and rod like with no processes visible (Budras, 2001). The disc from an equine caudal spine is utilised in the work described in this thesis.

For the most part stresses are placed on the caudal spine not by weight bearing but by muscle contraction during tail movement. There are four distinct muscle groups surrounding the vertebral body. Anteriorly, two sets of sacrocaudal ventral muscles are present. Posteriorly, two sets sacrocaudal dorsal muscles are present. Each set is divided into a lateral and a medial muscle. Laterally, between the ventral and dorsal muscles is a smaller Intertransversarii muscle.

1.4 Nutrition

1.4.1 Introduction

It has long been established that the intervertebral disc is one of the largest avascular structures in the body as discussed in the review by Urban & Winlove, 2007. In humans, cells at the centre of the disc can be as far as 8mm from the nearest vessel (Urban & Winlove, 2007). The disc is a living structure and therefore requires a nutritional route, which is thought to be dependent on diffusion through the extracellular matrix (Bogduk, 2001). The pathways for diffusion are not well understood (Rajasekaran, 2004). A link has been established between degeneration and a lack of nutrient supply to the disc (Nachemson, et al., 1970).

There has been much debate concerning the transport of solutes within the disc and whether this is due primarily to convection or diffusion. In the disc this is a complicated process as there are two nutritional routes which are described below. Some previous studies have been undertaken in tissues such as cartilage, where nutrient supply is of interest in relation to osteoarthritis. Cartilage is a 'porous tissue', the transport of fluid and solutes in this type of tissue are governed by solute diffusivity and hydraulic permeability (GU, et al., 1998). It is generally believed that diffusion is the main transport mechanism for

small solutes with convection playing a more important role in the transport of larger solutes (Maroudas, 1978) (Urban, et al., 1978) (Urban, et al., 1982). Convection is described as the bulk movement of fluids, diffusion is defined later in this section and in chapter four; it is described by the well-known Fick's law (see chapter 4). Numerous studies have confirmed theoretical considerations that diffusion of solutes depends on solute size; diffusivity decreases with solute size (Maroudas, 1970). Studies have also shown that solute diffusivity increases with tissue water content; which itself corresponds to an increase in the pore size of the tissue (Maroudas, 1970). Diffusion in the disc has also been seen to be direction dependent with relation to collagen fibre direction (Jackson, et al., 2006). Interestingly, and important in this study, diffusion was seen to vary by region, possibly due to differences in water content (Leddy, et al., 2006). In general, studies have shown the partition coefficients of solutes decreases with the increasing molecular size of the solute in cartilage (Maroudas, 1976) (Quinn, et al., 2000). Maroudas has also shown that the partition coefficient is also dependent on other tissue properties such as water content and fixed charge density (Maroudas, 1976).

The cells of the disc require nutrients to maintain their viability (Urban & Winlove, 2007). Two vascular sources supply the cells. Vessels have been seen to penetrate the subchondral bone at the ends of the vertebral bodies and terminate just before the cartilaginous endplate (Urban & Roberts, 2003). The second vascular network penetrates into the outer annulus from surrounding soft tissue (Urban & Winlove, 2007).

1.4.2 Vasculature of the human vertebral body

In the human lumbar spine, four pairs of arteries originate from the aorta in front of each of the vertebrae (Ratcliffe, 1980). These arteries pass backwards and around the vertebra, supplying many extra-osseous branches (Ratcliffe, 1980). These arteries at the point of the intervertebral foramina break into many fine unnamed branches (Crock & Yoshizawa, 1976). A smaller fifth pair of lumbar arteries arises from the median sacral artery (Crock & Yoshizawa, 1976). Branches occur from the ilio-lumbar arteries which anastomose at all levels but are more pronounced at the level of the fourth and fifth lumbar arteries (Ratcliffe, 1980). Each of the lumbar arteries bifurcates over the vertebral body (Crock & Yoshizawa, 1976). The first are short centrum branches which penetrate the vascular foramina of the vertebral bodies next to the lumbar artery. The second are longer ascending and descending branches which forms a vascular network over the vertebral bodies (Crock & Yoshizawa, 1976). The intra-osseous vessels are arranged in a defined pattern. The vessels are distributed in three main sections of the vertebral bodies; the equatorial region and superiorly/inferiorly to the equatorial region (metaphysial arteries) (Ratcliffe, 1980). An arterial grid is formed by a horizontal vessel, at the upper and lower surfaces of the vertebral body to the superficial beginning of the annulus fibrosus which anamastoses with the vertical primary periosteal vessels (Ratcliffe, 1980); ending in arteriole terminations in the vertebral end-plate capillary beds (Crock & Yoshizawa, 1976).

The venous system of the vertebral bodies flows in conjunction with and follows the lumbar arteries, eventually draining into the inferior vena cava and left common iliac vein (Crock & Yoshizawa, 1976). The major venous system of the vertebral body is the basivertebral system of veins (Crock & Yoshizawa, 1976).

These run horizontally along the middle of the vertebral body.. Posteriorly, it drains into the anterior internal vertebral venous plexus and anteriorly into the anterior external vertebral venous plexus (Crock, et al., 1973). The system forms a large scale venous grid into which vertical veins flow from above and below (Crock, et al., 1973). At the superior and inferior aspect of the vertebral bodies adjacent to the vertebral end-plate, large veins run horizontally; parallel to the end-plate (Crock, et al., 1973).This is termed the horizontal subarticular collecting vein system (Crock, et al., 1973).

The capillaries of the subchondral bone drain into a system of smaller veins running parallel to the disc-bone interface; this is called the subchondral post capillary venous network (Crock, et al., 1973). From this network, short vertical veins join the larger horizontal subarticular collecting system. At the border between the subchondral portion of the vertebral body and cartilage endplate, the ends of the capillaries form distinct terminations (Crock, et al., 1973). The density of the capillaries varies, with the greatest density being over the nucleus area (Urban & Winlove, 2007).

Crock and Goldwasser in 1984 in their paper studying the circulation in the vertebral end plates of dogs found a distinction in the type of termination of these capillaries depending on their location, see Figure 1 below. They found that at the area where the bone-disc interface lay over the nucleus pulposus, the terminations were large and disc like; they could not move freely but were 'sessile' in nature, forming a plexiform of venules, see Figure 2 below.
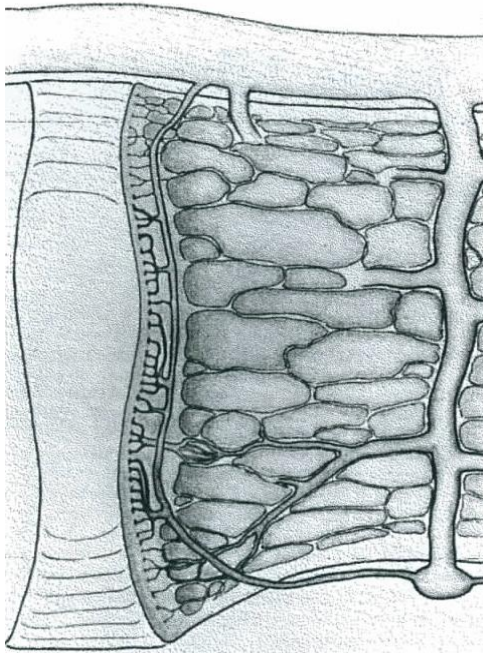
Figure 1: Capillary bed at the bone-disc interface. This composite drawing shows the vertebral body of adult greyhound dogs. The disc is shown on the left of the image. At the disc-bone interface the anatomy of the capillary bed is shown. The variability in vessel terminations across this boundary from nucleus pulposus to annulus fibrosus is clearly evident. It can be seen that subarticular collecting system is a continuous channel from the ventral longitudinal vertebral venous sinus in the spinal canal to the external vertebral veins. In the centre of the capillary bed the subchondral post capillary venous network can be seen to drain into the collecting system via individual channels. Alternatively, at the bottom of the drawing these can be seen to drain directly into the metaphysial or centrum veins. (Crock & Goldwasser, 1984). Reproduced by kind permission of Wolters Kluwer Health (licensed content publisher, license number-3430141304161).

At the part of the interface that resides over the inner annulus the terminations are smaller and they drain into only two or three venules (Crock & Goldwasser, 1984). The terminations at the outer annulus differ still further; in that they form discrete loops (Crock & Goldwasser, 1984).

Figure 2: The above image is a photomicrograph; it has been obtained from a 200 μm thick sagittal section. The image illustrates the capillary bed and the subchondral postcapillary venous network at the bone-disc interface over the nucleus pulposus region. The appearance of terminations at the area of the nucleus pulposus is discoid in shape and sessile (Crock & Goldwasser, 1984). Reproduced by kind permission of Wolters Kluwer Health (licensed content publisher, license number-3430141304161).

The zoned nature of the blood supply to the end (discal) surfaces of the vertebral body means the supply of oxygen and nutrients to the disc from this region is also zoned (Ratcliffe, 1980). As previously stated, the outer ring of the annulus fibrosus is supplied by metaphysial anastomoses in the superficial layers of the annulus fibrosus. The central zone of the disc is supplied by nutrient and metaphysial arteries of the adjacent vertebral body (Ratcliffe, 1980).

1.4.3 Nutrient transport into the disc

It has been established that the concentration of cells in the disc is low (Urban & Roberts, 2003). Cells require oxygen, glucose and other substrates for metabolism. As a result of metabolic activity, waste products are also produced which need to be disposed of (Bogduk, 2001). Due to the lack of

34

vascularisation, diffusion is responsible for the disc receiving an adequate supply of small molecules such as glucose and oxygen (Ferguson, et al., 2004). For larger molecules it is thought that convective flow, driven by water movement as the mechanical loads on the disc change, may perform a substantial role (Ferguson, et al., 2004). Small solutes are seen to diffuse readily towards the centre of the disc; this is due to the concentration gradient between the capillary bed and the disc (Ferguson, et al., 2004). Under normal mechanical loading fluid is pushed out of the disc. As the loading is altered, a flow of fluid both in and out of the disc occurs, transporting the larger solutes along with it (Ferguson, et al., 2004). The rate of solute diffusion is dependent on three main factors; the concentration gradient of the solute, resistance offered by the end plate or annulus and the resistance given by the proteoglycans within the nucleus (Maroudas, 1988). The proteoglycans form the small-pore structure of the extracellular matrix and are therefore the primary determinants of hydraulic resistance within the nucleus.

The cells of the disc rely on glycolysis (Bogduk, 2001). This is a form of anaerobic metabolism, and hence can occur in tissues where low oxygen levels are present. [Oxygen concentrations at the centre of the disc are in fact only 2-5 % of those at the periphery (Holm, et al., 1981). There is evidence that the metabolism of the disc is mainly anaerobic, even at high oxygen concentrations (Holm, et al., 1981).] In glycolysis, a six-carbon glucose molecule is broken down to produce two three-carbon molecules of pyruvic acid with a net gain of two molecules of adenosine triphosphate (ATP). ATP enables the transfer of energy to cellular activities (Tortora & Grabowski, 2003). In low oxygen environments most of the pyruvic acid is converted into lactic acid.

The concentration gradient of a nutrient or metabolite is dependent on the rate of transport compared to the rate of consumption (Urban, 1990). It is noted that oxygen has a steep concentration gradient from the blood (where it is high) to the centre of the disc (where concentration is lower), as its consumption is high relative to its transport. Lactate also has a steep concentration gradient, being a metabolite of anaerobic respiration; its production is high relative to its transport so its concentration is higher in the centre of the disc compared to the blood (Urban, 1990). The sulphate concentration gradient is different in that it is flat; this is due to sulphate consumption being relatively low (Urban, 1990). The large amount of lactic acid produced means that the disc environment is acidic, with a pH in the range of 6.9 to 7.1 (Holm, et al., 1981). The metabolic activity of the disc cells is very sensitive to changes in pH; in fact below a pH of 6.8 activity falls steeply and below 6.3 activity is only about 15 % of its maximum (Ohshima & Urban, 1992). The status of the matrix and in particular proteoglycan synthesis can be disturbed by changes in acidity. The build up of lactic acid causes the acidity of the disc to increase, decreasing metabolic activity and the production of proteoglycans (Bogduk, 2001).

Within the nucleus, there is a relatively high overall negative charge, due to the carboxyl and sulphate components of the proteoglycans (Roberts, et al., 1989). The fixed charge on the proteoglycans has no effect on the distribution and mobility of neutral molecules like glucose or oxygen, but positively charged species including ions like sodium and calcium have high partition coefficients in the matrix; the diffusion coefficient of all small solutes is around one third that of the diffusion coefficient in free solution. [The partition coefficient of a solute is its distribution between two immiscible phases in which it is soluble (Leo, et al., 1971). The diffusion constant of a substance is its rate of flow in a particular

steady state as a result of the molar flux of the species and its gradient of concentration.] Conversely, those negatively charged ions like sulphate and chloride have much lower partition coefficients in the matrix (Bogduk, 2001). The annulus, having a lower concentration of proteoglycans, and therefore a lower negative fixed charge density offers less resistance to the negatively charged ions; most diffusion of negative ions into the nucleus arrives via this route (Coventry, et al., 1945). The attraction of H^+ ions into the extracellular matrix (resulting from the negative fixed charge) causes the environment of the matrix to be slightly acidic; the acididty of the environment is also increased by lactic acid produced by the preponderantly anaerobic metabolism (Urban & Winlove, 2007). To maintain equilibrium, the ions are distributed between the plasma and the extracellular matrix following the Gibbs-Donnan equilibrium (Urban, 1990). The high osmotic pressure generated in the extracellular matrix is consequent on the excess of ions necessary to maintain electrical neutrality in the face of the fixed charge on the proteoglycans (Urban, 1990). The osmolarity of the disc is higher than that of the surrounding tissue; hence water is imbided into the disc until the osmotic pressure is balanced by tension in the collagen network and applied loads (Urban, 1990).

The metabolic activity of the cells within the disc is dependent on the amount of fluid present (Ishihara, et al., 1997). If fluid is lost from the disc, then matrix synthesis rates fall dramatically; fluid may be lost by osmotic or mechanical means (Ishihara, et al., 1997). The change in fluid content alters the concentration of the aggrecan (proteoglycan) in the extracellular matrix (Ishihara, et al., 1997). Therefore hydration determines the fixed charge density which (see previous paragraph) determines tissue osmotic pressure and therefore the mechanical functioning of the tissue.

The collagen network forms a mesh producing the equivalent of large pores within the extracellular matrix. Within these pores, the proteoglycan in its aggregate form lies forming a system of smaller pores (Urban & Winlove, 2007). This fine pore matrix will affect the movement and transport of solutes (Urban & Winlove, 2007). Molecules are excluded from an area of water volume around each aggrecan chain by virtue of their size (Urban & Winlove, 2007). For small solutes such as glucose, this excluded volume may only be 5 to 10% of the total water volume. However, for larger molecules such as the protein albumin, this may be 99% of the total volume (Urban & Winlove, 2007).

Roberts et al (1996), noted the size and shape of solutes affected their transportation through the cartilage matrix; as stated above, in fact, larger molecules were more highly excluded and diffused more slowly (Roberts, et al., 1996). It is believed that the presence of proteoglycans in the endplate regulate the movement of solutes into and out of the disc.

1.5 Biomechanics

A primary function of the intervertebral disc apart from providing mobility is to act as a 'shock absorber' (Urban & Winlove, 2007). In vivo, the intervertebral disc is continually subjected to varying loads as a result of body mass and the activity of muscles (Nachemson, 1981). As mentioned above (section 1.4.1) transport of larger solutes is affected by convection of fluid within the disc; hence transport of these larger solutes is affected by musculoskeletal movement. Prolonged loads especially may cause disc degeneration by affecting the transfer of nutrients (Holm & Nachemson, 1983). Prolonged loading is not necessarily caused by physical activity; sitting for long periods can produce a prolonged static load (Sato, et al., 1999). Insufficient nutrient

transfer and the accumulation of waste products occur because of inadequate fluid exchange (Holm & Nachemson, 1983). It has been noted that fluid content within the disc varied with load application and falls during prolonged loading (Adams & Hutton, 1983). Under a static load, pore pressure within the disc is decreased with time as the disc becomes deformed and fluid is expelled (Tak-Man Cheung, et al., 2003). As a result matrix destruction may occur as a result in the imbalance of constituents. This may cause a loss of nuclear hydrostatic pressure and a buckling of annular lamellae causing the annular tears and disc disruption leading to pain (Nachemson, 1960).The intervertebral disc plays a major mechanical role in the flexibility of the spine during everyday movements. The disc is always under a load of certain magnitude, even when lying supine the muscles and ligaments will exert a force of 0.1-0.2 MPa. This force may increase by 5 to 10 times on rising and be as much as 3.0 MPa when bending or twisting (Grodzinsky & Urban, 1995). The intervertebral disc has to cope with varying and high levels of stress and strain. If the disc is pushed beyond its limit then damage may occur (Tak-Man Cheung, et al., 2003).

The biomechanics of the nucleus are strongly determined by the rate of fluid redistribution under load, which may be approximately analysed using Darcy's Law, stating that flow is directly proportional to the prevailing hydrostatic pressure gradient. The constant of proportionality, the specific hydraulic conductivity of the tissue is strongly related to the concentration of proteoglycans (Tak-Man Cheung, et al., 2003). As already established, the nucleus is essentially fluid, making it incompressible under rapid loading. Under static loading, the increased pore pressure of the nucleus leads to a flow of water towards the boundary and surrounding structures (Tak-Man Cheung, et al., 2003). This flow of water decreases the volume of the nucleus and its pore

pressure (Tak-Man Cheung, et al., 2003). The deformation of the nucleus reduces its height making it bulge outwards and exert pressure on the annulus (Bogduk, 2001). Over a diurnal cycle the disc loses and regains about 25% of its water content (Urban, 1990). The amount of water, which is lost under loading, is dependent on several factors: the osmotic, elastic and permeability properties of the tissue. These factors are controlled by the relative concentrations of proteoglycans (Grodzinsky & Urban, 1995).The higher the concentration of proteoglycans, the lower the hydraulic permeability of the tissue (Urban, et al., 2000).

The annulus complements the function of the nucleus as its fibres prevent the annulus from bulging outwards under the pressure exerted by the nucleus, making it a relatively stiff structure (Tak-Man Cheung, et al., 2003). Best et al, 1994, found this compressive stiffness to be uniform across the annulus, although, stiffness has been found to correlate weakly with water content making the inner annulus slightly less stiff than the outer annulus (Best, et al., 1994). However, Tak-Man Cheung et al, 2003 suggested that this effect means that the axial effective stress of the annulus is increased more than the nucleus causing compressive failure in the annulus (Tak-Man Cheung, et al., 2003).

At equilibrium the radial pressure exerted by the nucleus will be matched by the tension developed in the annulus (Hirsch & Nachemson, 1954). It was found that this equilibrium is achieved with only minimal radial expansion of the nucleus, if the disc is healthy. In fact, it was found that a 40 kg applied load would only cause 1mm of vertical compression and 0.5 mm of radial expansion. The degeneration of the intervertebral disc and the subsequent reduction in proteoglycans results in the disc losing osmotic pressure and is therefore less

able to retain its water content (Urban & Roberts, 2003). As a result when placed under load these discs lose water content and have a reduction in height more readily than a normal disc; the loss of water also causes the disc no longer to behave hydrostatically under loading (Urban & Roberts, 2003). Stress concentrations in the degenerate disc under load occur differently than the normal disc causing disc bulging and herniation.

The vertebral end plates also have a biomechanical role to play. The nucleus, as it expands radially not only places pressure on the annulus but on the vertebral end plates as well (Hirsch & Nachemson, 1954). The end plates are anchored to the vertebral bodies, which enable them to resist being deformed. The pressure exerted on the vertebral end plates enable the load to be transmitted from one vertebral body to the next (Hirsch & Nachemson, 1954). It has been shown that nuclear fibres insert into the endplate, providing structural continuity (Wade, et al., 2011).

Bogduk, 2001 has noted that the disc acts as an energy storage device: As the nucleus expands radially, energy will be used to stretch the collagen network of the annulus. The network is able to store the energy used to stretch it. As the load is lessened, the stored energy is released and exerted back towards the nucleus causing it to recoil and restore any deformation. This property enables large forces to be temporarily diverted to the annulus, thus protecting the vertebral bodies by slowing the rate at which the force is transmitted to them.

The forces applied to the disc and the subsequent stress the disc is placed under will affect the activity of the cells in synthesising and degrading the extracellular matrix result of this activity in healthy tissue is to produce a matrix

which is able to cope with the demands placed on it and minimise the stress it is placed under (Urban, et al., 2000).

The disc necessarily needs an elastic component to help it maintain its structure during and to assist recovery after deformation (Urban, et al., 2000). This is provided in the form of elastin fibres. The elastin fibres within the nucleus are radial in nature. It is thought that this structure would permit the nucleus to transmit loads to all parts of the annulus equally (Szimai, 1970). In the annulus elastic fibres are also present. These fibres occur between the lamellae and are thought to play a similar role as in the nucleus in helping the annulus regain its shape after deformation (Yu, 2002).

 It has been found that the annulus contains a translamellar bridging network radially. This bridging network links lamellae at discrete positions around the disc and is thought to play a part in the biomechanical properties of the disc (Schollum, et al., 2009). The translamellar bridges have a width of 300-600 μm. The bridging fibres sit between the individual bundles which make up a lamella ring (Schollum, et al., 2009). After traversing the lamellar ring they merge with fibres of an adjacent lamella.

A study by Pezowicz et al (2005) revealed a remarkable resistance to tearing by the collagen fibres along their directional axis, even when lacerated (Pezowicz, et al., 2005). This was consistent with the primary strength of the fibres due to their insertion in the vertebral endplate. An interesting finding of the study was investigation transverse to the fibre orientation; interconnecting fibres were noted which formed an hierarchical structure (Pezowicz, et al., 2005). A role of these structures was thought to possibly act as a 'net' retaining proteoglycans while still allowing the movement of water.

The disc can change in height to a greater extent than the length of the collagen fibres would suggest (Viidik, 1973). It is thought that adjacent collagen fibres are able to slip past each other (Takeda, 1975). The hyaluronan acts a lubricant aiding the slippage of the collagen fibres (Inknen, 1999).

1.6 Intervertebral disc degeneration

Degeneration of the intervertebral disc not only affects the anatomical appearance of the disc but also its nutrition and biomechanical functioning. Discs show early degenerative changes such as a loss in disc height and bulging. Advanced degeneration can consist of: further loss in disc height, posterior and anterior osteophytes, facet hypertrophy and foraminal stenosis.

With degeneration the disc is not as well hydrated; this will affect its biomechanical functioning in terms of swelling and cushioning (Prescher, 1998). Hydration decreases because there is a diminishing amount of aggreccan (Buckwalter, 1995). The result is a disc with a more crumbly texture. The colour also changes from a greyish blue to yellow or brown (Prescher, 1998). Material within the disc starts to become replaced with fibrocartilagenous material until there is no longer a demarcation between the nucleus and annulus (Patel, 2005). The fibrosity of the nucleus means that it can no longer exert fluid pressure on the annulus making it less able to transmit forces (Bogduk, 2001). Fissures may be present in the disc which can extend into the annulus (Prescher, 1998). These fissures allow entry of blood vessels within the disc (Prescher, 1998).

Disruption of nutrition leads to cell death. It is not clear, however, that it leads to proteolysis, but in degenerate discs there is a much greater degree of proteolysis of matrix proteoglycans and collagen. The degradation products are

then lost from the disc by diffusion. There is a loss of fixed charge density and the structure of the collagen fibres becomes random and disorganised; this means that the disc is no longer able to support loading (Urban & Winlove, 2007).

The vertebral end plate also undergoes significant degenerative changes. It has been found to decrease in overall strength and be liable to micro fracture. The end plate bows into the vertebral body giving a concave appearance to the inferior and superior surfaces of the vertebral body (Bogduk, 2001). The central portion is seen to be the most fragile and liable to fracture under compressive loads (Bogduk, 2001).

Brodin, 1955, demonstrated that the vertebral end plate was the main nutritional route. With degeneration, this route may become occluded with calcification (Brodin, 1955). Within the disc an important type of collagen which is involved in calcification is Type X; this is because it is a marker of hypertrophic chondrocytes. Occlusion of endplate openings, which contain vessels transporting solutes into the disc, may limit the ability of these solutes to enter the disc. This will diminish solute transport; as a result less aggrecan is produced and the ionic composition around the disc cells become altered which affects metabolism and functioning of the disc. The density of openings in the endplate and the size of the capillary buds was seen to correlate to proteoglycan content in all regions, which is evidence of insufficient maintenance of matrix (Benneker, et al., 2005). Stairmand et al also demonstrated that the area available for exchange at the interface between bone and endplate is important in determining concentration gradients of nutrients into the disc. As this area decreases the number of cells able to be

44

supplied with nutrients decreases (Stairmand, et al., 1991).This causes damage to cells and a loss in matrix integrity (Stockwell, 1979). If nutritional routes become blocked, then lactic acid concentrations within the nucleus will increase as metabolites are unable to be transported away. This will cause a fall in pH,(Urban & Winlove, 2007).

As stated previously, the endplate is thought to regulate movement of solutes into and out of the disc. Hence, with degeneration of the endplate, removal of proteoglycans occurs, which allows proteoglycans within the disc nucleus to leave. A function of the cartilage endplate may be to prevent osmotically active proteoglycans from leaving the disc (Roberts, et al., 1996).

1.7 Imaging of the intervertebral disc

1.7.1 Introduction

It is apparent from the above brief summary that disc degeneration is associated with a wide spectrum of changes and the ongoing task of establishing the time course of change and, particularly, of identifying early causative changes, poses a challenge to methods of in vivo tissue imaging. Currently the most powerful technique and the focus of research in this thesis is Magnetic Resonance Imaging.

Magnetic Resonance Imaging (MRI) is a non-invasive diagnostic tool commonly used to evaluate intervertebral disc degeneration, infection and trauma (Antoniou, 2004).

Figure 3: T_1 weighted magnetic resonance image of a sagittal view of a lumbar spine. In classical T_1 weighted images fluid appears dark, hence the intervertebral disc having a high fluid content appears dark. This imaging technique is a Turbo Spin Echo; this is expanded on further in chapter 3. The critical parameters for this image are TR=539ms, TE=8ms, Flip angle=90°, NSA=6, Slice thickness=4 mm and Pixel size=0.497 mm × 0.497 mm. These parameters are discussed in chapter 3. This image is reproduced by kind permission of Dr J. R. Meakin, University of Exeter.

Figure 3 above is a sagittal section through a lumbar spine. Fluid appears dark on this image as it has a T_1 (spin-lattice) relaxation time weighting. T_1 relaxation time is the time required for the longitudinal magnetisation vector of the tissue's protons to be restored; this is further expanded on in chapter 3.

Figure 4: A sagittal T$_1$ weighted image of a lumbar spine. This sequence is a Turbo Spin Echo. The critical parameters of this image are TR=414 ms, TE=8 ms, Flip angle=90°, NSA=6, Slice thickness=4 mm and Pixel size=0.5 × 0.5 mm. The image clearly demonstrates a herniated disc between L4 and L5 vertebrae. This image is reproduced with kind permission of Dr J. R. Meakin, University of Exeter.

The image in Figure 4 shows a herniated L4-L5 (lumbar) intervertebral disc, which is herniating beneath the superior vertebral end plate of the L5 vertebra.

Figure 5: This image is an axial view of the same subject shown in Figure 4. This image is also a T$_1$ weighted image (with fluid appearing dark). The sequence is Turbo Spin Echo. The critical parameters of the scan are TR=400 ms, TE=8 ms, Flip angle=90°, NSA=4, Slice thickness=4 mm and Pixel sixe=0.497 mm × 0.497 mm. The herniation of the disc can be clearly seen posteriorly. The image is reproduced with kind permission of Dr J. R. Meakin, University of Exeter.

Sagittal and axial slices may be useful in disc evaluation, however, sagittal images visualise loss in disc height and disc bulging more effectively as can be seen in Figure 4 and Figure 5. Tears within the annulus fibrosus can be visualised as high intensity signal areas. In fact, MRI is 67 % accurate in detecting tears of the annulus (Patel, 2005).

Another example of a typical pathology, Schmorl's nodes demonstrated by MRI is shown below.

Figure 6: A T$_1$ weighted sagittal view of a lumbar spine. This is a Turbo Spin Echo sequence. The critical parameters of this sequence are TR=539 ms, TE=8 ms, Flip angle=90°, NSA=6, Slice thickness=4 mm, Pixel size=0.5 mm × 0.5 mm. This image clearly demonstrates Schmorl's nodes on L1/L2 disc and L2/L3 disc. This image is reproduced by kind permission of Dr J. R. Meakin, University of Exeter.

MRI is able to produce multiplanar images with good soft tissue contrast, as can be seen in the preceding images. It has been suggested that the signal produced by the intervertebral disc is dependent on the composition of the matrix and the structural integrity of the intervertebral disc (Antoniou, 2004). It

has been found that degeneration causes a decrease in signal intensity in scans using T_1 and T_2 (spin-spin) relaxation time weighting (Lauterbur, 1973). T_2 relaxation time is the time required for the transverse magnetisation vector of the tissue's protons to decay; this is further expanded on in chapter 3. This is due to the decrease in water content and increased collagen (Damadian, 1971). Parameters such as the relaxation times T_1 and T_2, spin density and magnetisation transfer can all be used in disc evaluation (Antoniou, 2004).

Spin density is also termed proton density; it relates to the number of hydrogen atoms in a given volume of tissue, as differing tissues have different proton densities MR images may also be weighted according to proton density (Mansfield, 1977).

1.7.2 Contrast enhanced MRI

A particular imaging technique which may be used to investigate transport into the disc involves the use of gadolinium. In the context of MRI, gadolinium compounds are T_1 contrast agents, i.e., the presence of gadolinium in a tissue produces enhanced gray-scale (brightness) in the MR image.

1.7.2.1 Choice of gadolinium contrast agents

Gadolinium compounds are available in a range of molecular sizes, and with different charge states, allowing the effect of these variables on transport to be studied. Of the commonly used agents, Magnevist (gadopentetate dimeglumine) is negatively charged, while Omniscan (gadodiamide), ProHance (gadoteridol) and Gadovist (gadobutrol) are neutral. Transport of Magnevist into the disc is thus expected to be affected by the presence of negatively charged glycosaminoglycans. [A study by Bashir et al (1999) utilised gadolinium diethylene triamine pentaacetic acid; this complex is negatively charged (Bashir,

et al., 1999).The study found that the contrast agent distributed within cartilage in an inverse proportion compared to the concentration of glycosaminoglycan. This technique was validated by biochemical calculations and proved a useful tool in determining glycosaminoglycan concentration.]

1.7.2.2 Applications

The technique of delayed gadolinium-enhanced MRI of cartilage (dGEMRIC) involves comparison of pre- and post-contrast images, the latter taken after a delay of around 15 minutes or more (Williams, et al., 2007), using an ionic contrast agent such as Magnevist. In the context of disc imaging, dGEMRIC can provide information on the distribution of proteoglycans and changes related to disc degeneration.

Similar techniques using either ionic or non-ionic contrast agents can provide information on transport of solutes within the disc – the contrast agents act as mimics of naturally occurring solutes. Time-intensity curves, calculated from sequential images of a particular region of interest, can provide information about the time course of the transport process.

1.7.2.3 Early studies on normal discs

In the 1990s, a number of studies demonstrated the potential of contrast-enhanced MRI for imaging transport processes within the disc:

In a study on rabbits using Magnevist (Ibrahim, et al., 1994), comparison of pre-contrast images and images taken at 2 hours after contrast administration demonstrated the presence of contrast agent in the intervertebral discs. In a related study (Ibrahim, et al., 1994), also on rabbits, a non-ionic contrast agent (ProHance) produced greater enhancement than a negatively charged ionic contrast agent (Magnevist), which the authors interpret as due to the negatively

charged glycosaminoglycans in the disc. In a further related rabbit study (Ibrahim, et al., 1995), enhancement was greater in immature discs compared to mature discs (for both ionic and non-ionic contrast agents, i.e., this was not a charge-related effect).

Rabbits do not provide an ideal model of the human disc (Alini, et al., 2008). However, in a human study using ProHance administered intravenously (Akansel, et al., 1997), gray-scale enhancement was observed at the disc endplates after 20 minutes, with a much smaller effect at the disc centre. This is consistent with a picture of transport of contrast agent via the capillary beds in the endplates.

1.7.2.4 Studies on degenerate discs

Physiological changes associated with disc degeneration (see above), including changes in glycosaminoglycan content, are expected to affect transport within the disc and should thus be detectable using contrast-enhanced MRI. In a human study (Nguyen-minh, et al., 1998) using ProHance (non-ionic), less gray-scale enhancement was observed (after 30 minutes) in discs showing signs of degeneration, compared to apparently healthy discs. Conversely, in a human study (Niinimaki, et al., 2006) using Omniscan, (non-ionic) gray-scale enhancement after 90 minutes was found to correlate with the grade of disc degeneration. This contradiction may be explained in terms of multiple effects of degeneration (see above) some of which might be expected to enhance transport and some to hinder it – the disc degeneration in the two studies may not be equivalent.

In another human study, again using Omniscan (Rajasekaran, et al., 2008), the time courses of gray-scale enhancement over a period of 12 hours post contrast

were found to fall into four distinct classes – showing, compared to normal discs, both increased transport (in severely degenerate discs whose structure is compromised) and decreased transport (in ageing discs where the porosity of the endplates may be reduced). Bydder et al investigated solute transport into lumbar discs using dGEMRIC (Bydder, et al., 2001). This study found a measurable difference in enhancement between less degenerate and more degenerate discs, with the latter showing the greater enhancement (again, this may be because their structure is compromised).

1.7.2.5 Effect of loading

As mentioned above (section 1.5) that fluid content within the disc varies with load application and falls during prolonged loading The effect of disc loadings has been investigated using contrast-enhanced MRI in a human study (Arun, et al., 2009) using the non-ionic contrast agent ProHance. After 4.5 hours of spinal loading, gray-scale enhancement was less than that observed for unloaded controls, indicating that transport into the disc was reduced in the loaded case. An alternative strategy to observe the effects of mechanical load has been to image human scoliotic discs in-vivo (Rajasekaran, et al., 2010), with comparison of the left and right sides of the disc. Abnormal patterns of diffusion were observed, even in discs which appeared anatomically normal by conventional MRI, suggesting that impaired nutrition may be a precursor of disc degeneration induced by mechanical stress.

1.7.3 Magnetisation transfer

Tissue consists of two types of water hydrogen nuclei; free and bound. Free water molecules are those generally found in cytosol; they have many degrees of motion freedom and as such have resonance frequencies grouped around

the normal proton frequency of 63 MHz (at 1.5 T), producing good field homogeneity with a long T_2 relaxation time (Henkelman, et al., 2001). Bound water molecules are those generally bound to large macromolecules such as proteins and lipids; these molecules have extensive interactions with the local environment producing a wide range of resonant frequencies and field inhomogeneity (Henkelman, et al., 2001). The bound water nuclei because of their extensive interactions have very short T_2 relaxation times. Although, the bound water molecules are invisible to MR imaging due to their short T_2, magnetisation can be transferred from the bound to the free pool. This transfer decreases the speed at which the longitudinal magnetisation recovers therefore decreasing the observable MR signal. It has already been discussed that a degenerate disc has reduced hydration and therefore less free water molecules; this produces a greater effect and degree of reduced signal due to magnetisation transfer (Henkelman, et al., 2001).

An application of magnetisation transfer within cartilage is using gadolinium complexes to separate the effect of proteoglycan degradation, from the effect of collagen disruption, which is the major contributor to magnetisation transfer in this tissue (Kim, et al., 1993). A study by Gray et al studying cartilage did find magnetisation transfer effects were more strongly affected by collagen than the same concentration of glycosaminoglycans. However, it was found that macromolecular structure as well as concentration affects MT and magnetisation transfer could differentiate between different types of degradation (Gray, et al., 1995). A further study by Paajanen et al (1994) specifically investigated if Magnetisation transfer could provide new information about disc degeneration (Paajanen, et al., 1994). This study noted an increase in magnetisation transfer between free-water protons and macromolecule-bound

protons in degenerated discs. There was also a positive correlation between disc collagen, total protein concentration and the rate of transfer. More recent studies such as that by Antoniou et al (2013) have tried to establish links between magnetisation transfer and different grades of degeneration. The magnetisation transfer rate was seen to increase significantly with grade 4; this may suggest a low sensitivity with minor degradation (Antoniou, et al., 2013)   .

1.7.4 Apparent diffusion coefficient

Diffusion within the disc may also be studied. This is achieved by calculating the Apparent Diffusion Coefficient; the amount of 'random translational motion of protons in a tissue' (Antoniou, 2004). Pure water, for the purposes of diffusion is said to be isotropic; this means that the molecules are equally likely to diffuse in any direction. To measure the amount of diffusion in MR, diffusion gradients are applied; for pure water their effect on the MR signal should be the same in any direction (McRobbie, et al., 2007). As water molecules are the largest provider of protons for MRI and the transport of water is indicative of the condition of the matrix, such as proteoglycan content, matrix integrity and disc nutrition may be evaluated (Antoniou, 2004). This is because water diffusion in biological tissues is restricted by cell membranes; there may also be a preferential diffusion direction, for example, along collagen fibres (McRobbie, et al., 2007). The Apparent Diffusion Coefficient of water molecules is generally seen to decrease with age and degeneration (Antoniou, 2004). Diffusion weighted images are able to show small changes in structure (Bammer, 2003). In diffusion imaging, tissues with a high water content have very mobile molecules and produce a low signal intensity, whereas, those tissues which are more solid give a higher signal intensity (McRobbie, et al., 2007). Diffusion weighted imaging is obtained by using a short T_2 relaxation protocol because of the issue of magnetisation

transfer previously described (Miller, 2004). Due to these differences in proton mobility between tissues' diffusion weighted imaging may be useful in the evaluation of vertebral lesions, such as, benign compression fractures, metastases and hemangiomas. Also, as changes in diffusion within the intervertebral discs can be a sign of degeneration, these scans may be used as a measure of that change (Bammer, 2003).

The value of the apparent diffusion coefficient (ADC) is thought to be a useful tool in measuring degenerative changes because ADC provides an estimate of free diffusion of unbound water. A study by Niinimaki et al (2009) investigated human lumbar discs (Niinimaki, et al., 2008). It was found that there was a reduction in ADC between normal and moderately degenerated discs of 4%. However, in severely degenerated discs an increase in the ADC of 5% was noted; this may be due to free water present in discal cracks and fissures. There was no correlation found between ADC and the anatomical level of the studied lumbar discs. The conclusion of this study was that the value of the ADC had limited clinical value because of the overlap in values of normal and degenerated discs. In contrast Niu et al (2011) studying non-bulging/herniated, bulging and herniated lumbar discs found significant differences in ADC between non-bulging/herniated discs and bulging discs as well as herniated discs (Niu, et al., 2011). Their conclusion was that the ADC map of the nucleus pulposus is a useful tool for assessing molecular alterations accompanied with lumbar disc abnormalities.

1.7.5 Sodium imaging

There are several additional MRI techniques available for disc evaluation. Sodium imaging has been used in several studies. A study by Borthakur et al

into the sensitivity of sodium imaging in detecting proteoglycan depletion found the change in MR signal correlated well with changes in proteoglycan concentration (Borthakur, et al., 2000). A further study by Reddy et al, 1998, investigated sodium MRI of human articular cartilage in vivo and found an area of depleted proteoglycan could be distinguished from healthy articular cartilage; this may lead to the possibility of detecting arthritic changes in vivo (Reddy, et al., 1998). This correlation between signal and glycosaminglycogan has also been supported by Urban and Winlove, 2007. Miller, 2004, did however find sodium imaging to have a low signal to noise ratio which requires specialist software for analysis therefore reducing its ease of use. Proton density weighted T1 images can also be used to measure proteoglycan content within the disc; however, the signal produced does not consistently correlate with proteoglycan concentration (Borthakur, et al., 2000) . However, Toffanin, 2001 found no link between T2 relaxation time and proteoglycan concentration, therefore this type of weighted scan protocol would not be useful in determining proteoglycan loss as a result of degeneration.

Diffusion studies using MRI investigating the uptake of tracers within the intervertebral disc have been undertaken. In normal discs it was found that the tracer gadodiamide took 5 minutes to show peak enhancement of the signal in the vertebral body and subchondral bone, 2 hours at the endplate zone and 6 hours in the nucleus pulposus of the centre of the disc (Rajasekaran, 2004). A significant difference was found between those discs belonging to samples under 10 years old and over 20 years old with older discs demonstrating longer peak enhancement times; it was shown that this was due to disturbance at the end plate zone and that this area was important for diffusion in the nucleus pulposus (Rajasekaran, 2004). It has been shown that the size of the molecular

weight affects the diffusion of contrast media into the intervertebral disc; the larger the molecular weight of a paramagnetic contrast agent the slower its progress through the disc (Perlewitz, et al., 1997).

1.7.6 X-ray imaging

Anatomy of the vascular network within the vertebral end plate and the outer annulus may be visualised by X-ray. A radio opaque contrast agent is needed such as barium sulphate as in the case of Crock and Goldwasser in 1984, see Figure 2. In this way the capillary bed is quite well determined along with the vasculature of the vertebrae. However, this is not suitable for the disc as x-ray does not visualise the disc well. This is also not an in vivo procedure as thin slices of the sample are needed.

1.8 Thesis aims

The above review has illustrated some of the outstanding problems in the physiology of the intervertebral disc and our understanding of its pathology. It is clear that only very limited information can be derived from the study of human autopsy material and opportunities for in vivo measurement are extremely limited. This has led to the use of animal models ranging from small rodents to pigs and sheep. However, the species differences in disc structure alluded to above and further expanded on in chapter 2 cast doubt on the relevance of many of these models. A number of researchers have suggested that the discs of the bovine tail resemble those of the human for it to be a useful model. However, one of its limitations is that tissue is readily available only from young animals. The starting point of the work of this thesis was to investigate whether the equine tail may provide a better model, in that tissue is available from animals of a wide range of known ages.

In chapter 2 this thesis will initially establish the anatomy of the discs of the equine caudal spine and surrounding structures. As illustrated above, key questions in disc biology relate to the exchange of water, nutrients, and metabolites between the disc and the surrounding microcirculation and in chapter 3 we describe the development of an in vivo perfused preparation of the equine tail which can be employed in such investigations. We first describe the microvascular supply to the disc using a combination of x-ray, light microscopy and magnetic resonance imaging. We then demonstrate that these circulations can be perfused under controlled conditions of pressure and flow via the median caudal artery with drainage from the median caudal vein.

Transport studies in the perfused preparation will be possible using MRI tracer techniques. However, experiments on transport in the excised disc are also necessary both to determine transport rates throughout the tissue matrix itself and to calibrate MRI contrast concentration measurements for various tracers; these tracers have variable molecular weights and ionic charges to resemble important nutrients. This work is undertaken in chapter 4.

2 Anatomy Studies

2.1 Introduction

The work described in this chapter is intended to provide a framework for interpretation of the studies in subsequent chapters. Following a review of the anatomy of the equine tail in this section (section 2.1), we first investigate the blood supply to the intervertebral discs, based on x-ray imaging of the delivery of ionic and particulate radiopaque tracers in a novel preparation of the in vitro perfused equine tail in section 2.2. We then investigate transport beyond the microcirculation into the disc itself, using Evans blue as a low molecular weight diffusible tracer in section 2.4. Finally, we investigate the structure of the equine disc using polarised light microscopy in section 2.5 and classical histology in section 2.6.

The word *equine* comes from the Latin *equīnus*; *equus* horse and *īnus* pertaining to. Equines are quadrupedal ungulates.

When using animal models to represent human anatomy, it is important to understand differences between the species (Alini, et al., 2008). Some differences include type and numbers of cells, anatomy, mechanical properties, development and physiology (Alini, et al., 2008). An important developmental difference between species is the presence of notochordal cells. In all mammals, the intervertebral disc is formed from aggregating mesenchyme around the notochord (Alini, et al., 2008). These cells become highly orientated, forming the typical concentric lamellar structure of the annulus fibrosus (Alini, et al., 2008). The notochordal cells then disappear from the annulus remaining in the nucleus pulposus where they produce the cellular matrix necessary for the

physiological functioning of the nucleus (Alini, et al., 2008). How long these notochordal cells remain varies between species. In humans a few notochordal cells remain in the nucleus pulposus at birth but decrease rapidly after birth; by adulthood they have disappeared from the nucleus (Alini, et al., 2008). In the equine species there are no notochordal cells in the nucleus pulposus at birth. This is an advantage within this study as notochordal cells affect metabolism, therefore it is useful to have similar cells for comparison.

Endplate size and disc height variability along the spine varies between species. In humans both endplate size and disc height increases from cervical to lumbar vertebrae; in large quadrupeds this is not the case, with these two variables remaining constant along the length of the spine (Alini, et al., 2008).

Disc shape between humans and equines is of particular note. Human discs are convex both superiorly and inferiorly, while the caudal equine spine possesses concave discs both superiorly and inferiorly.

Biomechanical function of different disc regions may vary between the species. In humans lumbar vertebrae are placed under load due to the weight of the upper body acting upon them. It has often been suggested that loading of the lumbar vertebrae may be greater in humans than quadrupeds. In fact, this may not be the case as considerable tension is required to maintain a horizontal spine (Alini, et al., 2008).

Perhaps of particular interest within this study is the loading placed upon tail intervertebral discs. Tails are not weight bearing; stress is placed upon tail intervertebral discs by muscle contraction, hence tail swishing (Alini, et al., 2008). However, it has been suggested that in some quadrupeds, the swelling pressure of the intervertebral disc is remarkably similar to humans (Alini, et al.,

2008). The anatomy of the vertebral bodies is quite different in humans compared to equine caudal vertebral bodies; which appear to have an absence of transverse and spinous processes along with a lack of facet joints.

2.2 Gross anatomy of the equine tail

2.2.1 Tissue preparation

All samples used in this thesis were obtained from an abattoir, Lawrence J Potter, Staplegrove Mills, Taunton, Somerset, TA2 6PX. At the time of slaughter the equine samples were aged using dentition. Immediately after slaughter the main artery and vein which run anteriorly to the vertebral bodies serving the tail were cannulated (Simms Portex) and perfused with a saline solution to prevent blood clots from forming within the vessels. The bore of the cannula was just small enough to fit tightly within the artery. The artery was partially dissected away from the surrounding soft tissue. The cannula was inserted as far as possible into the artery until resistance was felt. The cannula was then able to be tied in place using thread to prevent it from slipping out of the artery. This same process was continued with the vein.
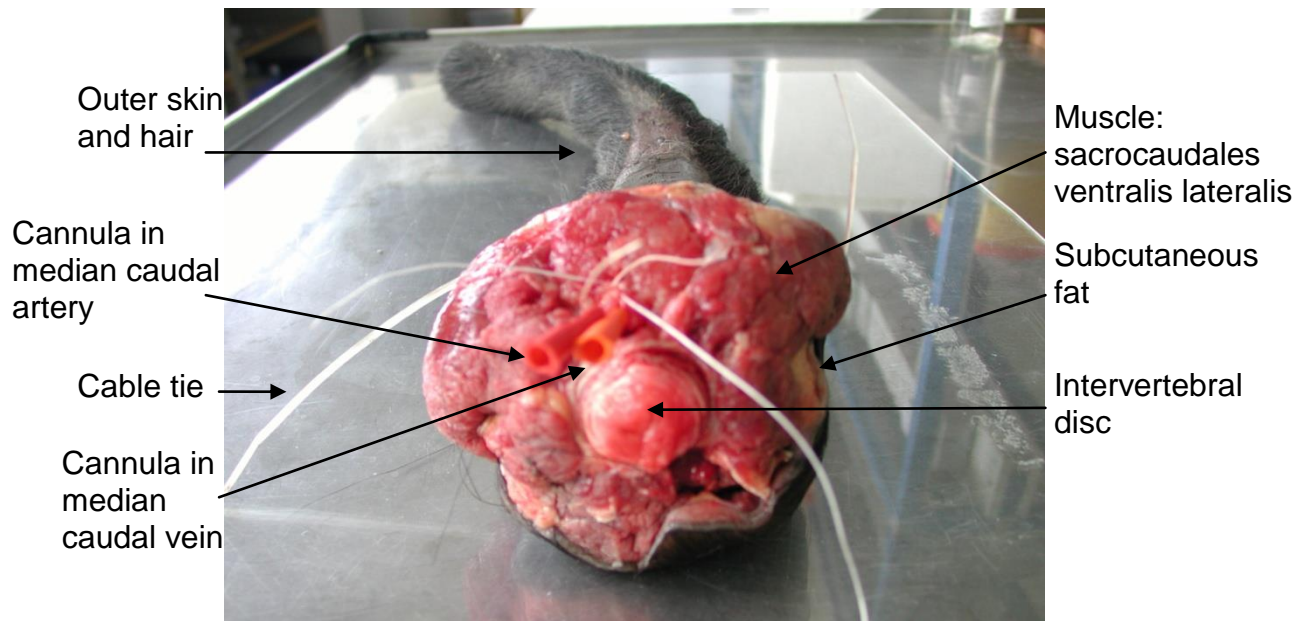
Figure 7**: Position of cannulae within the equine tail. Using a syringe attached to the median caudal artery, the tail vascular system is flushed through to prevent clotting.**

This process enabled adequate vascular flushing. A cable tie was fixed tightly around the whole of the tail at the cannulae end to prevent excess saline leeching into the surrounding soft tissue causing swelling of the tail; this tended to occur in parts of the vessel beyond the ends of the cannulae. The cannula within the artery was flushed through with saline until the fluid flowing out of the venous cannula was clear. The whole tail complete with cannulae was then transported back to the biophysics laboratory within the physics building at Exeter University.

2.2.2 Dissection of the equine tail

Figure 8 : The internal structures of the equine tail. A pair of scissors is initially used to trim the hair. A sharp scalpel is then used to make an incision in the skin. The skin is carefully removed followed by removal of the musculature and soft tissue until the vertebral bodies and discs are exposed. Mtion segments are then removed.

It is important within the context of this thesis to carefully examine the structure of the equine tail. It is important to understand the relationship between the internal structures.

The initial process of dissection involved the removal of the long hair using scissors. Using a fresh scalpel three axial incisions were made; these cuts were deep extending to the vertebral bodies. The muscle and soft tissue was then carefully eased away from the vertebral bodies.

It may be seen from Figure **7** and Figure 8 that the vertebral bodies and intervertebral disc of the equine tail are surrounded by several sets of muscles which are surrounded by fascia (Budras, 2001). Fascia is a form of connective tissue which may surround muscle, organs or lay under skin. Its role is thought to be mechanical in terms of absorbing stresses; it primarily consists of undulating collagen fibres. The muscles consist of four major groups which originate from the sacrum: sacrocaudales dorsalis medialis and lateralis and sacrocaudales ventralis medialis and lateralis (Budras, 2001).

There are numerous blood vessels and nerves associated with the caudal vertebrae, the major ones being the median caudal artery and vein. Ligaments also run the length of the vertebral bodies forming support and allowing flexibility.

2.3 Anatomy and vascularisation of the equine sample using x-ray imaging

2.3.1 X-ray imaging

All x-ray imaging was undertaken at The Centre for Medical Imaging, University of Exeter. The equipment used was a Siemens Multix-Top x-ray tube and a Konica Regius 150 computed radiography image receptor and processor.

Figure 9: The Centre for Medical Imaging at the University of Exeter. The imaging room consists of a standard clinical x-ray tube which is ceiling suspended via a gantry; the tube is manoeuvrable in 3-dimensions. The tube is powered by a high frequency generator. The room also consists of an x-ray table and associated bucky. (University of Exeter, 2013a).

The aim of this part of the thesis is to image the vascular system of the equine tail; it can be difficult to distinguish vessels from other surrounding soft tissue structures due to their similarities in atomic number and density. To overcome this various contrast agents can be used which are radioopaque; perfusing vessels with these emphasises their structure. Barium and iodine are common

contrast agents used in x-ray imaging clinically. The atomic number of barium and iodine is 53 and the densities are 3500 kg m^{-3} and 4930 kg m^{-3} respectively. The probability of photoelectric absorption occurring in the contrast agent is increased compared to the equine tail tissue structure. This enables structures containing contrast agent to be readily distinguished from surrounding structures.

The probability of photoelectric absorption occurring within the tissue decreases with increasing x-ray photon energy. It is essential therefore to pick a photon energy which provides adequate differentiation of the varying structures within the equine tail.

When the x-ray beam travels through the equine tail the processes of transmission, absorption and scatter happen simultaneously according to the various tissues through which it passes (Graham, et al., 2012). The exiting beam has been attenuated and holds a record of the various tissues. In this thesis depending on the thickness of equine tissue being imaged an anti-scatter grid was sometimes used.

2.3.2 Perfusion of the equine sample with potassium iodide

2.3.2.1 Aim

Iodine is a well-used radiographic imaging contrast agent. Typically, clinically it is injected intravenously to highlight vasculature. In the following experiment potassium iodide is introduced directly into the vessels of the equine sample.

2.3.2.2 Method

The equine tail sample was obtained and prepared as described in section 2.2.1. After the sample was returned from the abattoir it was then further

prepared in the Biophysics laboratory of Exeter University. The cannula was flushed through with a saline solution until the saline was seen to escape through the ends of the veins. The cut surface of the tail contains many open vessels allowing saline to escape from all the open veins in addition to the cannulated vein. To enable the vessels to be filled with contrast agents effectively the open vessels were clamped using two sets of Spencer Wells' forceps. The specimen was placed within a plastic tray; this was to enable minimum handling of the specimen and to enable a constant position to be obtained during imaging. The sample was then taken to the x-ray room of the Medical Imaging Centre at Exeter University.

An image was obtained by placing the sample and tray on the x-ray couch. A computed radiography image receptor was placed within the bucky in the couch; the bucky is an accessory cassette holder which also contains the anti-scatter grid. The bucky was used to ensure the sample is not moved between exposures; this ensures the central ray is over the same part of the sample and the field of view is maintained. The position of the specimen was with the posterior aspect of the tail on the image receptor surface. The exposure factors for the images taken were 60 kVp (peak kilovoltage) and 20 mA s. These factors were chosen as the tail is relatively thick consisting of vertebral bodies, muscle and soft tissue; adequate penetration and density of the final image is required.

After taking this initial image pre-contrast, 50ml of a solution of 1 molar of potassium iodide was injected through the arterial cannula; although the pressure of injection was not directly measured as a syringe was used, the contrast agent was injected as fast as possible to ensure filling of the vessels.

An image was taken using the same exposure factors. It is important to use the same exposure factors to ensure the probability of photoelectric absorption and Compton scatter remains similar pre- and post-contrast (Graham, et al., 2012). The image on evaluation showed minimal presence of contrast agent. An anteroposterior and lateral image was obtained. The vessels were seen to be filled with the contrast agent. The lateral image enables the 3D orientation of the vessels to be determined; it is important to understand if the vessels are anterior or posterior as this will determine viable routes to the disc for nutrition.

The specimen was then returned to the laboratory and the soft tissue was dissected away from the vertebral bodies as much as possible to expose just the vessels of the vertebral bodies and any possible vessel associated with the intervertebral disc.

The specimen in its plastic tray was then returned to the x-ray room and further images were obtained. Exposure factors of 60 kVp and 5 mA s were used for these images due to the removal of soft tissue absorption effects, keeping kVp constant to maintain contrast.

Tthe processor used in processing the computed radiography image receptor; is a typical clinical computed radiography instrument. The raw data is termed a gradation curve and is illustrated below in Figure 10. The resulting raw image is of low contrast (Carlton & Adler, 2013).
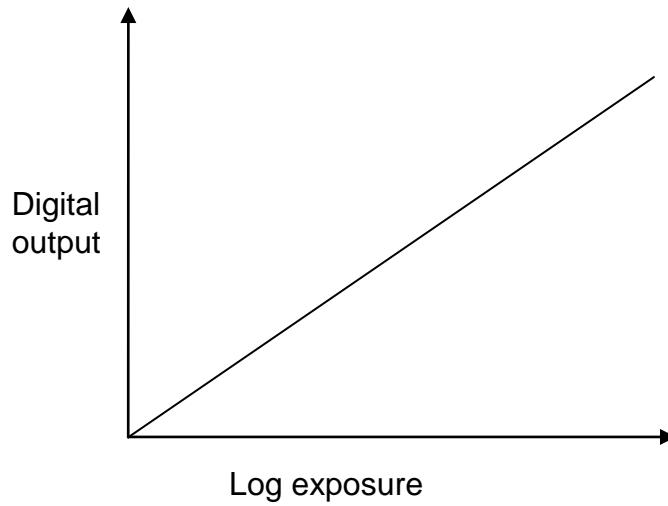
Figure 10: Gradation curve; for equal changes in exposure of the image receptor there is an equal change in digital output; this is classified as a linear relationship. This relationship gives a wide range of latitude in terms of useful exposure to produce a diagnostic image.

Clinically, a look-up table is applied to the raw data according to the anatomy being imaged.
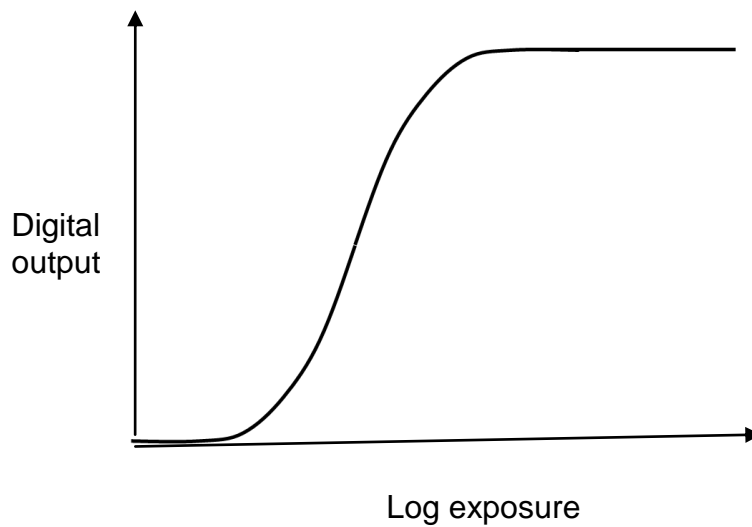
Figure 11: Illustration of a look-up table curve applied to the raw gradation curve; it can be seen that the look-up table does not produce equal changes in digital output for equal changes in exposure. There is a portion of the central part of the curve which does have a linear response. At the beginning and the ends of the curve the exposure will not produce a diagnostically useful image

If the anatomy being imaged has tissues which are very different in terms of atomic number and density it is said to have a high subject contrast and generally produces an image with extremes of gray value (Carlton & Adler, 2013). The curve used will minimise the extremes of contrast. If the anatomy imaged is an abdomen for example, it is said to have a low subject contrast as the tissues are very similar. In this circumstance a curve is applied which maximises differences in contrast (Carlton & Adler, 2013). In the present study pre- and post-contrast images were to be compared. Data were processed using a linear test look-up table to enable percentage changes in gray value between images to be compared.

The images were viewed using the software package Image J WCIF. A line Region of Interest (ROI) was selected through a vertebral body or intervertebral disc and a plot profile of gray values along that ROI determined.
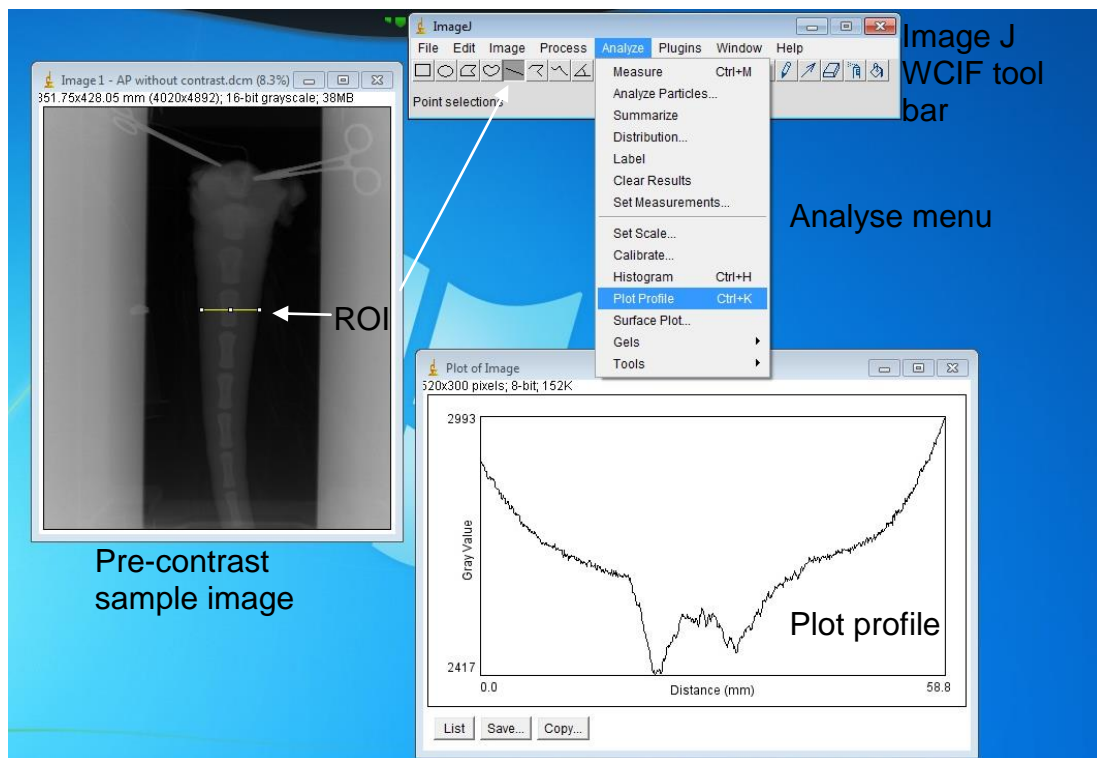
Figure 12: An illustration of a screen saver of an active screen; the pre-contrast image has a line ROI placed over a specific vertebral body; the ROI is used to provide a plot profile of gray values along the ROI.

These gray values were then compared between images to determine the percentage change in gray value on addition of the contrast agent using the following equation:

$$\frac{Postcontrast\ image - Precontrast\ image}{Precontrast\ image} \times -100 \quad \text{Equation 1}$$

This equation (Equation 1) enables the percentage change in gray value of a particular region to be determined on the addition of the contrast agent. Using Image J a boxed shaped region of interest (ROI) instead of a line was selected on Figure 13. The middle vertebra within this ROI was the same vertebra which had the line ROI previously. This same area was highlighted on Figure 15. Within Image J, using the function EDIT SELECTION, the images were made the same size. MANUAL TURBOREG was used to mark the same reference point in both Figure 13 and Figure 15. IMAGE CALCULATOR was then used to subtract Figure 13 from Figure 15 leaving only contrast highlighted areas.

2.3.2.3 Results
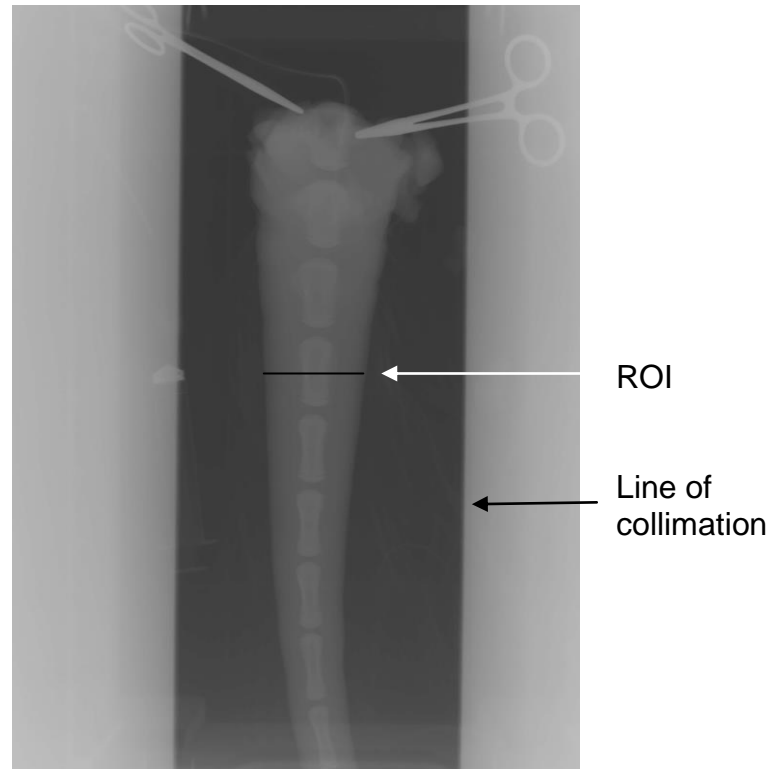
Figure 13: Anteroposterior equine sample without contrast: at the top of the image forceps can be seen, to the left of the image the syringe can be seen. The black line represents the ROI. The fouth vertebra from the superior aspect was selected; due to its size being suitable for imaging and slicing. The region of interest was drawn using Image J software.

A vertebra was selected, in this case the fourth one from the superior aspect; this vertebra was selected as it is well into the caudal spine but is still a relatively good size for imaging, later vertebrae become quite small. Using the ROI tool in Image J, a line was drawn from the outer margins of the soft tissue through the vertebra. A plot profile of the different gray levels along this line was then plotted.

Representation of gray value orientation
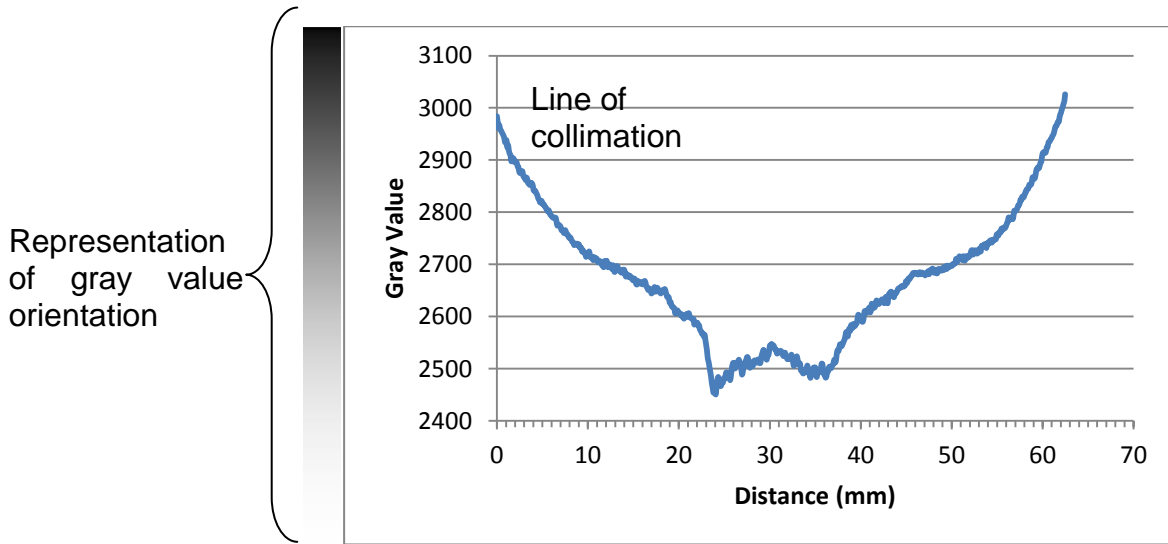
Figure 14: Plot profile across the ROI of the anteroposterior pre-contrast equine sample; the orientation of the ROI is left to right of the image (right to left of the actual sample). The representation of gray value illustrates that the higher the gray value the darker the pixel on the image. It can be seen that the edges of the vertebral body are clearly delineated as the lowest points in the graph.

Figure 14 is a representation of the plot profile shown in Figure 13. 0.0 mm is the skin margin on the right of the sample (the left of the image). The troughs on the graph above represent the dense cortical edges of the vertebral body. Within the centre of the body the bone is more porous and therefore has lower x-ray absorption. The brightest part of the image had a gray value of 2451.The highest gray value is 3026.The range of gray values is 575 levels. The importance of these values is to demonstrate a reference point for the typical image contrast when there is no contrast agent.
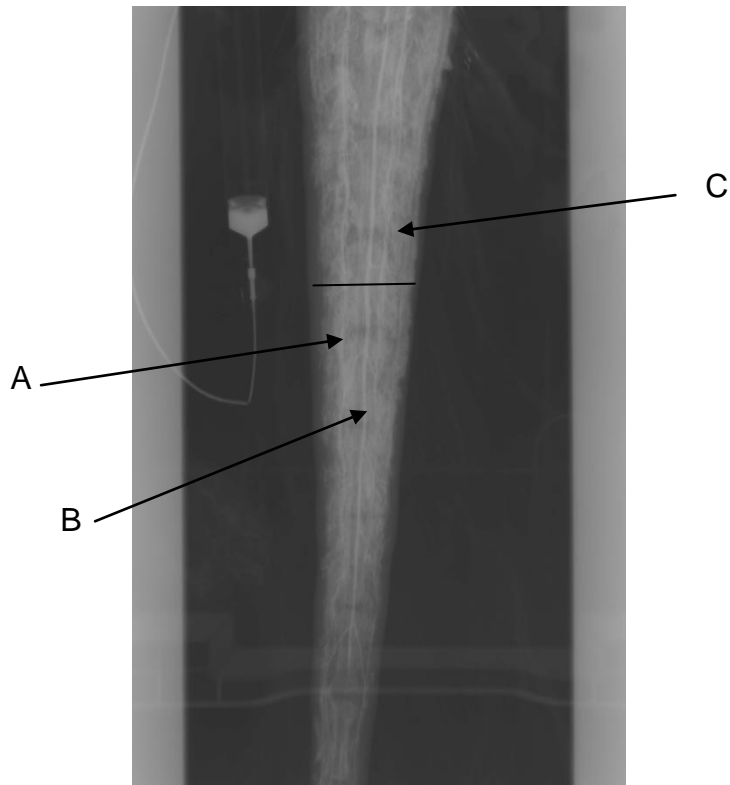
Figure 15: Anteroposterior equine sample perfused with 50 ml of a 1 molar solution of potassium iodide; the light areas signify the presence of contrast within the vessels of the sample. A, B and C are major vessels such as the median caudal artery and vein. Numerous vessels are obvious which are likely to be soft tissue vessels.

On Figure 15 the same vertebra was localised and a ROI line placed across the vertebra and soft tissue. A plot profile was then drawn as previously.
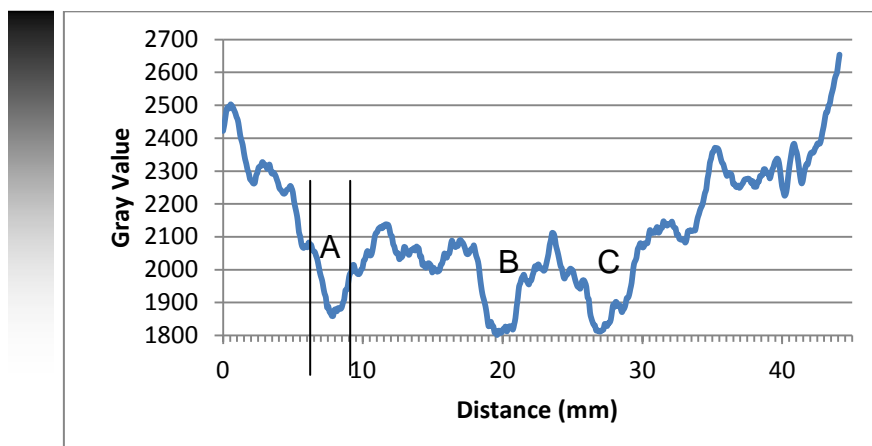
Figure 16: A plot profile of anteroposterior equine sample perfused with 50 ml of a 1 molar solution of potassium iodide. This ROI illustrates vessels in the soft tissue and vertebral body at this point it cannot be distinguished where the vessels are. The vessls A, B, C are the three major vessels indicated on the image in Figure 15. The smaller troughs are indicative of soft tissue vascularisation.

The diameters of the major vessels are approximately 5 to 6 mm in diameter as shown in Figure 16. The measurements are obtained by setting the scale in Image J; the size of cassette is known to be 35 × 43 cm, this field of view is over 4020 × 4892 pixels providing the spatial resolution.

The lowest gray value once the contrast has been added is 1800 and It can be seen from Figure 15 that there are three vessels in particular which have been well perfused by contrast agent; the central artery, B, is the main median caudal artery. As shown in Figure 16 many smaller troughs representing various intensities are evident; these indicate the presence of smaller vessels, these can be distinguished from noise by examining the smoothness of the plot profile for the pre-contrast image as a reference (Figure 13).However, it is not possible to say whether these vessels are in soft tissue, bone or intervertebral disc. The range of gray values is 853 gray levels. The large range of gray values is due to the large vessels being well perfused with contrast agent, leading to a greater variation between perfused vessel and non-perfused tissue. Although this does not give absolute values of contrast uptake, it does give a good indication of areas which are well perfused.

In the lateral view (Figure 17) and the plot profile (Figure 18) the three major vessels A, B and C are evident. Interestingly, in can be seen that vessels A and C are in fact laterally placed with respect to the vertebral bodies. The peak gray value of this lateral view is higher than the anteroposterior view. This is because iodine diffuses readily through the capillary walls into soft tissue, giving rise to a diffuse background which increases with time; the lateral view was taken a short time after the anteroposterior view. The range of gray values is 1000 gray levels.
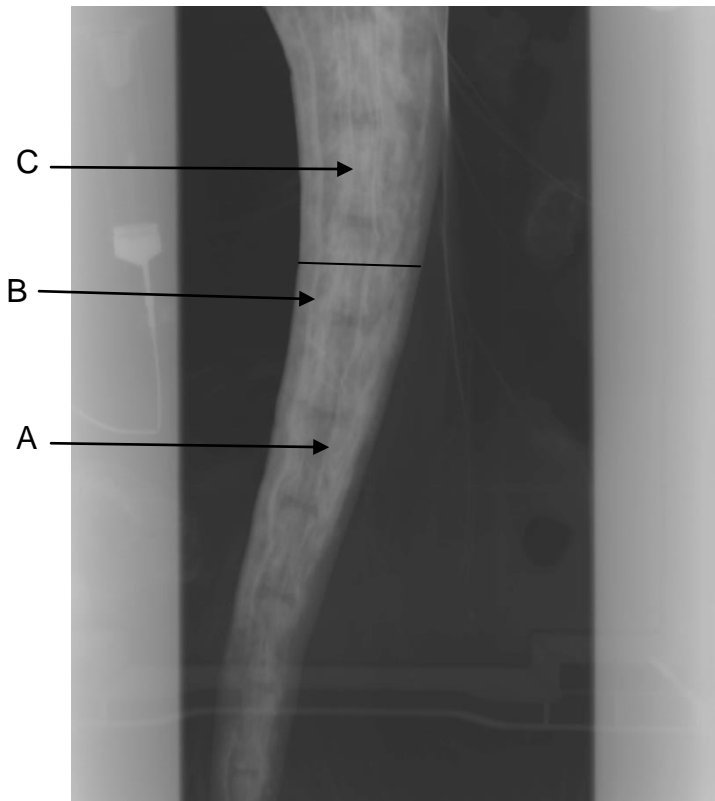
Figure 17: A right lateral view of the equine sample perfused with 50 ml of a 1 molar solution of potassium iodide. This lateral view gives an excellent indication of the positions of the three major vessels, A, B and C. A ROI is placed over the same vertebral body and a plot profile is drawn in the usual way.
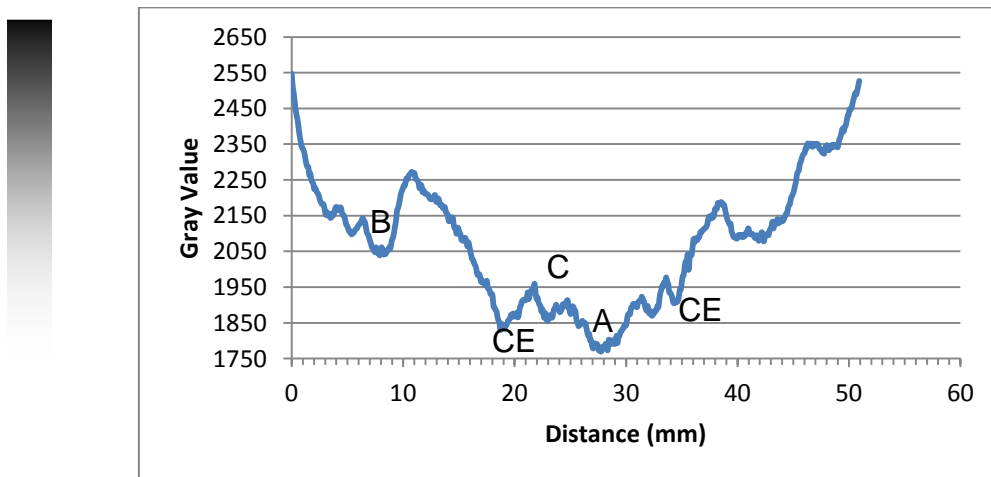
Figure 18: Plot profile of ROI of lateral equine sample perfused with 50 ml of a 1 molar solution of potassium iodide. A, B and C are the previously labelled vessels in the anteroposterior view. CE is the cortical edge of the vertebral body. In the lateral view it is evident that vessel B is not as well perfused as A and C. Cortical bone is denser than trabecular bone, hence the lower gray value indicating CE.

Line of collimation
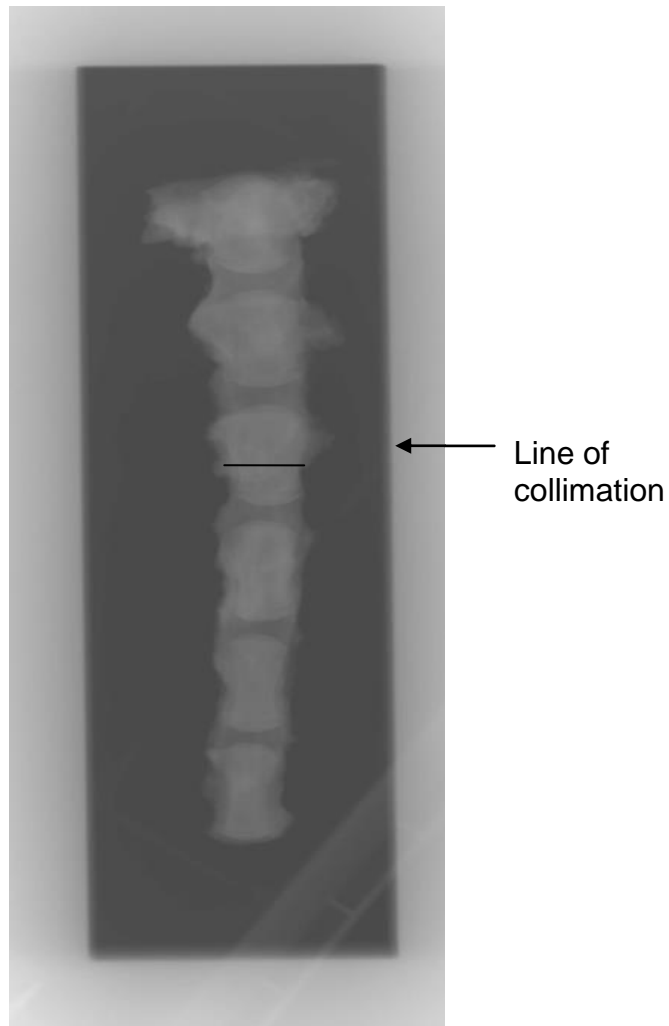
Figure 19: Anteroposterior image of vertebral bodies and intervertebral disc with 50 ml of a 1 molar solution of potassium iodide. This image is produced after the majority of the soft tissue has been removed; it can be seen that the three major vessels A, B and C are mo longer present, indicating that they were in the soft tissue. However, lighter areas can be seen which may be indicative of vessels in the vertebral bodies.

In order to distinguish between vessels in the soft tissue and vertebral body an x-ray was repeated after removal of the soft tissue.

As can be seen from the plot profile in Figure 20, the peak gray value has increased, meaning the x-rays have been attenuated less. The three large troughs are absent in this plot profile; this was expected as the vessels were continuous along the tail showing that they were in the soft tissue. However, the gray value of the brightest pixel is still lower than the image pre-contrast,

77

therefore there are vessels present in the vertebral bodies which has taken up

the contrast.
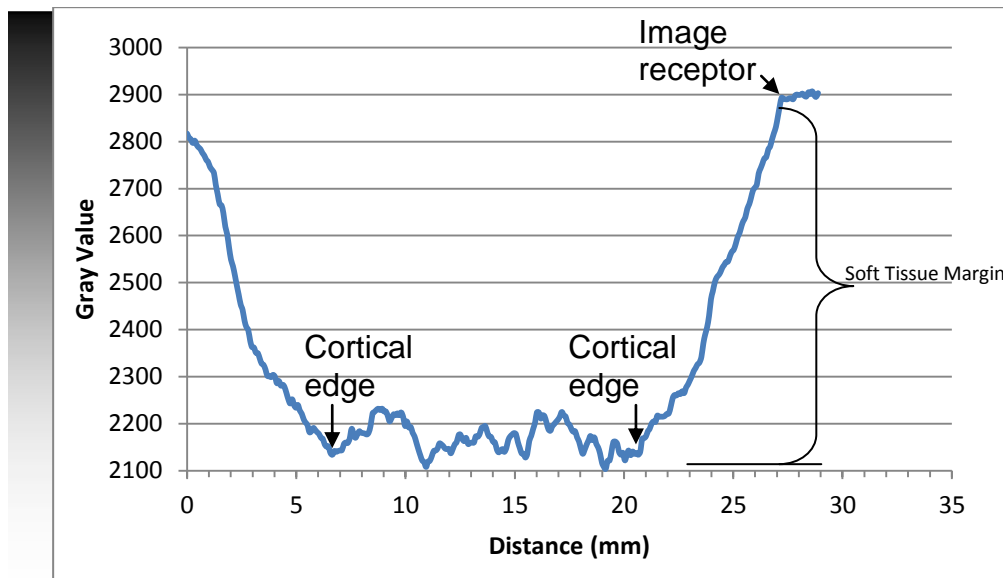
Figure 20: Plot profile of anteroposterior vertebral bodies and discs perfused with 50 ml of a 1 molar solution of potassium iodide. In this plot profile, the cortical edges of the vertebral bodies are again well defined as bright areas. The troughs within the vertebral bodies are likely to be vascularisation within the vertebral bodies.

Within the vertebral body (6.5-21 mm) the gray level fluctuates and each trough

represents a small vessel; we know that this is a vessel instead of noise

because noise would be evident throughout the plot profile and this cannot be

seen in the soft tissue area of the plot profile. Similar behaviour is evident in the

lateral view, Figure 21 and Figure 22.

Figure 21: Lateral view of vertebral bodies and intervertebral discs perfused with 50 ml of a 1 molar solution of potassium iodide. A lateral view allows for accurate positioning of the vessels. An area of particular interest is the anterior edges of the vertebral bodies which appear quite light.
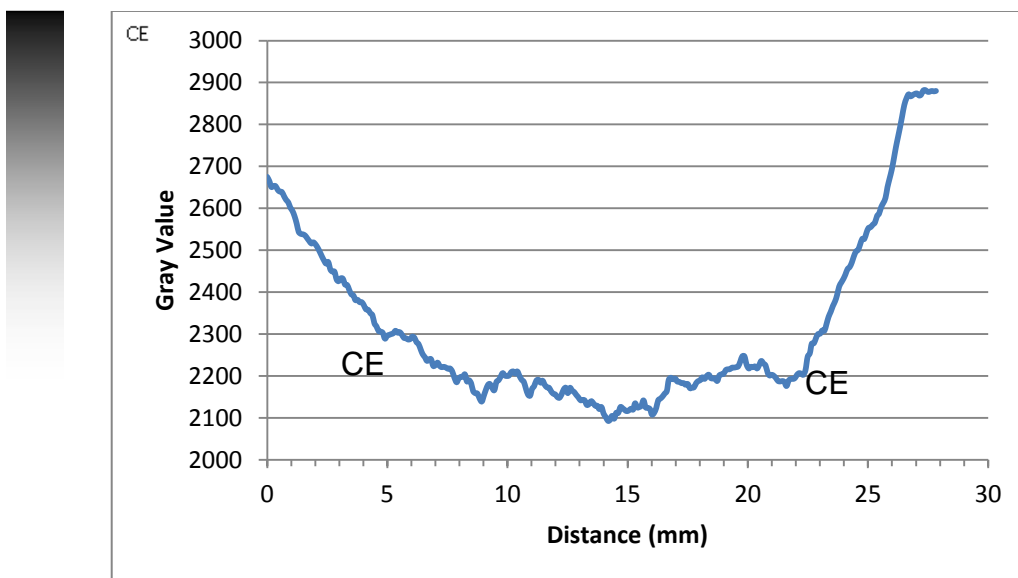
Figure 22: Plot profile of lateral vertebral bodies and intervertebral discs perfused with 50 ml of a 1 molar solution of potassium iodide. Evidence of the cortical edges are evident with the smaller vessels within the vertebral bodies producing the smaller troughs.

Digital subtraction was performed between the pre- and post-contrast undissected image to produce a clear visualisation of the vascularisation.

Figure 23: Digital subtraction of Figure 13 from Figure 15; major and minor vessels are left. Vertebral bodies which have contrast present can be detected. Digital subtraction involves digitally removing all tissue apart from vessels; this avoids issues of superimposition and enables vessel to be clearly seen.

In Excel a spread sheet was produced which calculated the difference in the line ROI in Figure 13 and Figure 15; this variation because the ROI and the kVp are constant is purely due to the addition of contrast.
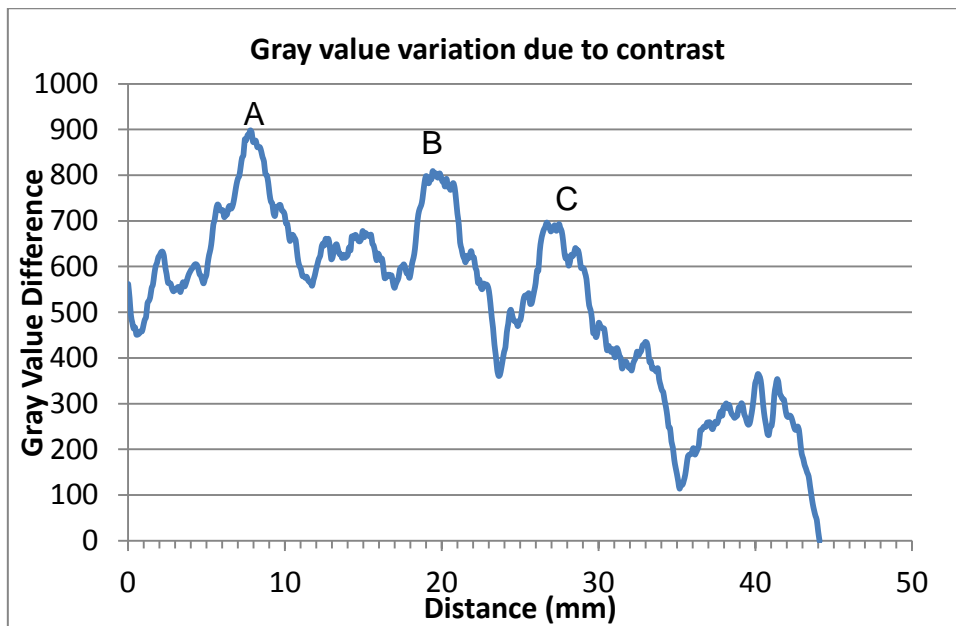
Figure 24: Illustration of change in gray value due to contrast; areas of vascularisation can be identified through increase in intensity of the image. Vessels A, B and C are the prominent vessels which can be seen on Figure 23, Vessels of varying sizes can be seen between these major vessels; it is difficult to say whether these vessels are in the soft tissues or vertebral bodies.

Figure 24 illustrates large changes in gray value identifying each of the three major vessels. Smaller peaks are indicative of smaller vessels.
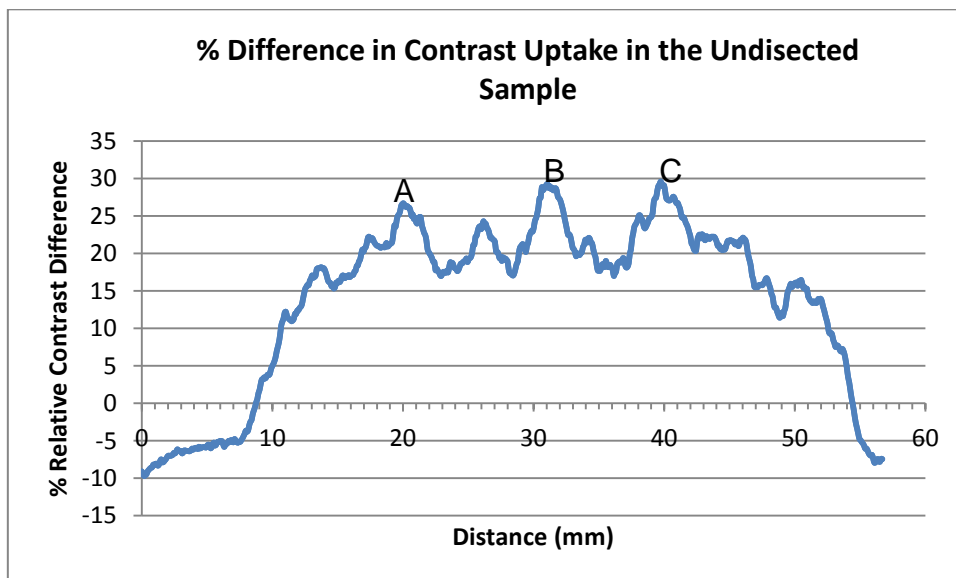
Figure 25: % relative contrast uptake between pre- and post-contrast undissected images; this is based on Equation 1. This is determined across the region shown in Figure 13 and Figure 15. Major vessels A, B and C can be distinguished. As would be expected the larger vessels take up more of the contrast agent.

In order to focus on intravertebral vessels a digital subtraction of Figure 13 from Figure 19 was performed.
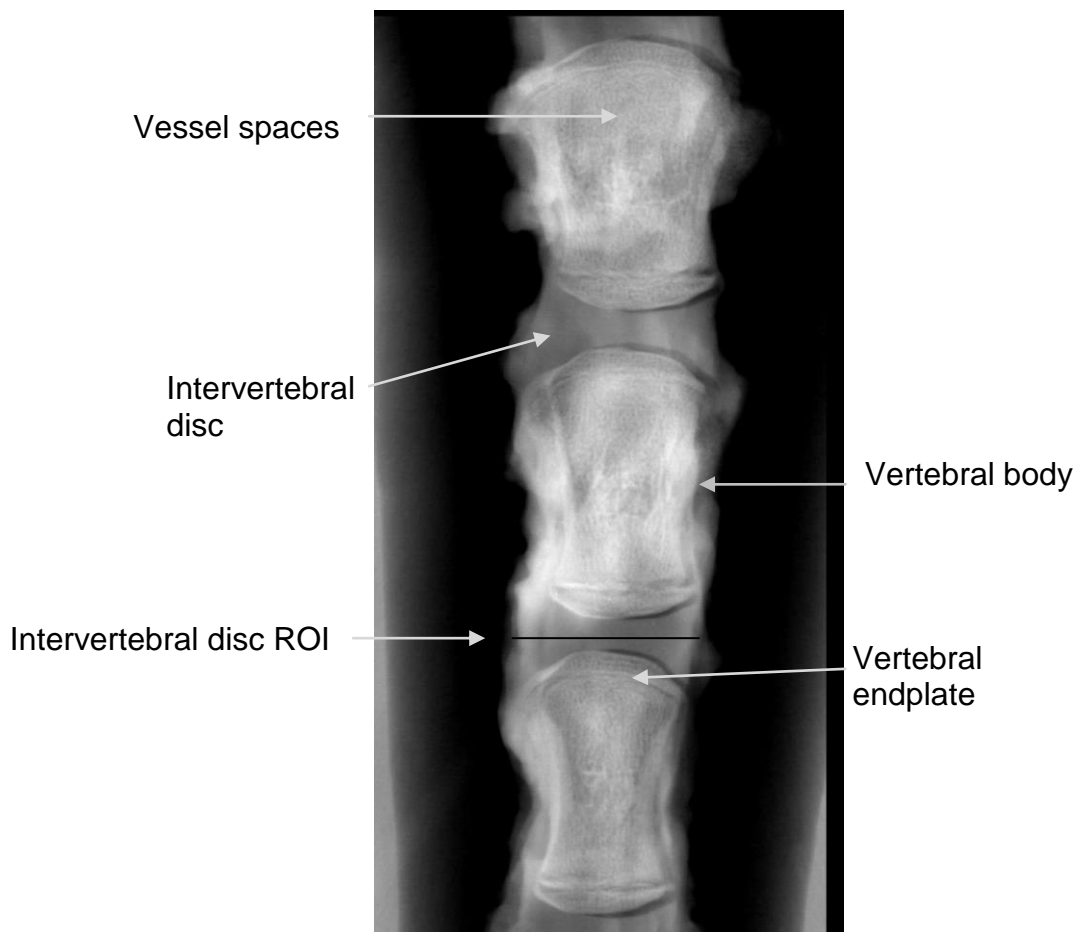
Figure 26: Digital subtraction of Figure 13 from Figure 19. This illustrates areas of uptake of contrast agent in both the vertebral body and intervertebral disc. In this digital subtraction we are able to eliminate vessels in the surrounding soft tissue.

In Figure 26 pores containing vessels are visible within the vertebral bodies. The cartilage endplate is also visualised; contrast can be seen to be pooling at the vertebral endplate/intervertebral disc interface. The discs are well visualised demonstrating contrast uptake. Figure 26 also provides good visualisation of the shape of the endplates in the horse; they are more highly convex, whereas in the human the endplates are slightly concave. This means that the equine disc is thinner at its centre, whereas the human disc is thicker. Diffusion into the disc from the endplates is expected to be strongly dependent on disc thickness. The

change in the amount of contrast agent in the tissue with time will be investigated in chapter 4 utilising Magnetic Resonance Imaging.

Figure 26 demonstrates an intervertebral disc ROI. A line profile of this ROI was drawn.
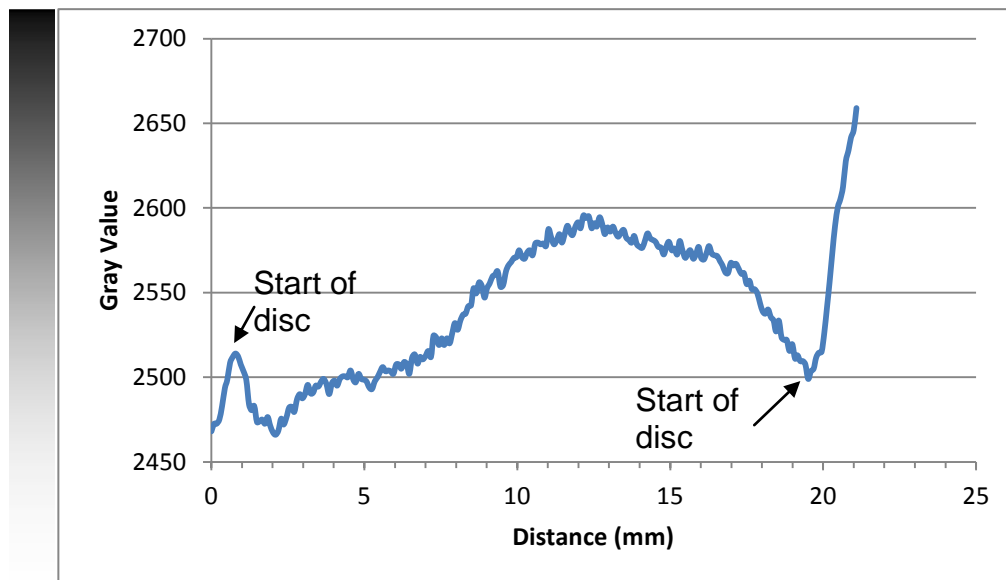
Figure 27: Plot profile of intervertebral disc ROI in Figure 26 .If this plot profile is compared to previous ones the peaks and troughs are on a smaller scale; this is because they are not due to vascularisation, but changes in photoelectric absorption as a result of differences in molecular structure of the regions of the intervertebral disc.

It can be seen from Figure 27 that the central disc has a lower gray value than its edges where there may be some remains of soft tissue. However, the annulus of the disc has less water content as it consists of more collagen. This will mean that the probability of photoelectric absorption occurring will be increased in the annulus; a lighter part of the image will be produced at this point. Generally, it can be seen from the plot profile that there is no major vascularisation hence the relatively smooth line. This supports current literature which states the disc is an avascular structure. There was also some time delay between initial perfusion, dissection and imaging of the intervertebral discs and

intervertebral body of about 30 minutes. Therefore partial diffusion of contrast agent into the outer annulus of the disc may have occurred.

2.3.2.4 Discussion

Figure 13 illustrates that exposure at 60 kVp allows the different major anatomical structures such as skin and bone be distinguished from each other, but it does not allow different types of soft tissue to be distinguished one from another. The addition of potassium iodide via the main caudal median artery reveals the vasculature of the perfused tail. Anteriorly the equine sample has one prominent vessel with another prominent vessel either side on the lateral aspect of the tail. On removal of the soft tissue (muscle, ligaments, tendons, fat and skin), variation in gray value still persists revealing numerous vessels which perfuse the vertebral bodies. The intervertebral disc shows little gray value variation apart from at its edges and no evidence of vessels.

The Beer-Lambert Law states:

$$I_x = I_0 e^{-\mu x} \quad \text{Equation 2}$$

This equation is an illustration of the variation of the intensity of x-rays as a result of an attenuator. Where I_x is the intensity of electromagnetic radiation after it has passed through an attenuator of x thickness, I_0 is the original intensity and μ is the linear attenuation coefficient of the attenuator. Therefore it can be seen that how well x-rays are attenuated depends only on the thickness of the attenuator and its attenuation coefficient. In each case the attenuator is the equine sample. The attenuation coefficient of the sample changes with the

addition of iodine; the amount it changes by depends on the amount of iodine directly. Figure 25 illustrates relative contrast uptake obeying Beer-Lambert's Law. Larger vessels in the soft tissue have peak intensity 30 % greater than the same vessel pre-contrast. The smallest vessels in the vertebral bodies have a peak enhancement between 10 % and 25 % depending on their circumference. The gray value within the disc changes very little, consistent with it being an avascular structure.

2.3.3 Perfusion of the equine sample with barium sulphate

2.3.3.1 Aim

In the previous section potassium iodide illustrated the extent of vascularisation of the soft tissue and vertebral bodies of the equine sample. This needs to be studied in more depth, particularly to look at the endplate and disc region. Barium sulphate is a particulate contrast agent so it will not cross the capillary walls as in the case of potassium iodide; this will prevent a steady rise in background/soft tissue gray value and therefore improved vessel enhancement.

2.3.3.2 Method

To be able to effectively visualise the vessels within the vertebral bodies it is important to select a concentration of barium sulphate which will provide adequate contrast between the vessels and vertebral bodies. A 97% pure specimen of barium sulphate powder manufactured by Alfa Aesar was made up into small quantities of varying weight per volume using a solution of 0.15 moles of sodium chloride; concentrations between 200 g/100 ml and 0.1 g/100 ml.

These suspensions were injected into plastic tubing which was sealed at both ends. The tubing was placed in a row on a sheet of 3 mm thick Perspex. The tubing had an internal diameter of 1.0 mm +/- 0.5 mm and an external diameter

of 2.0 mm +/- 0.5 mm. Two animal vertebrae were placed alongside the contrast filled tubes and an initial exposure of 60 kVp and 5 mA s was taken to enable a comparison between the vertebrae and tubes. The x-ray images were processed using the linear look-up table described previously.

200% 100% 50% 25% 10%
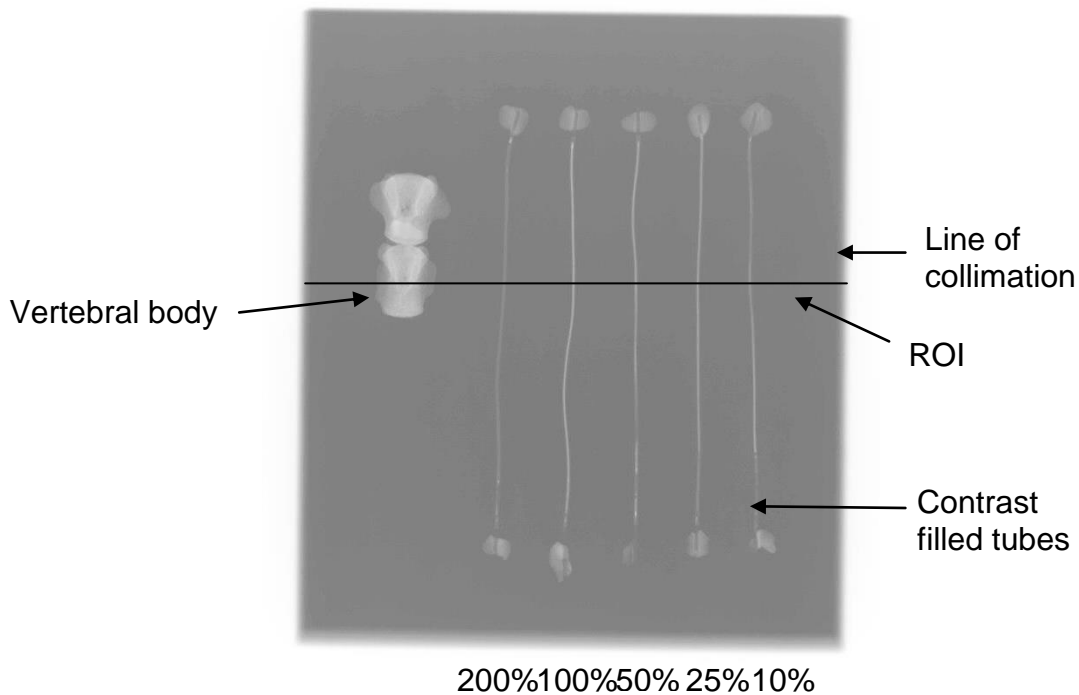
Figure 28: A comparison of contrast obtained with vertebral bodies against various concentrations of barium sulphate. The hollow tubes are filled with variable concentrations of barium sulphate; increasing in concentration from right to left. A ROI is placed across the vertebral body and the filled tubes; this will enable a conclusion to be drawn as to a suitable concentration to enable vessels to be distinguished from the vertebral bodies.

As the weight per volume was increased, the suspension became progressively more viscous, until at 200% weight by volume it was not able to be injected via syringe into the tubes. As can be seen from Figure 28, the 100% weight by volume provides the greatest contrast between the tube and vertebral body.

Using Image J WCIF, a region of interest (ROI) line was drawn across the vertebra and contrast filled tubes, shown in Figure 28. A plot profile of this ROI was produced.
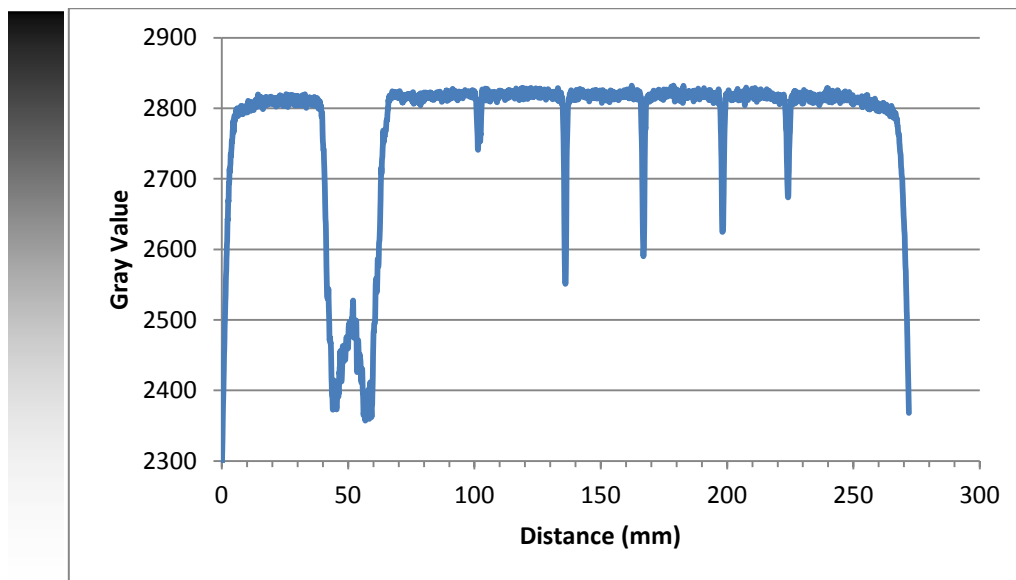
Figure 29: Plot profile of ROI shown in Figure 28. On the far left of the image the vertebral body, can be clearly seen. To be able to clearly distinguish a vessel from a vertebral body the barium needs to produce an adequately bright area. However, barium suspension is quite thick, which makes it difficult to inject as it increases in concentration.

In Figure 29, the two spikes on the left are those of the vertebra; the cortical edges being dense producing a greater level of photoelectric absorption than the centre of the vertebral body. The small spike of the 200% weight by volume (W/V) is due to incomplete filling, can be seen followed by 100%, 50%, 25% and 10% W/V. The concentrations and their gray value can be seen to decrease steadily.

The next stage of investigation was to lay the vertebrae over each of the contrast filled tubes in turn. An exposure with more penetration was given of 90kVp and 32mA s, to determine whether the tubes, representing a vertebral vessel, could be visualised through the vertebral bodies.

From these images it was determined that the 50% W/V suspension would be used to perfuse the equine sample. The advantages of contrast enhancement compared to the viscosity of the suspension had to be considered. The 200% W/V suspension was too thick to inject. The 100% W/V suspension gave the

best contrast enhancement; however, the viscosity of the suspension could mean the fine vertebral body capillaries would not be filled. 25% and 10% W/V had inadequate contrast enhancement.
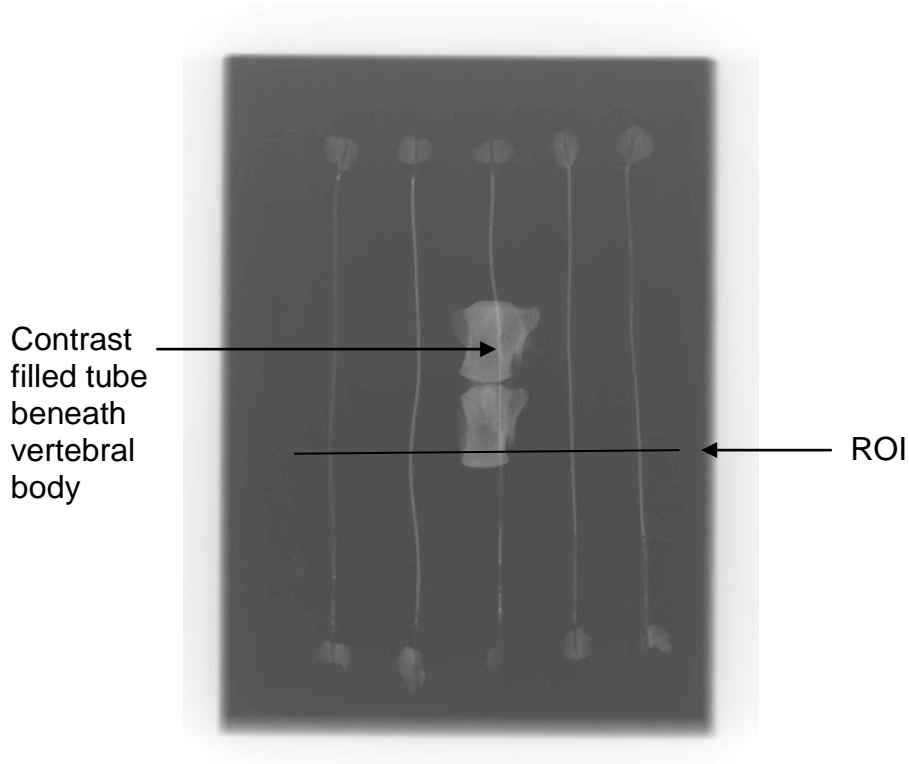
Figure 30: Illustration of contrast enhancement of 50% W/V suspension. The vertebral bodies were placed over each of the tubes in turn; it was then possible by means of a plot profile to determine if vessels would be able to be distinguished within the vertebral bodies.

A ROI was drawn as shown in Figure 30 and a plot profile drawn of this ROI to illustrate the level of contrast enhancement produced by the barium sulphate suspension. This is important in enabling the correct suspension to be selected; suspension filled vessels in the vertebral bodies need to be clearly visualised.
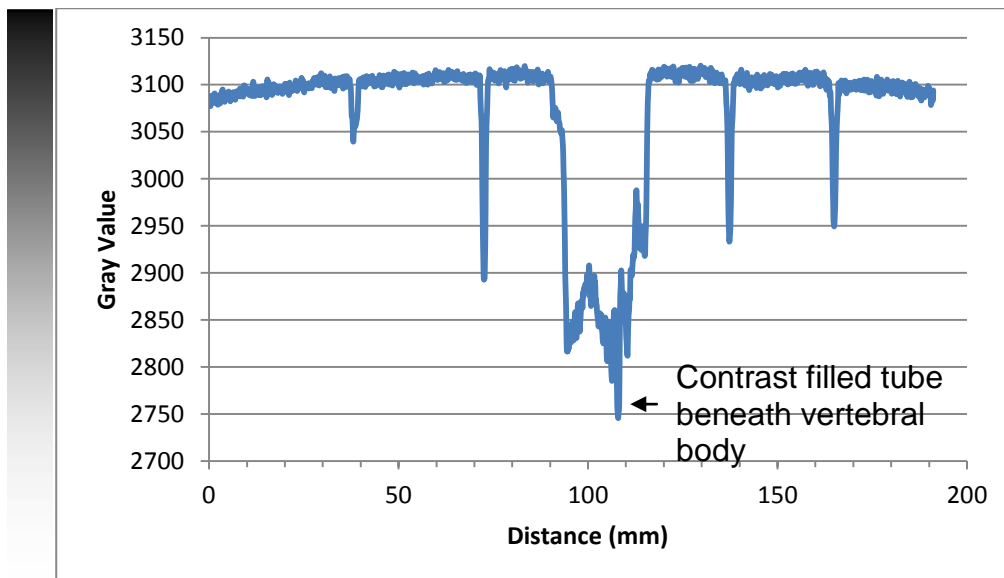
Figure 31: Plot profile of ROI shown in Figure 30. The vertebrae are overlying the 50% W/V suspension. The hollow tube which contains the barium suspension consisting of 50% W/V produces a clearly defined spike beyond the vertebral body. This would make it an adequate concentration to enable vessels to be distinguished.

From Figure 31, it can be seen that the 50% W/V produces an enhanced spike beyond the normal cortical edge spike.

A fresh equine tail sample was obtained from the abattoir and prepared as previously described. The sample was then brought back to the lab at Exeter where it was again perfused with saline. The tail was imaged to give a pre-contrast baseline. For all imaging, the tail was placed on a Perspex sheet of thickness 3 mm and then this was placed directly onto the imaging plate. The tube distance was set at 115 cm as previously. Exposure factors of 60 kVp and 20 mA s were used. Anteroposterior and lateral views of the equine sample were taken.

The sample was then returned to the Biophysics laboratory and perfused with 100 ml of 50% W/V barium sulphate suspension by means of the median caudal artery; a syringe of the suspension was attached to the catheter, the syringe was depressed by hand as fast as possible to ensure filling of the

smallest vessels. The sample was re-x-rayed using the same parameters and set up to allow comparison.

The sample was then further dissected in the laboratory; the majority of the soft tissue was removed to leave the vertebral bodies with the discs between them. This dissected sample was imaged using x-ray and anteroposterior and lateral views obtained.

The sample was returned to the laboratory and further dissected until a four vertebral body segment was obtained. This sample was placed in two litres of a 10% formic acid solution made with de-ionised water. Formic acid will dissolve away calcium present in the sample. The sample was placed in a fume cupboard and left for 48 hours. X-rays under the same conditions as previously were obtained.

The sample was returned to the laboratory and placed in a fresh solution of 10% formic acid and left for a further period of time to allow de-calcification. After a total of 120 hours of de-calcification the sample was re-x-rayed.

The sample was returned to the Biophysics laboratory and placed in a further freshly made solution of 10% formic acid for a further 24 hours.

The sample was then prepared in the following way. The central two vertebrae were selected; the vertebrae superior and inferior to these were removed by slicing through the adjoining discs. Sagittal slices were made across the motion segment of the two vertebrae and their joining disc by means of a saw and wet and dry sanding. These sections were approximately 5 mm thick. From the disc which joined the superior vertebral body to the section an axial slice was

obtained. These slices were arranged on the Perspex imaging sheet and x-rayed using exposure factors of 60 kVp and 5 mA s.

A control tail was imaged intact using 60 kVp and 20 mA s and then dissected to vertebral bodies and discs (removing soft tissue). This allowed profiles across the intervertebral disc to be imaged, calculated and compared; in the intact sample gray values within the x-ray images may be compared before and after infusion of the medium, however, the dissected specimen is compared with a dissected control because the barium suspension cannot be washed out of the dissected specimen.

2.3.3.3 Results
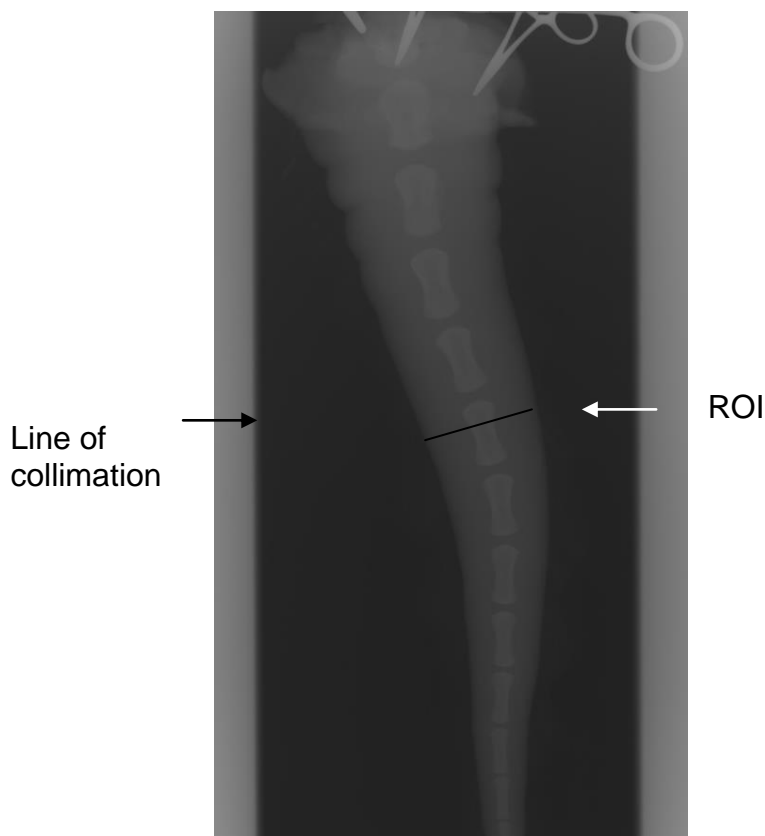
Figure 32: Pre-contrast sample; anteroposterior view, 60 kVp and 20 mA s. This image does not have a wide range of contrast; minimal structures can be distinguished such as soft tissue and vertebral bodies. A ROI is placed over a pre-determined vertebral body.

A plot profile was produced of the ROI demonstrated on Figure 32.
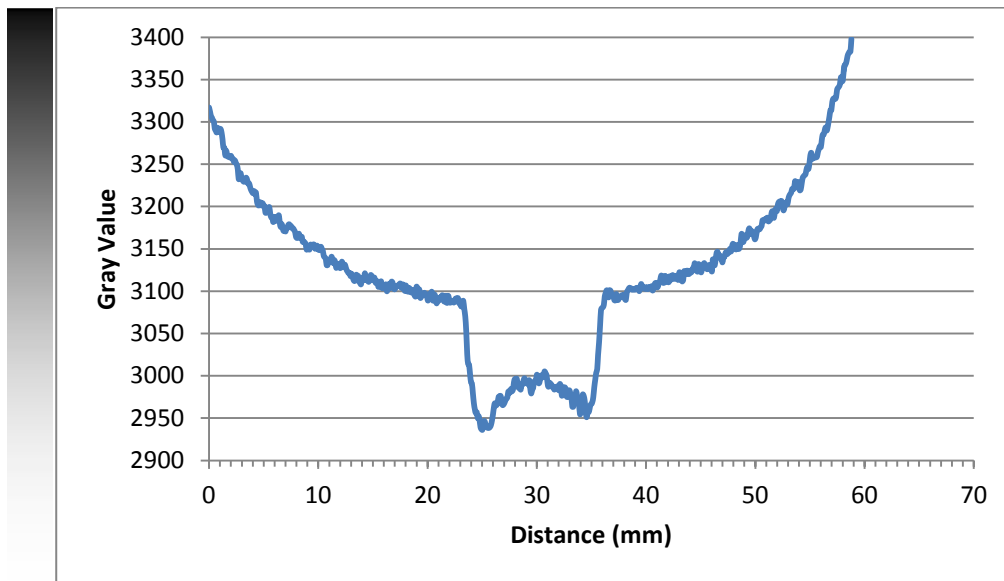
Figure 33: Plot profile of ROI illustrated in Figure 32; the pre-contrast sample. The plot profile clearly demonstrates the relatively smooth line of the soft tissue. The cortical edges of the vertebral body are well defined as bright areas; the centre of the vertebral body is darker as it contains the less dense trabecular bone.

The lowest gray value indicating the brightest area is represented by the two cortical edges of the vertebral body. The middle spongy bone is less dense and therefore photoelectric absorption at this point is reduced. The soft tissue surrounding the bone is also attenuating the x-rays less, producing a darker gray area on the image. As can be seen from this plot profile there are no major vessels visible.

A lateral view was also obtained:

92

Figure 34: Pre-contrast sample; lateral, 60 kVp and 20 mA s. The lateral view enables a conclusion to be drawn if there is any difference in gray value depending on orientation.

A ROI line is placed over the same vertebra as the anteroposterior ROI.
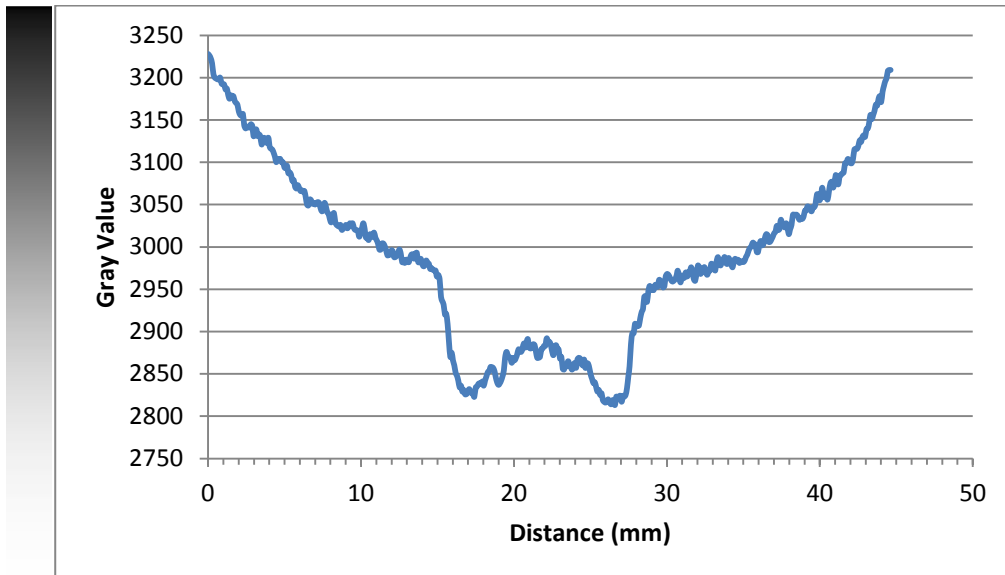
Figure 35: Plot profile illustrating the ROI placed on Figure 34. The lateral view shows a similar plot profile compared to the AP view. The relatively smoth lines of the soft tissue are evident moving into the cortical edges of the vertebral body. Again the darker trabecular bone is evident.

Figure 36: Anteroposterior post-contrast sample; 60 kVp, 20 mA s. The barium enhanced vessels are clearly distinguished; as previously stated there is evidence of a major vessel, probably the median caudal artery. Smaller vessel within the soft tissue may also be seen.

In Figure 36 the perfusion of the vessels, particularly in the skin and muscle by the barium sulphate can be clearly seen. Interestingly when this is compared to the potassium iodide the central major vessel (B) already identified is well perfused, however, in this particular sample either lateral vessel (A and C) is not well perfused. An intensity profile of the ROI shown in Figure 36, passing through the vertebral body was produced.
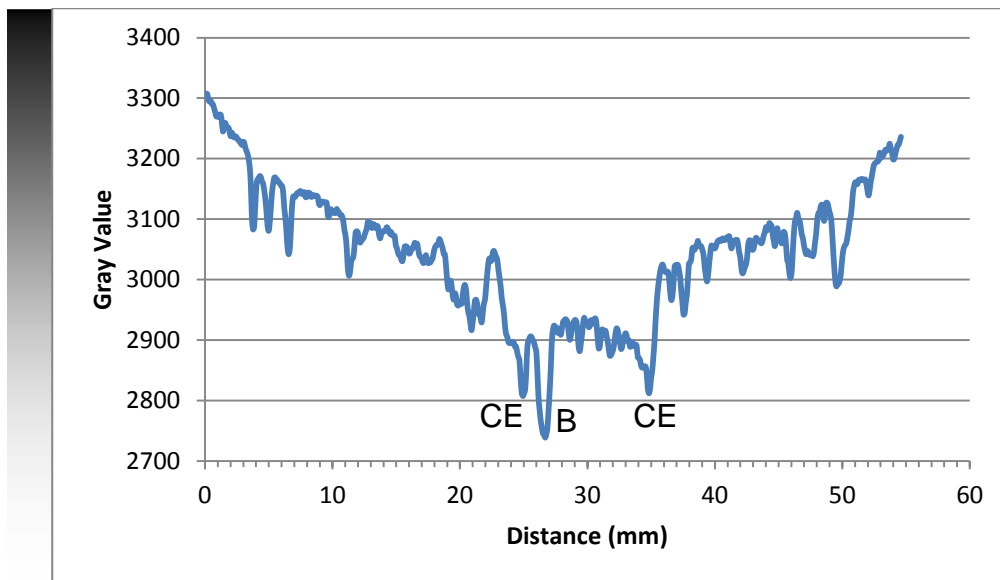
Figure 37: Intensity profile of ROI in Figure 36; CE-cortical edge of vertebral body and B-central median caudal artery. The plot profile shows that the major vessel actually produces a brighter area than the bony cortical edges. However, when compared to the sample perfused with potassium iodide only one major vessel is able to be distinguished.

Figure 37 reveals a number of vessels which have been contrast enhanced. We know that this is not noise and are vessels by comparison with Figure 35, the pre-contrast sample; this appears quite different and consists of a smooth line. The field of view is a 35×43 cm cassette corresponding to 4020×4892 pixels to provide the spatial resolution. The main vessel is clearly seen; however, at the point of the ROI the two lateral vessels identified on either side of this main vessel cannot be seen due to the poor filling of these vessels.

The intact sample was returned to the laboratory and as much soft tissue as possible was removed leaving the vertebral bodies and intervertebral discs.
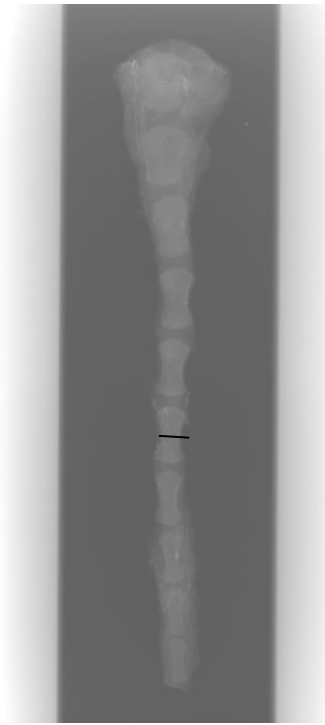
Figure 38: anteroposterior vertebral bodies and intervertebral discs; post-contrast, 60 kVp, and 20 mA s. The soft tissue is removed from around the spinal column; this allows us to clearly see vessels associated with the vertebral bodies and the intervertebral disc. A ROI is drawn across a specified vertebral body and a plot profile produced of this region, see below.
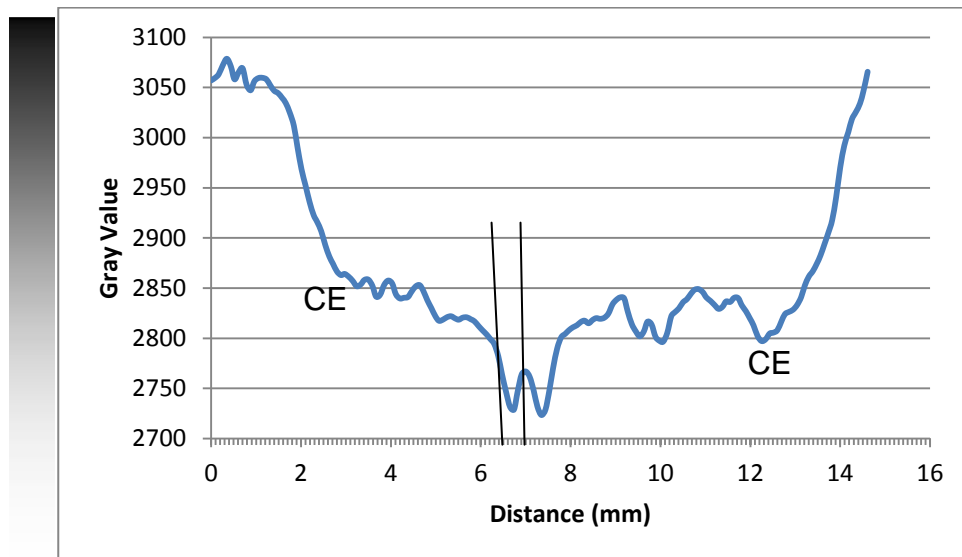
Figure 39: Plot profile of ROI in Figure 38; CE-cortical edge. The plot profile illustrates the cortical edges of the vertebral bodies, which appear bright on the image due to their density. Within the centre of the vertebral body two vessels can be clearly distinguished; the right (anatomically) vessel is highlighted by the two vertical lines.

After removal of soft tissue (Figure 39) two vessels are easily resolved, which are actually already apparent in Figure 38. These vessels arise from the main artery and apparently deliver nutrient to the vertebral body; their diameter is 0.5 mm. Smaller vessels within the vertebral bodies themselves are also discernible.

Figure 40: Lateral vertebral bodies and intervertebral disc; post-contrast, 60 kVp, and 5 mA s. The process is repeated taking an image in the anatomically lateral position to determine accurately the position of vessels which are present.

The lateral view (Figure 40 and Figure 41) provides a clearer picture of vessel orientation. There are two dominating troughs which represent the cortical edges and highlighted main vessel feeding the vertebral body.
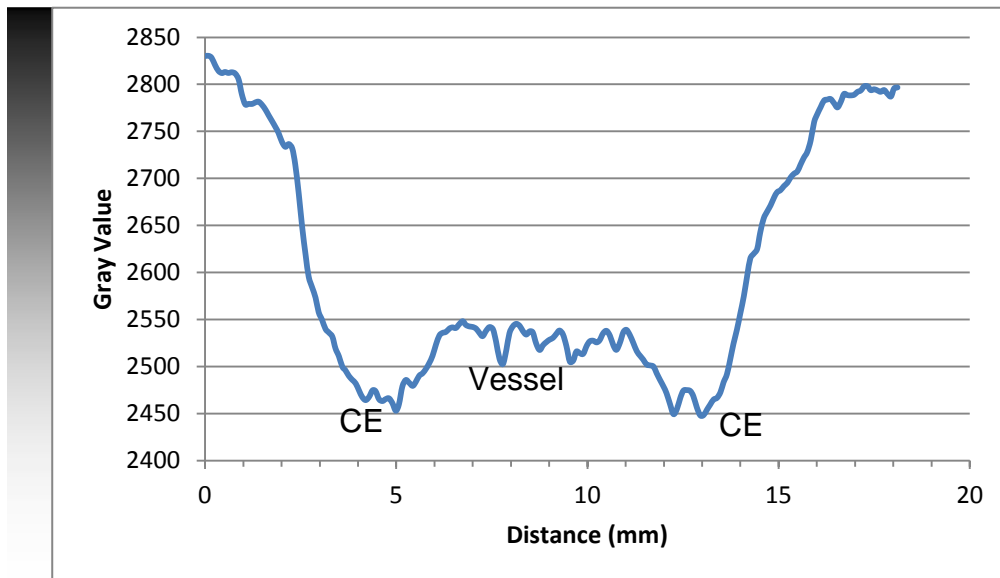
Figure 41: Plot profile of ROI, Figure 40; CE-cortical edge. In the lateral position the cortical edges of the vertebral body are again clearly seen. The two central vessels, although less prominent, can still be clearly see within the centre of the vertebral body.

A complex pattern of de-calcification was seen. This began in the core of the vertebral body and the denser cortical bone was de-calcified only after 120 hours of exposure to formic acid. At intermediate times of digestion it was difficult to distinguish absorption peaks arising from contrast agent from those due to remaining calcium deposits. The many peaks and troughs of absorption seen on the x-ray images are more likely to be from uneven de-calcification, the peaks and troughs are too large to be vessels within vertebral bodies. De-calcification visually affected the vertebral bodies making them appear to have a 'fluffy' appearance (Figure 42) with obvious radiolucent spaces. Vessels supplying the vertebral bodies as de-calcification progressed became quite obvious due to the lack of calcium and density in the vertebral bodies. The central portion of the vertebral body, after 120 hours of de-calcification (Figure 43), is more evenly de-calcified, demonstrated by smaller peaks and troughs.

Figure 42: Vertebral bodies and intervertebral discs post-contrast after 120 hours de-calcification; lateral view 60 kVp, 5 mA s. When compared to previous images, the de-calcification process is clearly seen; the well-defined cortical bone boundary is no longer evident and there is a lack of trabecular bone markings.
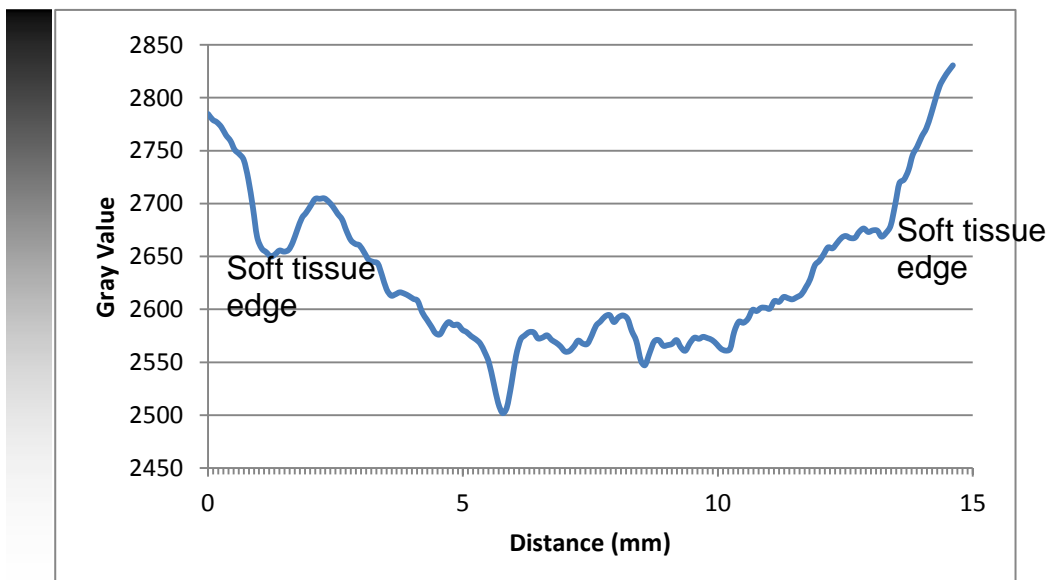
Figure 43: Plot profile of ROI in Figure 42.The lack of clear bony markings can be seen in the plot profile; it manifests itself as many peaks and troughs. The variable size of the peaks and troughs illustrate the unevenness of the de-calcification process. There does appear to be some vascularisation present demonstrated by the larger troughs.
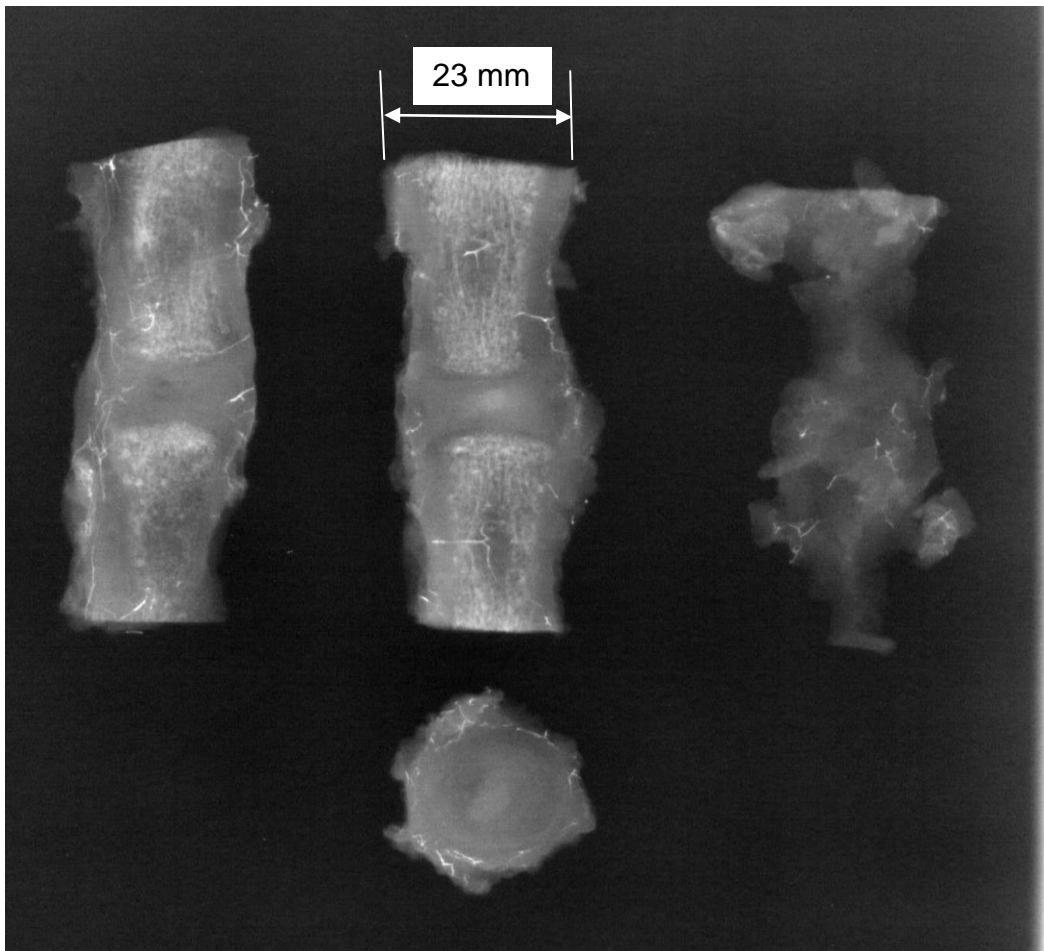
Figure 44: Sagittal slices of central two vertebrae from the four vertebrae section; 60 kVp, 5 mA s. The two central vertebral bodies in the group of four were removed and sliced thinly in the sagittal orientation using a saw and clamp. An intervertebral disc was removed from the surface of the remaining vertebral bodies and sliced in the axial orientation. In the sagittal slices various nutrient vessels are seen and barium filling vessel openings in the main vertebral body. The disc can be seen to have a ring of vessels surrounding it; however, there is no evidence of major vascular penetration into the disc.

Figure 44 shows two vessels, one running anteriorly and one posteriorly, which branch into the centre of each vertebral body. From these main vessels, smaller branches evolve in a mesh-like structure tracing trabeculae and moving through pores within the structure to appear end-on in the x-ray. These vessels appear to end at the vertebral body/disc interface. The axial view of the disc shows a ring of vessels around the disc which penetrate into the outer annulus..

The first 2 slices in Figure 44 were magnified using Image J WCIF.
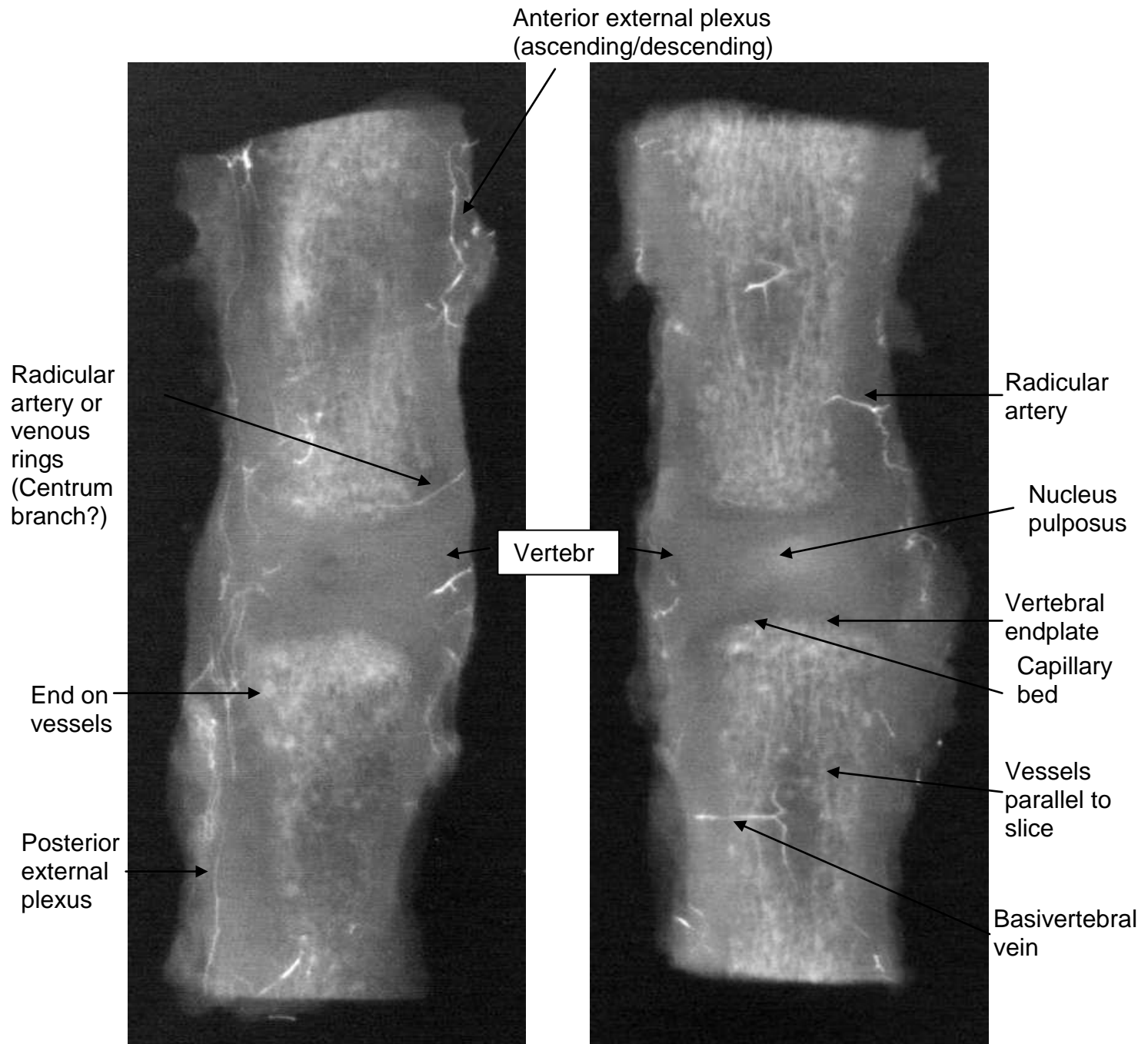
Figure 45: De-calcified perfused motion segment. The two best slices from the previous image were magnified; the trabecular nature of the bone can be seen and the nutrient vessels which anastomose over the surface of the vertebral bodies. It can be seen that there is no evidence of major vascular penetration of the intervertebral disc.

The posterior external plexus has a diameter of 0.26 mm. The radicular artery

has a diameter of 0.24 mm. The basivertebral vein has a diameter of 0.32 mm.

Capillaries
fed by
venous
plexus

Outer
annulus

Nucleus
pulposus

Inner
annulus
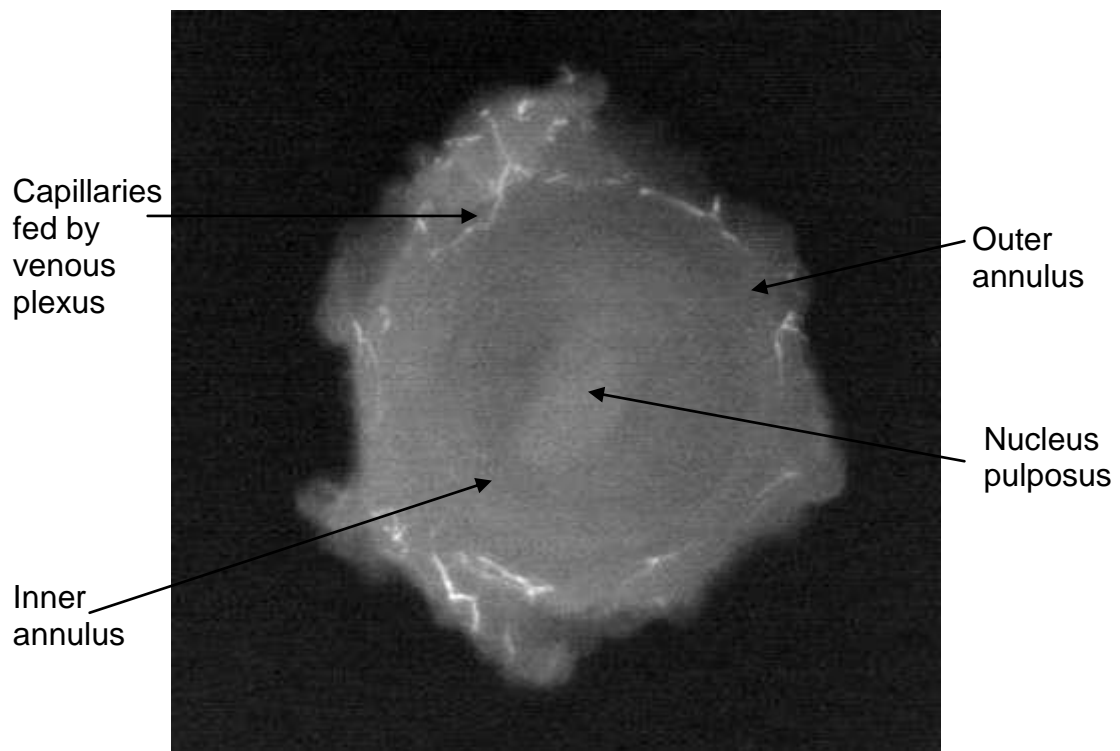
Figure 46: Perfused axial disc slice. The axial view of the intervertebral disc is useful in determining the extent of vascularisation of the intervertebral disc. The vessels are seen to penetrate a little way into the annulus; however, no major penetration is evident.

Figure 46 illustrates that vessels penetrate only into the very outer part of the annulus; there appears to be no vessels in the main body of the disc. Around the intervertebral disc vessels appear to form a circular structure and have a diameter of approximately 0.17 mm.

The control tail was imaged in a similar way; no contrast has been added. The plot profile gives similar values to the pre-contrast barium sulphate sample; this is reassuring when using this sample as a control.

Using the dissected control equine sample and the dissected barium sulphate equine sample (Figure 38) the % uptake in contrast within the vertebral body and intervertebral disc can be calculated. The method is as described in section 2.3.2.3. A new ROI over the same vertebra used previously allowed the same length of ROI to be used in the control sample and perfused barium sulphate

equine sample; the ROI was transferred between the samples using Image J

WCIF.

Control tail

Post-contrast tail
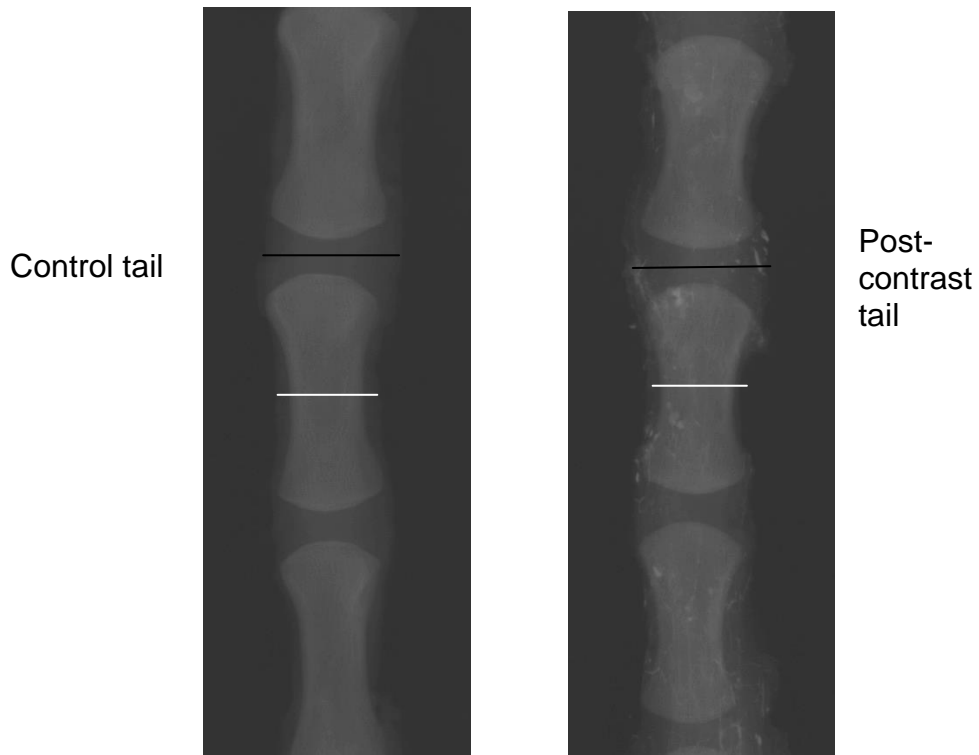
Figure 47**: An Illustration of vertebral body and intervertebral disc ROI. The vertebral body is the one used in previous ROI. It is important to understand the true extent of the appearance of de-calcification on the x-ray image. The best way of achieving this is to use a control tail which has not been perfused with contrast agent and to compare the two tails. In the control tail the only anatomical structures visible are the vertebral bodies and the soft tissue as a whole. The vessel can be seen in the post-contrast tail.**
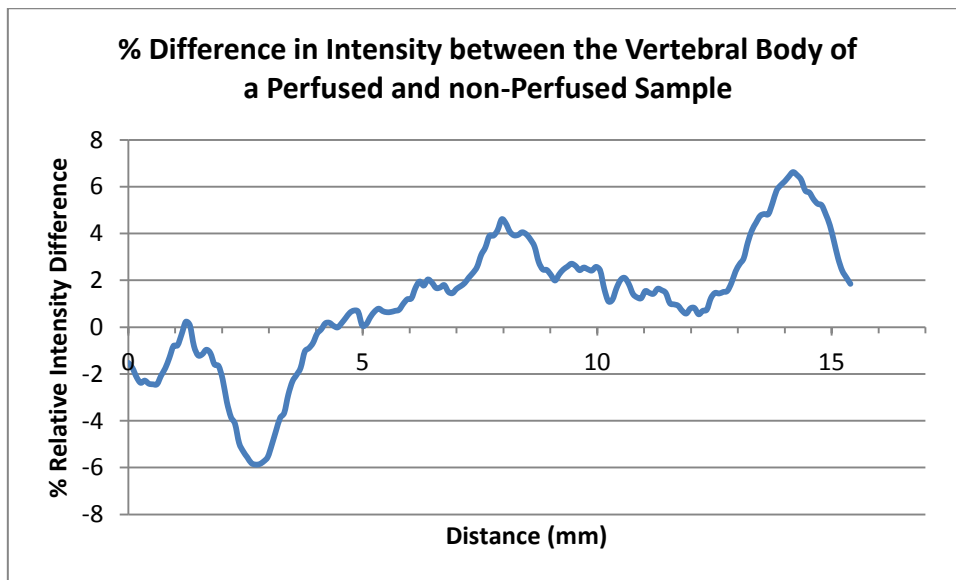
Figure 48**: Illustration of contrast uptake based upon change in gray value (intensity); positive values show the barium sulphate perfused sample showing an increase of intensity in the image due to contrast uptake. The highest areas of uptake when compared to the previous image are areas defined as vascular regions.**

It can be seen from Figure 48 that the highest change in gray value and therefore the area of largest contrast uptake is ~7 %. There are two areas in Figure 48 which show signs of largest contrast uptake. The largest area of contrast uptake, if Figure 38 is studied, represents a light area over the right of the vertebral body; this is one of the vessels which circle the vertebral bodies to provide nutrition to them. The large trough to the left of Figure 48 is where the ROI has extended to the image receptor.

The same process was repeated with ROI placed over the intervertebral disc. Figure 49 illustrates the uptake of contrast across the intervertebral disc. It is an extremely interesting profile. From 0 to 3 mm is the remaining soft tissue. The peak in contrast uptake is a vessel running along the edge of the intervertebral disc. It can be seen that along the disc itself is a fairly uniform change in gray value; there was some delay, approximately thirty minutes from perfusion to dissection and then imaging. The second peak at 23 mm is another vessel

present along the side of the disc. The maximum relative % increase in contrast across the intervertebral disc is 3 %. Comparing Figure 48 to Figure 49, the maximum peak rise in contrast in the disc is half as much as the peak contrast rise in the vertebral bodies.
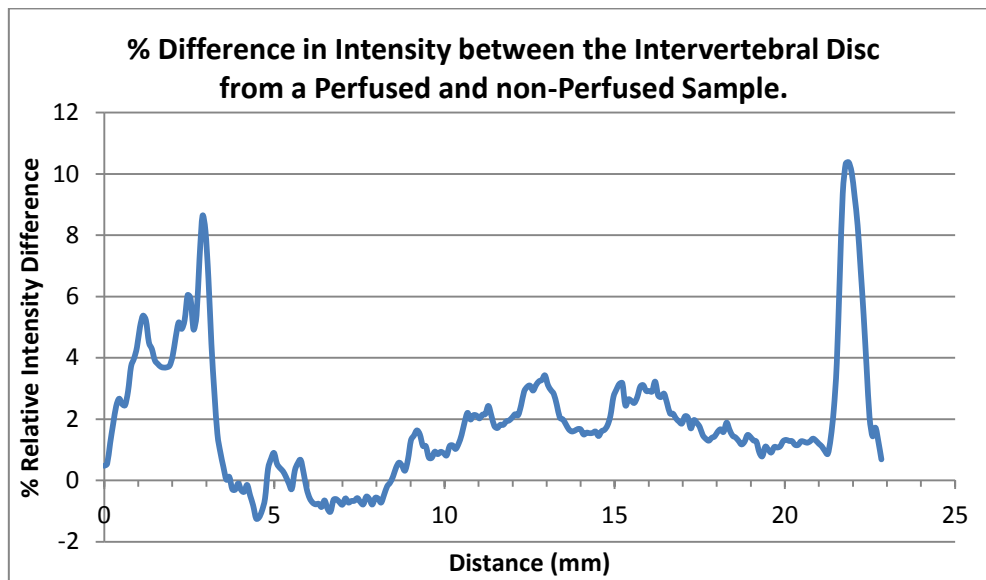
Figure 49: Illustration of contrast uptake across the intervertebral disc. Positive values are indicative of the barium sulphate sample having an increase in intensity. The plot profile across the width of the intervertebral disc is fairly uniform in the amount change in intensity between the control and the perfused sample. The two major peaks to the left and right of the plot profile are indicative of vessels running alongside the disc which are evident in the previous x-ray.

2.3.3.4 Discussion

This experiment has shown that the 'backgrounds' in the intervertebral disc and the vertebral body are higher in the perfused sample than the non-perfused sample. This indicates uptake either by diffusion out of the vasculature or of barium contained in capillaries which are below the resolution of the individual vessels.

It had been highlighted in section 2.2.3 when the equine sample was perfused with potassium iodide that there were three main vessels anteriorly. Barium sulphate perfused the median caudal artery well; however it did not perfuse the

other two vessels well. One explanation may be that the initial flushing with saline was not adequate allowing for the opportunity for clots to form. Barium sulphate is particulate in nature; an experiment focussing on imaging of the upper gastrointestinal tract found the particles in their low viscosity barium suspension settled into mucosal grooves (Anderson, et al., 1980). The two main lateral vessels are likely to be venous return (it is likely that the two lateral vessels are the cutaneous branch of the internal pudendal vein); therefore it is possible barium sulphate has not penetrated the capillary bed. Although barium sulphate is a difficult suspension to inject, its viscosity makes it ideal for sectioning. On sectioning there were found to be vessels which ran longitudinally along the vertebral bodies; these vessels branched into smaller vessels which penetrated the vertebral bodies and encircled the intervertebral disc. The vessels appear to end at the vertebral end-plate in a discoid shape. The vertebral bodies have many small vessels throughout, the largest of which altered the intensity of the image by~7 %. The intervertebral disc showed no evidence of vessels being present. Vessels penetrate the very outer part of the annulus only. The gray value peak in the intervertebral disc was 3%.

The discoid shape of the vessels at the vertebral endplate is similar to the findings of Crock and Goldwasser (Crock & Goldwasser, 1984). They noted in canines this discoid shape and its variability along the endplate with larger terminations occurring over the area of the nucleus. This was also found in humans (Urban & Winlove, 2007); rather than size of the terminations density of the capillaries varied with the highest density over the area of the nucleus. In the x-rays obtained the intensity of the barium contrast along the vertebral endplate area is variable, however, it is difficult to exactly determine this variability. The use of Evans blue in the next section will aid investigation of the

capillary bed. Physiologically, this is important; nutrients accessing the nucleus of the disc via the annular route have a greater distance to diffuse than those nutrients diffusing via the vertebral endplate. A sensible biological adaption is increased density and/or size of vessels at the endplate to aid diffusion to the nucleus.

2.3.4 Perfusion of the equine sample with barium sulphate and Evans blue

2.3.4.1 Aim

In the previous section particulate barium sulphate has been used to visualise the vasculature, but it is impossible to say whether the diffuse background distribution in the vertebral body and disc arises from soluble material in the barium sulphate or from particles contained in small capillaries. For the later work of this thesis it is important to establish boundaries between vascular delivery and transport through the tissue matrix. To this end, further experiments were undertaken in which tails were perfused with a mixture of barium sulphate and Evans blue, a highly diffusible tracer with a molecular weight of 960.81 g mol^{-1}, which is easily visualised by light or fluorescence imaging.

2.3.4.2 Method

Two tails were used, one sample as a control and the other perfused with barium sulphate and Evans blue. The two tails were prepared as described in section 2.2.1.

The barium sulphate/Evan's blue perfusate was prepared; 100 ml of 50 % W/V suspension of barium sulphate and 0.15 m of sodium chloride with an added 1 g of Evans blue. The test tail was then perfused with this solution using a syringe

via the cannula in the median caudal artery and x-ray imaged under the protocols described in sections 2.3.2.2. It might be expected that the particulate barium will become lodged in the capillaries, but it appears that this was not the case because it was possible to establish full perfusion from the arterial side into the venous side.

The sample was then divided into two; the superior section consisted of 3 ½ vertebral bodies the inferior section consisted of 3 plus two ½ vertebral bodies. One section was placed in 10 % formic acid for de-calcification. The other was fixed in a 5 % formalin solution.

The control sample was also imaged and then divided into two for decalcification or fixation.

After a period of seven days the sections in 10% formic acid were placed in 5% formalin for preservation whilst the sections in 5 % formalin were removed and sectioned, as shown in Figure 50.
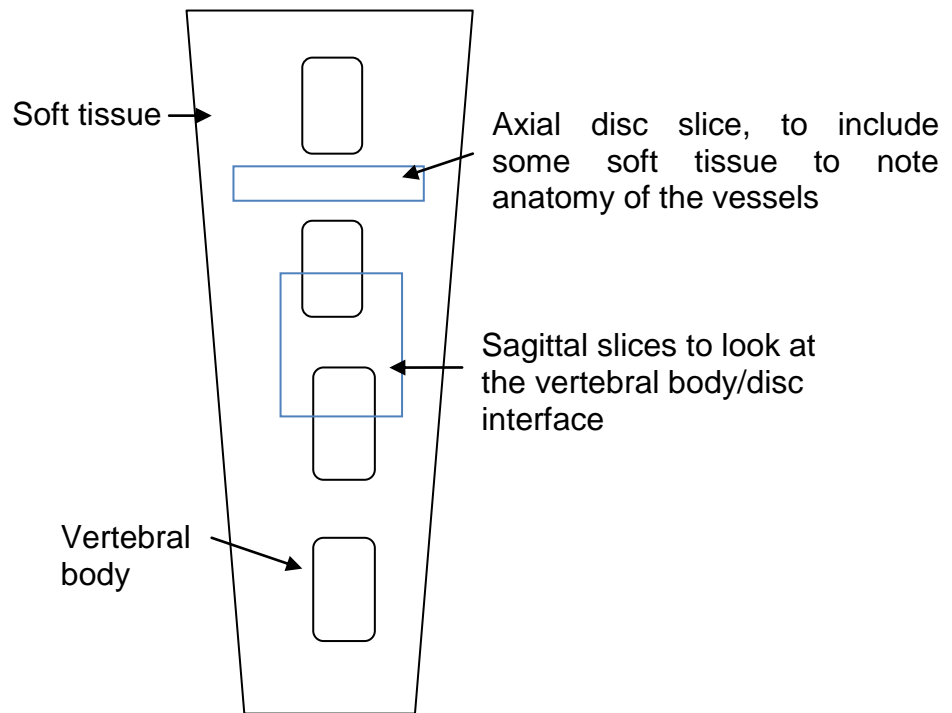
Figure 50: Schematic of slices obtained from the sample sections; the slice regions are illustrated in blue. The sagittal slice incorporates the vertebral end-plate of a superior and inferior vertebral body adjoining a whole disc. The axial slice only incorporates the intervertebral disc.

The slices were initially prepared using a saw and reduced in thickness to 5 mm by sanding. The four separate samples were all imaged as previously described.

2.3.4.3 Results

The images of the whole tail samples and pre-treatment sections are not shown here; plot profiles and average gray values were comparable with the two previous samples.
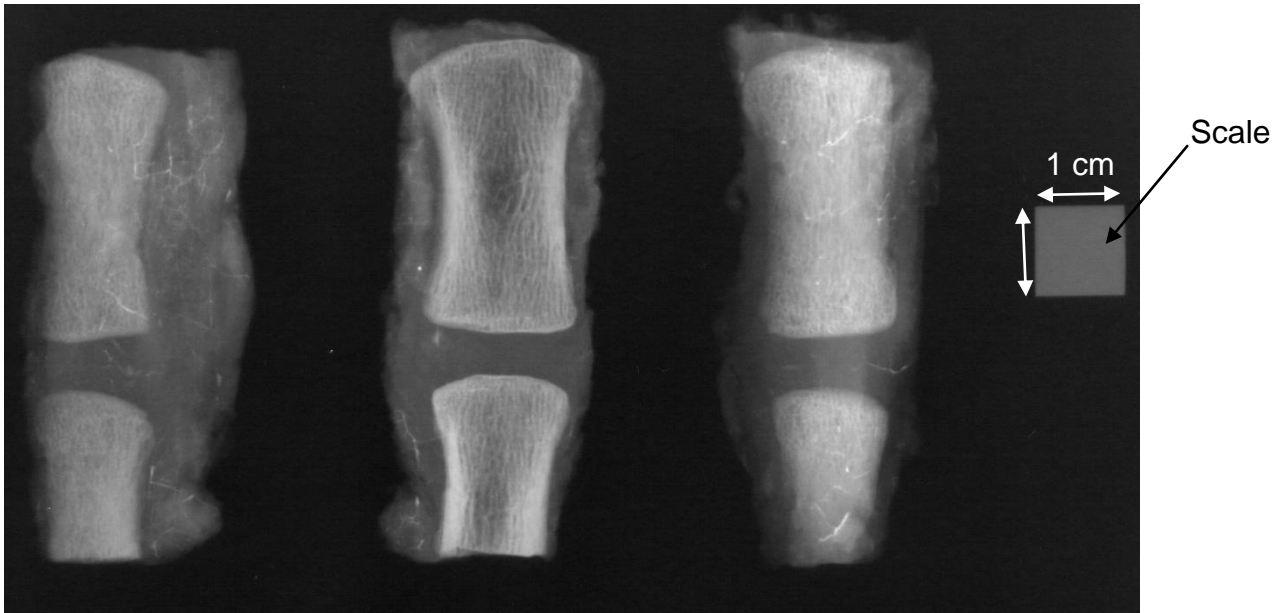
Figure 51: Barium sulphate/Evans blue sections, preserved in 5 % Formalin. This is a sample which has been perfused but is not undergoing the de-calcification process; the is extremely important in determining how the de-calcification process appears on x-ray. Several nutrient vessels may be seen.

In Figure 51 the contrast perfused sample is illustrated. The vessels which feed the vertebral bodies are clearly evident. Vessels which encircle the intervertebral disc are also visible. Contrast has concentrated along the cortical edges of the vertebral bodies and at the end-plates. The trabeculae of the vertebral body structure are well visualised.
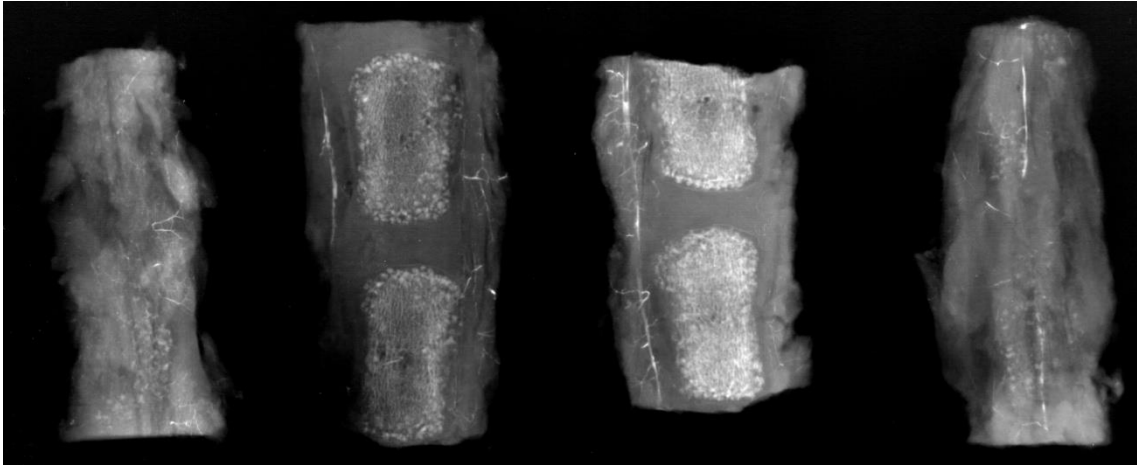
Figure 52: **De-calcified barium sulphate/Evans blue section, 10% formic acid plus 5% formalin. This specimen has been perfused with contrast agent, then de-calcified and finally preserved. If this image is compared to the previous image, the change in appearance as a result of de-calcification is notable; the barium perfusate in the above image can be clearly distinguished.**

Figure 52 illustrates that after de-calcification the vertebral bodies have a distinctive appearance. The dense calcium scaffolding structure of bone has been removed. The barium sulphate is now the densest material remaining. The far left and right slices show a main posterior and anterior artery. The two central slices show ascending and descending arteries. A mesh of vessels appears to feed the vertebral bodies, with a vessel coming from the side into the centre of the vertebral body. At the end-plate region the vessels appear to terminate in buds.
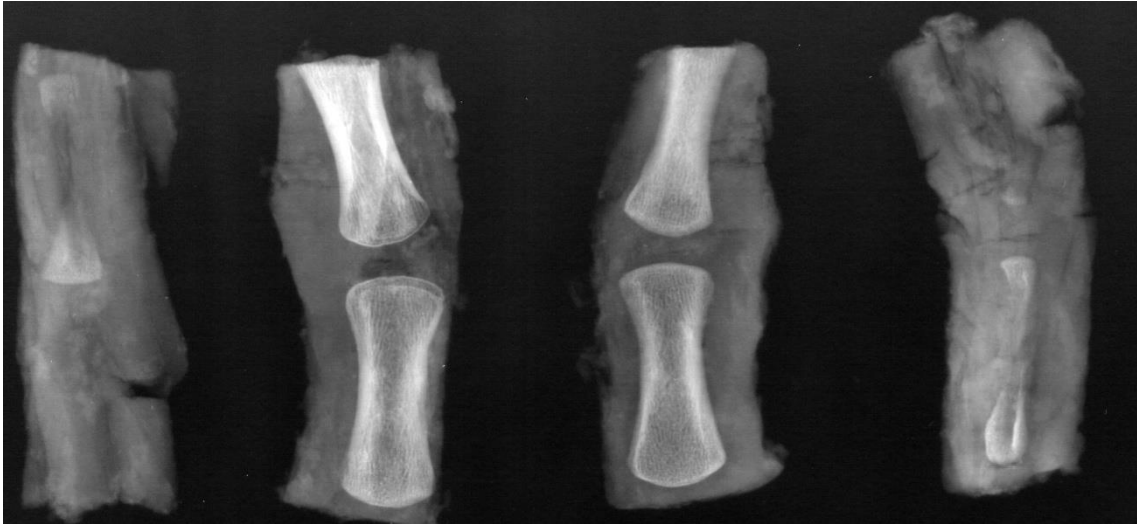
Figure 53: Control sample, preserved in 5% formalin. This specimen has had no contrast agent added, therefore when compared to the previous two images it is evident that vascularisation cannot ne determined apart from other soft tissue structures. However, the two different types of bone within the vertebral body, cortical and trabecular is obvious.

Figure 53 shows the control sample. If this figure is compared to the equivalent barium sulphate/Evan's blue sample (Figure 51) it does not have such an even distribution of image contrast. The cortical edges of the vertebral body are whiter than the spongy central portion and vessels cannot be distinguished.

The de-calcified control sample has a different appearance to the de-calcified barium sulphate/Evans blue sample. The extensive beading appearance in Figure 52 is not seen in Figure 54. The vertebral bodies have an even image contrast due to de-calcification; less distinction between cortical edges and spongy central bone.
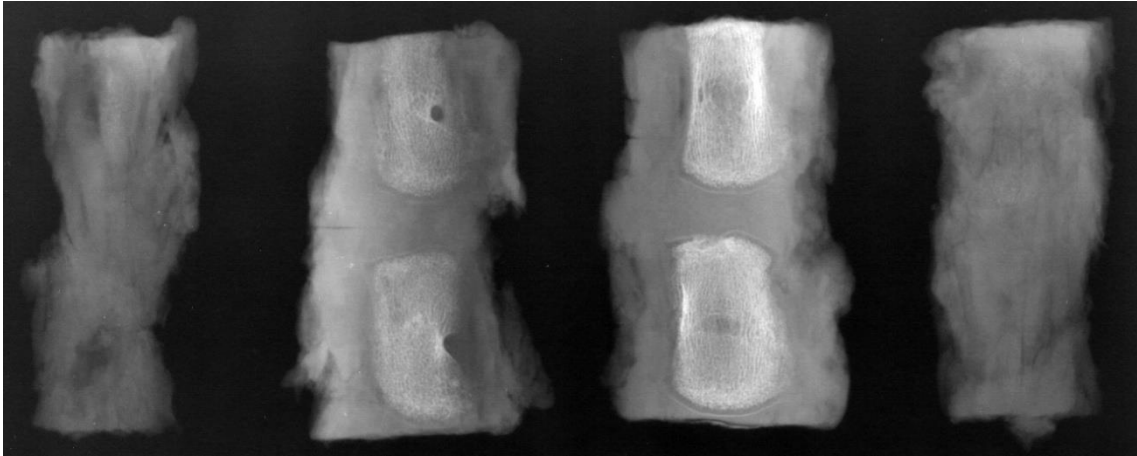
Figure 54: De-calcified control sample; 10% formic acid and 5% formalin. This sample has not been preserved with contrast agent; however, it has been de-calcified. On comparison with the previous image the effect of the de-calcification process is notable. There is a lack of a clear boundary between the cortical and trabecular bone and generally the vertebral bodies have a 'woolly' appearance. Having said this even though the sample is de-calcified the vasculature cannot be identified.

It is clear from Figure 55 below that the barium sulphate has completely filled the vessels of the vertebral bodies. Main vessels which run alongside the vertebral bodies within the soft tissue can be seen. These vessels branch to the centre of the vertebral body where they form a mesh of nutrient vessels. The capillary terminations at the endplate next to the nucleus are discoid in shape and are 0.1 cm in size, next to the outer annulus these terminations are not in the form of discs but small buds which are 0.6 mm in diameter. Horizontal venous collecting ducts are evident which have a diameter of 0.2 mm.
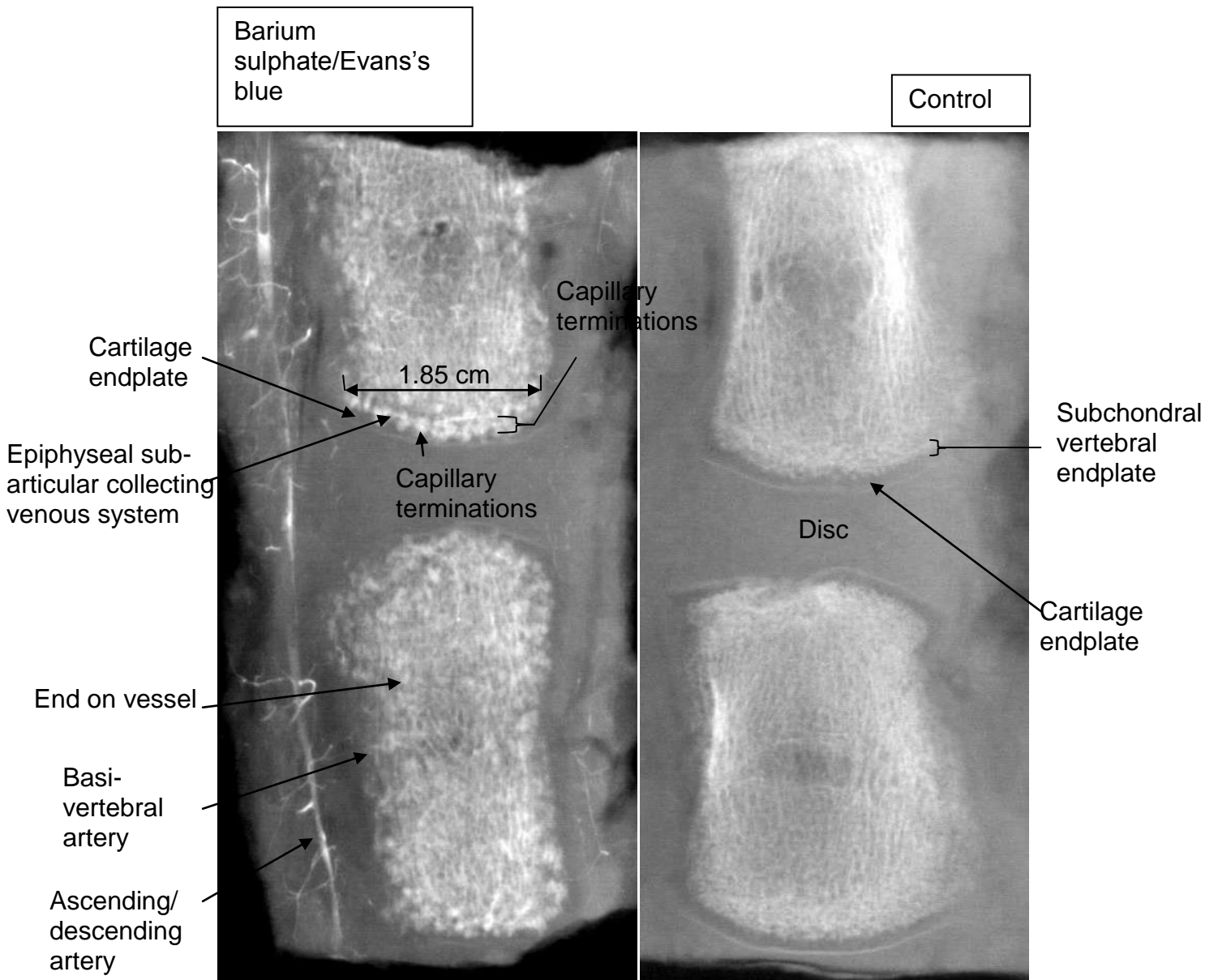
Figure 55: Comparison of a perfused and non-perfused de-calcified sample. This image clearly demonstrates the effect of the de-calcification process. The barium within the sample on the left can be easily identified. The right image demonstrates the vacuoles, but vessel positioning cannot be determined.

Although difficult to measure, visually it is evident from Figure 55 that there is an increased density of capillary terminations alongside the nucleus.

Figure 56 below illustrates axial disc slices. Barium sulphate reveals a vascular system which forms a ring of vessels around the disc. These vessels have branches which also partially penetrate the outer annulus. The depth to which the outer annulus is penetrated is approximately 1 to 2 mm.
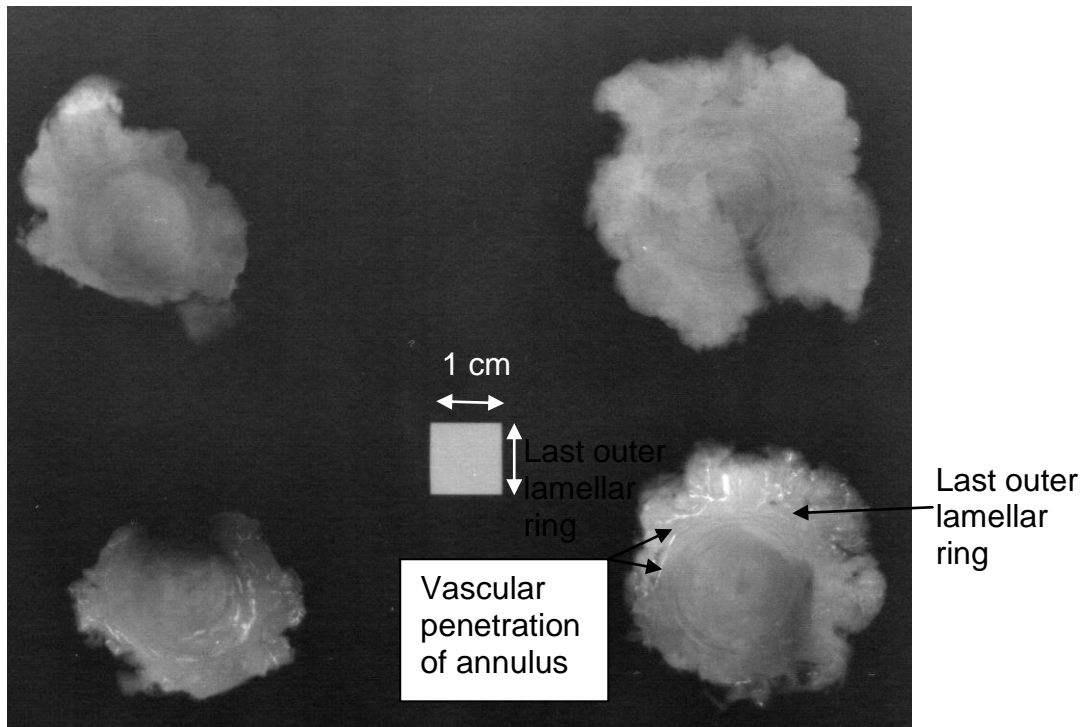
Figure 56: Four axial disc slices from the four sections, from the top left in a clockwise direction: control (calcified), control (de-calcified), barium/Evans blue (calcified) and barium/Evans blue (de-calcified). The de-calcification process seems to make very little difference to the appearance of the intervertebral disc, whether it is perfused or not. This is due to the constituents of the intervertebral disc.

2.3.4.4 Discussion

This experiment the sample, unlike the previous sample perfused with barium sulphate, when compared to a control, allowed the effect and presence of the barium to be determined with confidence.

It can be seen from Figure 55 that the capillary terminations are barium filled; over the area alongside the nucleus these terminations are large discs, next to the outer annulus these terminations are not in the form of discs but small buds. This is consistent with data from other species as described in the previous sample (section 2.3.3.4).

An important structure identified in this sample is the horizontal venous collecting ducts between capillary terminations; these distinct horizontal collecting ducts have also been seen in humans (Urban & Winlove, 2007).

This sample had also been perfused with Evans blue. The remaining portions of the tail were not adequate in size to perform light imaging of the distribution of Evans blue; therefore, a new sample was prepared as detailed below.

2.4 Vascularisation of the equine sample using Evans blue

2.4.1 Gross vascularisation

A fresh equine sample was collected from the abattoir and prepared as described in section 2.2.1. The equine sample was perfused with a 1 % solution of Evans blue and sodium chloride using a syringe via the median caudal artery. The sample was dissected as described in section 2.2.2.

Figure 57: Tail sample perfused with Evans blue; varying shades of blue denote varying levels of vascularisation. One of the most vascular anatomical structures is muscle due to its high metabolic state; this is represented by the dark blue, many vessels have taken up the Evans blue. Fat does not possess as many vessels as muscle and therefore has a pale blue appearance.

Figure 57 clearly illustrates areas of highest vascularisation. Muscle is the darkest and the connective tissue of the fascia is a mid-blue, illustrating its lack of Haemoglobin in comparison to muscle tissue. Skin is a light blue and the sub-dermal fat layer is very pale blue. The sample was dissected further removing most of the soft tissue. A segment of two vertebrae were obtained. Initially the motion segment was clamped and sawn into 5 mm slices.

Cortical bone of the vertebral body

Muscle

Ligament

Trabecular bone of the vertebral body

Annulus of the intervertebral disc

Nucleus pulposus of the intervertebral disc
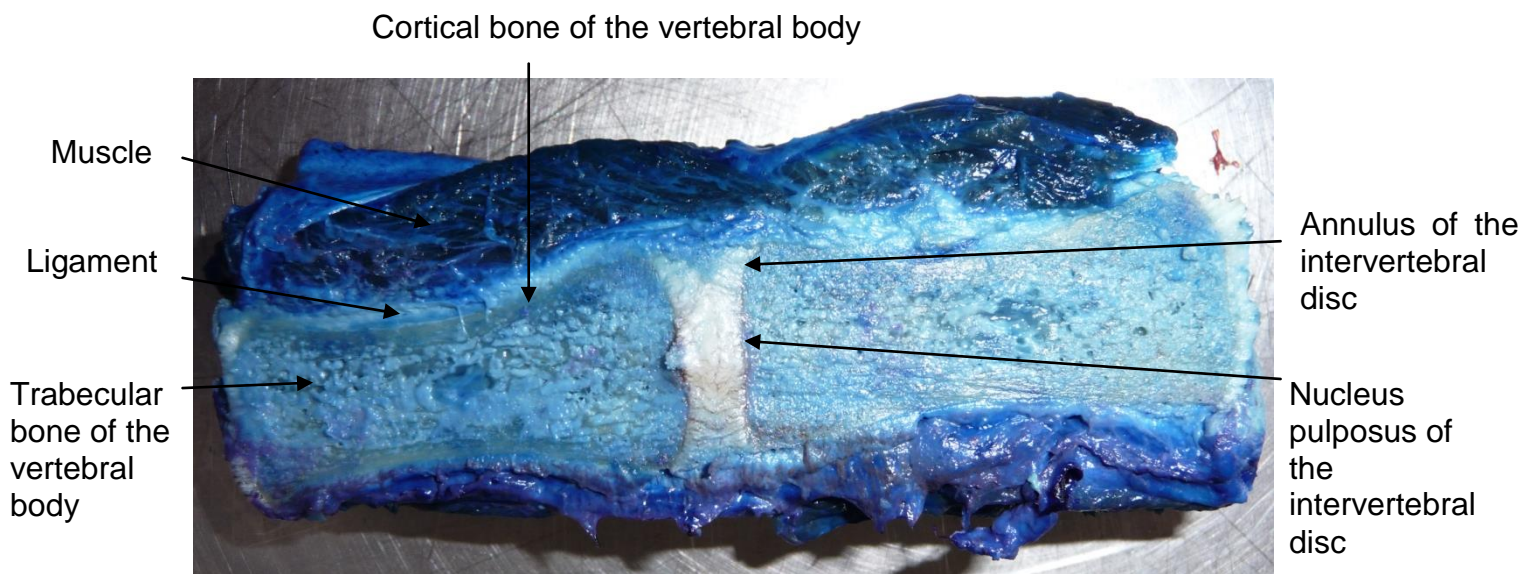
Figure 58: A motion segment of the equine sample; perfusion of Evans blue represents level of vascularisation. The previous sample had a motion segment removed and thinly sliced with a clamp and saw. In this thin section it is easier to see the various anatomical structures such as bone, muscle and ligament; their variable shades of blue, again indicate the extent of vascularisation. It can be seen that the intervertebral disc is almost nearly white due to an absence of vessels.

Figure 58 illustrates the level of vascularisation within the caudal spine and its surrounding soft tissue structures. Muscle is the soft tissue structure with a high level of vascularisation; cells of the muscle have a high metabolism, due to their function in providing energy to enable the muscle to do work **Invalid source specified.**. Ligaments have less vascularisation compared to muscle tissue, therefore they are a light blue. The intervertebral disc can be seen as almost completely white. This is due to its avascular nature. Parts of the outer annulus

do have some Evan's blue present; but it is likely that this is due to spreading of dye during the slicing process. Imaging occurred 30 minutes post perfusion for Figure 57 and 2 hours post perfusion for Figure 58.

2.4.2 The vertebral endplate

The sample shown in Figure 58 was reduced in thickness to 1 mm by wet and dry sanding. This sample was photographed using a video microscope (Nikon Eclipse 200 at varying magnification) to produce images of the vessels at the vertebral endplate.
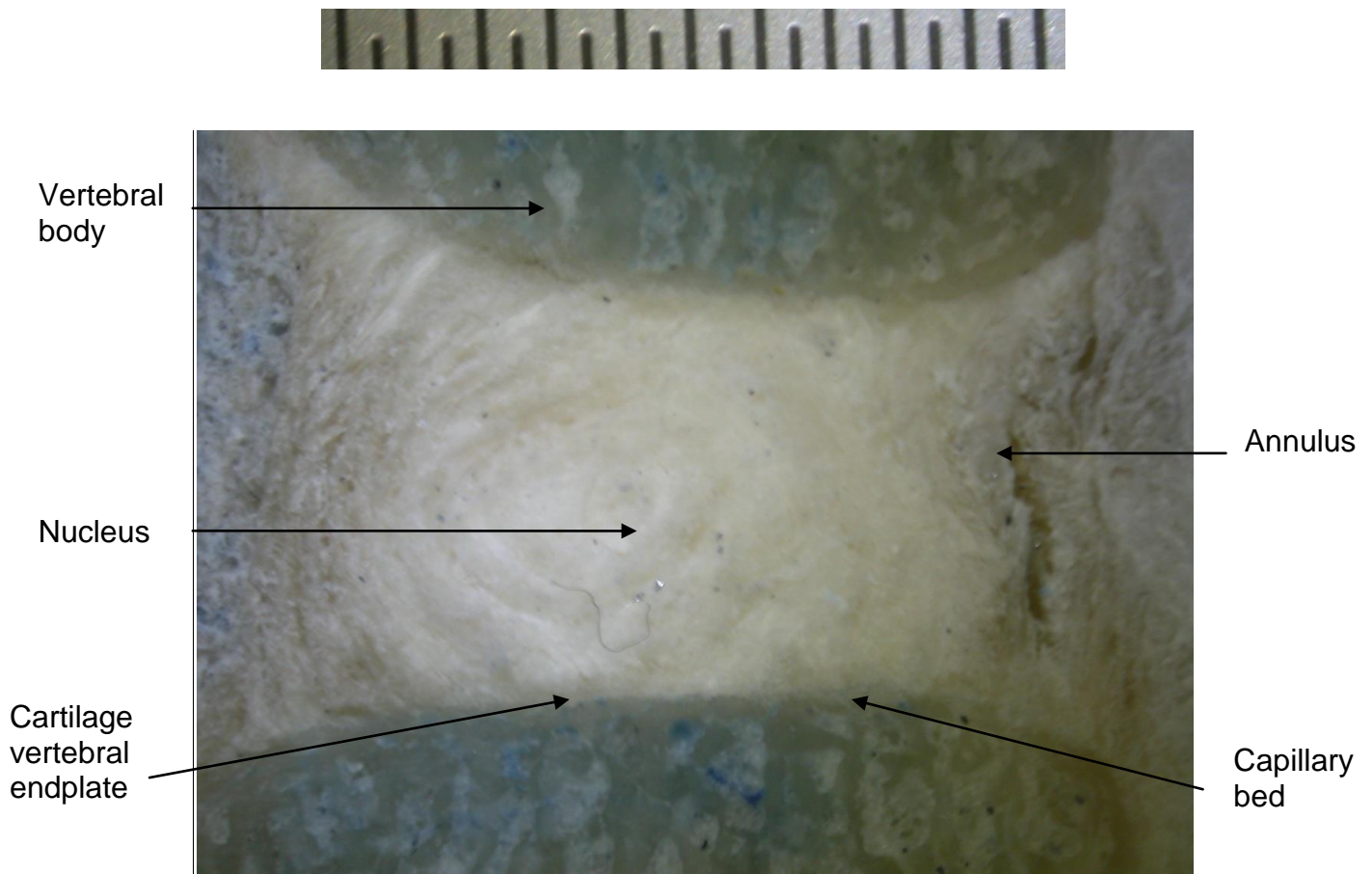
Figure 59: Sagittal section of vertebral endplate and intervertebral disc. The scale above is imaged under the same magnification; the smallest division is 0.5 mm. This sample is perfused with Evans blue and sliced thinly with a saw and wet/dry sanding. The Evans blue can be seen within the vertebral body. At the area of the cartilage endplate terminations of these vessels in their characteristic bud shape are noted. The cartilage endplate itself can be seen to contain no vessels at all.

Sections were imaged along the border and the vertebral endplate's thickness measured across the nucleus and the inner and outer annulus.

Cartilage vertebral endplate
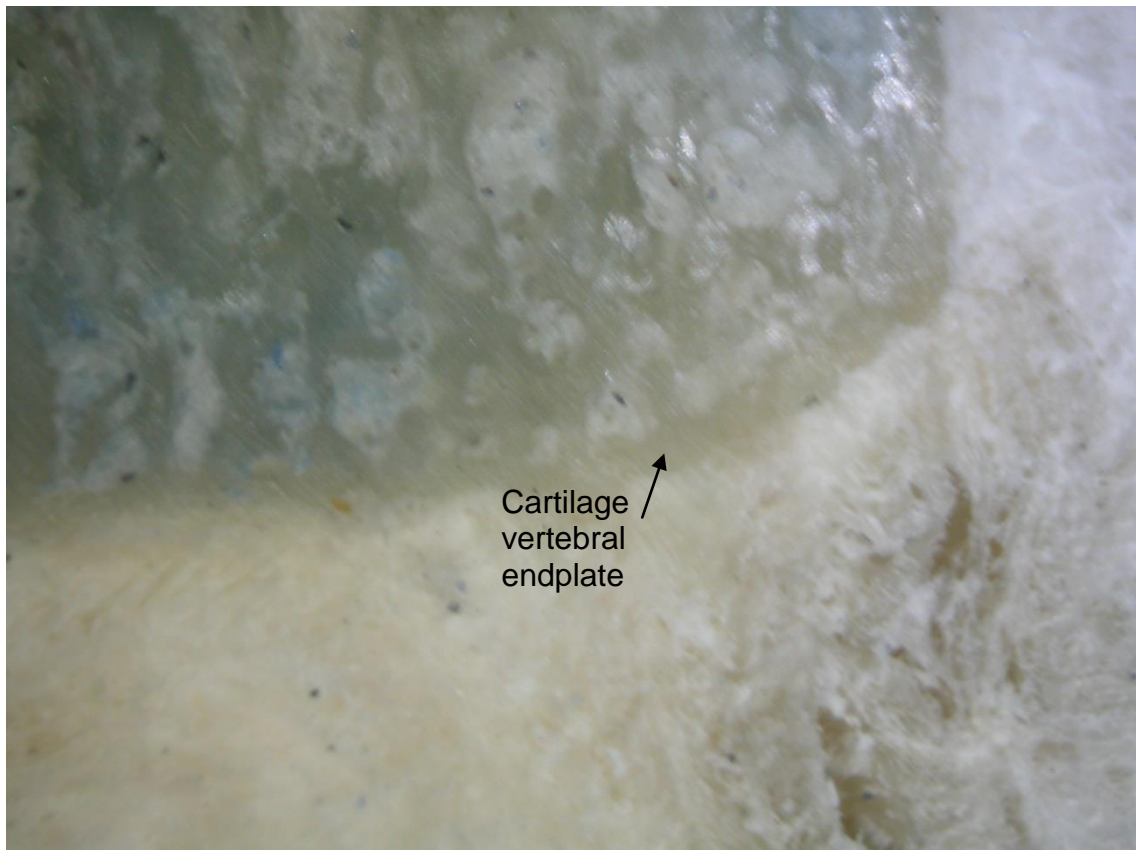
Figure 60: Vertebral endplate over the annulus at superior right border; the scale has a smallest division of 0.5mm. Under greater magnification when compared to the previous image, the capillary terminations are easily seen. A clear boundary, absent from vascularisation is seen between the vertebral body and intervertebral disc which is the cartilage endplate.
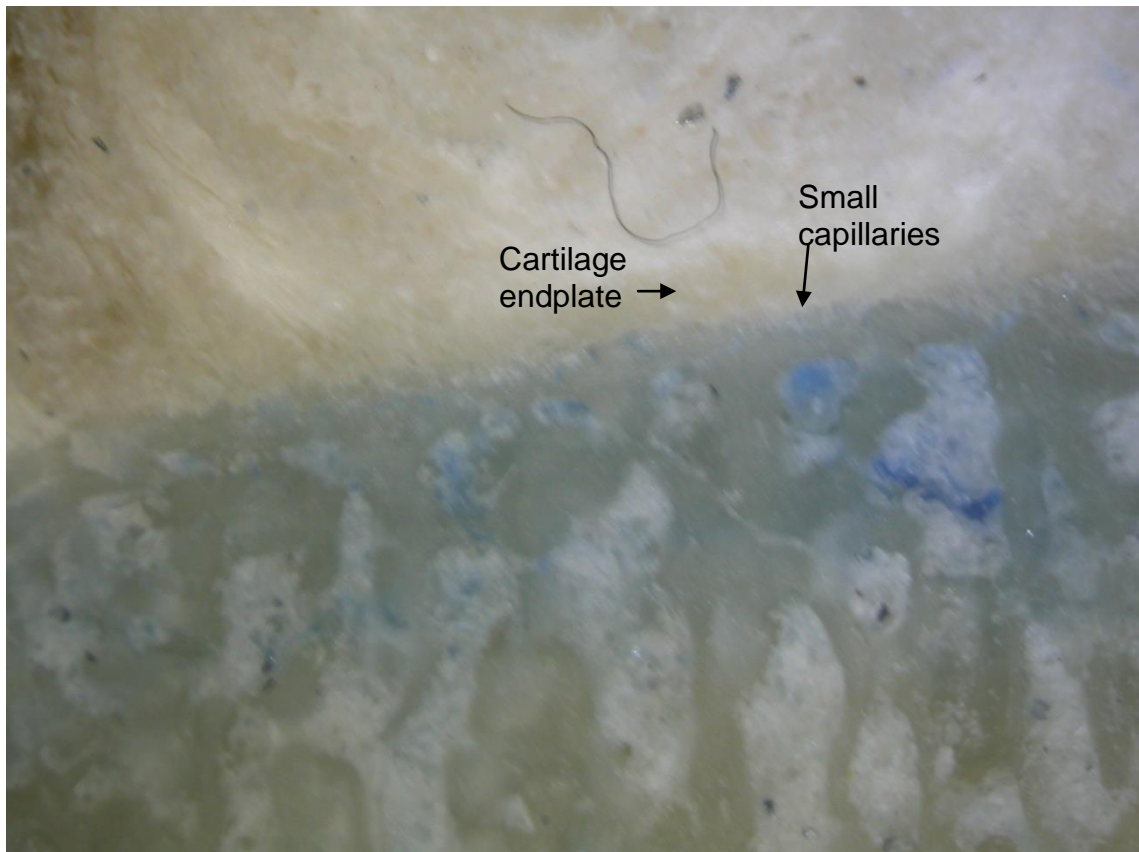
Figure 61: Vertebral endplate at inferior border over the nucleus pulposus. When compared to the previous image it can be seen that the density, size and shape of the vascular terminations are different in the region adjacent to the nucleus pulposus. At the point of the nucleus the terminations are more numerous, smaller and discoid in shape.

The images were opened in Image J WCIF (image viewing software) enabling measurements to be achieved with accuracy above the visual scales shown above. Measurements of an area were taken several times and averaged. The average dimensions of the vertebral endplate were found to be: Outer annulus 0.16+/-0.06 mm, Inner annulus 0.21+/-0.04 mm, Nucleus 0.33+/-0.11 mm.

On studying Figure 60 and Figure 61, there appear to be a greater density of the capillary terminations at the area next to the nucleus, the disc-like terminations branch into much smaller vessels which touch but do not infiltrate the cartilage endplate. These are not evident next to the annulus.

2.4.3 Gross vascularisation of the intervertebral disc

2.4.3.1 Anatomy
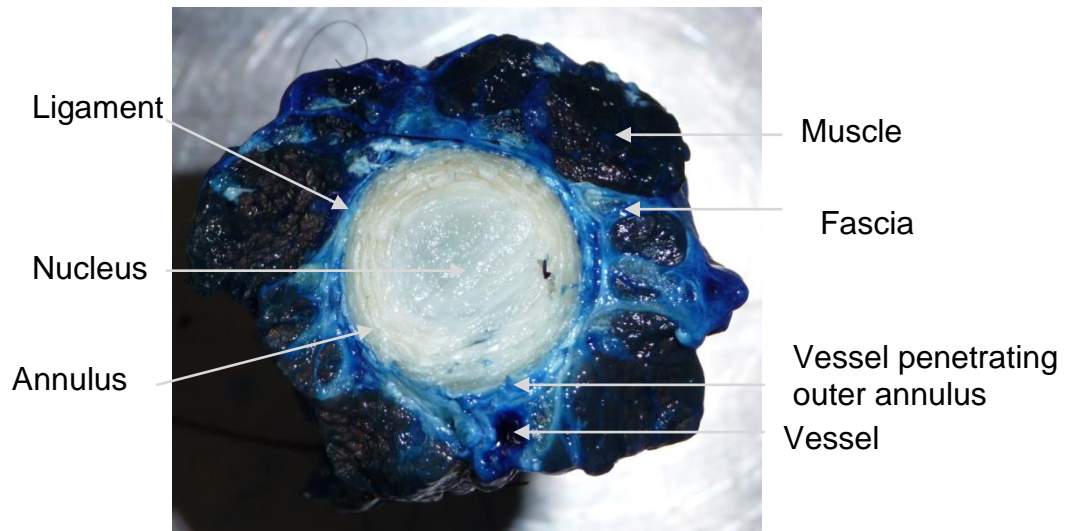
Figure 62: Axial view of the intervertebral disc. The extent of perfusion of the Evans blue is dependent upon the extent of vascularisation. The central intervertebral disc can be seen to be for the most part free of vascularisation apart from a few small vessels which penetrate a little way into the annulus. Ligament and fascia surround the disc which generally has a low density of vessels, hence their pale blue appearance. The major muscle groups within the spine (there are four described in chapter 3) and the two smaller inter-medail muscles are clearly seen as dark blue.

Figure 62 illustrates an axial view through the intervertebral disc. The disc can be seen to not have major vessel penetration; however, there are some small vessels just penetrating into the very outside of the annulus. The 23 samples used in Chapter 4 were incubated at 37° for at least 120 hours; the annulus ranged in water content between 55 and 69 % and the nucleus between 75 and 82 %. On dissection the texture of the nucleus is more pliable and gelatinous compared to the annulus.

2.4.3.2 Diffusion in the intervertebral disc

A fresh specimen was obtained from the abattoir and prepared as described in section 2.2.1. The sample was perfused with 100 ml of a 1 % Evans blue (with

sodium chloride) solution. The solution was injected with a syringe via the cannula in the median caudal artery. After one hour from perfusion the first intervertebral disc from the cut end was removed. It was photographed under magnification. This was repeated hourly, removing a successive intervertebral disc from the sample. Removing discs hourly enabled the disc to be kept in near natural in vivo conditions; diffusion would take place in the normal way. Up to three hours post perfusion there was no penetration of the outer annulus of the intervertebral disc. After four hours, there was seen to be some diffusion:

Vessel penetrating the outer annulus

Soft tissue surrounding the disc

Diffusion in the outer annulus
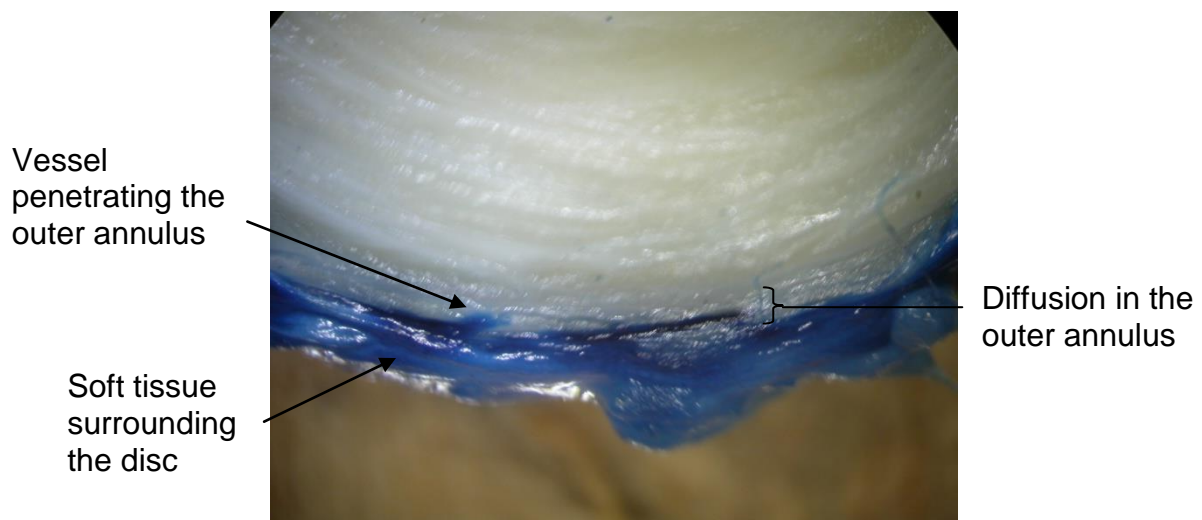
Figure 63: Axial slice of the intervertebral disc 4 hours post perfusion with Evans blue. The main portion of the disc is white and unperfused with Evans blue. However, Evans blue can be seen in the surrounding ligament; there is evidence of small vessels penetrating the outer annulus.

The average distance of diffusion was found to be 0.52 mm. This was measured accurately by putting the sample into Image JWCIF and using a rule which had been imaged in the same way to set the scale.

The equine sample was left overnight. After 22 hours from the point of perfusion a final intervertebral disc was removed from the sample:

Diffusion
of Evans
blue
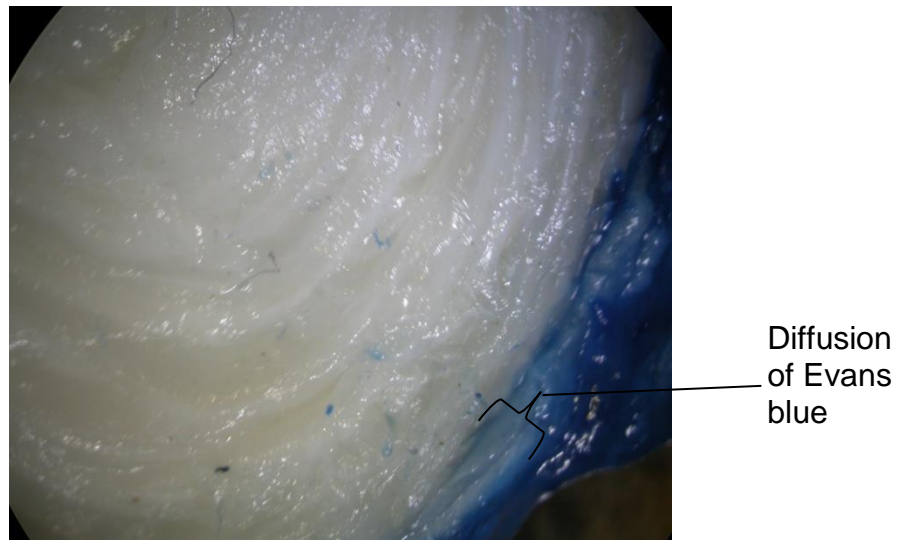
Figure 64: Axial disc slice 22 hours post-perfusion. Even after this length of time the Evans blue has not made substantial progress into the disc; Evans blue is extremely reactive, it binds well with proteins etc, meaning even if vessels were present its diffusion would be slow.

After 22 hours from perfusion of the sample with Evans blue, the extent of diffusion was measured to be 0.673 mm. There may be several reasons why diffusion of Evans blue is slow. The matrix of the annulus may be binding with or preventing the transport of Evans blue. There may be diffusion; however, the amount may be so small it cannot be detected. Evan's blue has a molecular weight of 960.82 and a chemical formula of $C_{34}H_{24}N_6O_{14}S_4Na_4$, (Sigma-Aldrich, 2013). This experiment cannot measure quantitatively diffusion but it does give approximate time scales which may be needed for the transport studies in Chapter 4. (The disc in Figure 58 shows greater dye penetration on a similar time-scale but, as explained above, this is probably due to the spreading of dye during sectioning.) The free diffusion coefficient of Evans blue has an approximate value of 10^{-6} cm^2 s^{-1}. Evans blue is generally only used as a qualitative marker; it is extremely reactive and binds to proteins and elastin.

2.5 Light microscopy of the equine vertebral body and intervertebral disc.

2.5.1 Aim

To the best of our knowledge there have been no histological investigations on the equine caudal discs. We have therefore employed classical staining techniques for the principal matrix components together with polarised light microscopy to visualise collagen both in disc and bone.

2.5.2 Method

Small segments of tissue were cut from tails used in the experiments described above and snap frozen. 20 μm frozen sections were cut either of disc tissue alone or disc and a thin layer of vertebral bone using a Cryocut E microtome.

Samples with bone attached were difficult to cut and handle subsequently and of variable thickness. However, they did allow investigation of the end plate, which is an important element in solute transport. Sections were stained with haematoxylin and eosin to differentiate cells and matrix with van Gieson stain for collagen, using established procedures (Bancroft & Gamble, 2002).

To view the sample a Nikon Eclipse 200 microscope was used with 4 × and 10 × objectives. For polarised light investigations a polariser was placed in the incident beam and a rotatable analyser in the transmitted beam. Images were recorded on 0° and 90°.

2.5.3 Results

2.5.3.1 Polarised light microscopy

Panel A of Figure 65 illustrates the nucleus pulposus of the intervertebral disc. There appear to be lines running in the same orientation through the disc; it

may be the case that these are cut marks, although it is unlikely as the top of the image shows a portion of the inner annulus where the orientation alters. The cartilage endplate appears void of features. The vertebral body has a woven structure with marrow spaces and blood vessels running throughout. Panel B illustrates the appearance of the annulus of the intervertebral disc. Even in unpolarised light the orientation of the fibres within the annulus can be seen. They appear to run in bundles at approximately 45° to each other.
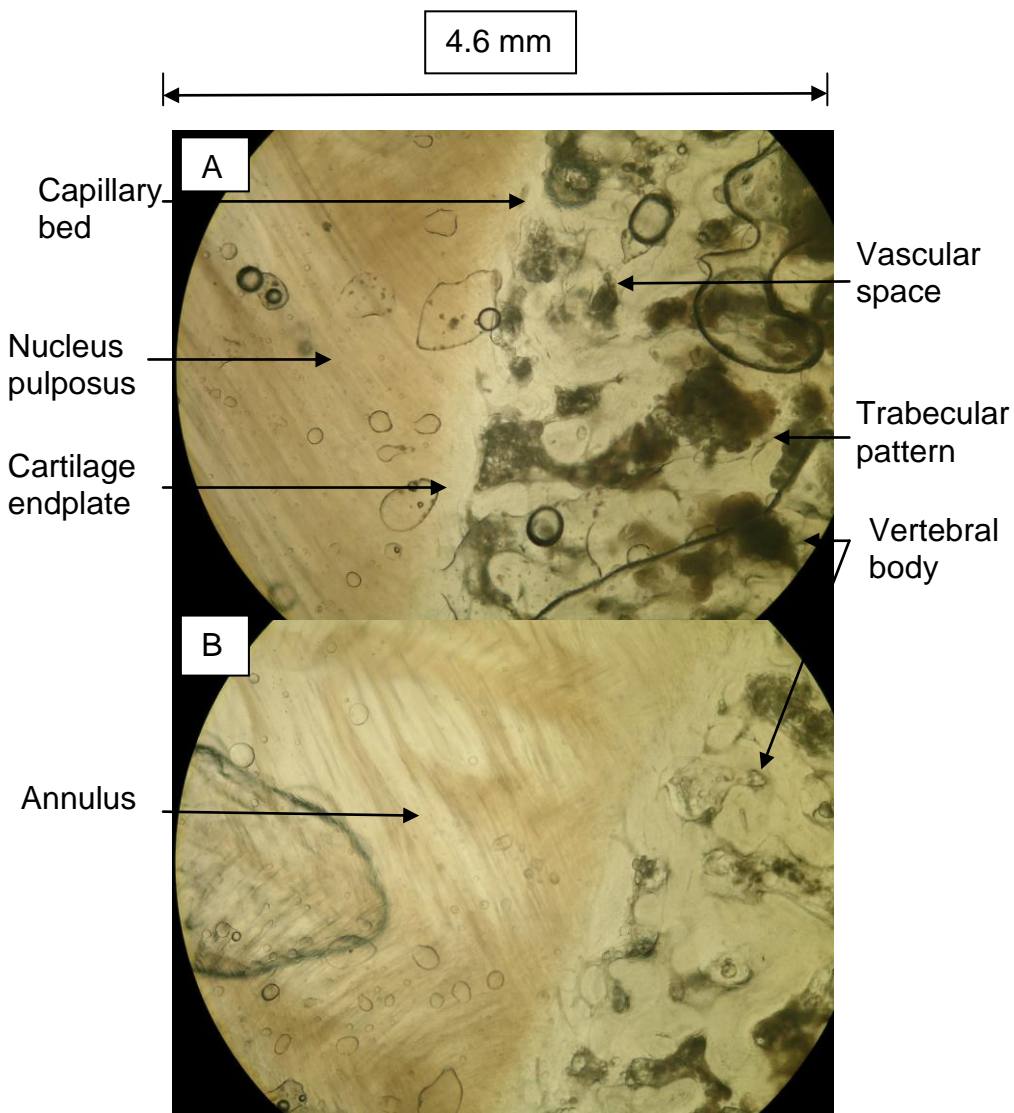
Figure 65: Vertebral body and intervertebral disc equine sample, a 20 µm thick slice at 4 × magnification; A illustrates the nucleus pulposus of the intervertebral disc and B illustrates the annulus. Under the microscope, it can be seen that the nucleus area appears quite random and lacking in structure. The annular area, however, has a well defined structure, with consecutive bundles of collagen fibres at alternate angles to each other

Figure 66 panel A below illustrates some birefringence. The collagen fibre orientation in the nucleus appears quite random, but there is local order in the organisation of collagen in the trabecular bone. Panel B illustrates the difference in the structure of the annulus from the nucleus of the disc is marked. At the outer border of the nucleus the collagen fibres become aligned perpendicular to the annulus. In the annulus the orientation of collagen and the changes in successive lamellae are clearly evident.
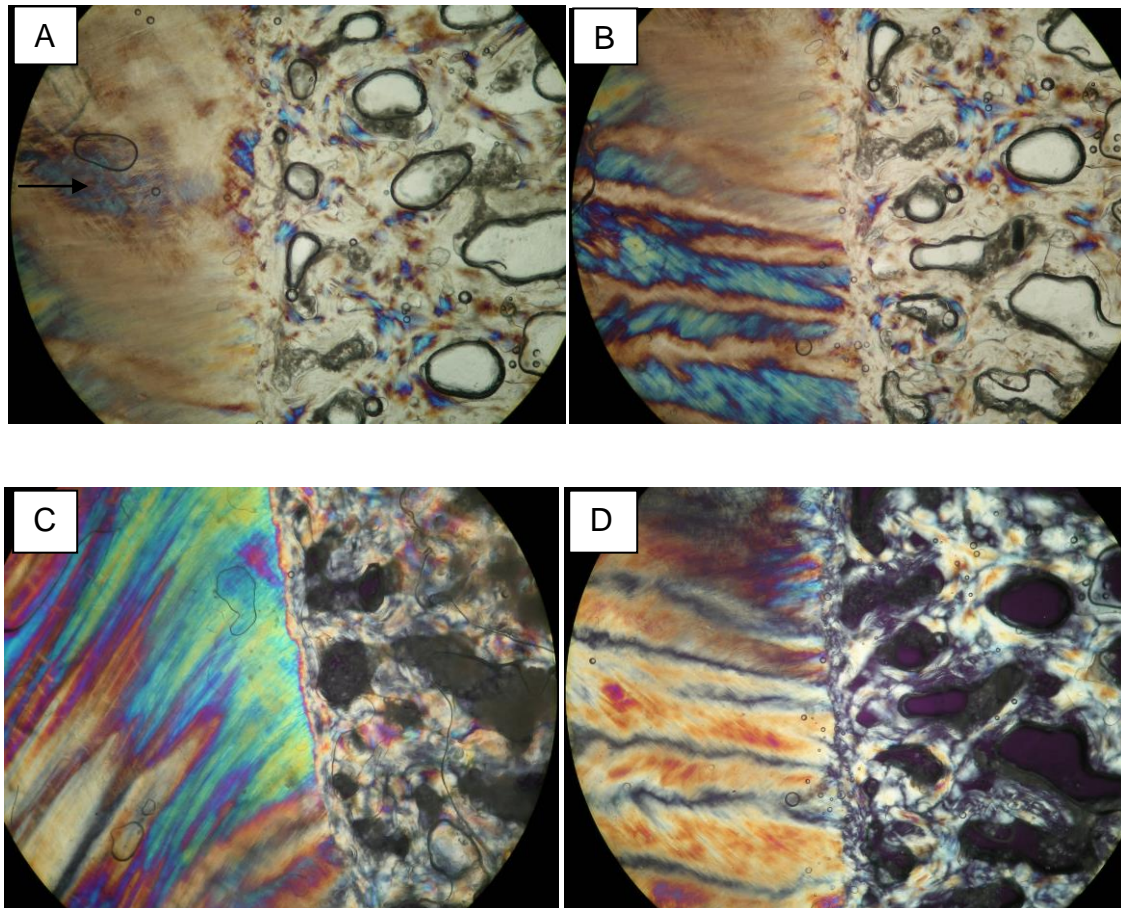
Figure 66: Vertebral body and intervertebral disc using polarised light, 20 µm thick slices at × 4 magnification; these samples are the same shown in Figure 65, A and B are under linearly polarised light and C and D are under crossed polarisers. The polarising of the light allows specific structures to be identified because of refraction. The crossed polarisers allow structures with specific orientations to exhibit birefringence; this can be clearly seen with the collagen fibres in the annulus.

Figure 66 panel C illustrates an interesting property of the nucleus pulposus of the disc. Under crossed polarisers some birefringence is evident. This would suggest there is some orientation dependant order within the nucleus, contrary to its appearance under linearly polarised light. Panel D illustrates the well ordered nature of the annulus of the disc. Alternating light and dark areas are seen. The lamellae are uniform in orientation and width along their length. The width of each successive lamellar ring is not uniform and range from 0.36 mm to 0.5 mm. There are 5 to 6 lamellar rings. The capillary bed in both Panels C and D is evident when using crossed polarisers. The vessels appear dark with crossed polarisers, illustrating their different orientation compared to their surrounding structures. The trabecular structure of the vertebral bodies is evident with dark vessels penetrating the structure.

2.5.3.2 Histochemical staining
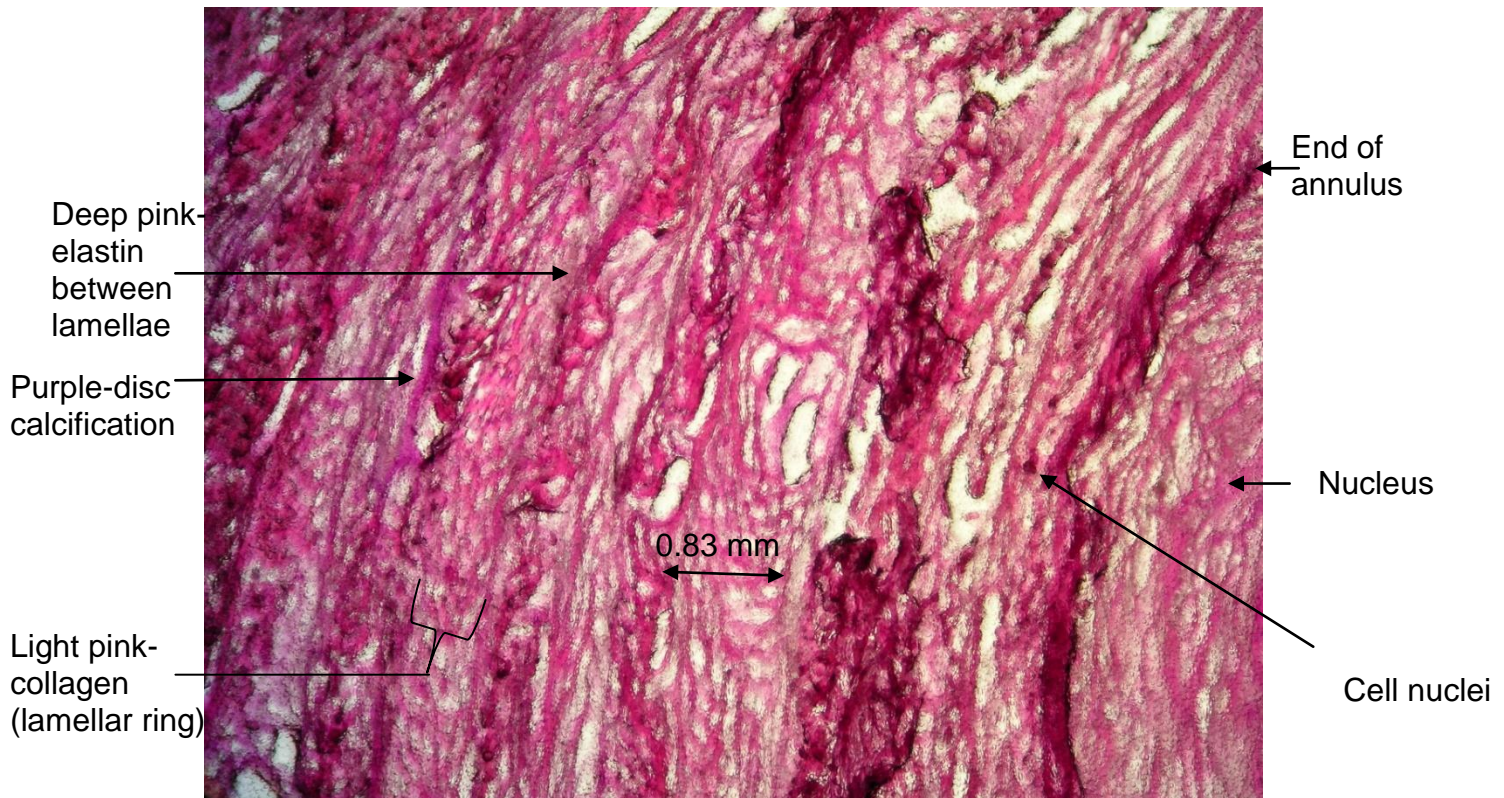
Figure 67**: Histological section of annulus of the intervertebral disc stained with haematoxylin and eosin (×4). The thin section above clearly allows individual lamellar rings to be seen. Within the lamellar rings themselves a mesh of fibres can be identified. These were discussed in chapter 1 as a hierarchical structure of fibres. There is also evidence of the trans-lamellar bridging network between separate lamellar rings.**

Histological results are presented for a single disc. The annulus, Figure 67, consists of ordered concentric rings made of collagen with elastin fibres between each lamellar ring. The sample shows signs of calcification within the annular rings.

Figure 68 illustrates well the random nature of the nucleus of the intervertebral disc. This section illustrates that there is a gradual boundary between the annulus and the nucleus and a thick elastin ring around the main part of the nucleus. The nucleus consists of many randomly orientated collagen fibres.

128
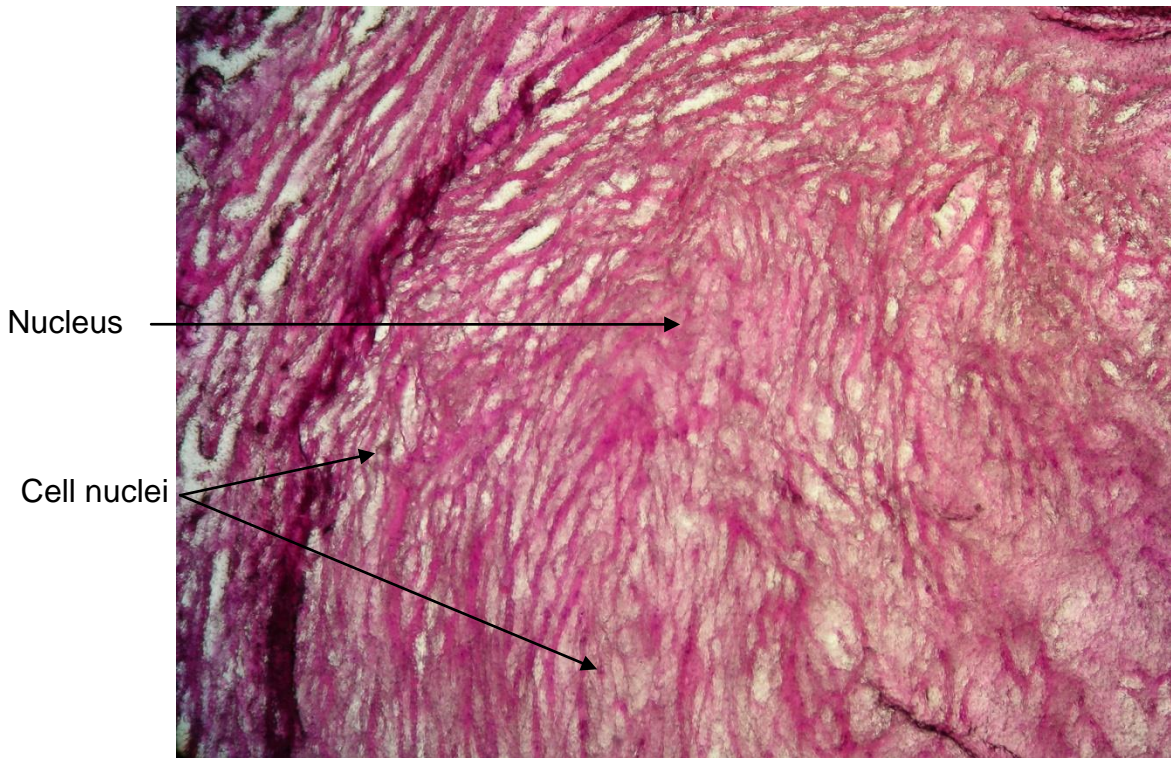
Figure 68: Histological section showing the nucleus pulposus, stained with haematoxylin and eosin (×4). Fibres within the nucleus can be seen to be approximately random in nature.
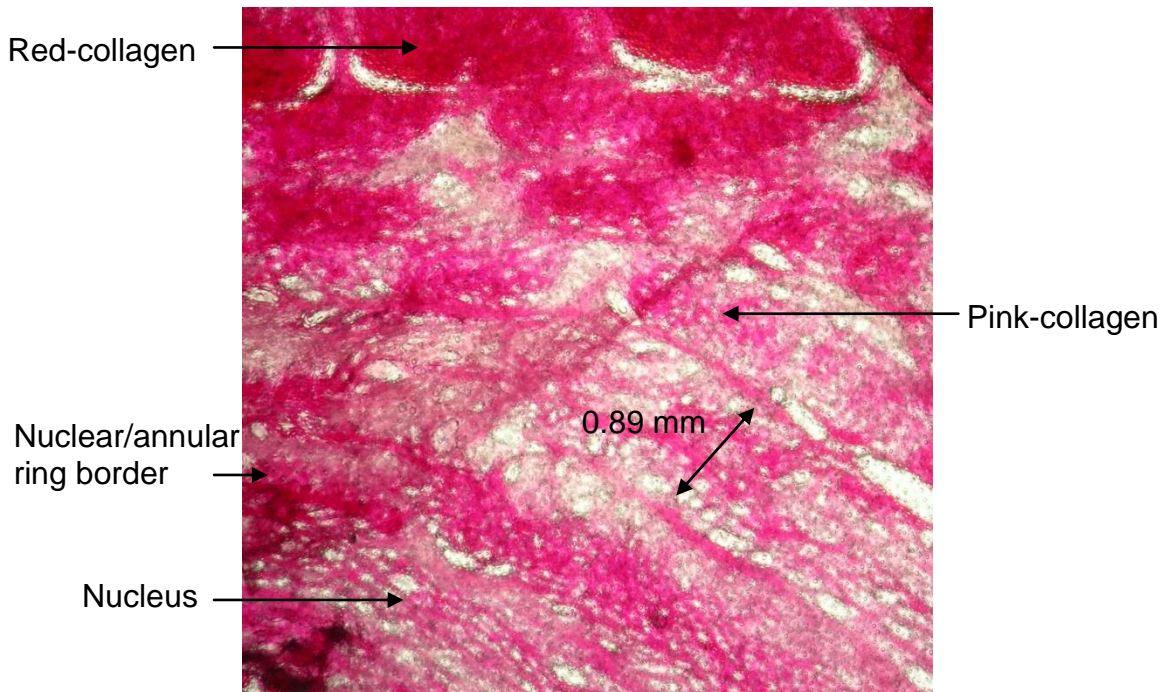
Figure 69: Histological section of an axial view of the disc stained with haematoxylin and Van Gieson (×4). When compared with the previous two images, the annular rings confirm previously noted structure.

Figure 69 illustrates the intricacy of the annular rings. Tightly woven collagen fibres form lamellar rings; a honeycomb structure. These images may be compared to those obtained by Rutges et al (Rutges, et al., 2013) for the human disc, by Clouet et al for the rabbit (Clouet, et al., 2011) and by Bergknut et al for the dog (Bergknut, et al., 2013). Images obtained by these researchers are broadly similar to those obtained in the present study. Compared to the human (Rutges, et al., 2013) the fibrous structure of the nucleus appears more ordered in the horse (present study); also the number of lamellae in the horse is less than that in the human. These differences may relate to differences in biomechanical function between the load-bearing human spine and the equine tail.

Gruber et al have demonstrated a novel staining method for the disc to give enhanced visualisation of some features; to visualise collagen and proteoglycan components on the same histological section (Gruber, et al., 2002). These researchers used haematoxylin, alcian blue and picrosirius; disc morphology was again seen to be broadly similar to the present study

2.5.4 Discussion

The histological sample illustrates that the annulus consists of rings of collagen. They are well ordered surrounding the nucleus in concentric rings. The collagen fibres form bundles which are joined by thinner collagen fibres; this structure is important in allowing the annulus to expand when under stress. The elastin fibres offer a restoring force to return the disc to its shape and maintain its integrity. The disc also consists of collagen fibres; however, in this case they minimal localised order. The elastin fibre surrounding the nucleus keeps its shape when under stress and prevents it from intruding too far into the annulus.

The lamellae in humans are 0.2 mm to 0.4 mm in thickness (Inoue & Takeda, 1975). The equine tail intervertebral disc consists of thicker lamellae; 0.36 to 0.89 mm. As in the human intervertebral disc the lamellae are made of collagen bundles which are angled and altering in orientation between successive bundles (Happey, 1980).

A striking difference between human and equine species is the number of lamellae; humans have 15 to 20 (Urban, 1990), while equines appear to have 5 to 6.

3 Anatomy Studies using Magnetic Resonance Imaging

3.1 Introduction

In this chapter Magnetic Resonance Imaging is used to examine the anatomical structure of the equine intervertebral disc and vertebral body. The technique of Magnetic Resonance Angiography is then utilised to examine vascularisation of the intervertebral disc and vertebral body for comparison with x-ray.

Magnetic Resonance Imaging (MRI) is excellent in visualising soft tissue structures making it an imaging modality of choice in examining the intervertebral disc. MRI also enables the functional aspect of a tissue to be examined. Early degeneration in the disc, associated with back pain such as changes in the concentration of the proteoglycans and water and the organisation of collagen may be correlated with specific MRI parameters to enable easier and earlier diagnosis (Toffanin, 2001). MRI can reveal important changes such as desiccation, disc bulging with or without herniation or the presence of high intensity zones within the annulus (Hickey, et al., 1990). MRI is useful in obtaining multi-planar images and 3D visualisation of the disc. MRI can provide high resolution and detail of small structures.

MRI has been able to demonstrate substantial abnormalities in approximately 30 % of asymptomatic people of all ages and in 57 % of those aged 60 years and older (Patel, 2005). Disc degeneration or a bulging intervertebral disc is demonstrated in 35 % of subjects aged 20-39 years and in nearly 100 % of those aged 60-80 years (Patel, 2005). Therefore, it can be seen this is a specific and accurate tool in illustrating pathologies, although their relationships

132

with clinical problems are not always clear. MRI can also be used in detecting changes in surrounding structures such as the vertebral endplate and vertebral bodies (Antoniou, 2004).

Initial studies using MRI utilised various rat tissues; which were either normal or containing tumours (Damadian, 1971). The justification of this study was the inability of x-rays to detect tumours and the radio frequency of the incident radiation being relatively safe (Damadian, 1971). A wide range of nuclei could be examined. Direct measurement of spin-lattice (T_1) and spin-spin (T_2) relaxation mechanisms can characterise biological tissue by their emitted radio frequency pulse (Damadian, 1971). These relaxation mechanisms are described in section 3.2.2. Damadian found that proton signals from water in cancerous tissues were distinct from the radio frequency signal of normal tissue; malignant tissue demonstrated an increase in the motional frequency of water (Damadian, 1971). Lauterbur further characterised MRI by discussing image formation by induced local interactions (Lauterbur, 1973). Lauterbur introduced a second field or gradient which limited the interaction of the object with the first field to a defined region. At a field strength of 1.6 mgauss, pure water produced a saturated signal compared to a sample whose T_1 relaxation time had been shortened by the addition of Mn^{2+} (Lauterbur, 1973). From this Lauterbur defined the contrast or relative intensities produced in an image is dependent upon relative nuclear relaxation times. Hence, the differences in water content and proton density will enable soft tissue structures to be selectively imaged (Lauterbur, 1973).

Lauterbur's image formation relied on complex calculations, Garraway et al demonstrated selective irradiation allowing a signal to be obtained directly by

the nuclear spins within a small region within the sample, we now term as slice selection (Garroway, et al., 1974). A static magnetic field gradient was applied in addition to the initial magnetic field as in Lauterbur's experiment above. The sample is imaged and the gradient direction switched. This will provide spatial selectivity. The radio frequency pulse is then applied which will only cause excitation of nuclei with the required resonance (Garroway, et al., 1974). This imaging sequence is the gradient echo sequence used in this study and further explained in section 3.2.3. Mansfield extended this work by applying time dependent magnetic field gradients; this exploits the sample spin echoes and is the Fourier transform of the previous experiment (Mansfield, 1977). In Mansfield's experiment the field gradients are switched periodically allowing the spin echoes to amplify after free induction decay has occurred (Mansfield, 1977). This enhances the signal to noise ratio.

The proton MRI signal intensity varies with three parameters, proton density and T_1 and T_2 relaxation times. These parameters will change depending on the type and biochemistry of the tissue (Hickey, et al., 1990). The biochemistry of the intervertebral disc changes with age and therefore so does these parameters. The intervertebral discs constitute the largest connective tissues and commonly show MRI detectable age related variations in structure (Hickey, et al., 1990). Chapter 1 established a link between matrix condition and age. During ageing degeneration is caused by a diminishing amount of aggregating proteoglycans (Patel, 2005). This leads to dehydration of the disc. Typically, gadolinium enhanced MRI is used to evaluate the proteoglycan content in a cartilage matrix. Transport of the gadolinium within the matrix is determined by the gadolinium concentration gradient and the electrostatic interactions due to the fixed charged density provided by the negative proteoglycans (Laurent, et

al., 2003). Gadolinium is negatively charged and is repelled by the presence of proteoglycans. Diminished proteoglycan content increases the uptake of gadolinium. This will shorten the T_1 relaxation time of the tissue producing a signal of higher intensity on a T_1 weighted image (Laurent, et al., 2003). Consequently, positively charged MRI sensitive compounds such as Manganese can equally be used; in this case the MRI signal loses intensity with proteoglycan loss.

In the work described in this thesis the samples were collected from the abattoir and prepared as detailed in section 2.2. All MRI imaging took place at Exeter MR Research Centre, the University of Exeter. Technical scanning advice was given by Dr Abdelmalek Benattayallah.

Figure 70: The Philips Intera MR scanner at the Exeter MR Research Centre, (University of Exeter, n.d.).

3.2 MRI imaging

3.2.1 The scanner

Primarily MRI imaging utilises sensitivity to the presence of water; the intervertebral disc on average is 70 % water and therefore it is the ideal imaging technique. One of the primary components of the scanner is a magnet. InFigure 70, the magnet is contained within the cylinder. This magnet is a superconducting magnet and in the case of the magnet at the Exeter MR Research Centre produces a magnetic field of strength 1.5 T. The Exeter MR Research Centre magnet has a homogeneity of ≤ 0.5 ppm at $50 \times 50 \times 45$ cm.

3.2.2 Relaxation mechanisms

In this thesis a number of contrast mechanisms are used based on changes in the rate of proton relaxation.

When the radiofrequency signal is removed, the MR signal in the receive coil begins to decay, this is termed Free Induction Decay. Two separate processes occur. The net magnetisation vector in the transverse plane, M_{xy}, begins to decay (T_2 relaxation) and the net magnetisation vector in the longitudinal plane, M_0, (T_1 relaxation) is restored (Graham, et al., 2012). This is the basis of MR image contrast. These are two independent mechanisms.

Time (after RF pulse is switched off)
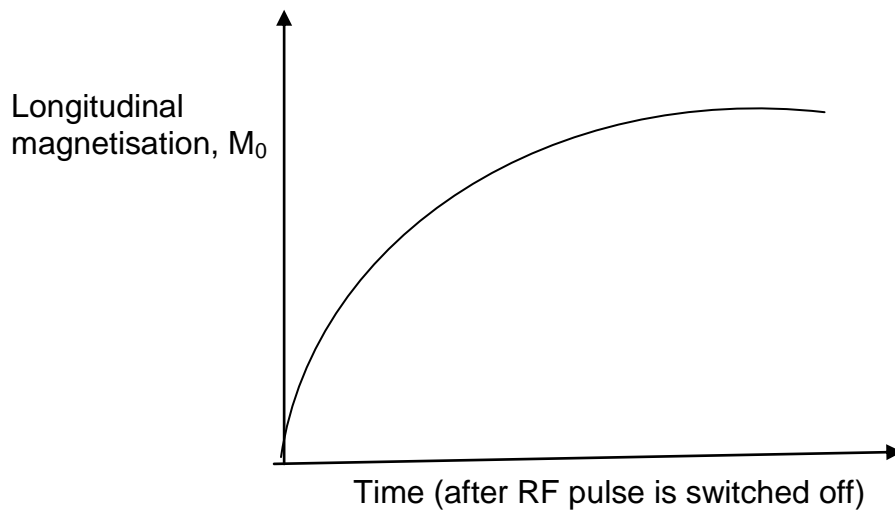
Figure 71: T_1 relaxation. This is defined as spin-lattice relaxation and is the restoration of the magnetisation vector in the longitudinal direction (that is the scanner field direction) by the giving up of energy to the surrounding lattice.

Figure 71 illustrates the appearance of T_1 relaxation. This type of relaxation is also termed as spin-lattice relaxation because energy is imparted to the surrounding structure by the protons as they de-phase.

Figure 72 illustrates T_2 relaxation. T_2 relaxation is known as spin-spin relaxation. Spin-spin relaxation is the de-phasing of the protons by the interaction of the individual magnetic moments of the protons with each other

Time (after RF pulse is switched off)
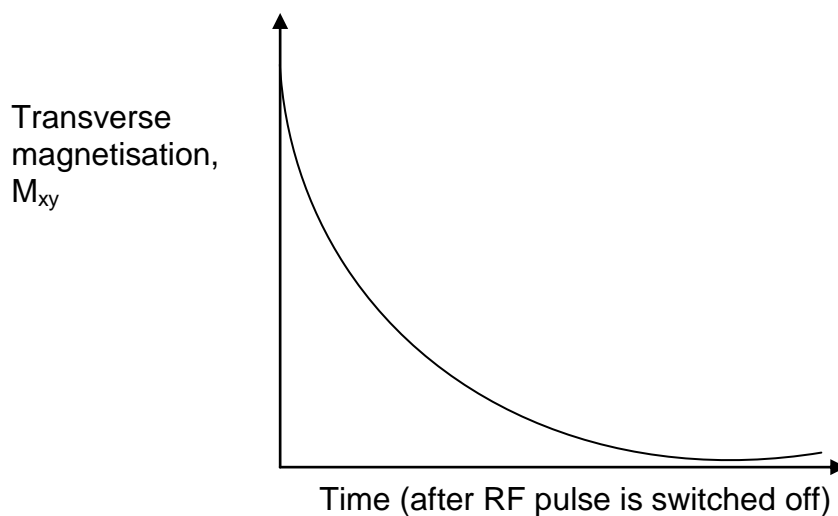
Figure 72: T_2 relaxation. This is the degradation of the transverse magnetisation, by local interactions of the protons with one another; also known as spin-spin relaxation.

137

Different tissues such as fat and water, (these represent the extremes of intensity in a MRI signal), have differing T_1 and T_2 relaxation times, see Figure 73 and Figure 74.
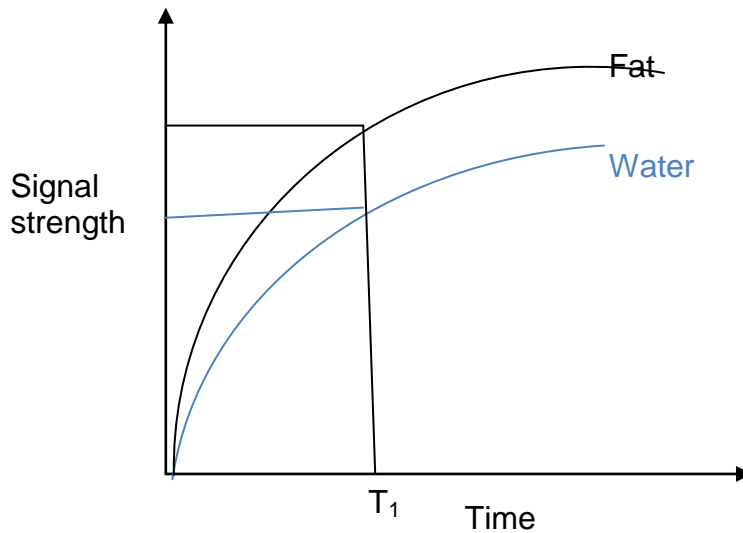
Figure 73: A schematic comparison of T_1 relaxation times for fat and water; the difference in signal strength will depend on the amount of fat or water present, the strength of the scanner magnet and the protocols within the chosen scan sequence.

The longitudinal magnetisation M_0 of fat recovers quicker than that of water because its greater density enables it to transfer energy at an increased rate to the surrounding lattice, (McRobbie, et al., 2007). Hence an appropriate T_1 relaxation time can be chosen so that fat will give a brighter signal than water.
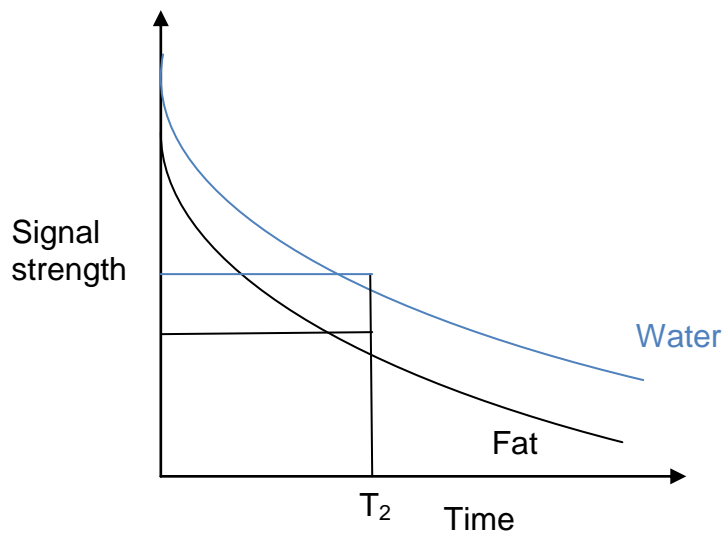
Figure 74: A schematic comparison of T_2 relaxation times for fat and water; the difference in the MRI signal strength obtained for fat and water will depend on the amount of fat and water present, the strength of the scanner magnet and the protocols within the chosen scan sequence.

Figure 74 illustrates that the transverse magnetisation, M_{xy}, of fat decreases at a faster rate than the transverse magnetisation, M_{xy}, of water. The density of fat ensures the magnetic moments of the individual photons interact more readily than those of water. It can be seen that at a set relaxation time T_2 the signal of water will be brighter than that produced for fat (McRobbie, et al., 2007). Inhomogeneities in the magnetic field provided by the scanner will also affect the T_2 relaxation time of a particular tissue. This is because de-phasing of the protons would occur even in a perfectly homogenous MR scanner field. All magnetic fields are in fact inhomogeneous, as described in section 3.2.1. This results in different areas of the tissue being in different magnetic field strengths while being imaged. As a result the T_2 relaxation time (spin-Spin) is speeded up. This is further enhanced by gradient echo sequences (these are described in the section below). This will have an impact on scanning as the T_2 relaxation time may become so short a signal cannot be detected during scanning (Lauterbur, 1973)..

The intervertebral disc and associated vertebral body has a matrix made of a variety of substances. The MR signal produced will have a range of gray values associated with the matrix composition which is between the extremes of fat and water. A very simple classification of body tissues uses three categories: fluids (cerebrospinal fluid, synovial fluid, oedema, inter/intra cellular fluid), water-based tissues (muscle, brain, cartilage, kidney) and fat-based tissues (fat, bone marrow). The intervertebral disc has two distinct tissue regions. The annulus consisting of a collagen based matrix which is still 70 % to 80 % water and the nucleus, which is predominantly water with finer collagen fibrils in a semi-fluid matrix (Fawcett & Jensh, 2002).These are both water based tissues. In a T_1 weighted image the nucleus will produce signal strength of less intensity than the annulus. However, in areas where the collagen fibres are densely packed and strongly orientated as in the lamellae of the annulus the signal strength will increase in intensity.

3.2.3 Image sequences

There are two main types of pulse sequence, the spin echo and the gradient echo (Graham, et al., 2012). As the radiofrequency pulse is turned off the MR signal becomes weaker due to Free Induction Decay. Figure 75 illustrates the appearance of the free induction decay signal. This decay process is as a result of T_1 and T_2 relaxation times (Graham, et al., 2012). The signal becomes weaker over time; therefore, either spin or gradient echo sequences are used to refocus the signal.
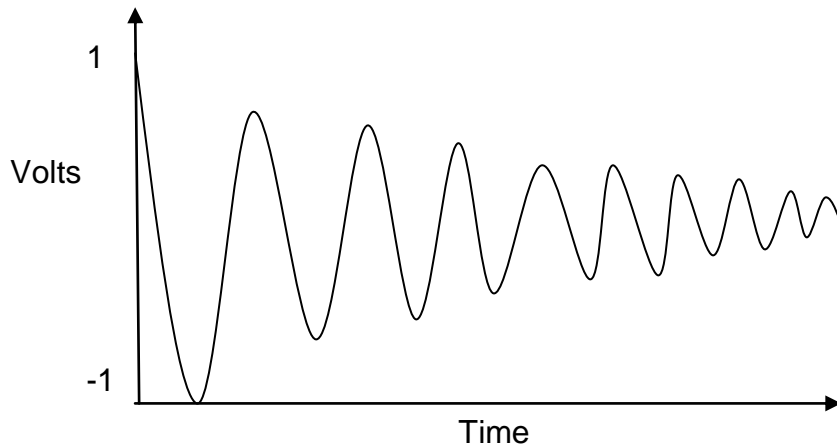
Figure 75: Free Induction Decay of the MR signal in the receive coil. This signal will need to be refocused to allow a signal to be determined.

A spin echo pulse works in the following way. A 90° radiofrequency is applied to the precessing protons; resonance occurs, the protons precess in phase and their net magnetisation vector is moved to the transverse plane. The radiofrequency pulse is stopped and Free Induction Decay of the MR signal in the receive coil occurs (Mansfield, 1977).. A second radiofrequency pulse of 180° is applied, tipping the net magnetisation vector 180° to B_0. This causes the protons to re-phase.

Leading edge   Trailing edge

A-nuclei precessing in phase

B-Dephasing of the protons

Leading edge

C-180 RF pulse

D-Protons come into phase
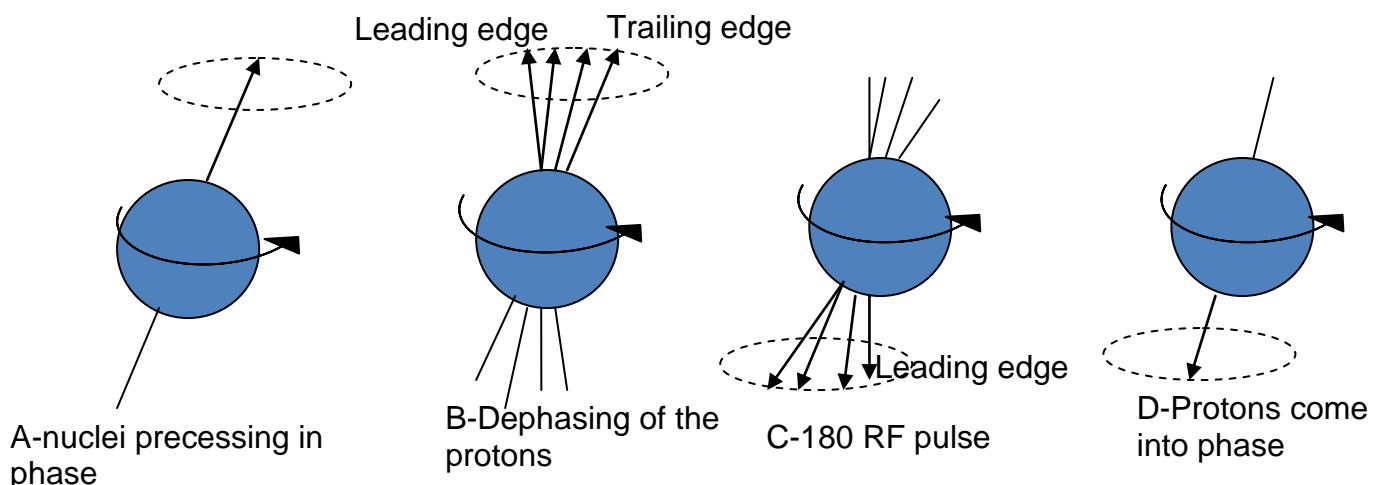
Figure 76: A spin echo sequence: A-application of 90° pulse, B-Free Induction Decay, C-180° RF pulse, D-re-phasing. This sequence allows the free induction decay to be re-focussed to allow a signal to be detected.

When the 180° radiofrequency pulse is applied, the slower trailing edge becomes the new leading edge and is caught up by the new faster precessing trailing edge.

The second type of image sequence is a gradient echo sequence. A gradient echo uses a partial flip angle (Garroway, et al., 1974). Gradients are applied to the MR signal. The gradient is applied in first one direction, which speeds up de-phasing (Garroway, et al., 1974). The gradient is then applied in the reverse direction to re-phase the protons.

3.2.4 Image contrast

Image contrast is controlled by various parameters depending on the pulse sequence selected. We have already seen in section 3.2.2 that fat has a shorter T_1 recovery and T_2 decay, and fluid such as water has a longer T_1 recovery and longer T_2 decay (McRobbie, et al., 2007). In a spin echo sequence TE (echo delay time) and TR (repetition time) are important variables in tissue differentiation. TE is the time between the initial 90° RF pulse and reading the signal back from the tissue created in the receiver coil (McRobbie, et al., 2007). TR is the time between the initial sequence pulse and the next; that is in a spin echo sequence the time between 90° pulses.
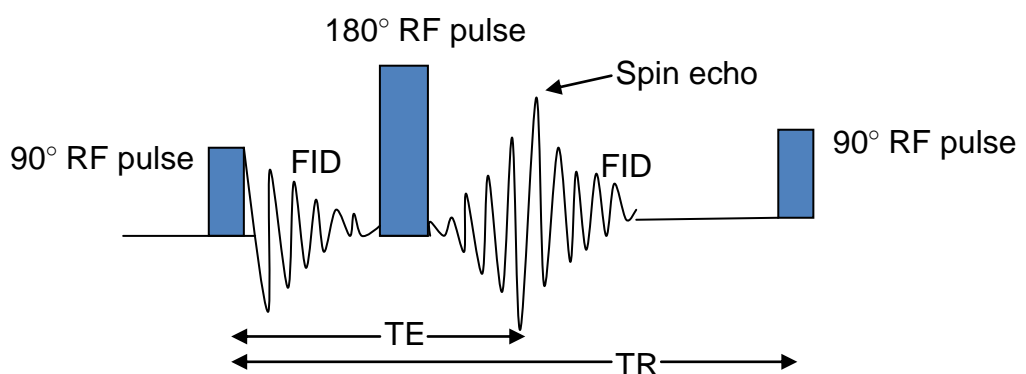
Figure 77**: Representation of TE and TR in a spin echo sequence. TE is the time until the echo is read and TR is the time until the sequence is repeated.**

Figure 77 illustrates the parameters TE and TR and how they are measured in terms of the spin echo sequence. Both TE and TR can be set at different lengths; these times will determine which tissue contrast will predominate, T_1 or T_2. In terms of T_1 weighting, this is actually controlled by the choice of TR (McRobbie, et al., 2007).
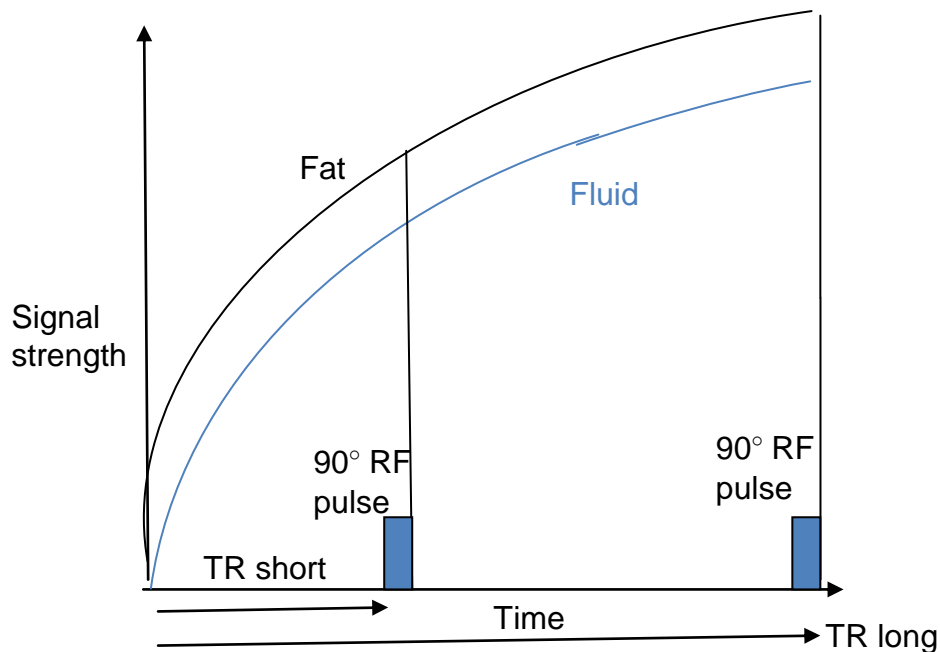
Figure 78: A spin echo sequence with spin-lattice relaxation (T_1); with a short TR fat produces a higher MR signal making it bright on an image.

It has already been discussed that the longitudinal magnetisation vector of fat, M_0, recovers more quickly than that of fluid. Figure 78 illustrates that when a short TR is used there is a higher longitudinal net magnetic moment of fat protons to undergo resonance and produce a higher signal (McRobbie, et al., 2007). A short TR maximises T_1 contrast and a long TR minimises T_1 contrast (Graham, et al., 2012).

T_2 (spin-spin relaxation) weighting or the decay of the transverse magnetisation vector, M_{xy}, is determined by the choice of TE, (McRobbie, et al., 2007).

As already discussed T_2 relaxation is the decay of the transverse magnetisation vector, M_{xy}. Fat decays more quickly; a short TE will not allow the signal difference between fat and fluid to be perceived if the echo is read too soon. A long TE allows the difference in decay rate to be measured; ensuring fluid will give a high signal due to its transverse magnetisation vector, M_{xy}, decaying more slowly (Lauterbur, 1973)..

In a gradient echo sequence a T_2 weighted image is achieved is the same way as described above and shown in Figure 79 with an appropriate choice of TE.

A T_1 weighted image in a gradient echo sequence does not depend on TR as described in a spin echo sequence but on the choice of flip angle produced by the radiofrequency pulse (McRobbie, et al., 2007). So far it has been discussed that an applied radiofrequency pulse will move the proton net magnetic moment from the transverse plane. A gradient echo sequence uses a partial flip angle of

less than 90°. A flip angle of this size will mean the net magnetic moment of the protons is not moved completely into the transverse, M_{xy}, plane. Instead the net magnetic moment has a transverse and longitudinal component (McRobbie, et al., 2007). See Figure 80 below:
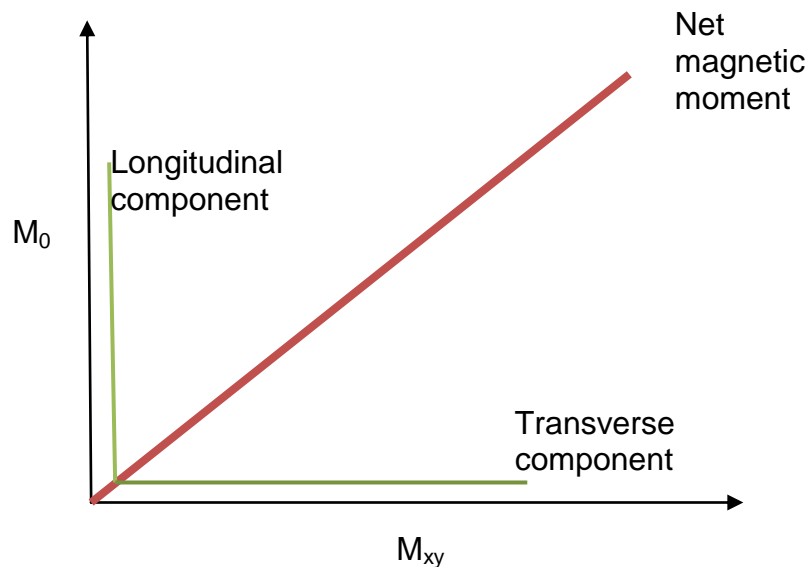
Figure 80: A gradient echo sequence with a flip angle of less than 90°; the net magnetic moment has a transverse and a longitudinal component.

If a flip angle of less than 40° is used the magnitude of the longitudinal and transverse components is similar for both fat and fluid; this would provide a low contrast image and poor tissue differentiation (McRobbie, et al., 2007). A flip angle of between 50° and 90°, produces longitudinal and transverse components which are not the same for fat and fluid (McRobbie, et al., 2007). In fact, fat has a larger transverse component to its magnetic moment; therefore when T_1 relaxation occurs, fat produces a larger MR signal making it appear bright on the final image, enabling fat based tissues to be distinguished from water based ones.

3.3 MRI of the anatomical structure of the equine sample

3.3.1 Aim

Chapter 2 of this thesis described imaging the whole equine tail and the dissected tail using x-ray. This is a useful tool for bony anatomy and contrast enhanced vessels. However, MRI is designed for imaging bone and soft tissue even without exogenous contrast. In this section high resolution axial and sagittal images were taken of six tail samples of varying ages and the structure of the annulus and nucleus were quantitatively analysed.

3.3.2 Method

Six fresh equine tails were collected and prepared as described in section 2.2.1. A difference in the preparation of these samples was the addition of heparin. Heparin causes the blood to lose its ability to clot (MedlinePlus, 2013). It is important to use the correct amount to enable the Heparin to be effective. The literature quotes 10 u/ml of Heparin in a solution (Niesen, 2003). A 0.15 M solution of sodium chloride was made in the normal way. The Heparin used was Sigma Heparin sodium salt from bovine intestinal mucosa at 146 units/mg. To ensure the correct concentration was used 68.5 mg of the Heparin salt was used in 1l of saline; this gave 10 u/ml. The samples were flushed through with this solution at the abattoir immediately post slaughter.

 MR imaging is multi-planar, orientations are shown in Figure 81 (assuming the sample is in the scanner head first and supine). The body coil within the scanner is utilised in transmitting the signal. The receive coil was a Phillips microscopy coil of diameter 45 mm which was laid directly on the uppermost surface of the tail. In each case the tenth disc from the bottom of the caudal spine was imaged; this disc was chosen as it is centrally placed in the caudal

spine and therefore representative of discs in that area. A sagittal localiser scan was initially undertaken to determine the position of this disc; the microscopy coil was then placed directly over this disc.
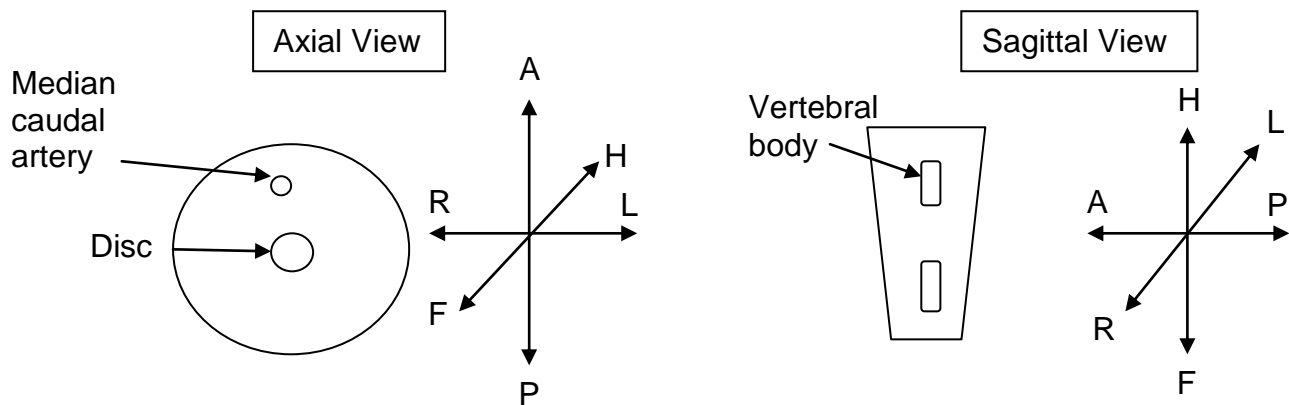
Figure 81: 3D representation of the position of axial and sagittal slices within the MR field of view: A-Anterior, P-Posterior, R-Right, L-Left, F-foot, H-head.

An initial localising scan was performed to locate an appropriate disc. The typical sequence selected for the samples was a gradient echo sequence. Gradient echo sequences allow for faster imaging, because the 180° radio frequency pulse found in spin echo sequences is omitted, and flip angles less than 90° can be used to allow shorter TR. A potential disadvantage of gradient echo sequences is their sensitivity to magnetic field Inhomogeneities; but this proved not to be an issue in the present study. The particular sequence used is a specialised gradient echo sequence known as Fast Field Echo (FFE) (Van Der Meulen, et al., 1988). This sequence uses balanced gradients whose net value is zero; this enables two signal echoes to be acquired for each radio frequency excitation, giving a further reduction in imaging time (MR-Technology Information Portal, 2013). In the present context where high resolution multislice imaging is required, fast imaging is an important requirement; the FFE

sequenced used allowed each disc to be imaged in around 30 minutes. The other parameters used were a TE of 11 ms, a TR of 30 ms and a flip angle of 30° these values provide a limited amount of T_1 and T_2 contrast, allowing good visualisation of a range of anatomical features. The resolution of the images was 0.104×0.104 mm.

Two files were produced from each scan, a PAR and REC file; the PAR file (see Appendix 1 for example) lists all the sequence parameters and the REC file contains the image data, broken down into separate slices. The Image J WCIF software is unable to work with these types of files and therefore MRIcro software (McCausland Center for Brain Imaging, n.d.), was used to convert theses files to IMG and HDR files to enable them to be opened by Image J WCIF. The Philips PAR file is imported and converted into an analyze format, that is a HDR file.
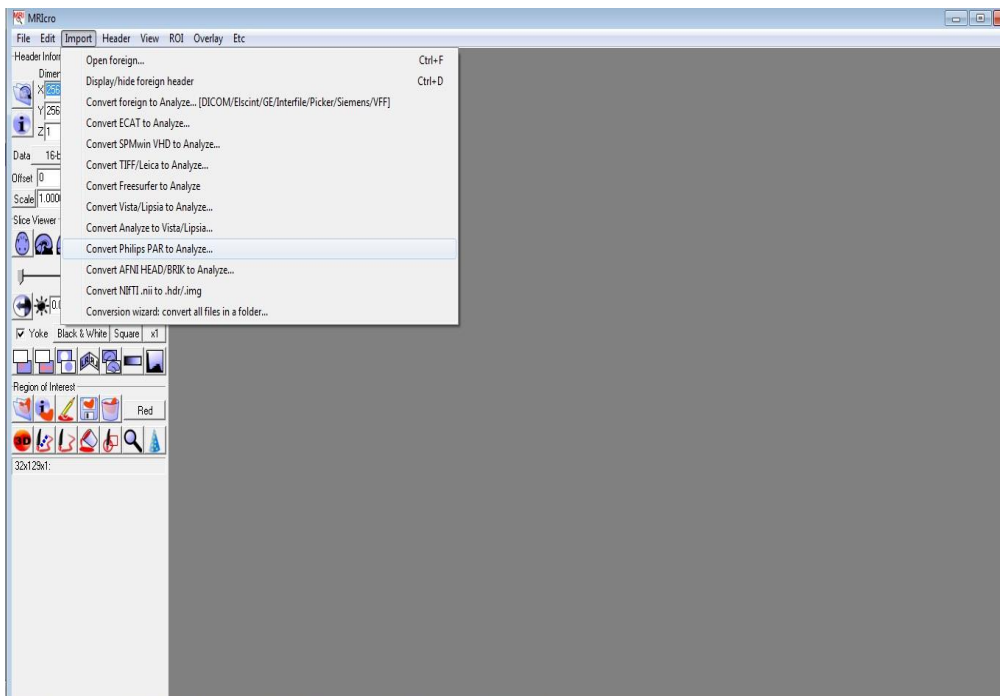
Figure 82: Main menu of MRIcro showing file conversion.

148

Axial and sagittal views were obtained. These two scans were imported into Image J WCIF to enable disc dimensions to be measured: annular thickness (inner and outer ring width, anteriorly, posteriorly and laterally) and the disc width anteriorly-posteriorly and laterally.

The entire intervertebral disc and a portion of the superior and inferior vertebral bodies either side of the tenth disc from the bottom of the tail were included in both scans. In one of samples, aged 14 years the separate slices are stacked using Image J WCIF; this entails using the IMAGE STACKS tab and then the CONVERT IMAGES TO STACK tab. This stack is then put into VOLUME VIEWER within Image J WCIF using the PLUGINS tab followed by STACKS Z FUNCTIONS tab and VOLUME VIEWER tab.

In chapter 4 as part of the series of diffusion scans a high resolution anatomical scan was produced; the associated parameters of the scan sequence are described in chapter 4. These scans were used to provide structural data. The explanted discs were from various locations within the caudal spine and were used to investigate the variations in lamellar width with disc size and age of sample. 14 out of the 23 samples were used. On one of the samples from chapter 4 the last disc in the caudal spine was imaged to investigate how the disc changes along the caudal spine.

3.3.3 Results

Figure 83 and Figure 84 illustrate an axial and a sagittal view of sample 1, aged 14 years. Both the axial and sagittal views are approximately placed as the central slice within the disc. Both figures show periodic variation of image brightness in the disc annulus (as 'rings' in Figure 83 and 'stripes' in Figure 84). These factors relate to the lamellate structure of the annulus. Dunn et al (Dunn,

et al., 2006) suggest that the bright and dark regions correlate with changes in orientation of collagen fibres which, because of magic-angle effects (Bydder, et al., 2007), produce changes in MRI signal intensity. It is a matter of definition as to whether the periodicity of the structure is measured as the width of a single bright or dark feature, or as the thickness of a bright-dark combination. Here we have defined the lamellar thickness as the width of a bright region in the image. Figure 83 and Figure 84 have line regions drawn on showing how lamellar and disc widths were measured. A lamellar ring was considered visually as an area of high signal intensity which was bounded by a thin low intensity signal area. Inner and outer lamellar rings were defined as a ring within the first two next to the nucleus and one of the last two outer rings respectively.
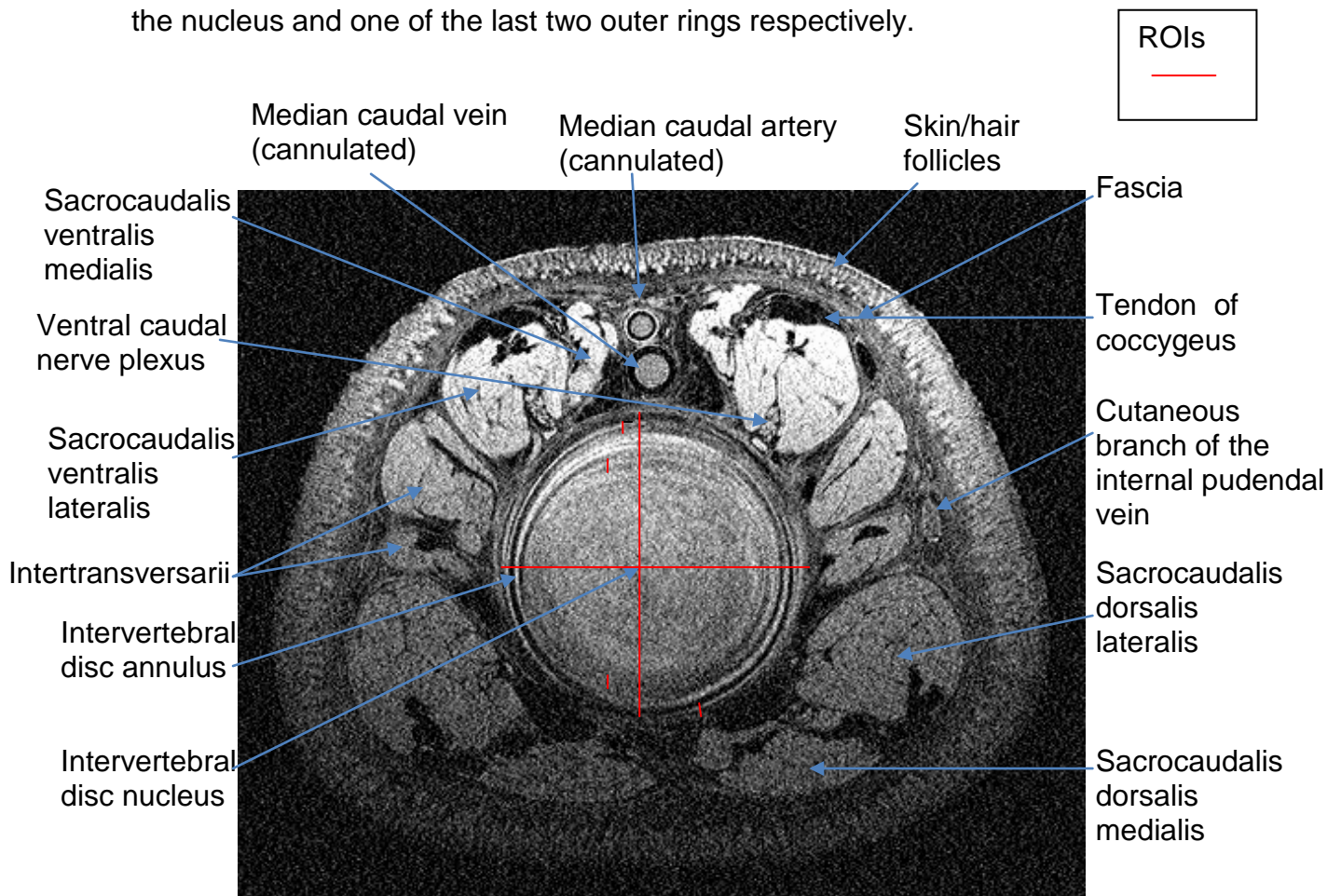
Figure 83: A central axial disc slice through the equine sample aged 11 years; there is some signal drop out at the bottom of the image due to the depth penetration constraints of the microscopy coil.

150
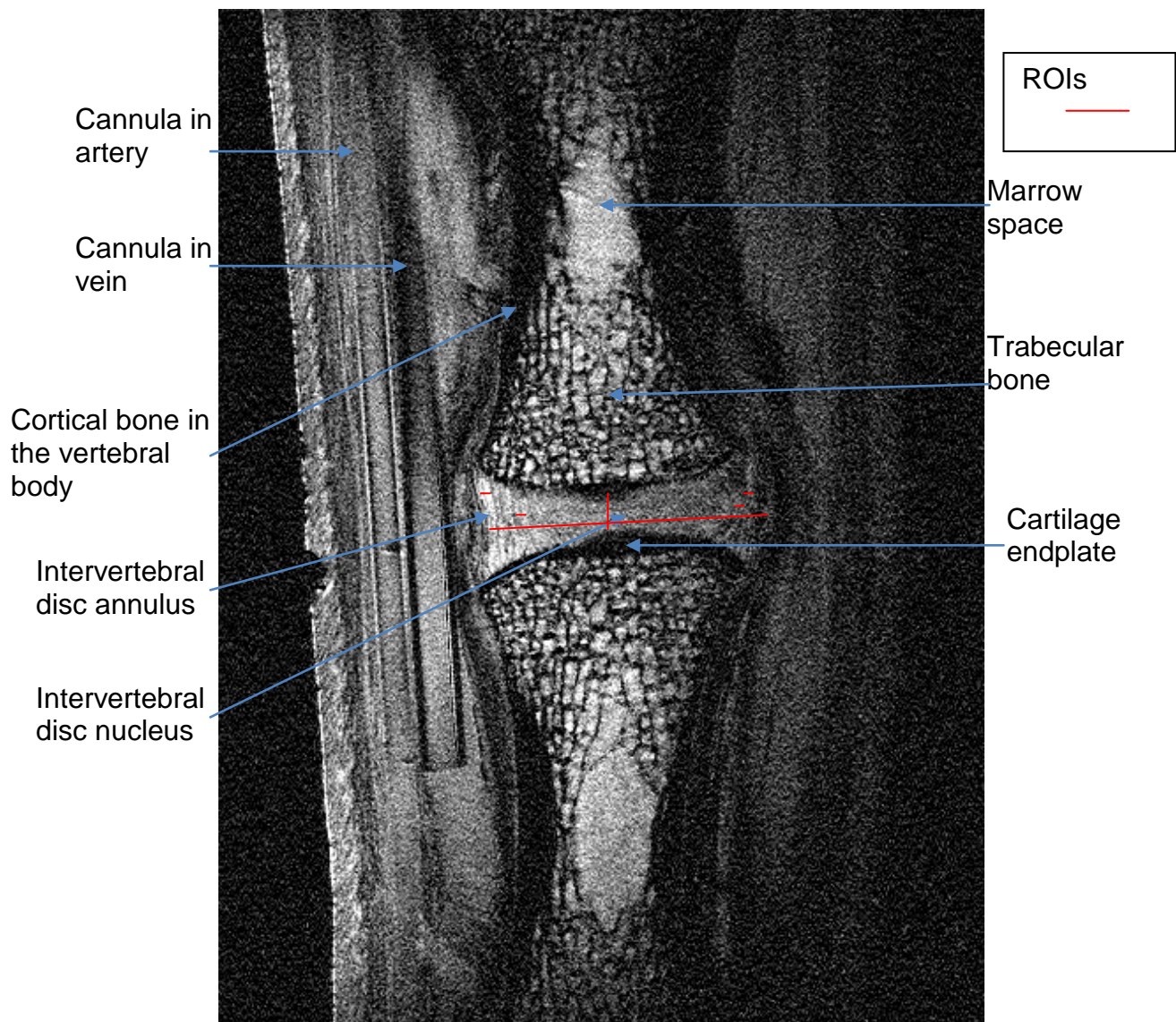
Figure 84: A central sagittal slice through the equine sample shown in Figure 83.

Figure 85 below shows a 3D reconstruction of an image stack in the axial plane.

Skin/hair follicles

Median caudal artery

Trabecular bone in the vertebral body

Muscle

Ligament

Subchondral vertebral endplate

Disc

Volume Viewer
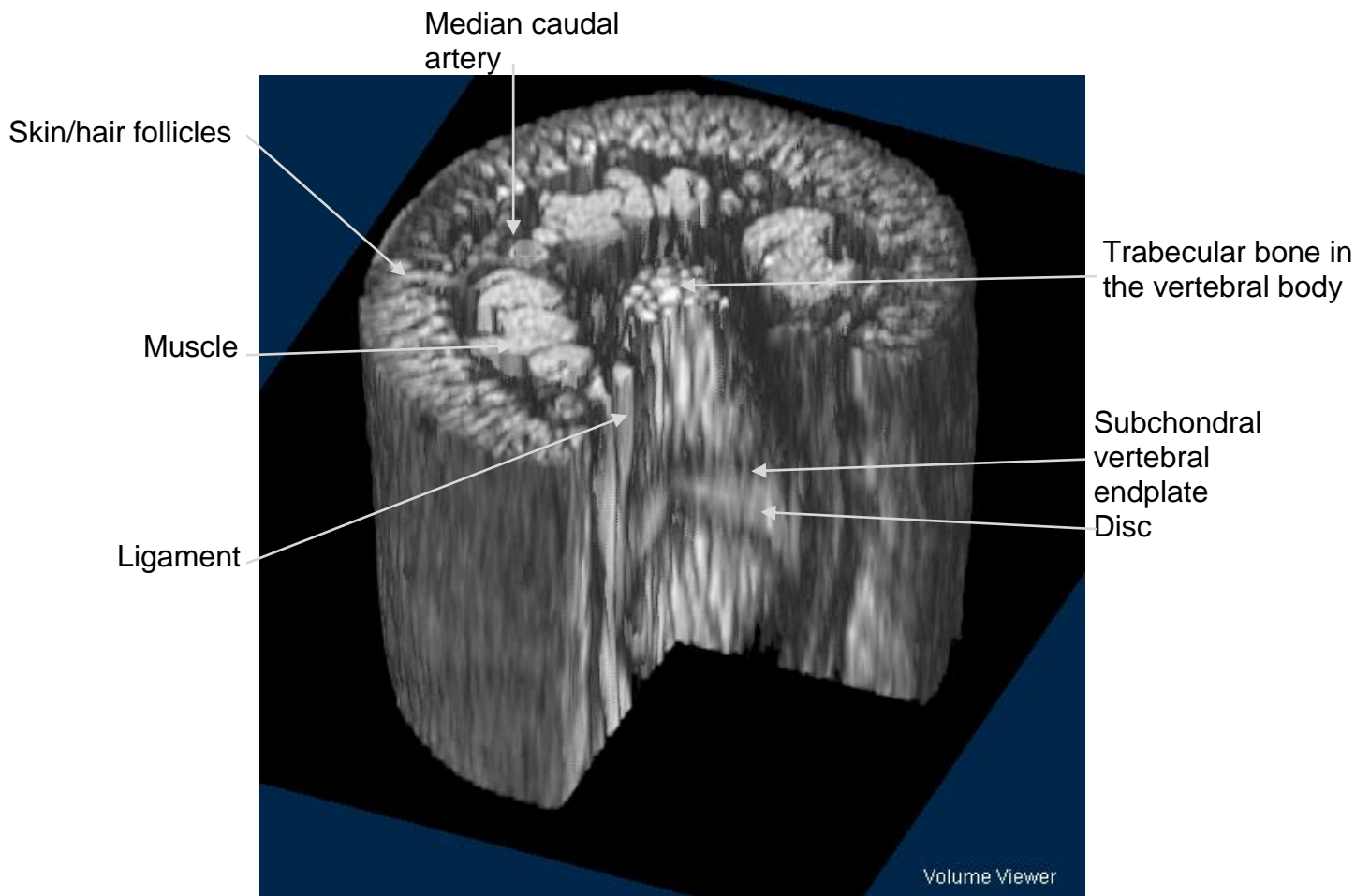
Figure 85: A 3D reconstruction of an equine motion segment aged 14 years. This is a high resolution image so that even hair follicles can be seen. The main median caudal muscles can be seen. Cortical bone produces no signal in MRI, therefore there is a dark area around the trabecular bone.

The 3D construction above illustrates the contrast produced by a FFE scan sequence; a fat based tissue such as bone and a water based tissue such as muscle both produce a high intensity signal. An absence of signal may be seen surrounding the trabecular bone and at the border between the vertebral body and the disc. This represents cortical bone; a lack of free protons results in no MR signal. A large longitudinal ligament extends the length of the caudal spine; this is evident on dissection and can be seen in the Evans blue perfused sections in chapter 2.

The actual dimensions of the central slice in the tenth disc were variable. The anteroposterior dimension varied between 11 mm and 21.9 mm and the lateral

dimension varied between 11 mm and 20.8 mm randomly in the samples for the same disc level.

The six tails investigated were from horses of different ages and the structural characteristics of the central slice through the intervertebral disc are summarised in Figure 86 to Figure 90. The nucleus has a uniform contrast, illustrating a lack of structure and consistency of matrix composition. The annulus consists of rings of high signal separated by rings of low signal; the high signal rings are produced by the tightly bundled collagen fibres of the lamellae and the low signal rings are the interlamellar spaces which consist of predominantly fluid matrix. The disc has an average of four to six lamellar rings; which corresponds to dissection shown in the Evans blue sample in chapter 2. The thickness of the units varied between inner and outer annulus in both the anterior and posterior sides. Outer anterior annulus lamellar rings have an average thickness of 0.43 mm ±0.06 mm, inner anterior annulus lamellar rings have an average thickness of 0.21 mm ±0.04 mm, inner posterior annulus lamellar rings have an average thickness of 0.21 mm ±0.04 mm and outer posterior annulus lamellar rings have an average thickness of 0.34mm ±0.05 mm. The lateral lamellae have the following dimensions: inner left annulus 0.48 mm ±0.03 mm, outer left annulus 0.35 mm ±0.04 mm, inner right annulus 0.47 mm ±0.04 mm and outer right annulus 0.40 mm ±0.04 mm. The differences in dimension between the lateral lamellae are small in the central slice when the measurement error is considered. From Figure 83 it can be seen that the lamellae are not continuous, with six anteriorly and four posteriorly.
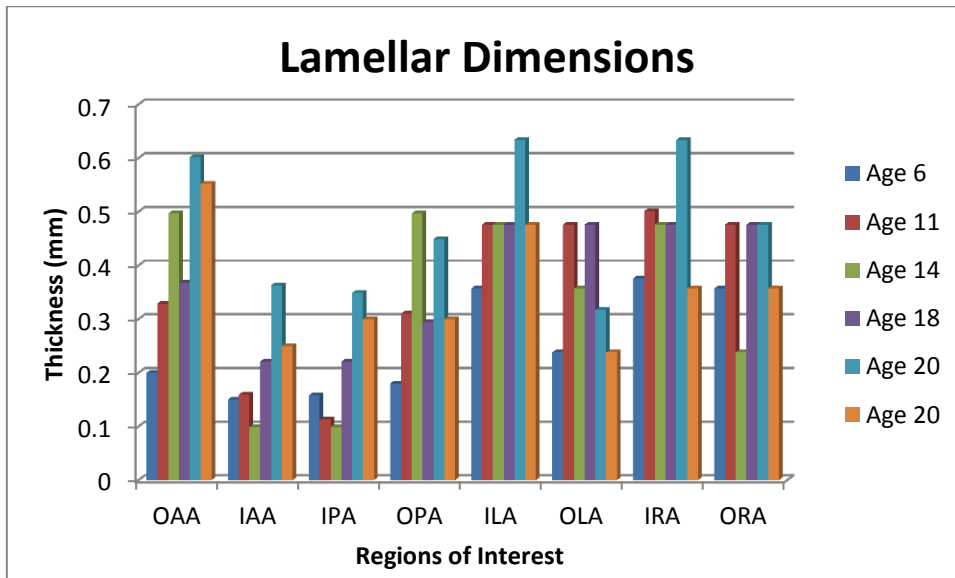
Figure 86: The thickness of the lamellar rings in the equine sample. These results are obtained from the tenth disc from the bottom of the samples: OAA-Outer Anterior Annulus, IAA-Inner Anterior Annulus, IPA-Inner Posterior Annulus, OPA-Outer Posterior Annulus, ILA-Inner Left Annulus, OLA-Outer Left Annulus, IRA-Inner Right Annulus and ORA-Outer Right Annulus. It can be seen that the outer lamellae are consistently thicker.
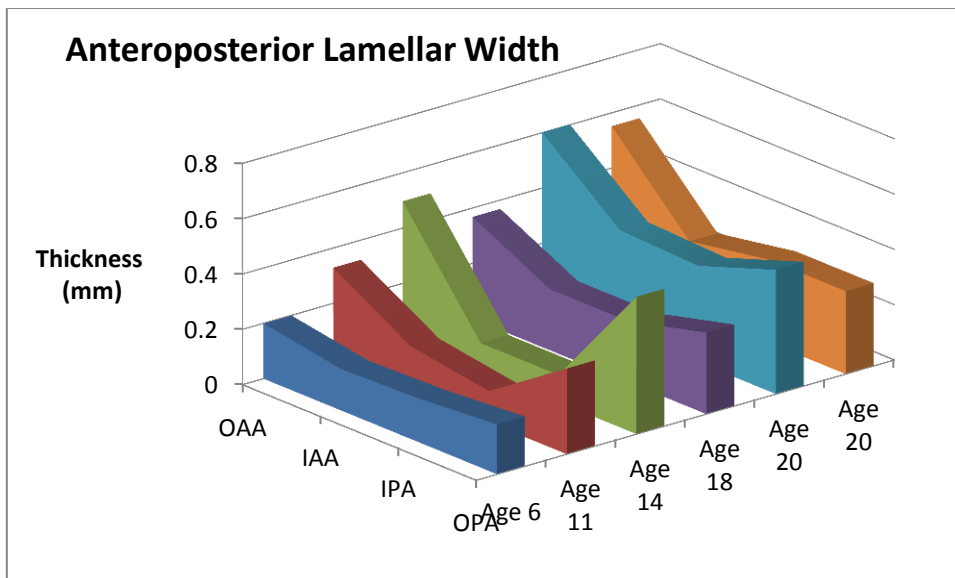
Figure 87: Variation in lamellar width from the anterior to the posterior surface of the equine sample. There is limited evidence in this graph that lamellae become wider with age and that anterior outer lamellae tend to be wider.

In all the tails the outer lamellae were the thickest. In this small sample there was also a suggestion that the lamellae become wider with age. A correlation

154

coefficient between age and lamellar width was determined using the Data Analysis Tools in EXCEL. A strong correlation of 0.87 was found between the outer anterior annulus and age. A strong correlation between the inner anterior and inner posterior annulus of 0.71 and 0.75 respectively with age was found. A weak correlation of 0.5 was found between the outer posterior annulus and age. It was also found that there was a strong association with the dimensions of the anterior lamellae and the posterior lamellae, regardless of their position anteriorly or posteriorly. The inner lamellae had a correlation of 0.95 and the outer lamellae a correlation of 0.76.

Figure 88 illustrates the behaviour of the lamellar rings above and below the central slice. It was observed previously that within the central slice the lamellar rings were not continuous; this is the case for the vertical direction also. The subchondral endplate is in view directly over the area of the nucleus (D); identified by the absence of MR signal. Anteriorly, four lamellar rings are identified. In C, the central slice, five lamellar rings are evident anteriorly. This may be as a result of the concave nature of the bone/disc interface.

Note that in Figure 83, Figure 84 and Figure 88, the signal level (image brightness) falls off with distance from the receiving coil (e.g., from top to bottom in Figure 83). The Philips imaging software incorporates a 'CLEAR' function which compensates for this fall-off-this option was used on the image slices in Figure 85, and for the diffusion studies in chapter 4.
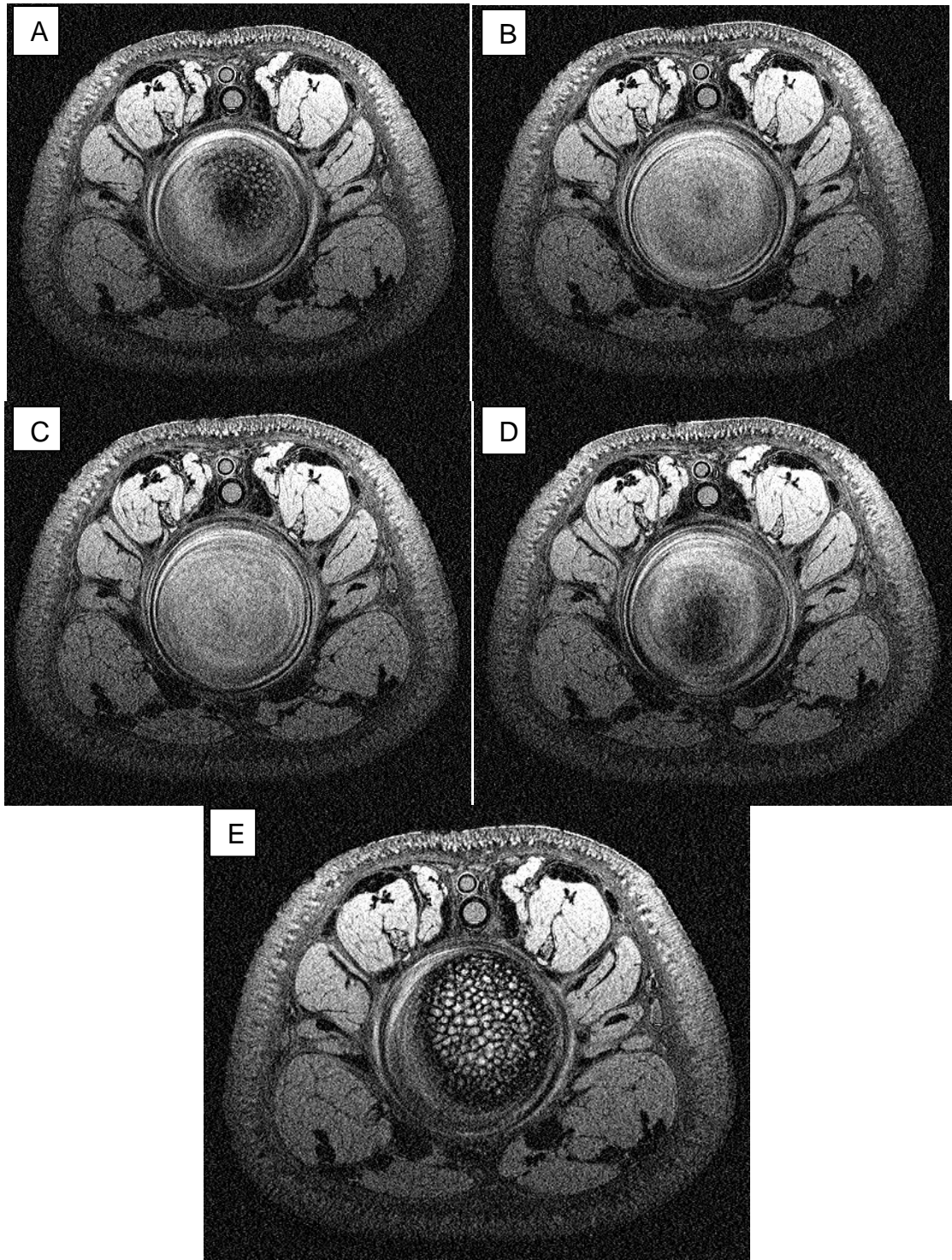
Figure 88: A panel of images illustrating the slices through a disc from the inferior to the superior surface.
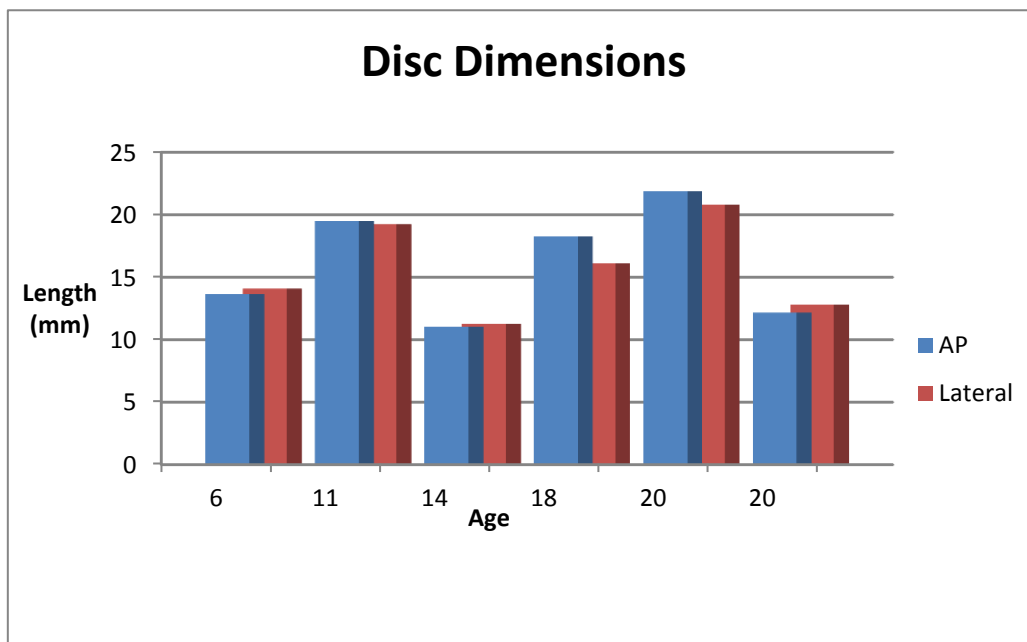
Figure 89: Anteroposterior and lateral disc dimensions of an axial view of the tenth disc from the bottom of the equine tail sample. There does not appear to be a certain direction for the long axis of the disc, but this does demonstrate that they are not completely round.

The disc from Figure 83 can be seen not to be perfectly circular. Figure 89 shows length (diameter, measured along AP and lateral directions, as illustrated in Figure 83) for six discs taken from the same area of the spine in horses of different ages. Again, discs are not exactly circular. There also does not seem to be any relationship between disc dimension and age. Differences between horses may relate to the breed type (i.e., overall size of horse). The measurement differences are greater than the error in measurement which is associated with the image resolution (0.104 mm $\times$ 0.104 mm).

Figure 90 shows the minimum and maximum thicknesses [as defined in Figure 84, measured at the centre and edge of the disc, respectively] for six discs taken from the same area of the spine in horses of different ages. In the sagittal view of the disc its thickness varies between 1.35 mm and 3.83 mm at its central minima and 4.47 mm and 11.8 mm at its edges. The superior and

157

inferior surfaces of the disc are concave. Differences between horses may relate to the breed type (i.e. overall size of horse) but also to the degeneration state of the disc.
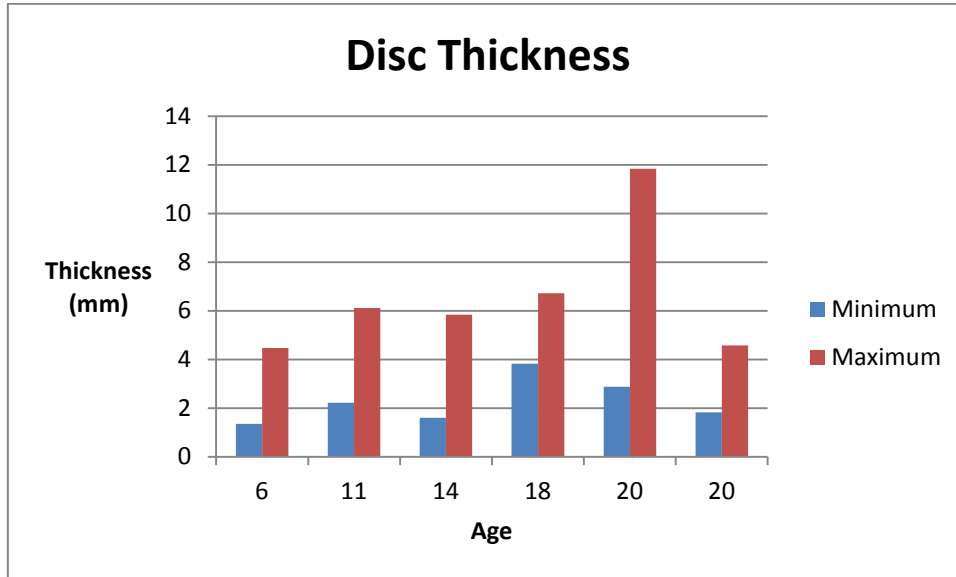
Disc Thickness

Figure 90: Thickness of the intervertebral disc in the sagittal view of the tenth disc from the bottom of the equine tail sample. There does not appear to be a relationship between age and thickness.

Figure 90 does not show a correlation between the thickness of the intervertebral disc and the age of the sample, which may happen with dehydration as a result of age related changes.

Average Lamellar Dimensions for Each Region

158
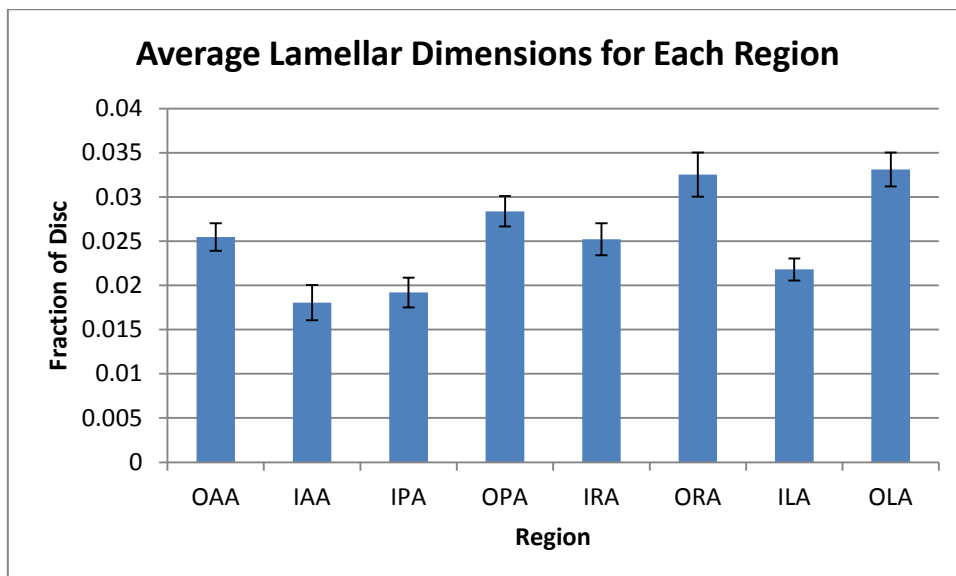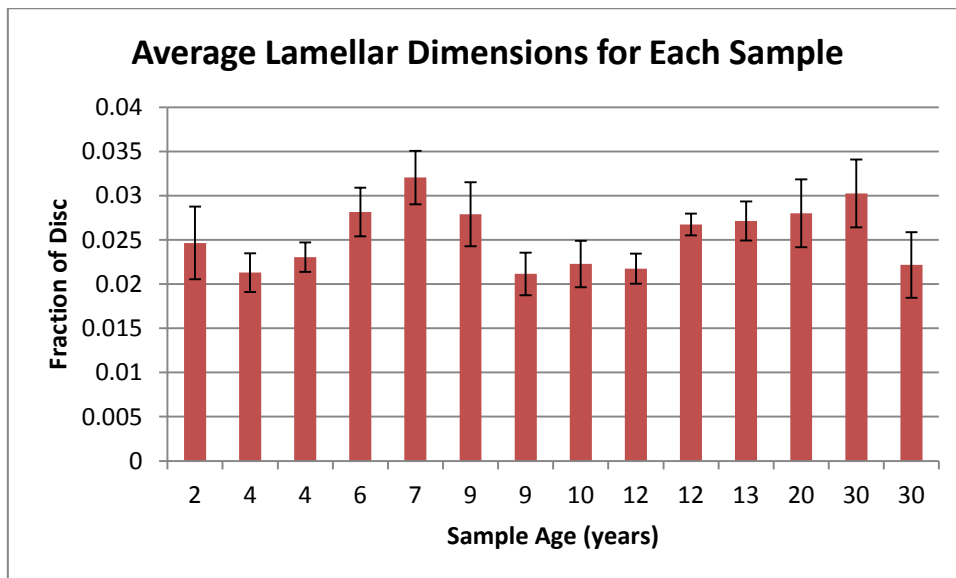
Figure 91: The explanted disc; the fraction each lamellae width represents in terms of the total width of the disc, the regions are as previously detailed. The outer lamellar regions appear to be consistently thicker. The bottom panel illustrates that there does not appear to be a relationship between age and lamellar dimension.

In Figure 91 the width of the lamellae as a fraction of the total width of the disc are shown. The outer lamellae are shown to be the widest as in the intact tail. However, with the larger sample there is no relationship with age and lamellar width. For all regions the range of lamellar width was from 0.14 mm to 1.11mm. This larger lamellar width was not the result of the size of the disc. Rather as a disc became larger so did its nucleus; although the nucleus was uniform in the overall proportion it represented of the whole disc. In the anteroposterior direction the nucleus on average occupied 0.6 (with a STD of $\pm$ 0.06) of the entire disc size.

159

	AP
AP	1
OAA	0.086414
IAA	0.177516
IPA	0.33578
OPA	-0.11858
IRA	0.247129
ORA	0.06686
ILA	0.42957
OLA	0.157781

Table 1: Correlation coefficients illustrating the relationship between lamellar width in regions and total anteroposterior (AP) disc width; regions are those specified previously. There does not appear to be a relationship between overall anteroposterior dimension and lamellar dimension apart from the Inner left annulus where there is a weak correlation.

In the caudal equine tail, each subsequent intervertebral disc becomes smaller; although the discs become smaller they are all structurally the same, they have a nucleus and an annulus containing lamellar rings. Figure 92 below illustrates an axial slice through the last intervertebral disc.

Lamellar ring

Subchondral end plate of the vertebral body
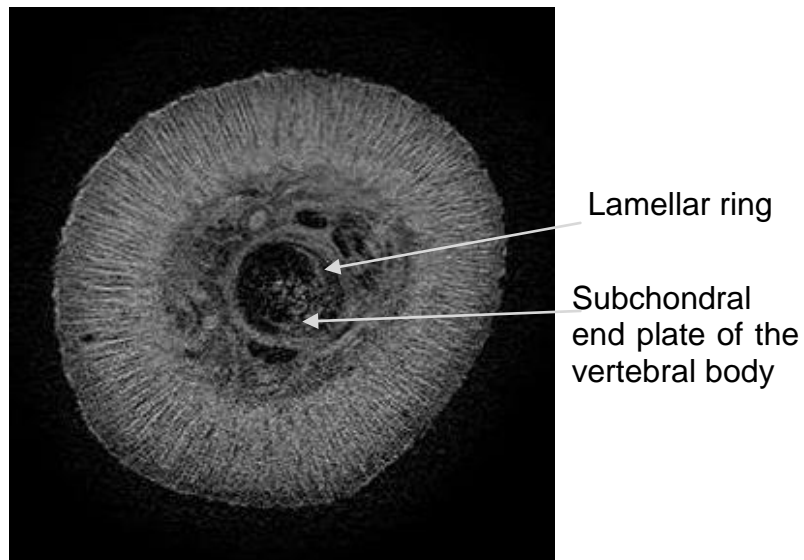
Figure 92: An axial slice through the last disc.

160

The dimension of this disc in the anteroposterior direction is 4.688 mm and in the lateral direction is 5.273 mm.
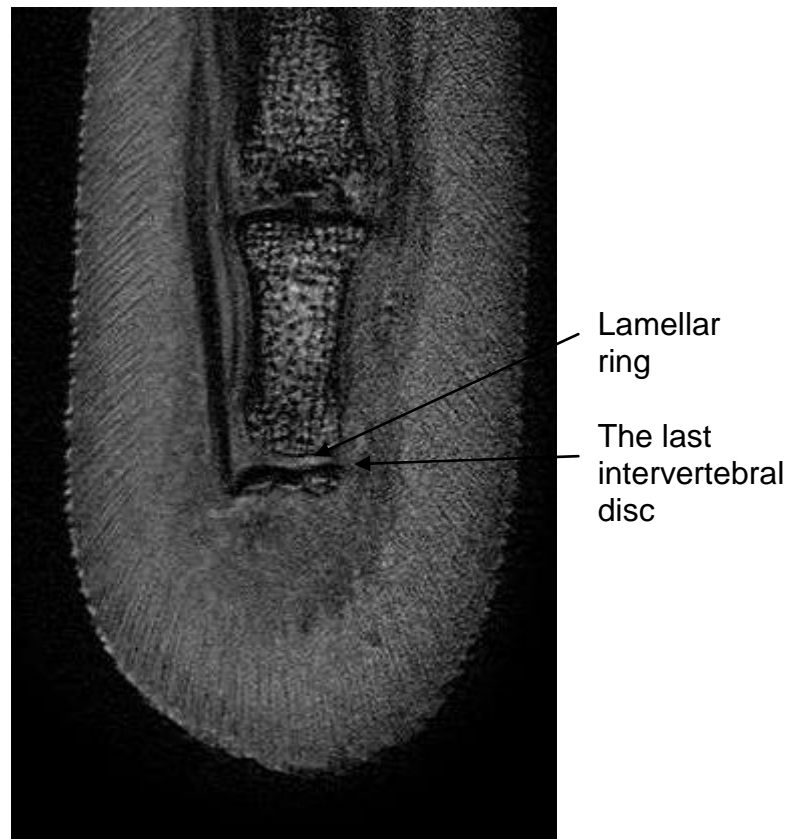
Figure 93: A sagittal slice through the last intervertebral disc.

The thickness of the disc is 0.293 mm; this last disc is uniform in its thickness.

3.3.4 Discussion

The human intervertebral disc is between 7 to 10 mm thick and 40 mm in width in the anteroposterior direction (Urban & Roberts, 2003). The caudal equine disc is thinner and smaller in diameter. The equine disc is concave on both its superior and inferior surface; in the human disc the surfaces are convex. This is perhaps due to requirements of the disc. The equine tail is not weight bearing as in the human lumbar disc and therefore can be smaller as it does not need to distribute large loads; although it has been suggested that quadrupeds'

161

intervertebral discs have similar or possibly higher compressive loads (Alini, et al., 2008).

In the human disc there are found to be 15 to 20 concentric lamellar rings (Urban, 1990). In Figure 83, the equine sample can be seen to consist of approximately 5 lamellar rings only. In Figure 83 the annulus appears as high signal thick rings alternating with low signal thin rings; this characteristic appearance is due to the dense collagen fibres of the lamellae interspersed with finer collagen and proteoglycan rich matrix. The lamellar rings in the human disc have a thickness of between 200 and 400 microns (Inoue & Takeda, 1975). This is different to the equine sample with rings of between 140 and 1110 microns; it may be that adequate biomechanical function is maintained by the thickness of the lamellae compensating for their small number. Similar to the human intervertebral disc the outer lamellae are thicker (Inoue & Takeda, 1975); although in humans they were thickest in the outer anterior lamellae. The human lamellae are arranged in concentric rings (Urban, 1990), the equine sample is seen to not always have continuous lamellae and a disc shape which is not perfectly circular. The human lumbar disc is kidney shaped and has a long axis laterally. The nucleus occupies a similar fraction of the entire disc irrespective of its size. The lamellar width does not appear to be dependent on disc size.

In the human vertebral column the last disc is between the fifth lumbar vertebra and the sacrum (Tortora & Grabowski, 2003).The discs of the lumbar region of the vertebral column dissipate load and are the largest discs in the human vertebral column (Tortora & Grabowski, 2003). The sacrum consists of five fused vertebral bodies in the adult skeleton and therefore does not contain

intervertebral discs. The coccyx is without intervertebral discs. The equine sample requires discs all the way along the caudal spine for movement and load dissipation; the tail is highly mobile. In the equine sample, the intervertebral disc changes from being concave and having a variable thickness, to being rectangular and of a uniform thickness.

There is also a lack of facet joints in the vertebral bodies of the caudal spine.

3.4 Contrast enhanced MRI

3.4.1 Introduction

In this section the tail sample is perfused with a MR sensitive contrast agent both to look at the structure of vasculature, complementing x-ray, and also to look at diffusional transport beyond the vasculature.

 MR contrast agents alter the signal produced by the tissue which has taken up the contrast agent (McRobbie, et al., 2007). This enables specific structures or pathologies to be highlighted on the image. Contrast agents may affect the T_1 and T_2 relaxation times of a tissue (McRobbie, et al., 2007). Contrast agents which have an effect on T_1 shorten its relaxation time. This means the net longitudinal magnetic moment recovers more quickly than normal producing a bright signal on the MR image (McRobbie, et al., 2007). Contrast agents which affect T_2 relaxation time again shorten a tissue's T_2 relaxation; the decay of the net magnetic moment in the transverse plane decays more quickly. This will produce a lower signal than normal for tissues on a T_2 weighted image.

3.4.2 In vivo perfusion

The original contrast perfusion apparatus is illustrated in Figure 94. Flexible tubing was attached to a plastic beaker which acted as a reservoir. The tubing had a length of 2.5 m ($\pm 0.5 \times 10^{-2}$ m).
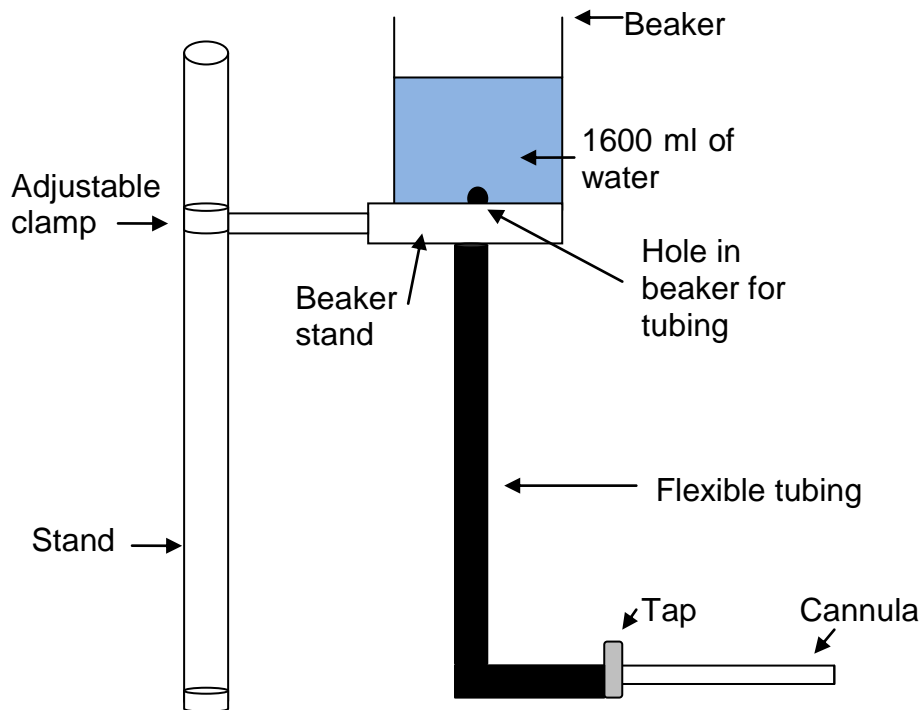
Figure 94: Equipment used to measure volume flow. Due to the height of the beaker, gravity produces a head of pressure which forces the fluid through the cannula.

The tissue was perfused via a cannula of external diameter 1.7 mm inserted into the median caudal artery. Perfusion was begun by opening the tap and allowing the fluid to flow from the beaker. In initial experiments fluid drained through the cut surfaces of skin and muscle rather than through the caudal veins. Therefore in subsequent experiments another cannula was inserted into the main venous return (the median caudal vein) and the cut surfaces were cauterised. With this arrangement drainage was through the venous cannula and arterial and venous pressures could be controlled by adjusting the heights

164

of the appropriate reservoirs. However, in most preparations venous return was poor unless the exit pressure was kept very low. Figure 95 and Equation 3 illustrate pressure, resistance and flow with the addition of the sample.
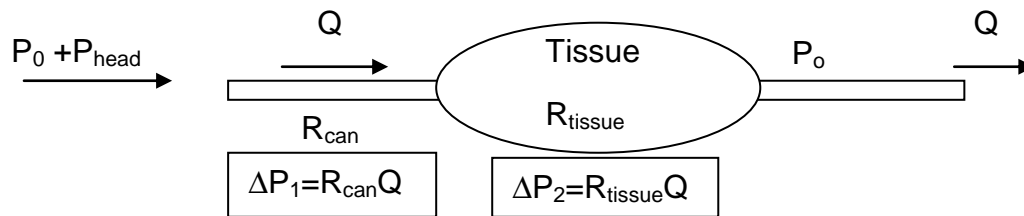
Figure 95: Flow in the tissue. P_0 is atmospheric pressure, P_{head} is the pressure due to the fluid, R_{can} and R_{tissue} is the resistance due to the cannula and the tissue, Q is flow and ΔP_1 and ΔP_2 is the pressure due to the cannula and tissue respectively.

$$P_{head} = (R_{can} + R_{tissue})Q$$ **Equation 3**

Equation 3 illustrates that flow is proportional to the head pressure and inversely proportional to the resistance offered by the cannula and tissue.

3.4.3 Vasovist perfusion

3.4.3.1 Introduction

Vasovist (Bayer Inc., 2007) is an intravenous contrast enhancement agent used for MRI containing the chemical gadofosveset trisodium at a concentration of 0.25 mmol/ml (Bayer Inc., 2007). This is an injectable contrast agent used in Magnetic Resonance Angiography (MRA) to visualise vessels of the abdomen or extremities (Bayer Inc., 2007). Vasovist has the molecular formula $C_{33}H_{40}GdN_3Na_3O_{15}P$ and a molecular mass of 975.88. In humans Vasovist binds reversibly to albumin in plasma, this promotes retention in the blood for

optimal vessel visualisation (MR-Technology, 2008). Vasovist increases the relaxivity of the albumin to which it has bound. On a T_1 weighted image Vasovist will give a bright enhanced signal (MR-Technology, 2008).

3.4.3.2 Vascular MRI using Vasovist

The tail of a 20 year old sample (used in section 3.3.) was perfused as described above with a solution containing 1.44 ml of Vasovist per litre of sodium chloride; this is the typical clinical dose per kg adjusted for the average adult blood volume (Bayer Inc., 2007) To this solution 4 % w/v albumin (Fisher Scientific) was added. This was necessary both to bind the Vasovist to ensure its retention in the vessels for as long as possible and minimises diffusion out of the vessels into the surrounding matrix and to maintain the colloid osmotic pressure of the perfusate and inhibit tissue oedema.

A scan protocol was established to track the filling of the vessels. As in the previous imaging (section 3.3), a gradient-echo FFE sequence was used (see section 3.3.2) which was T_1 weighted. A TR of 25 ms and a TE of 5.2 ms was utilised, with a flip angle of 35°; the values give more T_1 weighting and less T_2 weighting than those used for the anatomical images without contrast agent. Axial and sagittal views were alternately imaged; each scan lasted for 151 seconds. After the scan protocol was established the inlet tap was opened and the Vasovist solution allowed to flow into the arterial cannula; continuous scanning commenced.
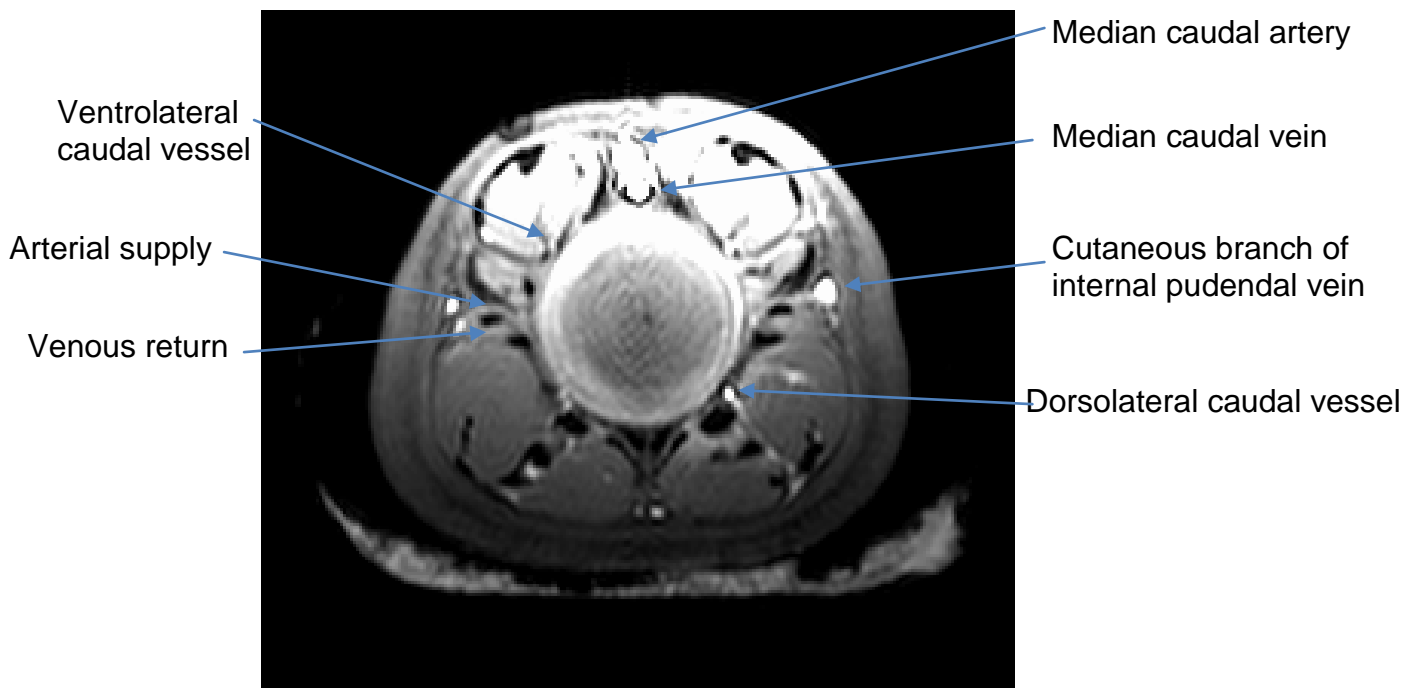
Figure 96: An axial slice at the tenth disc from the bottom of the sample; time since the start of perfusion is 733 s, this is the time after several scans. The contrast agent within the vessels can be clearly seen as very bright areas within the vessels. There also appears to be some enhancement of the annulus of the intervertebral disc.

Figure 96 and Figure 97 illustrate the success of the perfusion. Major and minor vessels are filled with contrast and are apparent by their bright signal. The axial view illustrates a cyclic vascular system which encircles the intervertebral disc. Branching from this circular vessel are vessels which radiate through the muscle groups. There are also major longitudinal vessels on both the dorsal and ventral surfaces. It can be seen from both figures that there is some filling of the tissue close to the artery.

The sagittal view illustrates the major sub-radicular artery which encircles the central portion of each vertebral body. The radicular artery can be seen to branch into numerous nutrient arteries which perfuse the vertebrae.
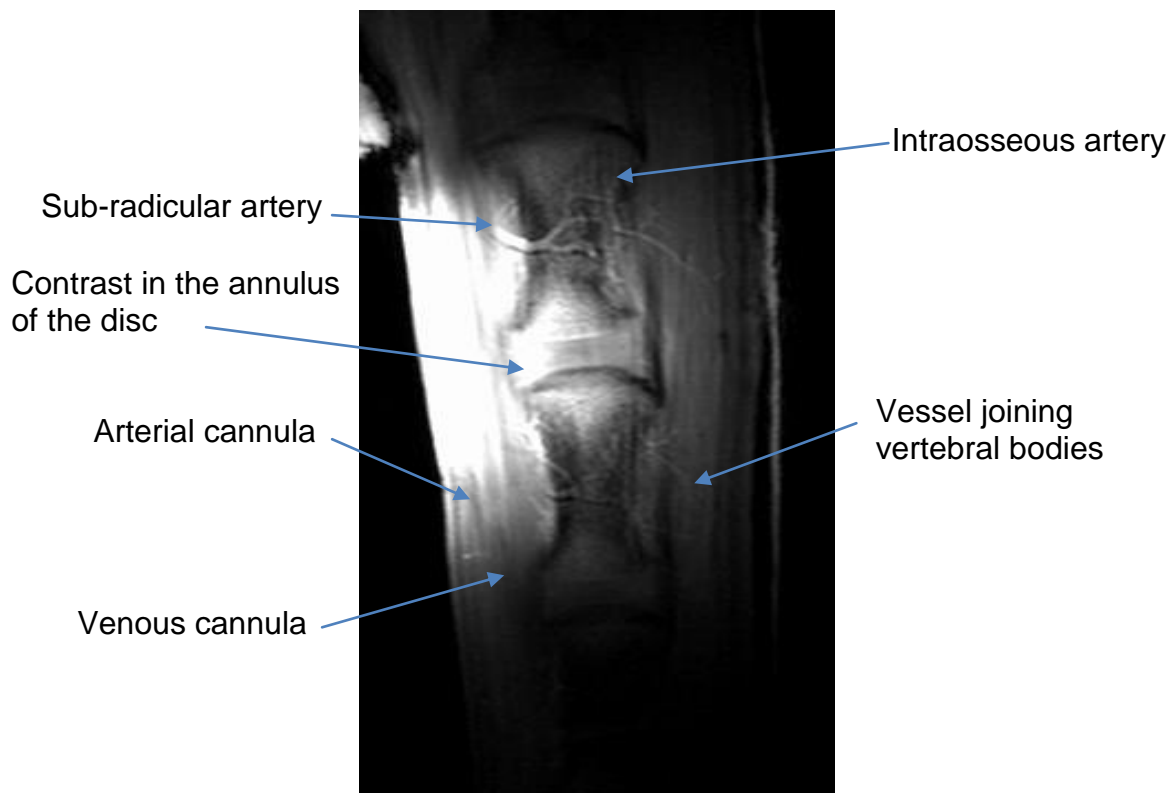
Figure 97: A sagittal view of the tenth disc; 581.76 s after perfusion. This sagittal view illustrates well the pairs of arteries which branch from the aorta. These vessels can then be seen to produce smaller vessels which anamastoses over the vertebral bodies.

To relate the vasculature to spinal structure high resolution scans as described in section 3.3.3 and overlaid with the perfusion scans using Image J WCIF. The overlaid images are then coloured using Image J RGB (Red, Green, and Blue) function placing the structural scan in the green channel and the perfusion scans are placed in the blue channel.

Figure **98** and Figure 99 illustrate the dispersal of contrast agent over time. Figure **98** shows the extent of perfusion after 51 s (based on length of scan duration). The artery has a blue colour illustrating the perfusate and the venous return still appears green. There are some vessels highlighted in the muscle structure. However, some of the annulus does appear to have contrast within it.
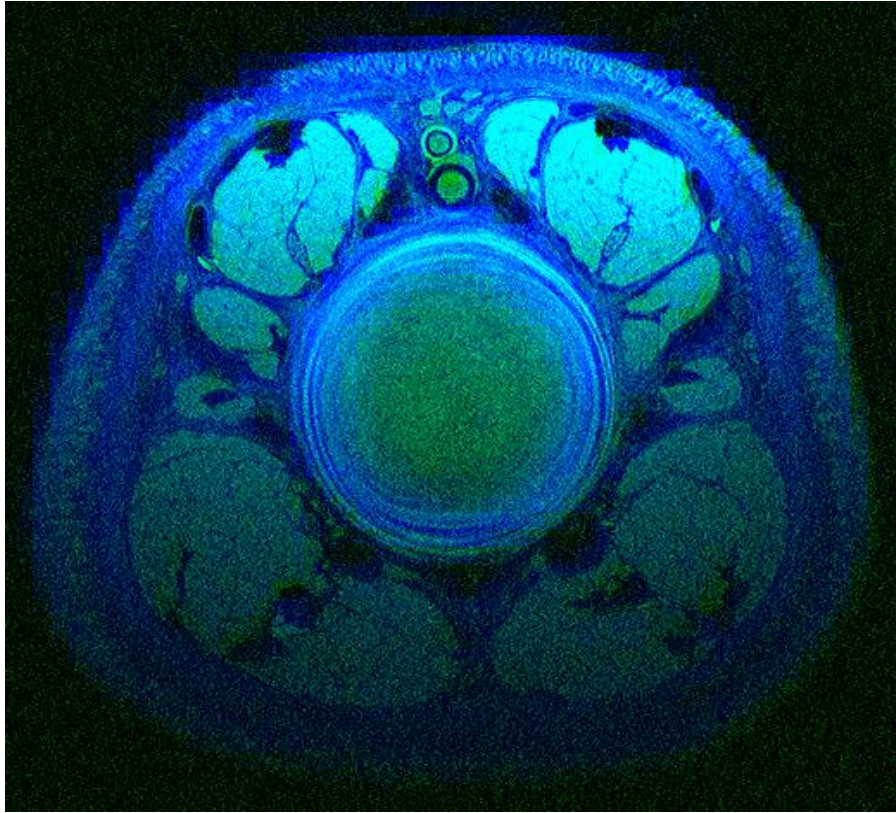
Figure 98**: Axial view of contrast dispersal, 51 s after the start of perfusion. The contrast appears blue on the image. Contrast can be seen in the skin, muscle and some of the peripheral vessels.**
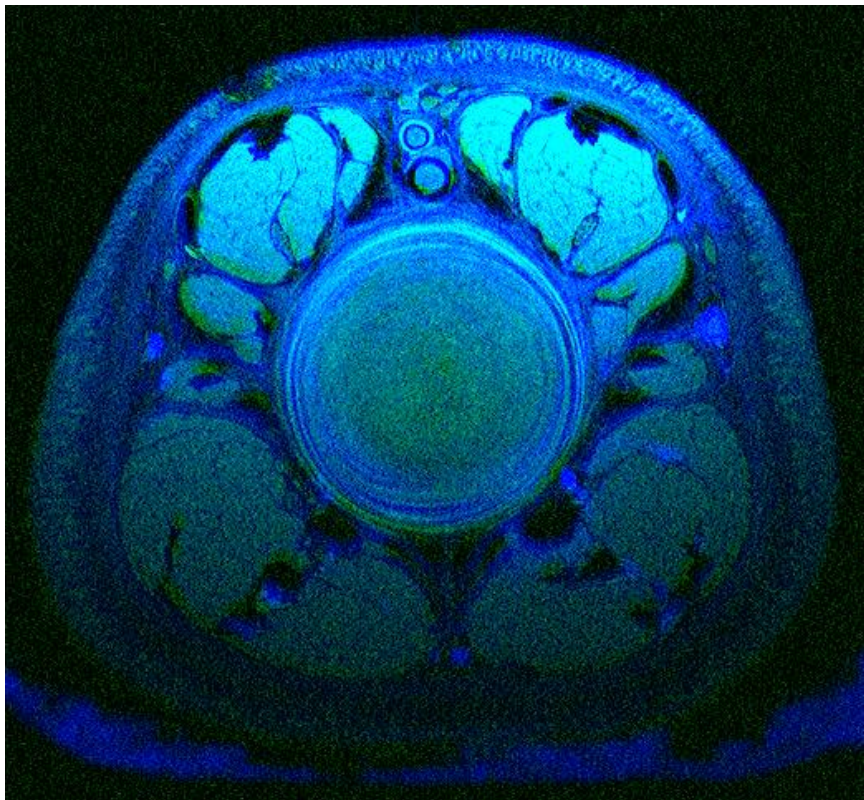
Figure 99: Axial slice of contrast dispersal, 730 s after the start of perfusion. This image shows the contrast distribution after an increased time. In this case, not only are the peripheral vessels highlighted but the centrally placed median vessels, including the median caudal artery and vein are bright blue.

Figure 99 illustrates the contrast dispersal after 730 s (based on scan duration). The median caudal artery and vein both contain contrast and some has penetrated as far as the nucleus of the disc. Some of the nucleus has blue of the contrast agent. The transverse and longitudinal vessel system is well perfused.

A 3D representation for the overlaid images is shown in Figure 100. This image illustrates pooling of contrast at the vertebral endplate and that large regions of the disc are still free of contrast agent.
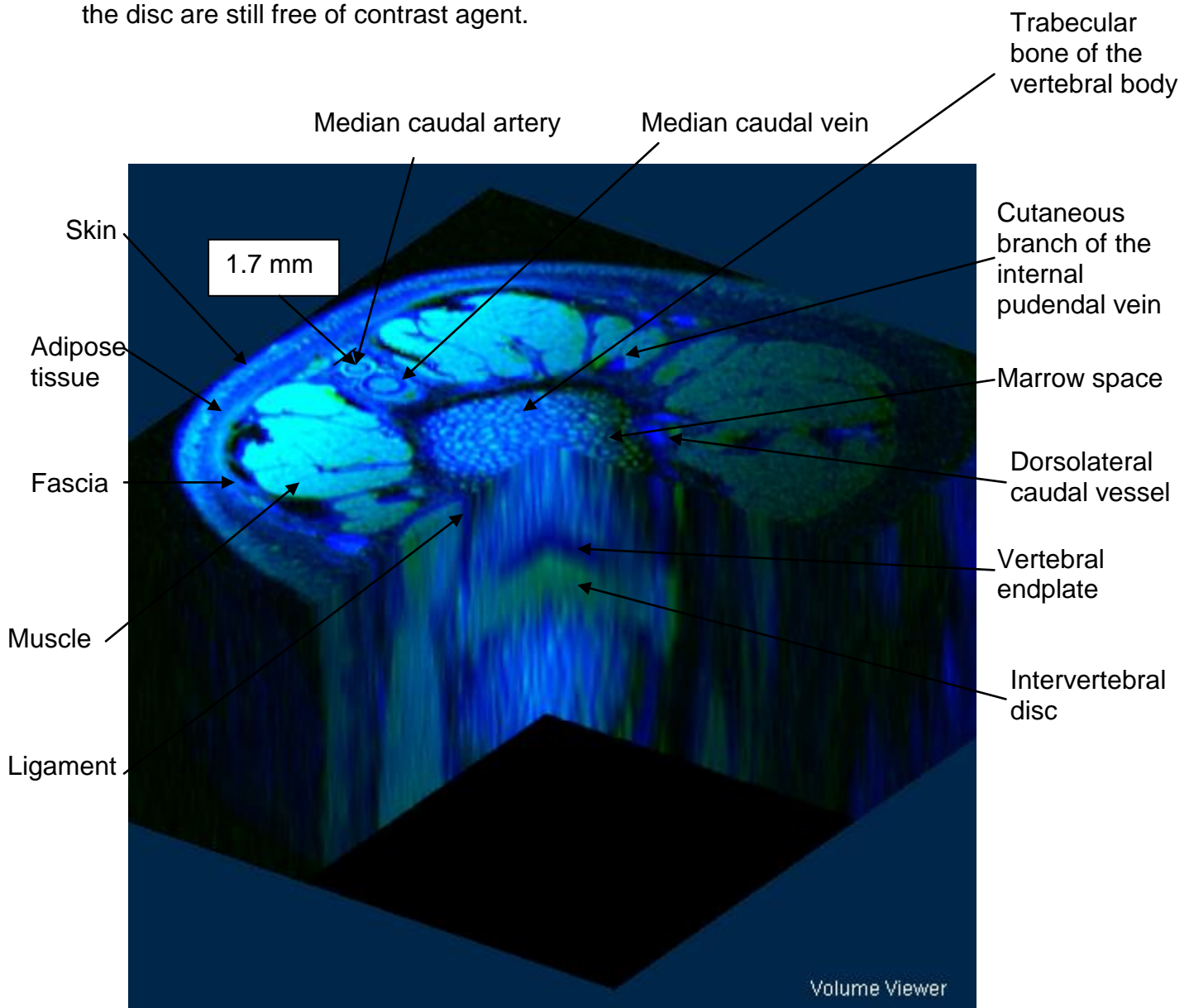
Figure 100: 3D reconstruction of the equine sample; the green colour represents the structural scan which is overlain by the blue diffusion scan. The cannula in the artery has an external diameter of 1.7 mm.

3.4.3.3 Magnetic resonance angiography

Magnetic resonance angiography (MRA) is an imaging technique which allows vessels to be highlighted over surrounding soft tissue and bony structures. In this technique flowing fluid will give a high signal on a T_1 weighted gradient echo image. This is achieved in the following way. If a flowing fluid, such as blood is present in a MR slice, when the imaging sequence is next repeated the fluid which was present within the slice has flowed on to be replaced by unlabelled fluid. This new bolus of fluid has not experienced the previous RF pulse and will therefore have no transverse magnetic vector; therefore it will give a high signal even though the T_1 of fluid is long and the TR of this particular imaging sequence is short (McRobbie, et al., 2007).

There is more than one way of generating an MR signal from flowing fluid; in this thesis phase contrast angiography is used. Phase contrast angiography detects the changing phase of the blood's transverse magnetisation as it moves along a magnetic field gradient (McRobbie, et al., 2007). Additional bi-polar gradients are required as part of the sequence; these enable a linear relationship to be established between blood velocity and the phase of the MR signal (McRobbie, et al., 2007). A parameter called velocity encoding is set which determines the maximum velocity which may be detected by the sequence. This is a number which is difficult to set for the equine sample as the speed of the perfusion is unknown; a series of velocity encoding values were tried based on human values and adjusted to improve the image quality.

In this thesis 3D Phase Contrast Angiography is used. This allows velocity in three dimensions to be measured by using a volume in a thin slice (McRobbie, et al., 2007). These are time consuming scans and spatial resolution must be

reduced otherwise the scan time may become too long. Therefore it is important to understand the resolution required to balance scan time and image quality and produce an image with adequate signal.

To collect the following data a 14 year old specimen was used; the MRA scans were produced after the structural scans in section 3.3.3.

A 3D phase contrast angiogram was performed. The sequence was a T_1 weighted FFE gradient echo sequence. Critical parameters used were a TR of 20 ms, a TE of 3 ms, a flip angle of $20°$ and a velocity encoding speed of 70 cm/s. A maximum intensity projection was created to highlight vessels; this is a scan protocol which is part of the Philips software. This scan series provides an anatomical slice and a slice which highlights just the vessels and minimises other soft tissue.

Figure 101 illustrates this approach in three important areas of spine anatomy. A1 and A2 are of the central portion of the vertebral body. The trabecular bone can be seen to be well perfused. The surrounding cortical bone has some vascularisation but not as much as the trabecular bone. There is then the main ring of the sub-radicular artery which encompasses the central portion of the vertebral body. Vascularisation of the skin and muscle can also be seen. B1 and B2 show the end of the vertebral body. Over this area the vessels appear to be at the edges of the vertebral body, gathering at the endplate area. Centrally within the end of the vertebral body there is a lack of vessels. C1 and C2 are of the intervertebral disc region. In the area of the disc there is an absence of vessels, however, a distinct vessel ring can be identified surrounding the disc. The perfusion of the musculature and skin can be seen.
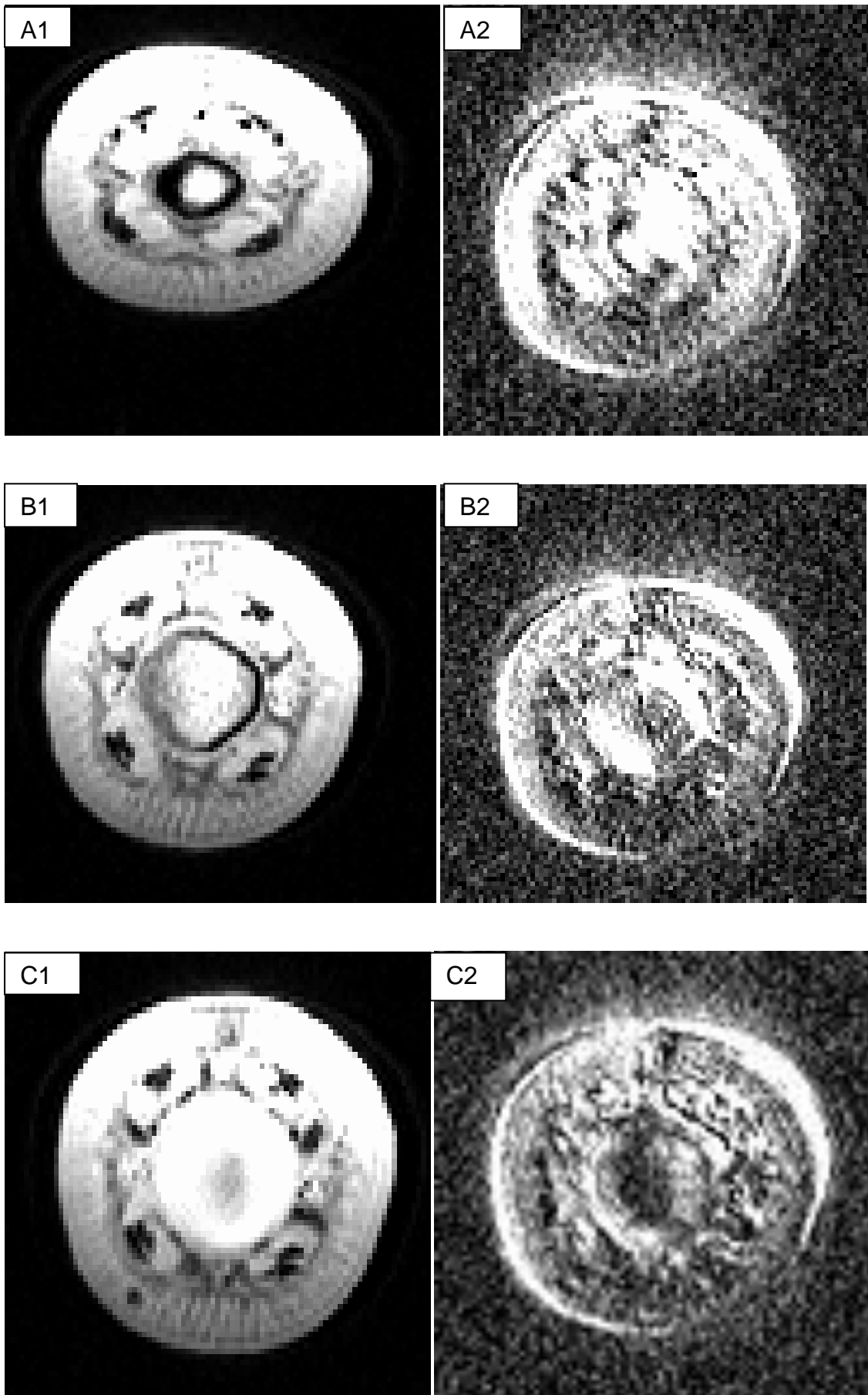
Figure 101: MRA an axial view: A1/A2, the central vertebral body, B1/B2, the vertebral endplate, C1/C2 the intervertebral disc. 1- anatomy, 2- maximum intensity projections.

A sagittal maximum intensity projection radial was then performed. The parameters were the same as the previous scan.

Vessels in the soft tissue

Median caudal artery

Vertebral body

Vertebral endplate

Posterior

90°

Y

X

Anterior

Y

Posterior

x

Anterior (coming out of the page)
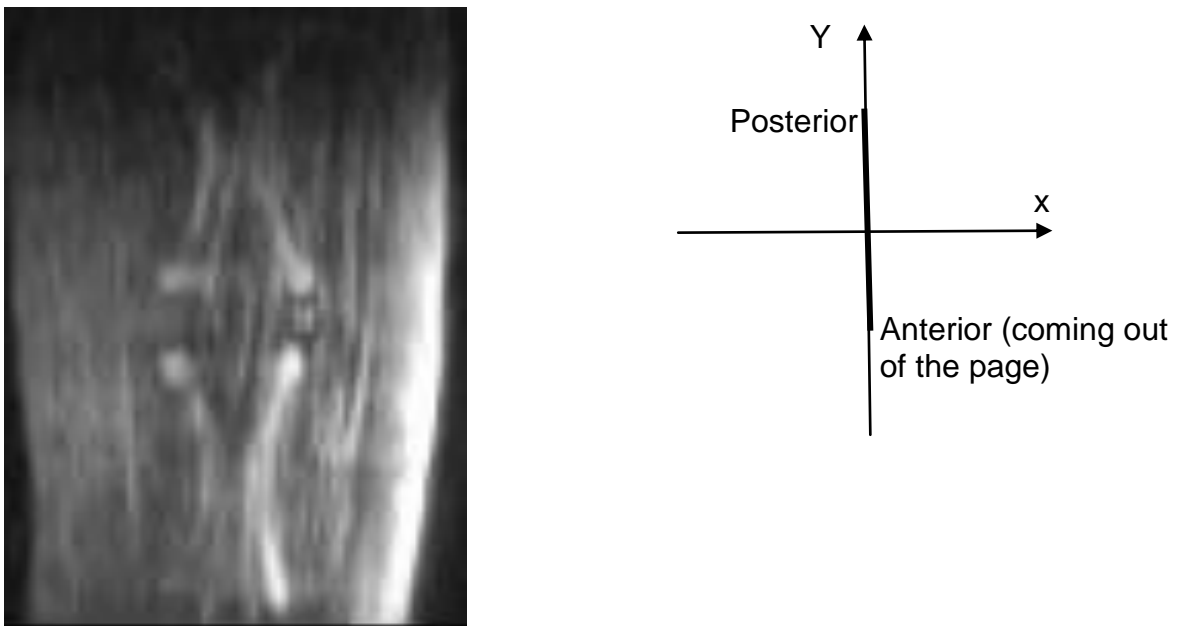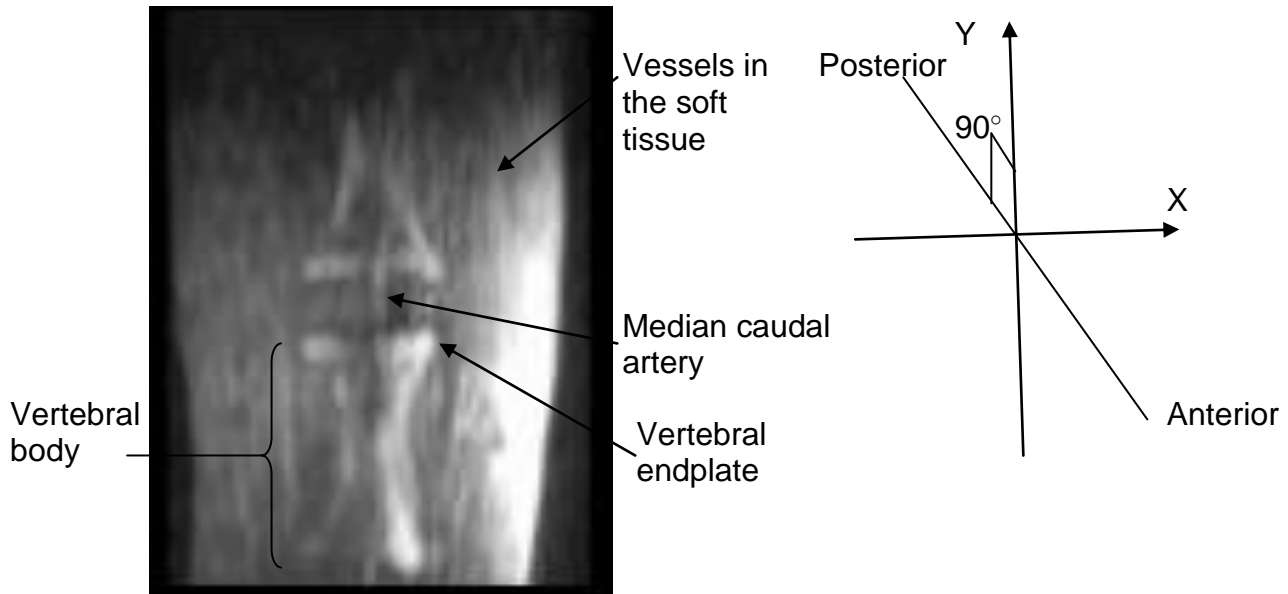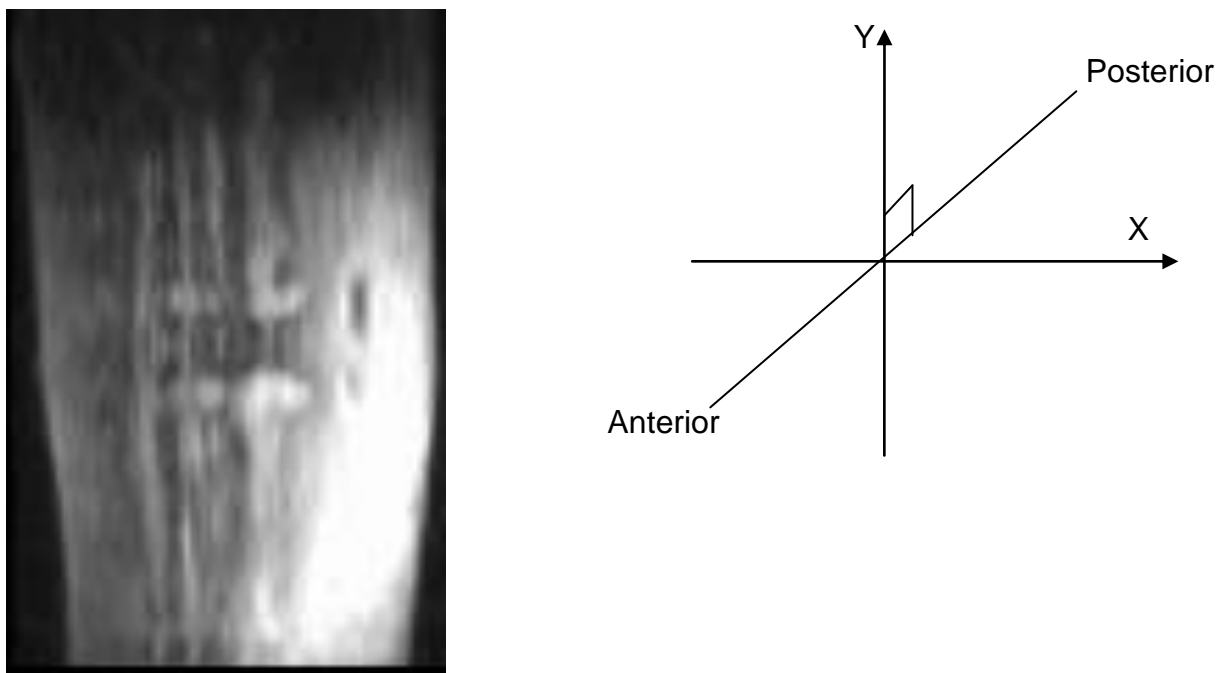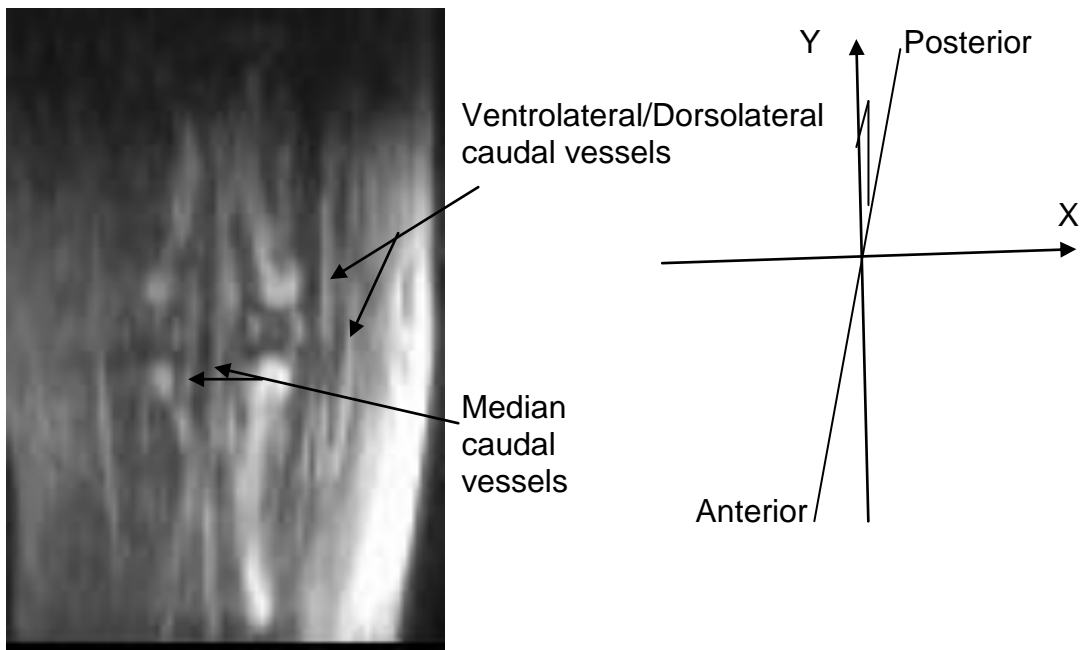
Figure 102: A radial maximum intensity projection of a sagittal orientation. It may be seen in these series of images that there are vessels at the edges of the vertebral bodies. Anteriorly, the main median caudal artery and associated veins can be seen. The ventral and dorsal lateral vessels in the soft tissue can also be seen.

Figure 102 illustrates the sample rotated through approximately 90°. These series of images reinforce and clarify the axial views in Figure 101. The centre

of the vertebral bodies is minimally perfused. There appears to be major vessels running along the edges of the vertebral bodies. It can be seen as expected contrast has gathered at the vertebral endplate. However, an interesting point is the contrast appears to pool along the lateral edges of the vertebral endplate rather than anteriorly or posteriorly. This may coincide with the fact that there are the major vessels along the edges of the vertebral body. These vessels follow the line of the cortical bone meeting in the large marrow space in the centre of the vertebral body; this is where the basi-vertebral artery feeds into the vertebral bodies.

3.4.4 Discussion

Human bone is abundantly supplied with blood this is especially the case in the areas where the red bone marrow is stored (Tortora & Grabowski, 2003). The vertebral body is an area of red marrow production. In humans periosteal arteries supply the periosteum and enter the cortical bone through many perforating (Volkmann's) canals (Tortora & Grabowski, 2003). Combining the x-ray and MRI structural and vascular data confirms that blood supply in equines is comparable. Near the centre of the bone a large nutrient artery passes through a hole in the compact bone called the nutrient foramen (Figure 97), this is similar for both humans and equines.

Although the MRA images are of relatively poor quality, it can be seen that the intervertebral disc is predominantly avascular, with a ring of vessels surrounding the annulus. As in humans the nucleus and annulus of the disc is supplied with nutrients by vessels which arise in the vertebral bodies (Grunhagen, et al., 2006). Evidence is seen in Figure 97 that a main nutrient artery branches from the anterior median caudal artery and encircles the central portion of the

vertebral body. Branches from this artery are seen to join anteriorly and posteriorly to adjacent vertebrae. These periosteal arteries are seen in human lumbar vertebrae in similar positions (Ratcliffe, 1980). The main nutrient artery supplies the central core as in humans. Metaphysial arteries supply the portion of vertebral body next to the annulus (Ratcliffe, 1980).The conclusion from the anatomical studies is that the equine model is a suitable model for the human lumbar disc.

4 Diffusion Studies using Magnetic Resonance Imaging

4.1 Introduction

4.1.1 Overview

As discussed in Chapter One the intervertebral disc in humans is an avascular structure (Tortora & Grabowski, 2003). Chapters Two and Three have illustrated the anatomical structure of the equine caudal intervertebral disc. The important conclusion was that in terms of its microcirculation it is a good model of the human lumbar and thoracic discs. It is predominantly avascular with vessels only penetrating a short distance into the outer annulus, small branches from metaphysial arteries anastomose over the outer surface of the annulus fibrosus (Bogduk, 2001).

The aim of this chapter is to use the equine disc to investigate solute transport. Solute transport is central to disc function. The disc undergoes respiration and produces metabolites which must be exchanged with the blood circulation (Tortora & Grabowski, 2003). The cartilage cells in the nucleus and fibroblasts in the annulus constantly synthesise and replace proteoglycans and collagen in the matrix and need nutrition to support this activity (Bogduk, 2001). This depends on diffusion from the vessels in the outer annulus and capillary plexus beneath the vertebral endplate which aid this process. Subsequent transport through the disc matrix depends on its hydration which is influenced by the osmotic and hydrostatic pressure in the disc (Antoniou, 2004). Transport into the disc is also of interest in connection with efforts to deliver drugs and antibiotics to the tissue.

In this chapter we describe the use of MRI to investigate transport: looking at the movement within the equine intervertebral disc of T_1 contrast agents.

Signal brightness in MRI depends on the proton density, ρ, and the T_1 and T_2 relaxation times of the object being imaged; hence image contrast depends on the tissue type and condition (Hickey, et al., 1990).The appearance of a tissue can be altered by the presence of an MR sensitive contrast agent (McRobbie, et al., 2007). The presence of a T_1 contrast agent shortens the T_1 relaxation time (gain of longitudinal magnetisation, M_0). Hence, the tissue will produce a brighter signal on a T_1 weighted image. The more contrast agent present, the greater the change in T_1 and the brightness of the tissue (McRobbie, et al., 2007).

Transport of contrast agents (solutes) into the disc will depend will depend on their size and charge. If a variety of contrast agents is used then the difference in their uptake due to size and charge may be investigated (Urban & Winlove, 2007). This is useful to determine how nutrients and other molecules bearing various charges and of different sizes may diffuse through the intervertebral disc. The rates of uptake of the contrast agent may also be dependent on the condition of the tissue matrix (Urban & Winlove, 2007). This may be useful in evaluating the tissue matrix integrity, due, in particular, to age related degeneration and changes (Antoniou, 2004).

In the experiments described in this chapter, three T_1 contrast agents were used: manganese chloride, Magnevist and Gadovist. Time-intensity curves were plotted for 13 separate regions in each sample; this enabled relationships to be investigated between charge and molecular weight/shape of the contrast

agent and its diffusivity through these regions and age related differences in diffusivity.

The literature contains very little quantitative data on contrast agent diffusion in cartilage, although there are numerous qualitative reports on the effect of molecular size and ionic state (e.g. (Perlewitz, et al., 1997); (Ibrahim, et al., 1994). An exception is the study by Gillis et al (Gillis, et al., 2000) quoting diffusion coefficients of (1.98 ±0.23) × 10^{-4} mm^2/s and (1.45 ±0.21) × 10^{-4} mm^2/s for Magnevist and Gadoteridol respectively in cartilage. However, Galbusera et al suggest that higher values than around 10^{-3} mm^2/s is appropriate for the disc (Galbusera, et al., accepted June 2014). In fact diffusion coefficients for small molecules such as manganese in the disc nucleus, which is used in this study, is approximately a third of what you would expect if the molecule was in free solution. Similarly, values of partition coefficient are scarce in the literature; however, Ibrahim et al (Ibrahim, et al., 1994) observed gray-scale enhancement by factors of 1.3 and 2.1 for Magnevist and Gadoteridol, respectively.

4.1.2 Theoretical model of transport in the disc

Diffusion into the excised disc occurs via its cut surfaces predominantly. For the purposes of diffusion we can think of the disc as a 1-dimensional slab. The solutions of the 1-dimensional diffusion equation are readily available in the literature, e.g. Caretto (Caretto, 2009). The 1D diffusion equation can be written as:

$$\frac{\partial c}{\partial t} = \alpha \frac{\partial^2 c}{\partial x^2} \quad \text{Equation 4}$$
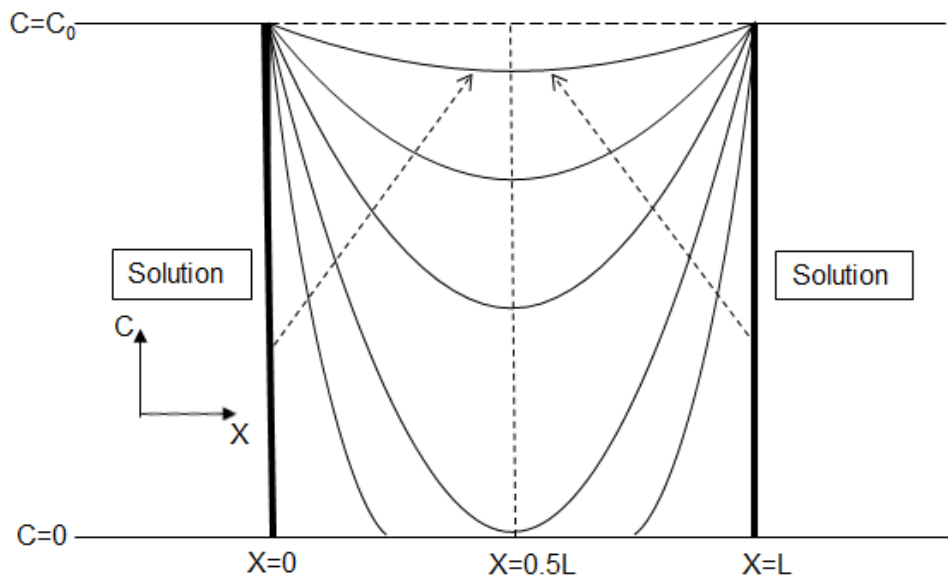
Figure 103: Schematic representation of diffusion within a disc of thickness L. X=0.5L represents the central slice used in these studies. The thick black lines are the disc/solution boundary. C is the concentration at a time t and C_0 is the asymptotic concentration. The dotted arrows indicate the time course of the concentration profiles.

At a time t, the partition coefficient, i.e., the ratio of the concentration of solute C at a time t in the tissue to the equilibrium concentration C_0, is given by:

$$\frac{C}{C_0} = 1 - \frac{4}{\pi} \sum_{n\ odd} \frac{e^{\frac{-n^2\pi^2\alpha t}{L^2}} \sin\frac{n\pi x}{L}}{n} \qquad \text{Equation 5}$$

Equation 5 is the ratio of a solute present in a tissue; L is the thickness of the tissue, X is the point in the tissue being examined and α is the diffusion coefficient (Caretto, 2009). Figure 103 shows predictions of concentration profiles during the time course.

At the centre of the disc, where x=0.5L, for values of n which are odd:

$$\frac{n\pi x}{L} = n\frac{\pi}{2} \qquad \text{Equation 6}$$

181

Equation 6 can be substituted into the sin term in Equation 5 to reduce the sin term to:

$$\sin \frac{n\pi x}{L} = \left(-1^{\frac{n-1}{2}}\right) \qquad \text{Equation 7}$$

The sin term reduces at the centre because X = 0.5L. Equation 5 will then become:

$$\frac{c}{c_0} = 1 - \frac{4}{\pi}\sum_{n\,odd}\left(-1^{\frac{n-1}{2}}\right)\frac{1}{n}e^{-n^2\pi^2 T} \qquad \text{Equation 8}$$

The ratio of solute present in a tissue; where T = αt/L^2 (Roura, et al., 2000). We can rewrite Equation 8 as:

$$\frac{c}{c_0} = 1 - \frac{4}{\pi}\sum_{n\,odd}\left(-1^{\frac{n-1}{2}}\right)\frac{1}{n}e^{-n^2 T'} \qquad \text{Equation 9}$$

The ratio of solute present in a tissue; where T'=π^2T=π^2αt/L^2. To recap, Equation 9 shows the time variation of solute concentration at the centre of a 1-D slab of thickness L.

When t is long, Equation 9 tends to:

$$\frac{c}{c_0} = 1 - \frac{4}{\pi}e^{-\frac{t}{\tau}} \qquad \text{Equation 10}$$

Equation 10 is the ratio of solute present in a tissue; where π is the time constant.

The time constant is given by:

$$\tau = \frac{\mathcal{L}^2}{\pi^2 \alpha}$$ **Equation 11**

The time constant of the process is proportional to the square of the thickness of the tissue, L, and inversely proportional to the diffusion coefficient.

A graph of Equation 9 and Equation 10 will look like Figure 104. We can see from this graph that in the centre of the 1-D slab there is an initial period before the solute reaches that point. This is the behaviour which we should expect in the disc during the following experiments. The green line is an exponential fit to the diffusion equation after the initial lag producing a value for the time constant, τ of the process.
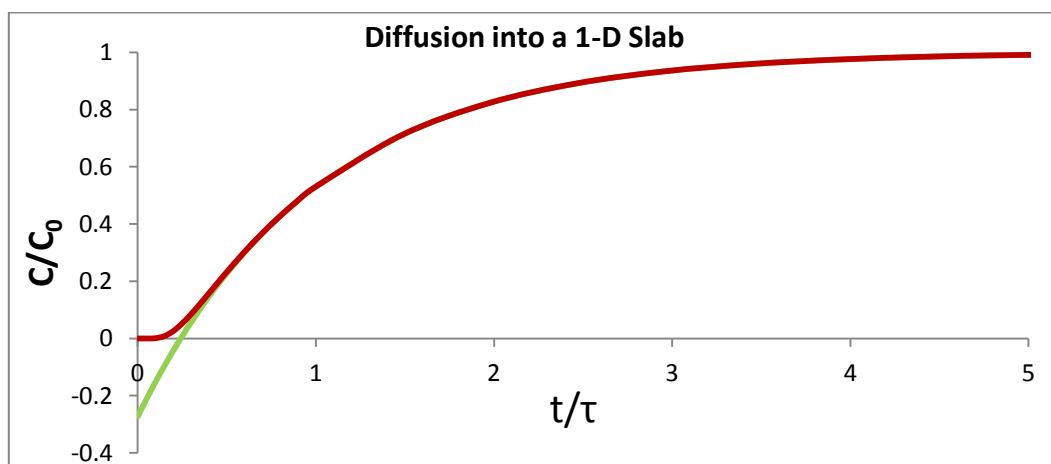
Figure 104: Diffusion into a 1-D slab; the red line represents the diffusion process (Equation 9) and the green line is illustrating the exponential part (Equation 10).

The T_1 weighted imaging sequence used in the present study gives signal intensity (gray value) which varies linearly with $1/T_1$ (see section 4.4 below for

more details). The action of the T_1 contrast agents is such that $1/T_1$ varies linearly with the concentration C of the contrast agent (see section 4.2.4.3 below, for more details). Consequently signal intensity (gray value) varies linearly with the concentration of contrast agent, and the expected variation of gray value G with time has the same form as the red line in Figure 104. As mentioned above, at longer times this variation is in the form of a rising exponential- the experimental data in section 4.4 are fitted on this assumption for a function of the form $G = A - Be^{-t/\tau}$ (where A, B and τ are constants).

4.2 Preliminary experiments

4.2.1 Maintaining the hydration of the intervertebral disc

4.2.1.1 Aim

The intervertebral disc is poroelastic; fluid flow within the disc is coupled with its deformation (Ferguson, et al., 2004). A substantial volume of fluid is expressed from the disc during daily loading; due to the osmotic potential of the disc this is reimbibed over night during rest when loading is substantially reduced (Ferguson, et al., 2004). The osmotic potential comes mainly from the aggrecan and its sulphinated glycosaminoglycan chains (Urban, et al., 2000). In vivo, the hydration of the disc is determined by the balance between the osmotic or swelling pressure, the applied load and tension in the collagen network. Our experiments were performed by incubating excised discs in phosphate buffered saline containing the chosen contrast agent. The disc is therefore freed of applied load and exposed directly to a solution of different osmotic pressure to that in vivo. It is therefore necessary to adjust the incubation conditions to ensure that the hydration level remains constant, and this was established in a series of preliminary experiments.

4.2.1.2 Method

Four defrosted explanted discs from two equine samples of ages 12 and 20 years old were dissected into their constituent nucleus and annulus. The nucleus and annulus were separated by scalpel at their visible border and each was weighed after gentle blotting ($\pm$ 0.05 mg). The explanted samples were each placed in dialysis tubing, (Medicell International Ltd); it is made of cellulose, has a diameter of 50.8 mm and a molecular weight cut-off of 12000-14000 Daltons. This means that substances with a molecular weight higher than this will not be able to pass through the pores of the cellulose. Before use the tubing is boiled twice for approximately five minutes each time; this removes sulphur impurities.

A small amount of 0.15 m sodium chloride was added with the disc samples inside the membrane; this helps the disc to equilibrate and provides a transport route. The open ends of the dialysis tubing were tied tightly with thread. Two litres of a solution of 0.15 m sodium chloride was made. This solution was divided into four batches of 500 ml. To each of these batches polyethylene glycol (PEG) of molecular weight 20 000 D and manufacturer Sigma Aldrich was added in varying amounts to make solutions of 5%, 10%, 15% and 20% W/V.

The dialysis tubing and intervertebral disc samples were placed in one of the four solutions; a nucleus and annulus portion was each placed in a 5%, 10%, 15% and 20% solution.

After one hour all the disc portions were weighed and placed into a fresh piece of dialysis tubing along with a fresh drop of sodium chloride, and then put back

into their respective solutions. This process was repeated every hour for five hours.

4.2.1.3 Results
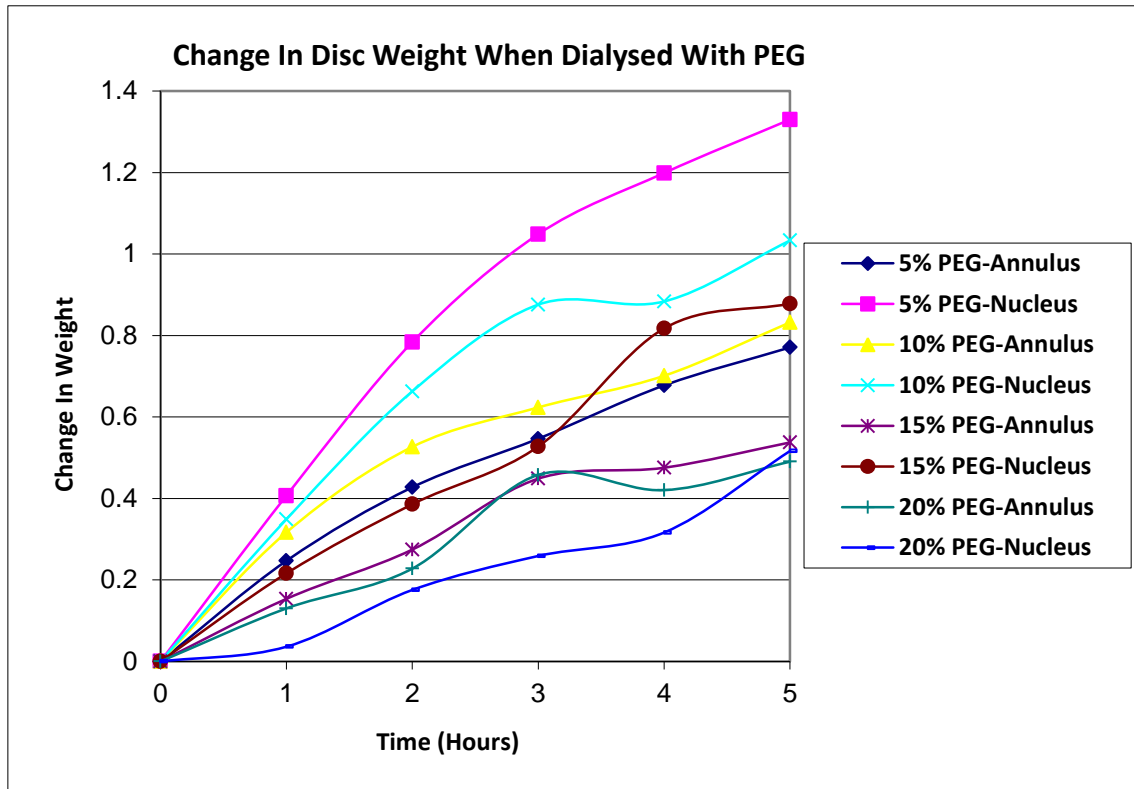
Figure 105: An illustration of the fractional change in the weight ((final weight-initial weight)/initial weight) of annulus and nucleus samples of the equine intervertebral disc when dialysed with a solution of polyethylene glycol and sodium chloride. Generally, the higher the concentration of PEG the lower the fractional change in weight, this is because the osmolarity of the intervertebral disc is balanced.

As shown in Figure 105 the tissues all swelled over a five hour time scale. Swelling was reduced as PEG concentration increased, and, except at 20 % PEG swelling was greater in the nucleus than the annulus. The nucleus sample in the 5% PEG solution gains the most weight; in fact the sample more than doubles its weight after five hours. The weight gain of the other nucleus samples are in descending order of weight gain, 10%, 15% and 20%.

186

4.2.1.4 Discussion

Whilst the greater swelling of the nucleus than the annulus is expected because of its higher collagen content and lower proteoglycan concentration increasing the osmolarity of the nucleus of the intervertebral disc compared to the annulus, these results were quantitatively unexpected (Happey, 1980).

An experiment by Robinson (Robinson, 1971), illustrated the efficiency of PEG in controlling the water content of tissue. Robinson, using kidney slices from rats increased the PEG concentration from 5.1% to 7.7%, (a change in osmotic potential of 15 mOsm), as sodium chloride was decreased from 770 to 77 mM, (a change in osmotic potential of 1200 mOsm). Water content of the tissue remained static.

A solution of PEG above 10% would be hyperosmotic when compared to the known osmotic pressure of the disc and would cause fluid to be lost by the disc (Wuertz, et al., 2007). PEG is a non-penetrating solute increasing osmotic pressure (Robinson, 1971). The presumption is that this experimental approach was unreliable and the tubing seals did not prevent ingress of PEG. A dialysis cell was therefore designed and constructed as described below.

4.2.2 The dialysis cell

4.2.2.1 Aim

It is critical when undertaking a complex physiological experiment that the method used is valid. A full appraisal of the equipment is critical to ensure its suitability for the method.

4.2.2.2 Method

The requirements of the cell are:

1. It is an appropriate size to accommodate the intervertebral disc,

2. It is of a design which holds the membrane tightly producing an adequate seal to prevent the contrast agent from avoiding passing through the membrane and gaining access to the disc,

3. It enables filling and emptying of the cell without disturbing the disc or moving the cell. This is important for the experiment as the sample will be lined up within the MR scanner for more than one scan; the slices need to be in the same areas.

Research was undertaken to establish typical cell design with the final design shown in Figure 106.
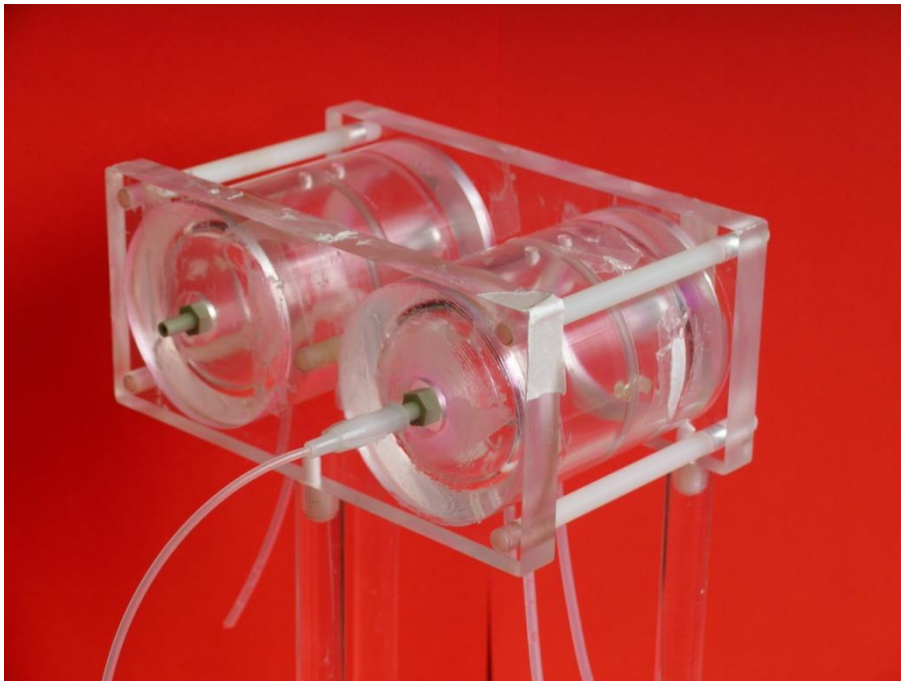
Figure 106: The dialysis cell. An important consideration in the design of the dialysis cell is being able to fill and drain the cell without it being moved while in the scanner; this is achieved by means of the drainage and filling tubes.

The intervertebral disc is placed with a small amount of 0.15M of sodium chloride into a piece of dialysis tubing. The internal diameter of a dialysis cell is 45 mm. This ensures the dialysis membrane protrudes beyond the cell; when

the two halves of the cell are securely fastened a tight seal is formed. The drainage tubes have caps on the bottom to prevent a solution running out. Each of the two halves is independently filled via a syringe attached to the filling tube. The caps sealing the air holes are removed during filling to ensure air within the cell is forced out as the solution is put in. The dialysing solution is put into the cell until it is completely filled; this will ensure all parts of the disc are bounded by solution. Sealing caps are then placed in the air holes. The syringe is removed and caps placed over the filling tube.

Four solutions were tested: Evans blue (1 % w/v in 0.15 M NaCl, 15 % PEG), potassium permanganate, fluorescein and rhodamine.

The disc was initially dialysed for 4 hours; after each hour it was weighed, visually investigated and placed back into the dialysis cell. After 4 hours the disc was then dialysed for a further 20 hours.

4.2.2.3 Results

Evans blue bound to the dialysis tubing, presumably due to reaction between its sulphinated residues and the cellulose of the membrane. The 15 % PEG caused a loss of weight of the disc of 10 %. For all other solutions 10 % PEG was used and the weight of the disc remained constant to within 1.7 %.

Potassium permanganate is $KMnO_4$ has a molecular weight of 158 D and by visual inspection penetrated the disc uniformly from both cut surfaces; a crust of potassium permanganate had form and because there was no excess fluid in the dialysis sack there was no transport across the outer annulus. Fluorescein has a molecular weight of 376 D and like permanganate is anionic. It diffused into both annulus and nucleus, but showed a different colour in each, presumably due to its different charge state. Rhodamine is cationic and has a

molecular weight of 443 D. It penetrated both annulus and nucleus through the cut surfaces but even after 24 hours had not stained the nucleus uniformly through its depth.

4.2.2.4 Discussion

These experiments demonstrated that the dialysis cell allowed the disc to be maintained at constant hydration when the dialysis solution contained 10 % PEG, which is consistent with the previous literature. Furthermore, they showed that transport of a range of solutes occurred across the cut surfaces only. They also confirmed the very long equilibration times required, even for relatively small solutes, in the intervertebral disc.

Using 10 % PEG, the overall water content of the disc was not exactly constant: there was a small change (1.7%) in overall mass. Moreover, it is likely that hydration was maintained differently in different regions of the disc. Since the nucleus and inner annulus have higher osmotic pressure than the outer annulus, it is possible that fluid will be expressed from the outer annulus, with an associated fall in diffusivity in this region. However,the experimental results (see below) show that diffusion coefficients for the outer annulus are higher than or similar to those for the rest of the disc, suggesting that any such water loss does not have a marked effect...

It can be seen that both surfaces of the samples at the nucleus and annulus have been penetrated by the compounds within 1 hour of diffusion. Due to the orientation of the samples the sample edges are not bordered by the solutions in the cell, therefore all diffusion is via the two surfaces which in vivo are the surfaces of the disc which bound the vertebral endplates. It can in fact, take up to 24 hours after the beginning of diffusion for the centre of the nucleus to be

penetrated fully. Rhodamine has an overall positive charge and is therefore attracted to the fixed negative charge of the nucleus (Lampidis, et al., 1989).

The charge exhibited by fluorescein depends on the ionic strength of the tissue; the variable charge will alter the appearance of the colour of the fluorescein. This is an explanation of the appearance of the two-toned nature of the disc; the nucleus and annulus are ionically different.

Potassium permanganate when placed into a solvent dissociates into a potassium cation and a permanganate anion. Potassium is more likely to diffuse into the nucleus due to its charge. This accounts for the crust of permanganate on the surface of the disc; its negative charge inhibits its diffusion beyond the annulus.

4.2.3 The choice of contrast agent concentration

4.2.3.1 Aim

The three contrast agents used in this thesis to study diffusion are manganese chloride, Magnevist and Gadovist. The rationale for this choice and a description of the compounds is given in section 4.3. The three contrast agents work by shortening the T_1 relaxation time, (the recovery of the longitudinal magnetisation vector, M_0). However if the concentration of the contrast agent is too high, T_1 is shortened to such an extent that a MR signal cannot be detected. Therefore, a compromise must be reached whereby the signal produced by the contrast agent and most importantly its change over time may be detected. This was investigated in a series of preliminary experiments.

4.2.3.2 Method

A starting point for the concentrations of Gadovist and Magnevist is the clinical dose commonly used.

The recommended dose of Magnevist (gadopentetate dimeglumine) per kg of body weight, (assuming 5 litres of blood circulate per 60 kg of body weight), is 0.24 ml made up to 100ml with de-ionised water, (0.24%) (Bayer Healthcare Pharmaceuticals, 2012).

The recommended dose of Gadovist (Gadobutrol) per kg of body weight, (assuming 5 litres of blood circulate per 60 kg of body weight), is 0.6 ml made up to 100ml with de-ionised water, (0.6 %) (Bayer New Zealand Limited, 2013).

Manganese chloride is not commonly a clinical MR contrast agent. However, there have been trials to investigate the visual appearance of various concentrations of manganese chloride over the range 20 to 60 mg/l (Bernardino, et al., 1994).

The concentrations of the three contrast agents were chosen to incorporate the clinical concentrations stated in the previous paragraphs. Further concentrations above and below the clinical concentrations were chosen to incorporate an adequate range.

Manganese Chloride mM concentration	Magnevist % concentration	Gadovist % concentration
1.0	0.96	2.4
0.5	0.48	1.2
0.25	0.24	0.6
0.125	0.12	0.3
0.0625	0.06	0.15
0.0312		
0.0156		

Table 2: The concentrations of the three contrast agents investigated in descending order of concentration. A wider range of manganese chloride was investigated as there is no clear clinical value. The Magnevist and Gadovist values are based around a central clinical value, with two values higher and two values lower.

An equine intervertebral disc was placed in each of the solutions illustrated in Table 2 for 48 hours before scanning; this allowed adequate diffusion to have occurred in the centre of the nucleus.

The samples were removed from their solutions and arranged together on a tray. Sagittal slices of each of the three groups of samples were performed; three different scans were used as a final scan protocol for the diffusion experiments had not been established at this point and therefore the general behaviour of the various contrast agent concentrations under a variety of scan parameters was of interest. The three scan's parameters are summarised below in Table 3.

Scan Type	Weighting	Time (s)	TR (ms)	TE (ms)	Flip Angle (°)
FFE	T_1	40.8	7	1.7	35
FFE	T_1	198	25	2.6	35
FFE	T_1	290	25	2.6	35

Table 3: The variation in scan parameters used to establish the behaviour of various concentrations of contrast agent.

Each of the scans produced a PAR and a REC file; these were converted into HDR and IMG files using MRIcro as described in section 3.3.2.

The images were imported into Image J WCIF and a region of interest selected which incorporated only intervertebral disc tissue. The gray value for each of these regions was measured.

A point to note is that the gray value measured is in fact the pixel value. Image J WCIF reads the data from the IMG and HDR file to display the image. This pixel value is a scaled value of the original signal; the original signal is a floating point and the pixel value is a scaled integer for ease of display. Each of the separate scans in Table 3 has its unique scaling factor called the scale slope. Therefore for the three scans to be compared the pixel value needs to be converted back to the original floating point. The PAR file gives the equation for this conversion:

$$FP = \frac{PV}{SS} \quad \text{Equation 12}$$

Equation 12 illustrates the conversion of pixel value back to original signal; FP-Floating Point, PV-Pixel Value and SS-Scale Slope.

Equation 12 illustrates how the three scans are normalised between each other. The gray value (pixel value) for each of the scans was then plotted on a graph as a function of contrast agent.

4.2.3.3 Results

Figure 107: A typical scan appearance of samples perfused with manganese chloride at 6 concentrations. Scan time 40.8 s.
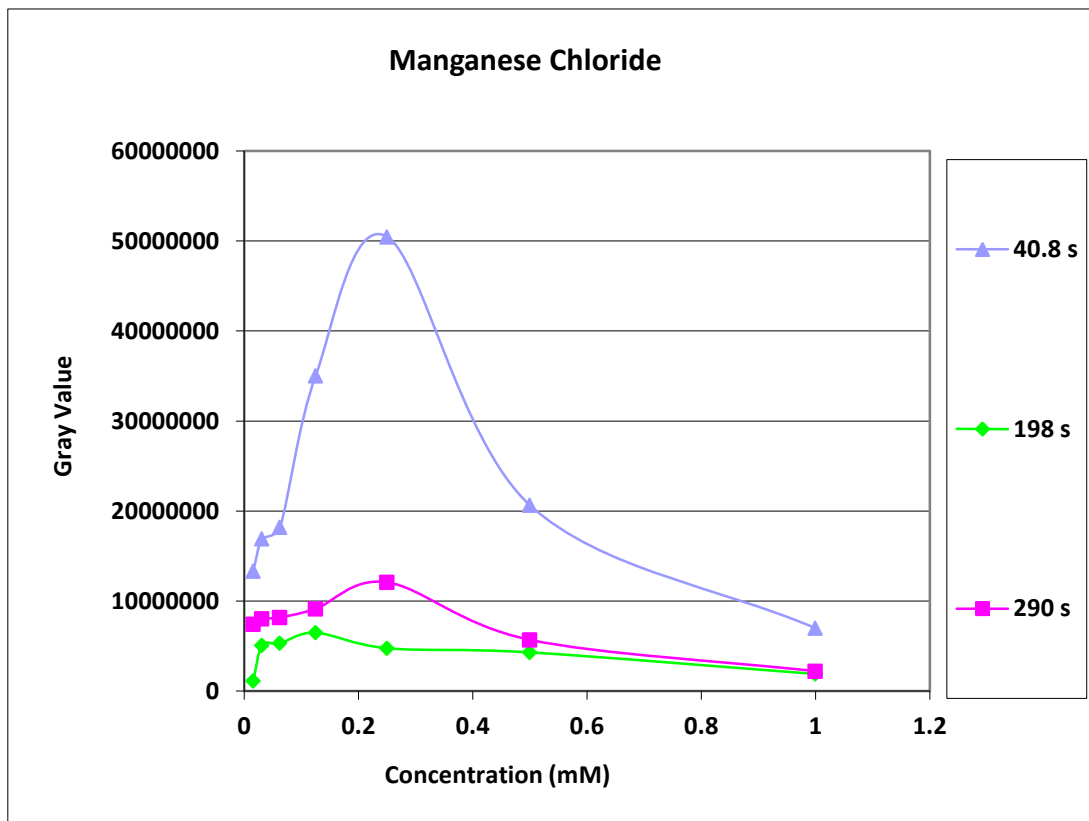
Figure 108: Gray value exhibited by various concentrations of manganese chloride for the scan protocols detailed in Table 3. Each of the scans has a linear portion on the left hand side; the linear portion is important to ensure there is equal change in gray value for equal changes in concentration.
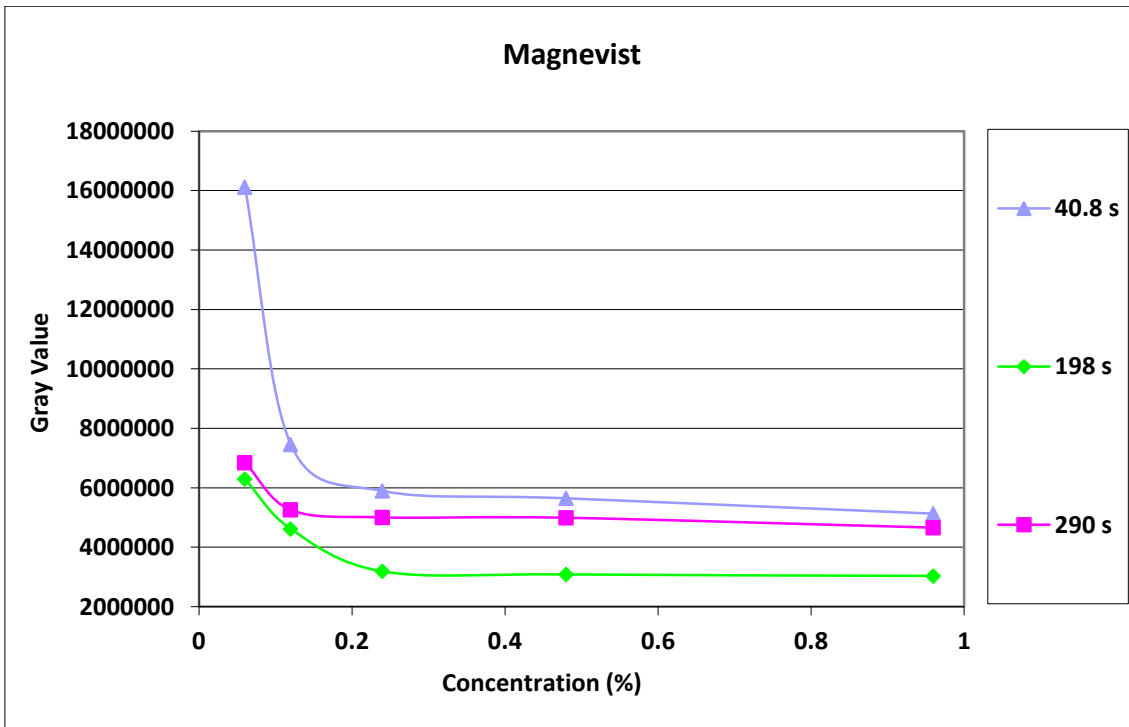
Figure 109: Gray value exhibited by various concentrations of Magnevist for the scan protocols detailed in Table 3.
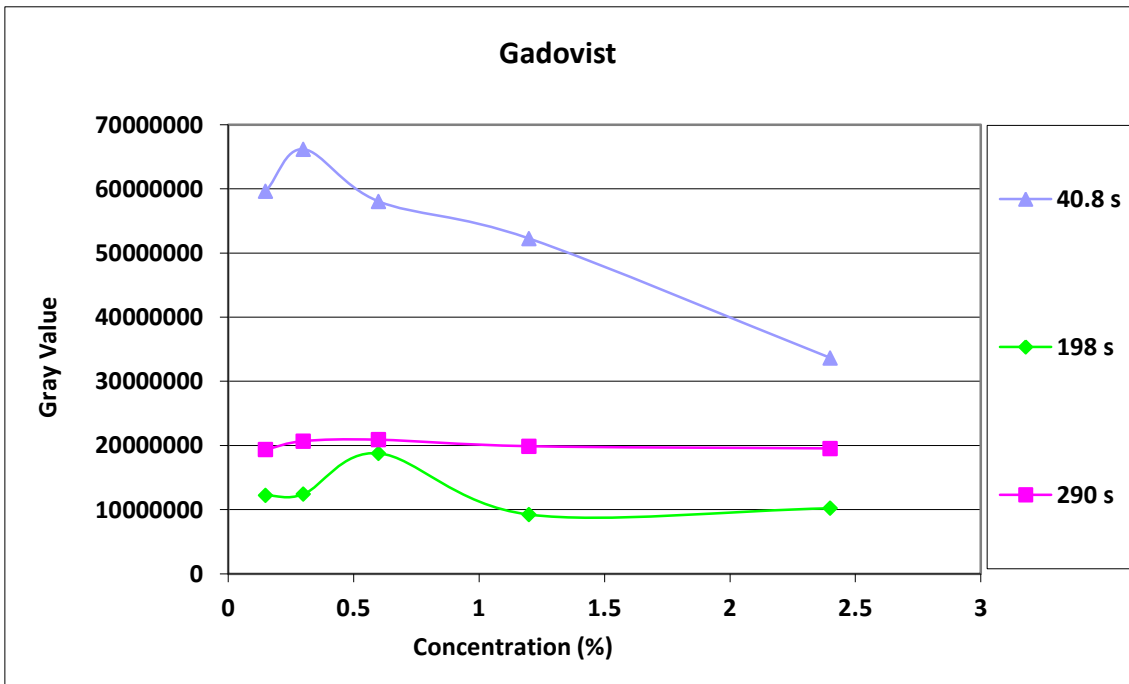
Figure 110: Gray value exhibited by various concentrations of Gadovist for the scan protocols detailed in Table 3.

Figure 107 shows representative images of manganese chloride uptake at different incubation concentrations. The scan sequence is noisy and the

196

annulus and nucleus of the intervertebral disc are indistinguishable, in part due to the swelling and distortion of the tissue in this preparation. That is not an important issue for the preliminary experiments as only the behaviour of the contrast agent is important.

4.2.3.4 Discussion

Figure 108, Figure 109 and Figure 110 show that uptake in the area of interest shows a concentration dependence which differs both with imaging sequence and between contrast agents. In each case there is a linear region over which it is possible to determine an actual contrast agent concentration in the tissue. However, if the concentration of the contrast is too high a phenomenon known as the T_2 effect occurs where the signal is lost due to an over shortening of the relaxation time.

It is therefore important to establish a concentration of contrast agent on the linear portion of the graph. In this way an absolute measure of the amount of contrast agent in a certain area will be able to be determined in the main diffusion experiment.

In Figure 108, the linear portion of the manganese chloride graph is from 0.0625 mM to 0.25mM. Therefore, a middle value or 0.125 mM would be a concentration to aim for in uptake experiments.

Figure 109 shows that Magnevist has a negative gradient at the lowest concentrations. This could be because even the lowest concentration exhibits the T_2 effect; this is extremely unlikely as the concentrations of the first two samples are 0.06 % and 0.12 %, which is very low compared to a clinical dose. It is more likely that the samples have failed to imbibe the contrast agent solution adequately or that the uptake is immeasurably small. There is a linear

portion between 0.24 % and 0.48 %, suggesting a target concentration of 0.36 %.

Figure 110, demonstrates that Gadovist gives linear concentration dependence between 0.15 % and 0.3 % for two of the scans protocols. The 198 s scan shows an improved linear relationship at a slightly higher concentration. A target concentration would be between 0.15 % and 0.3 % at 0.23 % concentration.

These target concentrations take in to account the scan dependence of gray value for all three scan protocols tested.

4.2.4 The relaxivity T_1 of the contrast agents

4.2.4.1 Aim

The T_1 relaxivity is the time taken for the longitudinal magnetisation vector, M_0, to be restored. The contrast agent at a particular concentration will have a specific T_1 value; this will provide an enhanced signal within the tissue. The degree of enhancement is a measure of the concentration of contrast agent. It is important to understand the relationship between T_1, concentration and gray value produced to enable us in the main experiment to quantify the amount of contrast agent in each region of the intervertebral disc.

4.2.4.2 Method

A range of ten concentrations for each of the three contrast agents was made and inversion recovery scans with different inversion recovery times were performed.

An inversion recovery sequence begins with a 180° RF pulse; this will invert the longitudinal magnetisation vector, M_0. After this RF pulse is switched off T_1 (spin-lattice) relaxation begins to occur and the inverted magnetisation vector

begins to decay. After a set time a 90° RF is applied. This brings the residual longitudinal magnetisation into the *x-y* plane (McRobbie, et al., 2007). This is then detected by the RF coil. The time between the initial 180° RF pulse and the 90° RF pulse is termed the inversion recovery time. The inversion recovery time will determine the strength of the signal from the contrast agents. Critical parameters used in the inversion recovery scans are a TR of 10000 ms, TE of 10 ms and a flip angle of 90°. A total of 11 inversion recovery times were used; the range of inversion recovery times was from 50 ms to 2000 ms.

The PAR and REC files were converted into an IMG and HDR file using MRIcro as described before. Image J WCIF was then used to place Regions of Interest (ROI) over each of the individual contrast solutions. The ROIs were as large as possible to encompass as much of each of the solutions as possible; this was to ensure the average gray value produced was as accurate as possible. A graph of inversion recovery time against gray value was plotted for each of the contrast agents.

The T_1 values for each of the concentrations of the three contrast agents were calculated using the inversion recovery graphs, which have the form of a rising exponential. By working relative to the end points of these curves, falling exponentials were constructed. T_1 is equivalent to the time constant of the falling exponential, which has the form shown in Equation 13.

$$y = y_0 e^{-\frac{t}{T_1}} \quad \textbf{Equation 13}$$

Equation 13 is a description of an exponential decay; y is the gray value, t is the inversion recovery time and T_1 is the time constant.

A graph was then plotted for each of the contrast agents of $1/T_1$ as a function of concentration. From the gradient of these graphs the relaxivity of the contrast agents may be determined, as shown by Equation 14 below.

$$\mathcal{R} = \mathcal{R}_0 + \alpha_{\mathcal{R}}\mathcal{C} \quad \text{Equation 14}$$

The relaxation time R of a tissue or contrast agent is dependent on the initial relaxation time R_0, plus a scaling factor determined by the relaxivity of the contrast agent, α_R and its concentration, C. R is in fact $1/T_1$; the relaxation time increases as the T_1 time shortens due to an increase in contrast agent concentration.

A further graph of gray value as a function of $1/T_1$ was then plotted.

4.2.4.3 Results
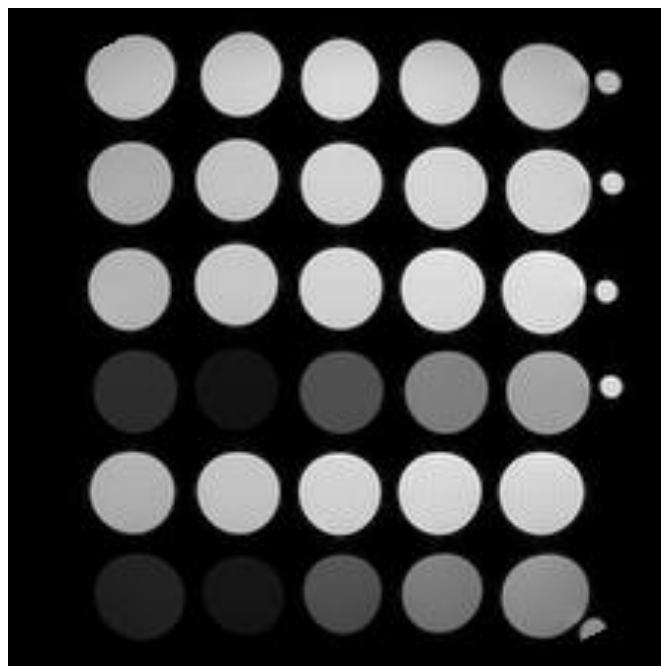
Figure 111: A typical inversion recovery image; this particular image has an inversion recovery time of 50 ms. It can be seen that the two highest concentrations of Magnevist and Gadovist are beginning to lose signal as their T_1 is quite short and almost matches the inversion recovery time of the scan. 1 is the highest concentration.

Figure 111 shows an example array of inversion recovery images. There are eleven such image arrays, for the various inversion recovery times. The variations of gray scale with inversion recovery time for each sample pot are plotted in Figure 112 and Figure 113, and from each curve the time constant τ, is obtained, as follows.
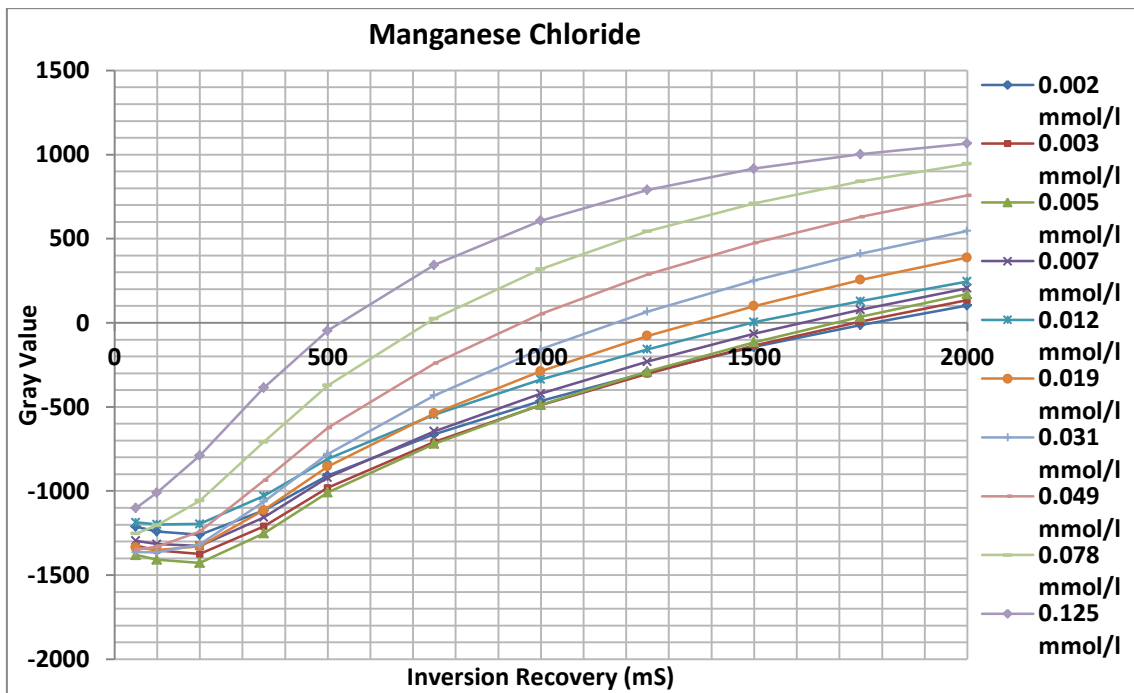
Figure 112: Inversion recovery of various concentrations of manganese chloride. Each of the lines represents a different concentration. The point at where the lines cross the x-axis is the inversion recovery time.
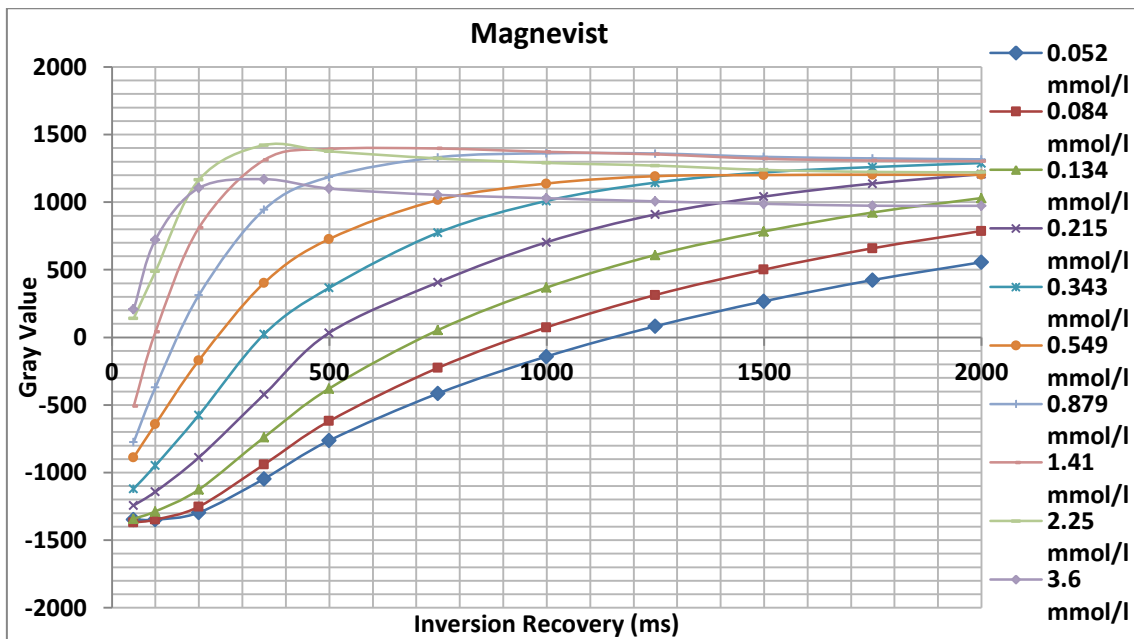
Figure 113: Inversion recovery of various concentrations of Magnevist. The lines represent various concentrations. The point at where the lines cross the x-axis is the inversion recovery time.
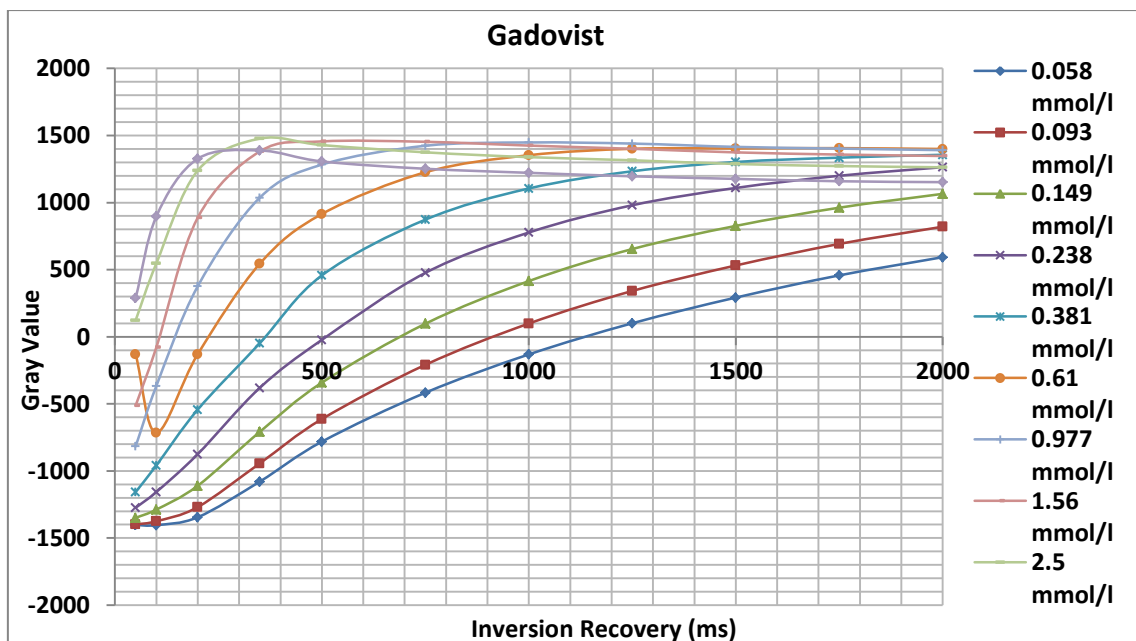
Figure 114: Inversion recovery of various concentrations of Gadovist. 9 concentrations are shown. Each of the lines represents a different concentration; where the lines cross the x-axis is the inversion recovery time.

Falling exponentials, constructed from the inversion recovery curves in Figure 112, Figure 113 and Figure 114 were plotted as shown in Figure 115, Figure

116 and Figure 117; from these curves the T_1 value of the various concentrations of the three contrast agents could be established.
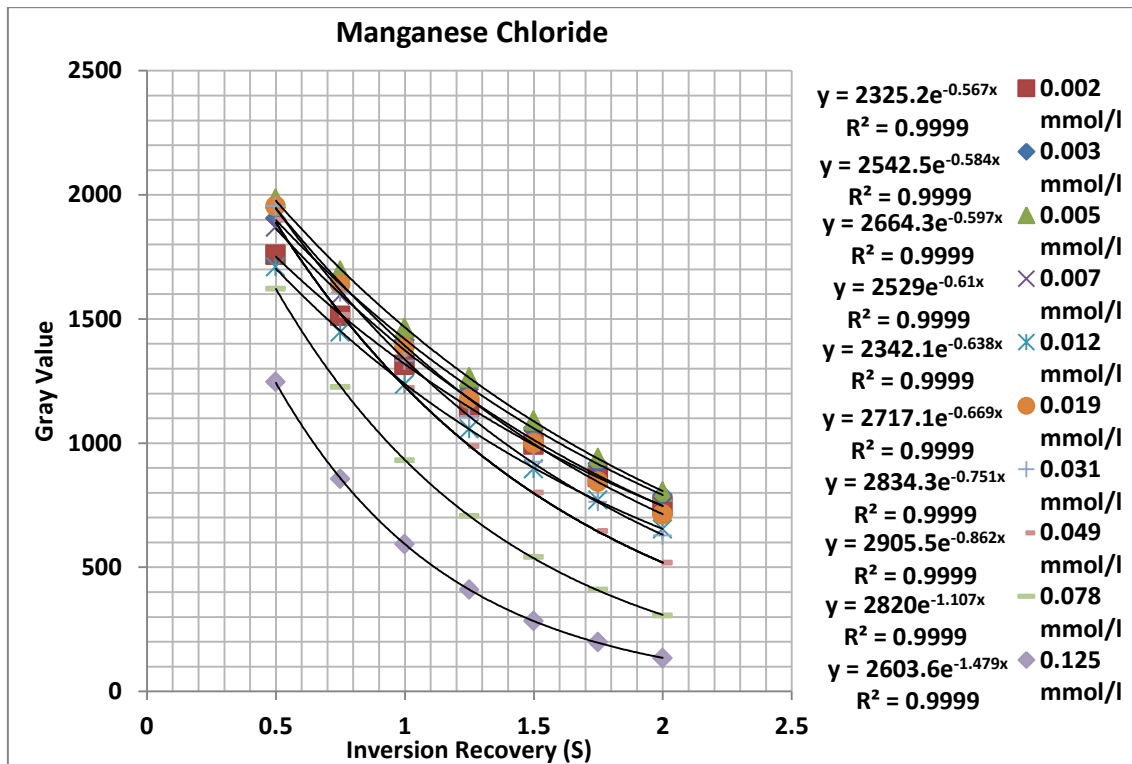
Figure 115: Data from Figure 112, re-plotted as falling exponentials. The data points are fitted with an exponential decay; the R^2 value illustrates the accuracy of the fit. The decay constants of these curves determine $1/T_1$, (Equation 13).

Concentration (mmol/l) (3sf)	$1/T_1$ (s^{-1}) (3sf)
0.002	0.567
0.003	0.584
0.005	0.597
0.007	0.61
0.012	0.638
0.019	0.699
0.031	0.751
0.049	0.862
0.078	1.11
0.125	1.48

Table 4: The $1/T_1$ values for Manganese Chloride.
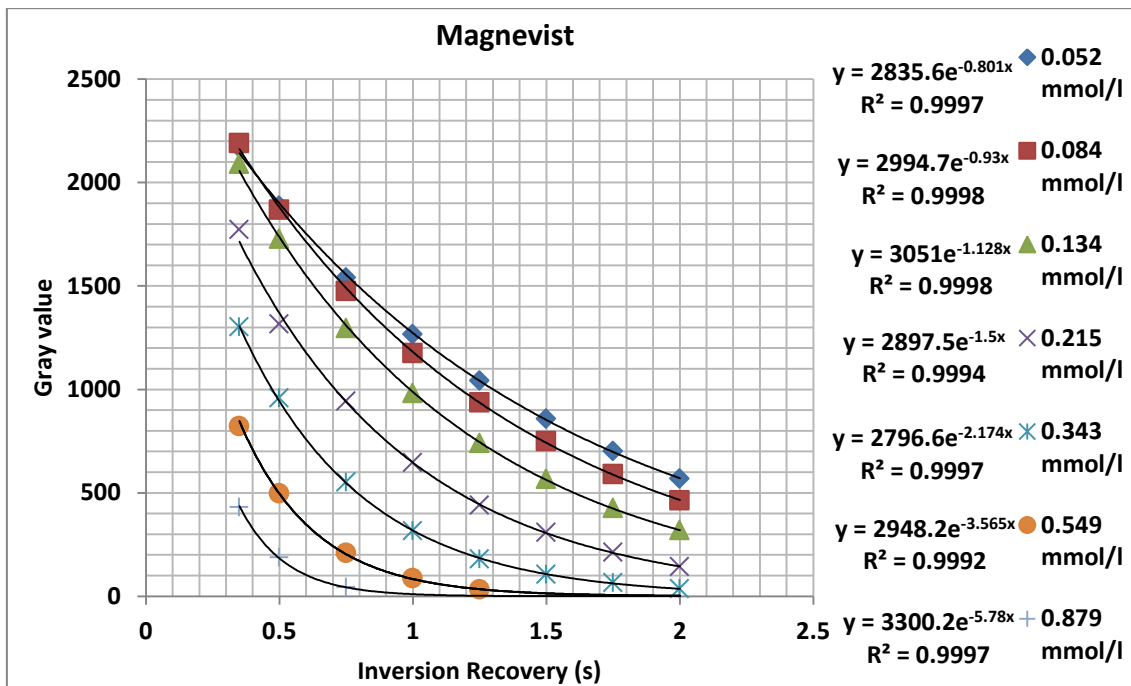
Figure 116: Data from Figure 113, re-plotted as falling exponentials. The three highest concentrations are not shown – their T_1 values were too short to be measured with the recovery times used (see Figure 113).

204

Concentration (mmol/l) (3sf)	$1/T_1$ (s^{-1}) (3sf)
0.052	0.801
0.084	0.93
0.134	1.13
0.215	1.5
0.343	2.18
0.549	3.57
0.879	5.78

Table 5: The $1/T_1$ values for Magnevist.
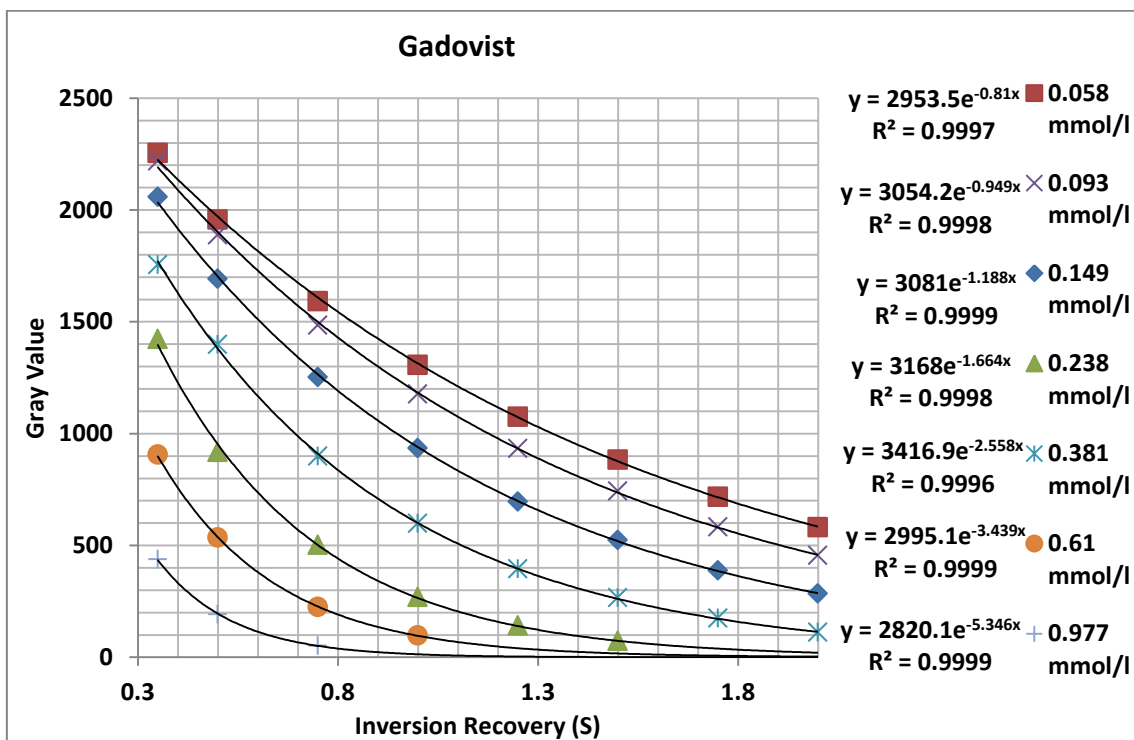
Figure 117: Data Figure 114, re-plotted as falling exponentials. The three highest concentrations are not shown – their T_1 values were too short to be measured with the recovery times used (see Figure 114).

205

Concentration (mmol/l) (3sf)	$1/T_1$ (s^{-1}) (3sf)
0.058	0.81
0.093	0.949
0.149	1.19
0.238	1.66
0.381	2.56
0.61	3.44
0.977	5.35

Table 6: The $1/T_1$ values for Gadovist.

Table 4, Table 5 and Table 6 are then used to plot a graph of $1/T_1$ as a function of concentration.
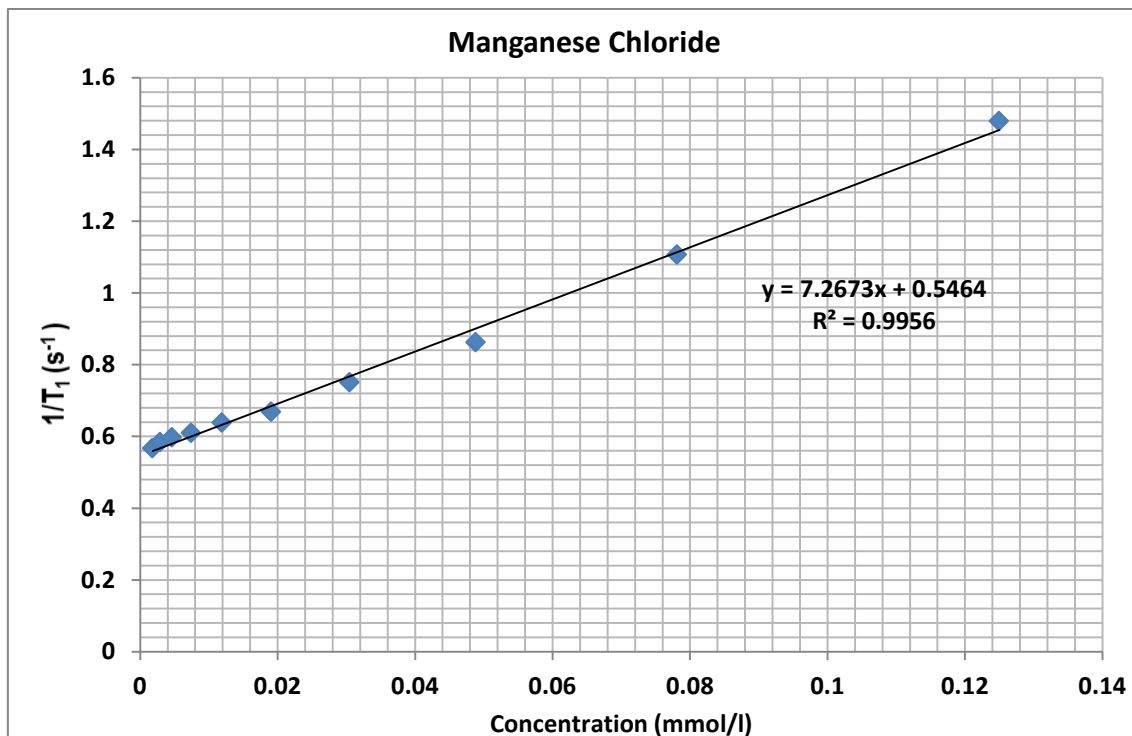
Figure 118: The dependency of the T_1 value on concentration for manganese chloride. It can be seen that this is a linear relationship.

206
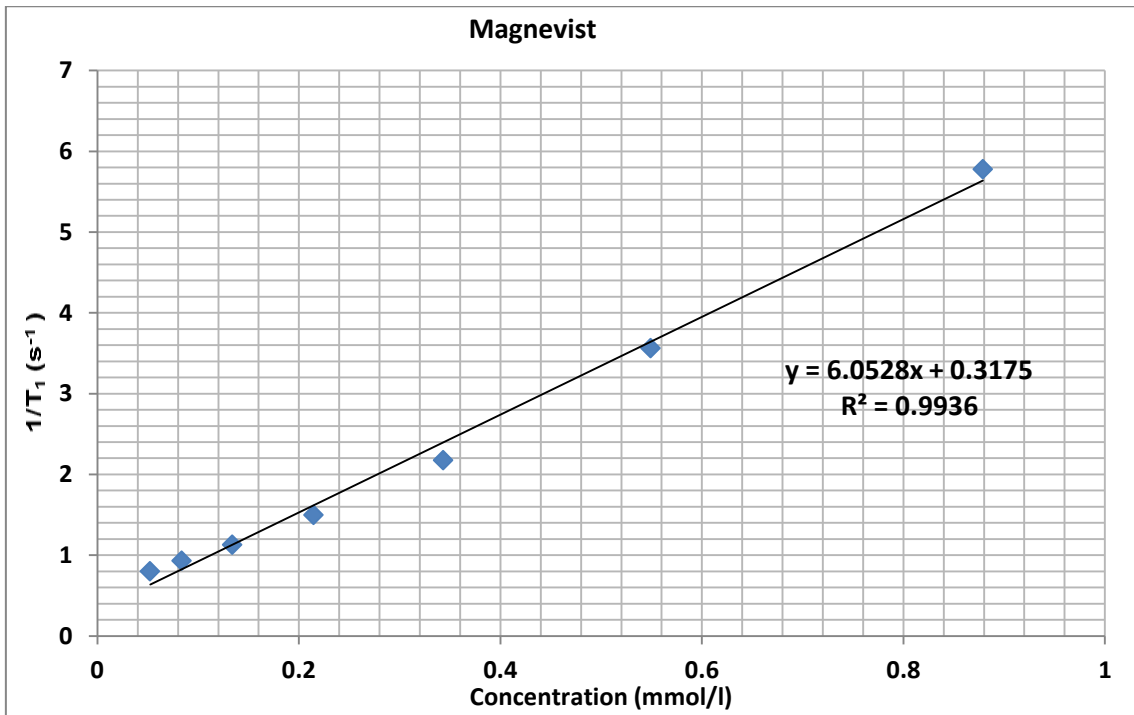
Figure 119: The dependency of the T_1 value on concentration for Magnevist. It is evident this is a linear relationship.
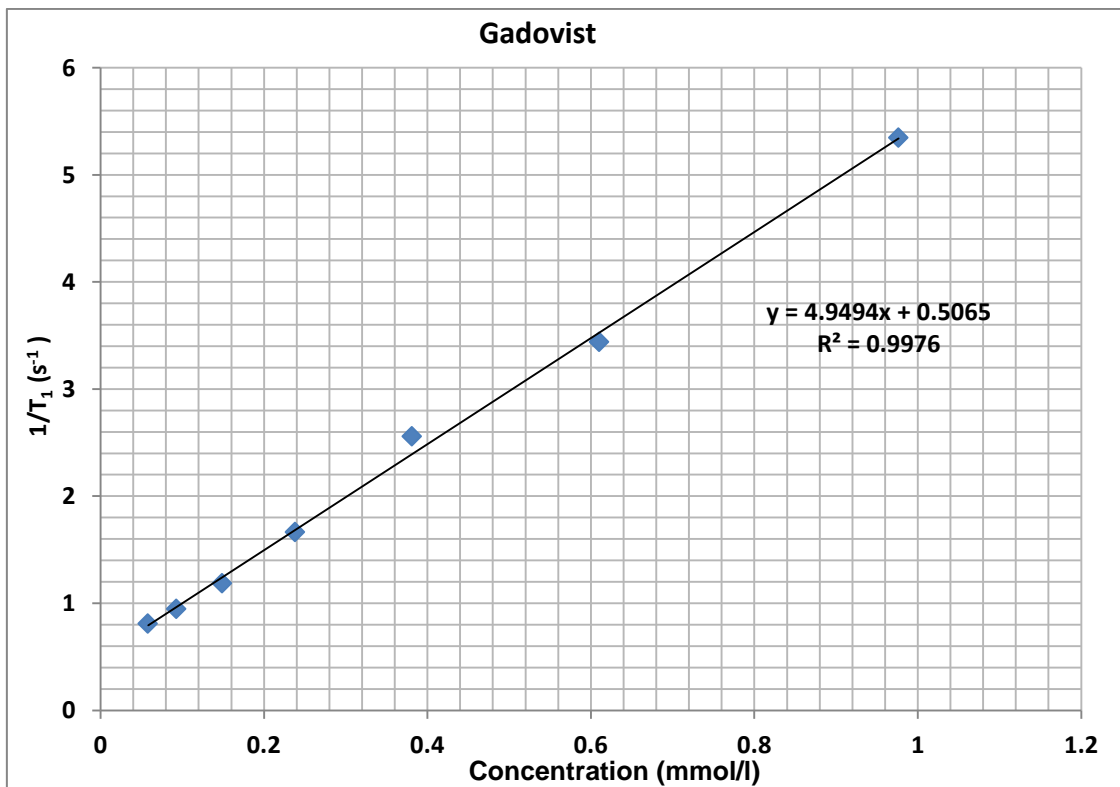
Figure 120: The dependence of the T_1 value on concentration for Gadovist. This is a linear relationship.

We can use Equation 14 and the gradients of Figure 118, Figure 119 and Figure 120 to determine the relaxivity α_R of the three contrast agents. Relaxivity has units of litres per mmol per second. The relaxivity of manganese chloride is 7.27 $lmmol^{-1}s^{-1}$. Magnevist has a relaxivity of 6.05 $lmmol^{-1}s^{-1}$. Gadovist has a relaxivity of 4.95 $lmmol^{-1}s^{-1}$.

A T_1 weighted sequence was applied to the set of 30 samples whose T_1 values had been established by the inversion-recovery technique, to investigate the effect of T_1 on gray value. Results are shown in Figure 121.

It can be seen that at large T_1 all three contrast agents give similar gray values. The manganese chloride concentrations investigated all give long T_1 values. As T_1 becomes shorter the gray values produced by Magnevist and Gadovist begin to deviate from each other; however, to a reasonable approximation the three curves coincide, as might be expected.
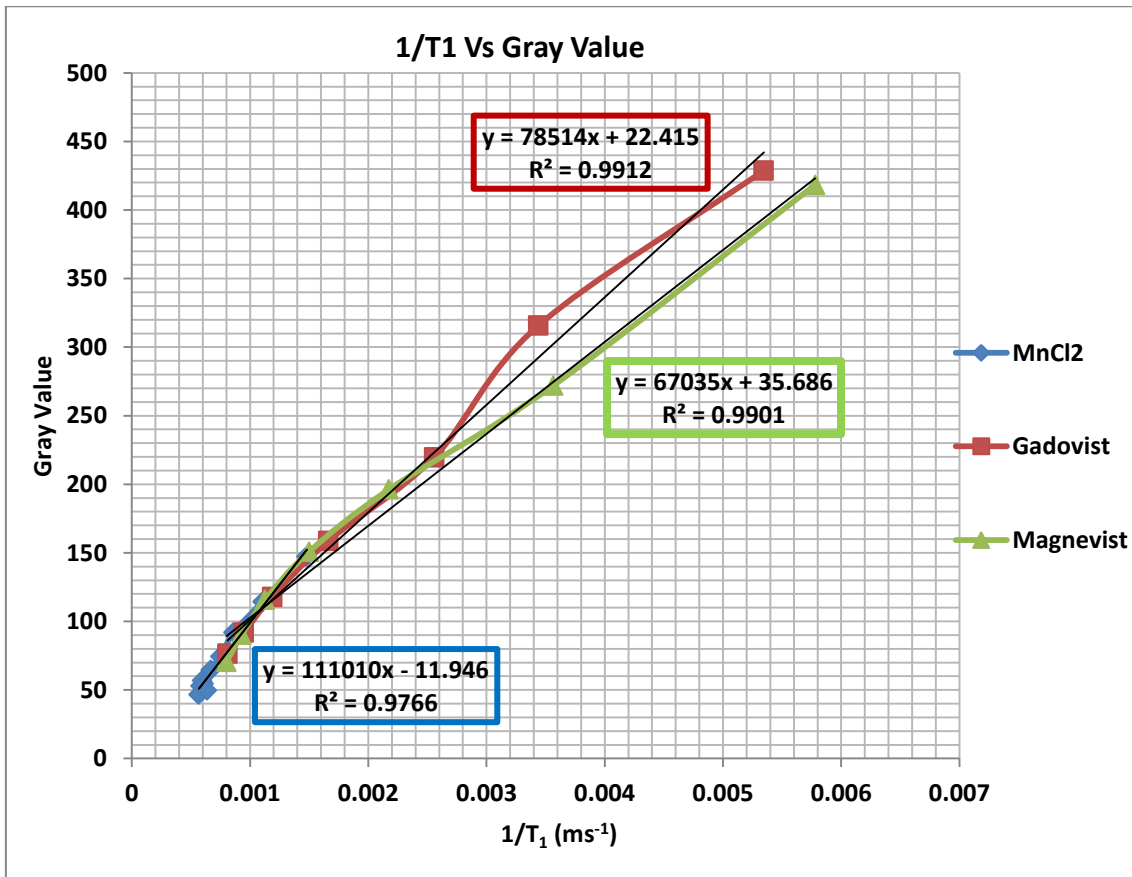
Figure 121: The relationship between T_1 and gray value for the three contrast agents manganese chloride, Magnevist and Gadovist. At a long T_1 the gray values are similar as shown by the regression lines fitted. It can be seen that for a set T_1, irrespective of the contrast agent involved, a set gray value is produced.

Figure 121 illustrates that gray value has an approximately linear dependence on $1/T_1$. The data show that irrespective of the contrast agent used, for a set T_1 value, the same gray value on the image is produced. This relationship is given by the equation below.

$$\mathcal{G} = \beta + \frac{\gamma}{\mathcal{T}_1} \quad \text{Equation 15}$$

The relationship between gray value and relaxation time is demonstrated by Equation 15. Where, G is the gray value intensity, β is the intercept (when G=0, T_1=0) and γ is the rate of change in gray value with respect to the change in $1/T_1$.

The average value of γ over the three contrast agents is 85.6 s ±22.8s. (The value of γ is expected to be independent of contrast agent, since equal changes in gray value represent equal changes in $1/T_1$.)

4.2.4.4 Discussion

Figure 111 illustrates the importance of inversion recovery scans in determining the effects of contrast enhancement on relaxation times for spin-lattice (T_1) relaxation. It can be see that the two highest concentrations for Magnevist and Gadovist produce a very low signal. This is due to the fact that they possess a T_1 relaxation time which is similar to the inversion recovery time for the particular scan. After the initial $180°$ RF pulse is produced the magnetisation vector decays along the longitudinal axis. There comes a point where it reaches the zero point and crosses into the positive longitudinal axis. If the $90°$ pulse is applied at this crossing point the contrast agent will produce no signal. The time between the $180°$ and $90°$ pulse is the inversion recovery time. The higher the contrast agent's concentration the quicker relaxation of the spin-lattice and the shorter the value of T_1. This also explains the higher signal in Figure 111 of the lower contrast concentrations (pot 10) for all three contrast agents. The lower concentrations produce a slower spin-lattice relaxation and therefore have a longer T_1 relaxation time. In this case when the $90°$ RF pulse is applied there is still a proportion of residual longitudinal magnetisation vector remaining; this becomes rotated in the xy plane to produce a high signal.

The relaxivity of Gadovist is the highest and manganese chloride the lowest. This means that Gadovist for a certain change in contrast agent has a larger effect on the spin-lattice relaxation compared to Magnevist and manganese chloride. Gadovist has a larger molecular weight and structure compared to the

other contrast agents; this causes a larger response to the external magnetic field of the scanner. The structures of the contrast agents are described in the next section.

4.3 Contrast uptake measurements

23 equine intervertebral discs were used from animals aged to the nearest year by their dentition. The samples on these occasions were not perfused and washed out with a sodium chloride solution; this is because a perfusion system as described in chapter 3 was not being utilised and it was preferable to maintain the discs in as natural a condition as possible. The samples were returned to Exeter University's biophysics laboratory and the discs were excised. The discs used for each session were a mixture of fresh or pre-frozen and defrosted slowly in refrigerated conditions overnight depending on when the sample was collected and imaging available. On some occasions more than one disc was utilised from one tail; when looking at age related changes these samples are considered as one sample and an average taken of the data.

The disc was placed in the cell with the anterior surface facing upwards and the superior surface facing the foot of the MR scanner, this was to enable complete orientation of the intervertebral disc during imaging. The two chambers were filled via the filling tubes using a syringe with a solution of 0.15 mmol of sodium chloride with the addition of 10 % PEG. The disc was allowed to equilibrate with this solution for at least 1 hour.

The equipment set-up was then taken carefully to the MR research centre at St. Luke's campus, the University of Exeter and placed within the scanner. A cod liver oil capsule and a small glass phial of distilled water were attached to the dialysis cell; these serve the purpose of providing the two extremes of signal to

enable normalisation within the series of dynamic scans and between the scans taken for each sample. The 45 mm microscopy coil was attached to the dialysis cell, laying it across its upper most surface.

Initially, a locator scan was performed to orientate the three planes for the actual data scans. The first scan performed was an initial high resolution anatomical scan. The purpose of this scan was to allow accurate location of the Regions of Interest for data collection. As previously, the scan technique was a FFE scan (using low flip angle to achieve fast imaging) with some T_1 and T_2 weighting. 20 axial slices were created which cover the whole of the disc from the superior to the inferior surface. The parameters of this scan were: TE = 11 ms, TR = 33 ms, flip angle = 30°, slice thickness = 1 mm, slice gap = 0 mm, pixel size = 0.104 × 0.104 mm, scan resolution = 576 × 576 pixels. (These sequence parameters are similar to those used for the anatomical scans in section 3.3.)

The second scan performed was a single dynamic scan. The purpose of this scan was to act as a baseline. The solution within the cell at this stage contains no contrast agent and therefore could be used to determine the change in gray value a known concentration of contrast agent produces. The parameters of this scan were: TE = 3.9 ms, TR = 20 ms, flip angle = 30°, slice thickness = 2 mm, slice gap = -1 mm, pixel size = 0.938 × 0.938 mm, scan resolution = 64 × 64 mm. (Compared to the anatomical scan, TR has been reduced, giving greater T_1 weighting at the same flip angle of 30°.)

As quickly as possible, the caps on the drainage tubes were released and both halves of the dialysis cell were drained. This was then replaced with a solution of 0.15 mmol/l of sodium chloride, 10 % PEG and one of three contrast agents

manganese chloride, Gadovist and Magnevist; of the 23 samples, 7 were perfused with manganese chloride, 8 with Magnevist and 8 with Gadovist. The concentrations used as determined by the preliminary experiments were: manganese chloride 0.125 mmol/l, Magnevist 1.8 mmol/l and Gadovist 2.25 mmol/l.

Figure 122 summarises the physical properties of the three contrast agents used in the diffusion experiments. The three contrast agents are termed paramagnetic contrast agents. Their strongest effect is on the T_1 relaxation time, hence the scan protocols used need to have T_1 weighting. The contrast agents were selected because of their differing charges and structure. The charge on a molecule is likely to influence its transport because of the fixed negative charge within the disc associated with the proteoglycans. The molecule Gadovist is a ring structure whilst Magnevist is linear. Together they cover a range of sizes and physical properties similar to those of molecules involved in metabolism and signal molecules and drugs whose rate of transport into the disc are important to determine. Manganese is a small cation. Ions are important both in determining the hydration of the extracellular matrix and in many cellular functions. Manganese is divalent, like calcium and other important trace ions its distribution is particularly sensitive to the fixed charge on the matrix.
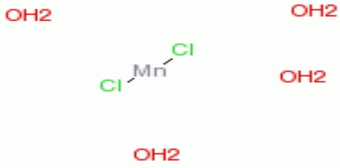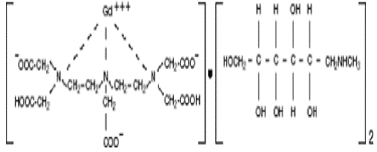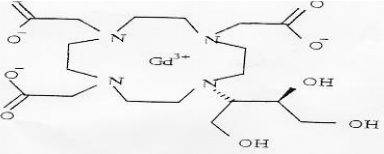
Contrast Agent	Size	Molecular Weight	Charge	Structure
Manganese Chloride	Small Ion	54.94	2+	
Magnevist	Medium Ion	469.01	2-	
Gadovist	Medium Molecule	604.7	Neutral	

Figure 122: The physical properties of the three contrast agents chosen for the dialysis diffusion experiments. These contrast agents were chosen because they represent differences in electrostatic charge, molecular size and shape.

Once the dialysis cell was completely full with the contrast containing solution repeated contrast dynamic scans identical to the pre-contrast baseline dynamic were continuously repeated for an average length of 17 hours although one dynamic series was left for 83 hours.

All three scans produced a PAR and REC file each, containing the scan information. These were converted into IMG and HDR files using MRIcro as previously described. ImageJ WCIF was used to view the images.

Initially, the pre-contrast anatomy and contrast (uptake) dynamics were viewed side by side at the same magnification. Using the pre-contrast anatomy the central axial slice through the intervertebral disc was established. The corresponding slice in each of the separate contrast uptake scans was selected. This is an extremely time consuming process as most experiments provided more than 300 individual contrast uptake scans. A macro to produce a

concatenation of these slices was written by John Hale (Exeter University); this macro selected the relevant slice and stacked all the slices selected sequentially with respect to time. The high resolution anatomy scan was used to position the 13 ROIs symmetrically in the nucleus and annulus as shown in (Figure 123); this required the position of the disc in this image to correspond with the disc position in the contrast uptake series; a second macro was produced by John Hale to register the two scans. Image J WCIF was used to create the ROIs which were Imm^3 in volume.
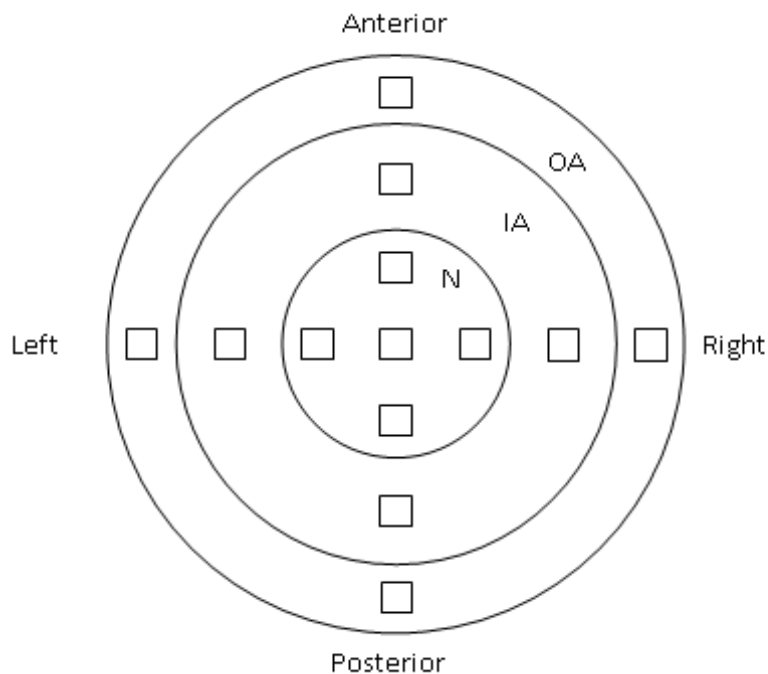
Figure 123: The 13 Regions of Interest used to obtain the time-intensity curve data within the intervertebral disc: N-Nucleus, IA-Inner Annulus, OA-Outer Annulus.

The intensity values of each ROI was then normalised using the oil and water capsule. Theoretically, throughout the time course the oil and water capsule intensity should have a constant value; there is in fact a phenomenon known as scanner drift, where the MR scanner loses its tuning only by a small amount but

still enough to affect the values of the oil and water. The water and oil capsule intensity for each slice within the contrast uptake images was determined (Figure 124) and a mean for each slice calculated to provide a normalisation constant which took into account how both the water and oil changed over time; this is useful as the oil and water represented how the extremes of signal changed with time.
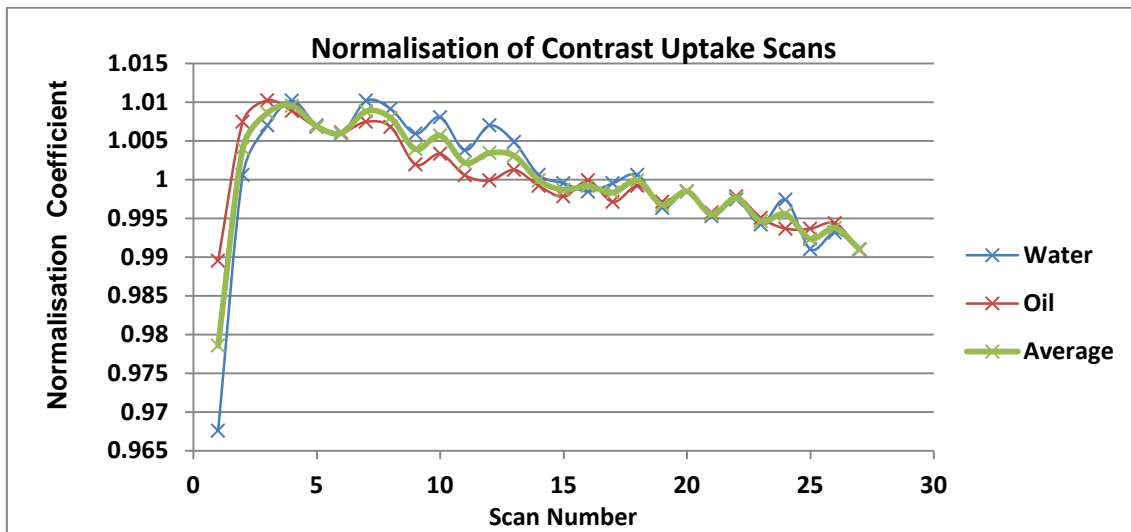
Figure 124: Scanner drift; the intensity of the oil and water capsule is determined for the contrast uptake scans and a normalisation coefficient determined using their mean values. The plot represents gray value intensity oil or water/mean gray value intensity oil or water.

For each normalised ROI a time-intensity curve was plotted by using Image J WCIF to plot a 'z-axis profile', which in this case was in fact a time-axis profile; this measured the value of the ROI through each subsequent slice in the stack of the contrast uptake images
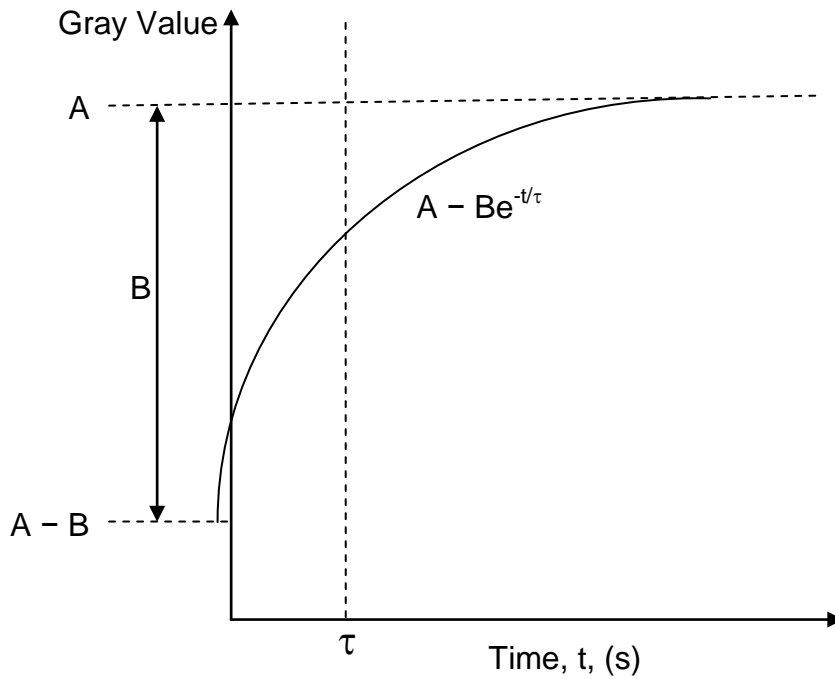
Figure 125: The key features of a time-intensity curve; A is the final gray value at time infinity, B is the scale of gray value change and τ is the characteristic time or time constant for the process. The exponential does not begin at zero as the tissue has an initial T_1 pre-contrast. Note this is ignoring the delay in the diffusion process, Figure 104.

A schematic representation of a time-intensity curve with its key features is illustrated in Figure 125. [For simplicity, an exponential function is shown. As mentioned previously (section 4.1.2), the expected variation of gray value with time has the same form as the variation of contrast agent modelled in Figure 104, so only the later part of the experimental time-intensity curve can be fitted to an exponential.]

For each of the ROIs the time-intensity curve was fitted to an equation of the form:

$$\mathcal{G} = \mathcal{A} - \mathcal{B}e^{-\frac{t}{\tau}}$$ **Equation 16**

The time-intensity curve is given by Equation 16. G is the measured gray value intensity, A is the asymptotic gray value, B is the magnitude or scale of gray

value change, t is the time of measurement and τ is the time constant of the process.

Only values from the exponential portion of the experimental data were fitted using the "Solver" function in EXCEL. This function was set up to perform a least-squares fit to determine the values of A, B and τ in the above equation, for each ROI. In fact – see next section – the experimental data were not quite as expected, making the fitting procedure more complicated than described here.

As mentioned above, the exponential rise of gray value described by Equation 16 corresponds to an exponential rise in the contrast agent of the form:

$$C = C_0 \left(1 - \frac{4}{\pi} e^{-\frac{t}{\tau}} \right) \quad \text{Equation 17}$$

Equation 17 demonstrates the exponential behaviour of the contrast agent: C is the concentration at a time, t, and τ is the time constant of the process (corresponds to Equation 8).This relationship between concentration of contrast agent and time is illustrated below in Figure 126:
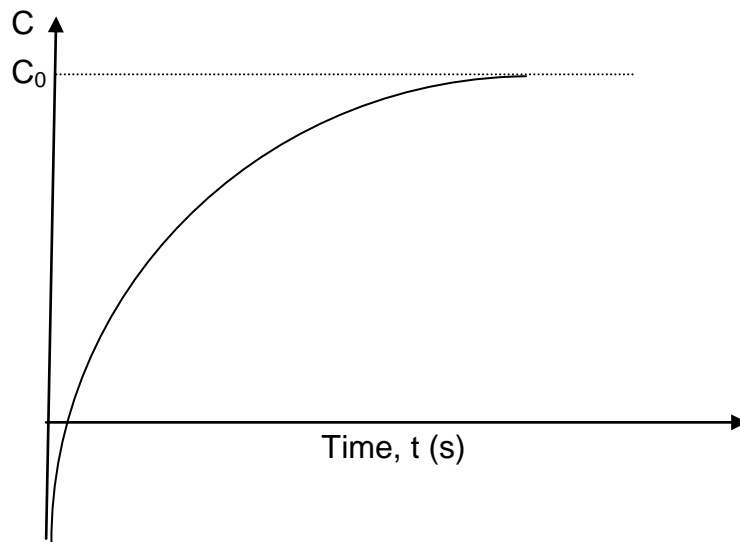
Figure 126: The variation of concentration of contrast agent with time. C_0 is the asymptote, which is the concentration of contrast agent in the tissue at infinity. The initial negative part of the curve is not valid (see Figure 104).Equation 14

Hence, for a particular region of interest, the equilibrium concentration C_0 can be calculated from the magnitude B obtained from fitting the experimental gray scale data, by means of an appropriate conversion factor. The following paragraphs outline how this conversion factor may be calculated.

Equation 14 can be rewritten as:

$$\frac{1}{\mathcal{T}_1} = \mathcal{R}_0 + \alpha_{\mathcal{R}} \mathcal{C} \quad \text{Equation 18}$$

The relaxation time T_1 is affected by the relaxation rate of the tissue, R_0, and the relaxivity and concentration of the contrast agent.

At time, t = 0, the concentration of contrast agent is 0 and from Equation 18 $R_0 = 1/T_1$. That is, even before the contrast agent has entered the tissue it has an inherent relaxation. This may be seen from Figure 125.

219

In section 4.2.4, Equation 15, illustrated how gray value altered with changes in relaxation time as a result of the change in concentration of contrast agent. Equation 12 established the original raw MR signal called the floating point. We need to work in terms of the floating point because each scan is inherently scaled uniquely for ease of display. To enable comparison of the pre-contrast dynamic and the contrast uptake scans the scaling needs to be normalised. The concentrations of contrast agent chosen provide a linear relationship between gray value intensity and T_1 value, (Equation 15).

$$\mathcal{FP}_{ref} = \frac{\mathcal{G}}{SS_{ref}} = \frac{1}{SS_{ref}}\left[\beta + \frac{\gamma}{T_1}\right] \quad \text{Equation 19}$$

Equation 19 demonstrates the conversion of the gray value intensity (Equation 17) into the raw signal produced by the MR scanner (Equation 14); SS_{ref} is a scaling factor already described which can be taken from the PAR file, ref stands for reference which is the contrast solution surrounding the disc. The purpose of Equation 19 is to establish the change in raw signal produced by the bathing solution from its pre-contrast to its contrast state. This change in signal is for a known concentration of contrast agent. We can then use this known change for a known concentration to establish the concentration in the tissue by adapting Equation 19. The adaptation needed is to take into account the difference in proton density between the bathing solution and tissue and the scaling factor in the contrast uptake scans, which is different to the pre-contrast dynamic (ref).

$$\mathcal{FP}_{tissue} = \frac{\mathcal{G}}{SS_{tissue}} = \frac{\mathcal{P}_{tissue}}{\mathcal{P}_{ref}}\frac{1}{SS_{ref}}\left[\beta + \frac{\gamma}{T_1}\right] \quad \text{Equation 20}$$

Equation 20 demonstrates the raw signal produced by the tissue in a MR image; P is the proton density and is important in T_1 weighted images; the proton density of the disc is less than a contrast agent solution as it contains less water molecules.

Rearranging this equation:

$$\mathcal{G} = \frac{\mathcal{P}_{tissue}}{\mathcal{P}_{ref}} \frac{SS_{tissue}}{SS_{ref}} \left[\beta + \frac{\gamma}{\mathcal{T}_1} \right]$$ **Equation 21**

Where G is the gray value intensity produced on the MR image by the intervertebral disc.

Substituting Equation 17 and Equation 18 into Equation 19 and rearranging gives:

$$\mathcal{G} =$$

$$\left(\frac{SS_{tissue}}{SS_{ref}} \frac{\mathcal{P}_{tissue}}{\mathcal{P}_{ref}} \beta + \frac{SS_{tissue}}{SS_{ref}} \frac{\mathcal{P}_{tissue}}{\mathcal{P}_{ref}} \gamma \mathcal{R}_0 + \right.$$

$$\left. \frac{SS_{tissue}}{SS_{ref}} \frac{\mathcal{P}_{tissue}}{\mathcal{P}_{ref}} \gamma \alpha_{\mathcal{R}} \mathcal{C}_0 \right) - \frac{SS_{tissue}}{SS_{ref}} \frac{\mathcal{P}_{tissue}}{\mathcal{P}_{ref}} \gamma \alpha_{\mathcal{R}} \mathcal{C}_0 \frac{4}{\pi} e^{-\frac{t}{\tau}}$$ **Equation 22**

Where, G is the change in gray value intensity as a result of the diffusion of contrast agent.

Equation 22 is of the same form as Equation 16 and therefore we can determine expressions for the parameters A and B of the time-intensity curve shown in Figure 125.

$$\mathcal{A} =$$

$$\frac{SS_{tissue}}{SS_{ref}} \frac{P_{tissue}}{P_{ref}} \beta + \frac{SS_{tissue}}{SS_{ref}} \frac{P_{tissue}}{P_{ref}} \gamma \mathcal{R}_0 +$$

$$\frac{SS_{tissue}}{SS_{ref}} \frac{P_{tissue}}{P_{ref}} \gamma \alpha_{\mathcal{R}} C_0 \quad \text{Equation 23}$$

Equation 23 is a theoretical description of the asymptote illustrated in Figure 125. The actual value of A for each sample's 13 ROIs is calculated by the curve fit of the time-intensity curves.

$$\mathcal{B} = \frac{SS_{tissue}}{SS_{ref}} \frac{P_{tissue}}{P_{ref}} \gamma \alpha_{\mathcal{R}} C_0 \frac{4}{\pi} \quad \text{Equation 24}$$

Equation 24 describes the scale of change in gray value, illustrated in Figure 125. The actual value of B for each sample's 13 ROIs is calculated by the curve fit of the time-intensity curves.

Rearranging Equation 24 to give the required conversion from B to C_0 (the description of the concentration at time infinity:

$$C_0 = \frac{\mathcal{B}}{\gamma \alpha_{\mathcal{R}}} \frac{\pi}{4} \frac{P_{ref}}{P_{tissue}} \frac{SS_{ref}}{SS_{tissue}} \quad \text{Equation 25}$$

All terms in the conversion factor $\frac{\mathcal{B}}{\gamma \alpha_{\mathcal{R}}} \frac{\pi}{4} \frac{P_{ref}}{P_{tissue}} \frac{SS_{ref}}{SS_{tissue}}$ are known, except

$\gamma \alpha_{\mathcal{R}}$ which is found experimentally, as explained below. Equation 25 was used

to calculate the amount of contrast agent in each of the 13 ROIs at equilibrium

in the following way. In the baseline pre-contrast dynamic, the bathing solution within the cell is 0.15mmol sodium chloride and 10 % PEG; that is a solution with no contrast agent. The slice from which the data was collected in the contrast uptake scans is the central disc slice and therefore the PEG and contrast solution in the cell is not well visualised, the dialysis membrane fills the cell in that particular image slice. The PEG and contrast solution gray value intensity of approximately 4 slices before and after this central disc slice which allowed good PEG visualisation was determined and a mean value calculated; this was also done for the water capsule in the same slices.

The scale slope between the pre- and post- contrast dynamic is different; to obtain accurate relative gray values between these two scans the scale slopes need to be normalised to each other. This is achieved by undertaking the same process as described in the previous paragraph on the pre-contrast dynamic. The water capsule gray value intensity in both scans is normalised to their respective true values (Figure 124). This corrected water value was compared to the average value obtained within the 8 slices in either scan to determine the amount of correction needed. This correction was applied to the gray value produced by the PEG solution both with and without contrast to give a true representation of its value.

The gray value difference between the pre-contrast and post-contrast solution was determined. As the first contrast uptake scan was used, all the contrast would still be in the bathing solution. The exact concentration for each of the three contrast agents is known; therefore this enables the change in gray value for a certain concentration to be known. This was done for each sample.

Consider Equation 25, the term $B/\gamma\alpha_R$ is given by comparing the change in gray value for each region (the B value from curve fitting) with the known normalised change in gray value for the bathing solution pre- and post-contrast. The SS_{ref}/SS_{tissue} has been determined by the normalisation process to the water capsule described above. The remaining term is the difference in proton density between the reference PEG solution (with contrast) and the tissue. This was established by calculating the water content of each sample; the proton density relates to the hydrogen nuclei in the water molecules. This was achieved by measuring the weight of the sample pre experiment and then incubating the sample after experimentation for a minimum of 120 hours at 37° until only the dry weight remained. The difference in weight ((wet-dry)/wet)) gave the tissue water content and therefore its difference in water content and proton density relative to the PEG solution which for this purpose was assumed to have the same proton density as water. There is also the remaining constant π/4 to be accounted for. The concentration of contrast for each of the 3 agents in the 13 ROIs for each of the 23 samples was calculated using this method.

4.4 Results
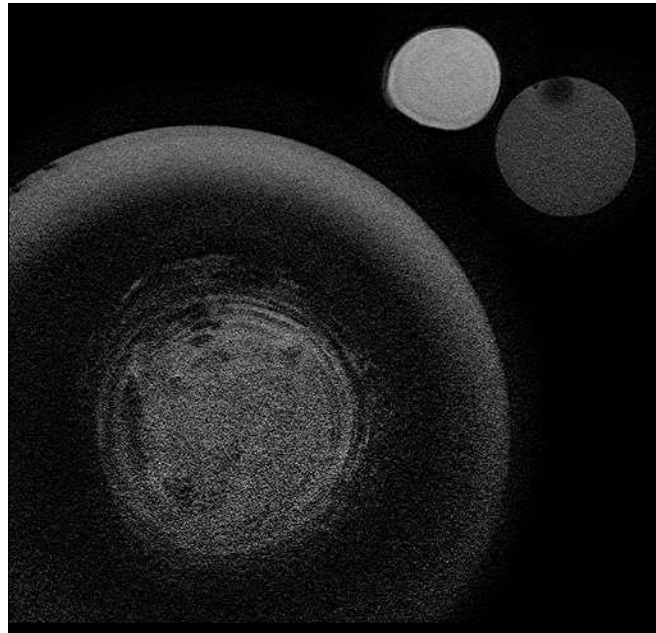
Figure 127: A typical high resolution anatomy scan of the central disc slice of sample 22. The bright halo is the solution surrounding the dialysis membrane. The inner annulus is defined as one of the first two inner rings. The outer annulus is defined as one of the outer two rings. A ring is one bright area width.

Both Figure 127 and Figure 128 are typical of the three scans obtained for each sample. Figure 127 is used to place the ROIs as the annulus and nucleus can be distinguished. These regions are then transferred to the images in Figure 128 below to enable data to be measured. Figure 128 shows clearly the effect of the scale slope applied by the MR scan. The intensity of the oil capsule signal should not change in value between images A, B and C. B and C have the same scaling factor as they are part of the same time-series. However, the scaling factor applied to the pre-contrast dynamic (A) is different; hence the brighter signal from the oil capsule. The process of normalisation described earlier takes account of the variable scale slope. Figure 128 also demonstrates the effectiveness of the CLEAR function which compensates for the spatial variation of the sensitivity of the receiving coil – there is no evidence of signal

drop-off over the workspace. (With hindsight, it would have been useful to demonstrate uniformity of sensitivity in a phantom study.)
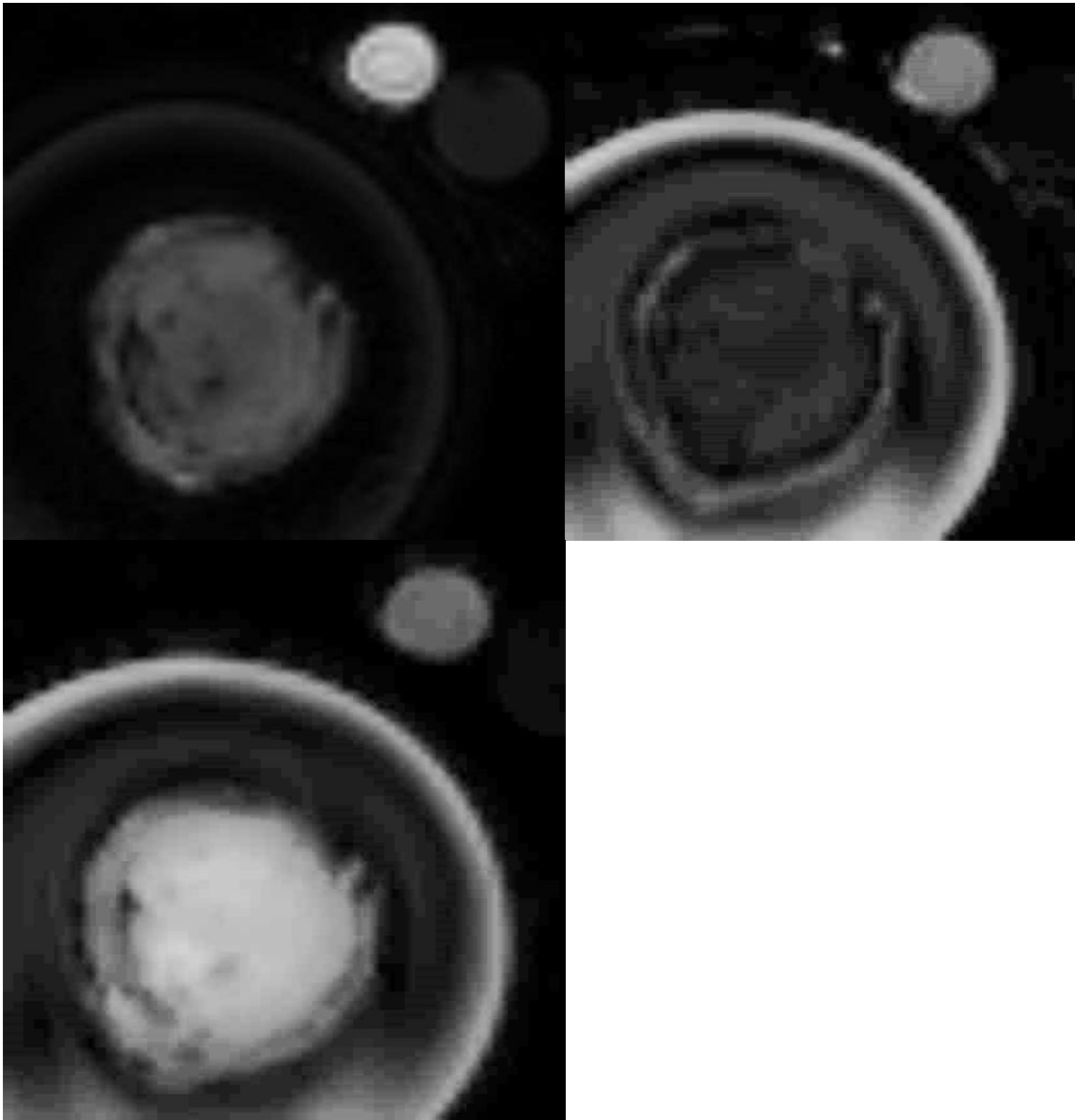
Figure 128: Typical dynamic low resolution scans of sample 22; A-Pre-contrast, B-179 s contrast incubation with Gadovist, C-18.9 hours contrast incubation. The two smaller circles are oil and water capsules, which should have a constant gray value; they are used for normalisation. The disc in panel C is bright due to the presence of contrast agent which shortens the T_1 value of the tissue.

Figure 129 below illustrates the typical appearance of the time-intensity curves. In a small number of cases (for example, see Figure 129, lower panel), the

time-intensity curves show a dip at the beginning of the diffusion process before the exponential rise begins. This is not what is expected theoretically (Figure 104). After much investigation, it was concluded that the imaging sequence only provides the expected linear relation between gray value and $1/T_1$ at shorter values of T_1: at longer values of T_1 (i.e. near the start of the experiment, when the concentration of contrast agent is low) the relation is non-linear. The measured non-linearity is shown in Figure 130.

Sample 22 Gadovist Diffusion within the Annulus

Legend:
- Outer Anterior Annulus
- Inner Anterior Annulus
- Inner Posterior Annulus
- Outer Posterior Annulus
- Inner Right Annulus
- Outer Right Annulus
- Inner Left Annulus
- Outer Left Annulus

Sample 4 MnCl$_2$ Diffusion within the Nucleus

Legend:
- Anterior Nucleus
- Central Nucleus
- Posterior Nucleus
- Right Nucleus
- Left Nucleus

Figure 129: Typical time-intensity curves for the 13 ROIs in Gadovist and Manganese chloride. The graphs are separated into nucleus and annulus for ease of display. It can be seen that the initial portion of the curves for Gadovist and manganese chloride are different. In this particular sample perfused with manganese chloride the 'problematic dip' takes up a greater proportion of the graph.

The fact that all 13 regions from a given sample produce the same measured non-linearity, even though their individual time-intensity curves are dissimilar, provides some evidence that the image sequence is the origin of this unexpected behaviour.
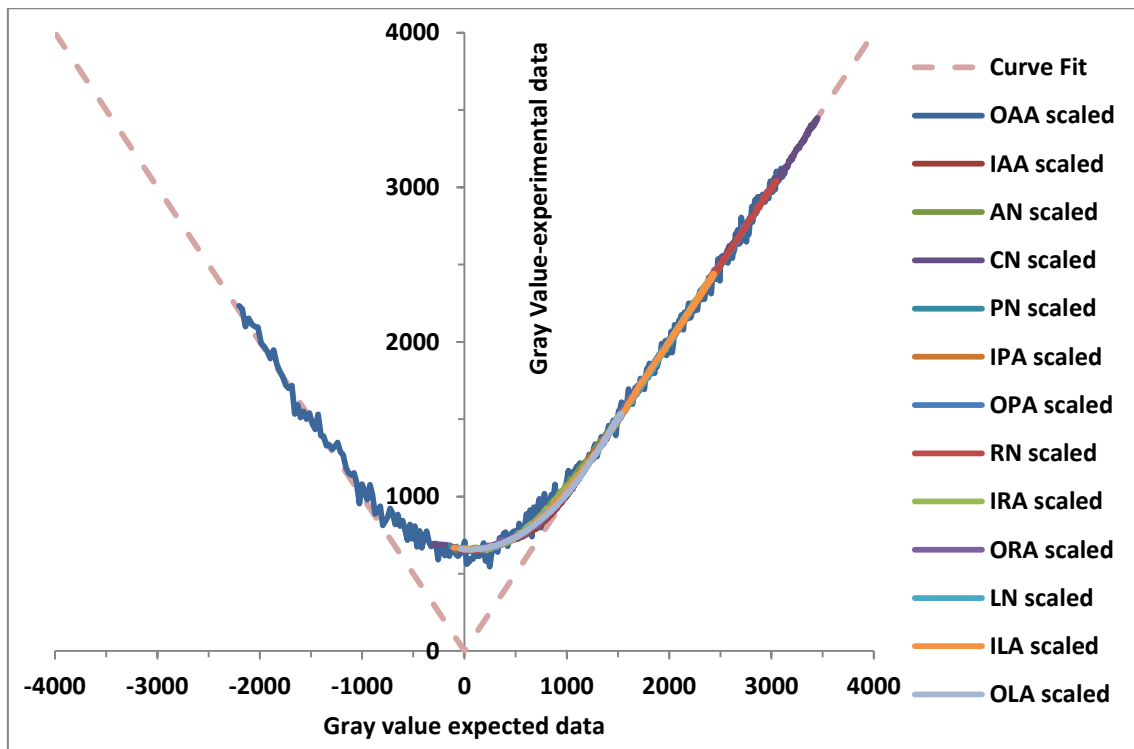
Figure 130: Measured non-linearity in the imaging sequence, shown as actual gray value vs. expected gray value (i.e. assuming linear behaviour). Data are shown from 13 ROIs for sample 7, which was perfused with manganese chloride. Offset and scaling have been used to normalise the individual data sets, after which there is a good match between them. For normalised gray values greater than around 1500, the experimental values match the expected linear behaviour. Surprisingly, the curve appears to have left-right symmetry.

If we consider the data after the problematic part of the time-intensity curve, the majority of cases it is possible to obtain a good fit to a rising exponential of the form $A - Be^{-t/\tau}$, as predicted by the solution of a simple 1-D diffusion equation, (Equation 9). An example of such a fit is shown in Figure 131. The fitted value of τ is the time constant for the diffusion process, the fitted value of B is used to calculate the equilibrium (asymptotic) concentration C_0 of the contrast agent in the tissue using Equation 24. (For example, from the data in Figure 131, B = 831 converts to $C_0 = 3.79$ mmol L^{-1}.)
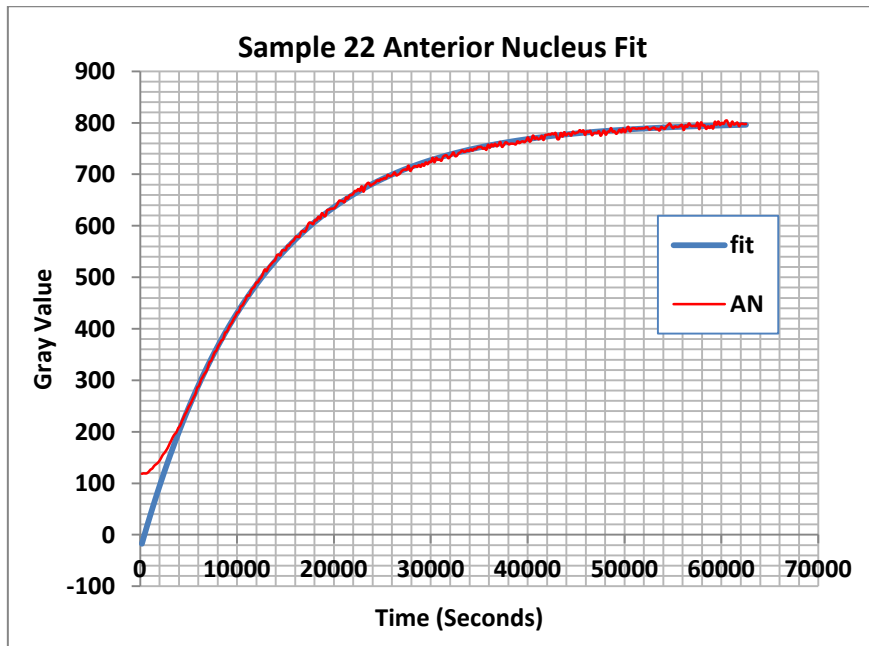
Figure 131: An illustration of a time-intensity curve (red line) in which most of the data follow an exponential curve (blue line). The departure of the experimental data from the exponential curve can be seen to the left. For the curve fit, A = 801, B = 831 and τ = 12400s.

Some of the data showed a curve which had a prolonged initial dip with insufficient data for a reliable exponential fit as seen in Figure 132. In such cases it is possible to compensate for the known non-linearity in the measurement process and produce corrected data, which can then be fitted with an exponential,

231
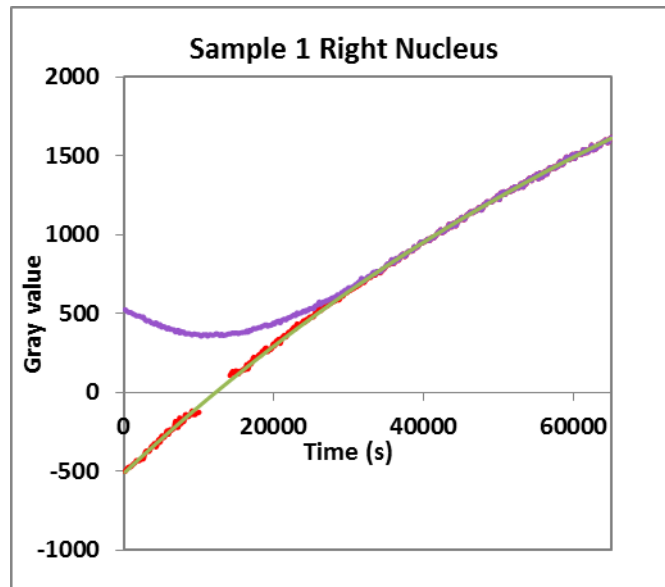
Figure 132: Sample 1, the right nucleus (purple line) initially shows a prolonged dip. The red lines are the same data after correction for the measurement non-linearity – the green curve is an exponential fit. (The flat section of the purple curve cannot be corrected.)

Even with the option of correcting for the measurement non-linearity a small number of regions, 3 in total, could not be fitted with an exponential: the right nucleus of sample 2, the inner anterior annulus of sample 21 (see Figure 133) and the anterior nucleus of sample 21. Those cases suggested a straight line fit, i.e. an infinitely long time constant.
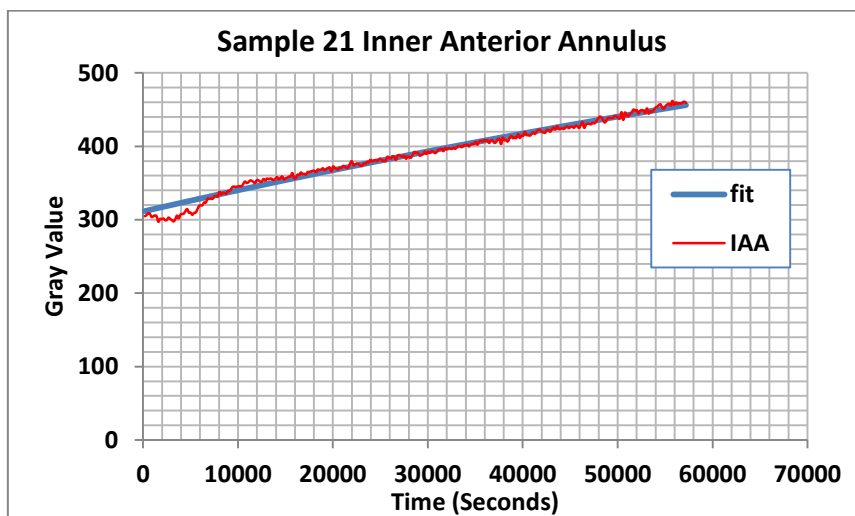
Figure 133: An example of a time-intensity curve that cannot be fitted to an exponential. (When τ is long.)

On three of the samples the pre-contrast dynamic was not usable due to technical difficulties; in these cases an average change in gray value for samples perfused with that contrast agent was used.

The time constant, τ in each of the 3 contrast agents is calculated as an average for all of the 13 regions, Figure 134. The data shown is raw and unnormalised. It can be seen that overall manganese chloride has the longest time constant followed by Magnevist and Gadovist. It is likely the fixed charge matrix of particularly the nucleus is affecting the transport of Manganese chloride and Magnevist. In particular the negatively charged proteoglycans will electrostatically interact with the positive manganese ion, slowing its transport. Gadovist is neutral and unaffected by electrostatic interactions with the matrix. The time constant shows a greater variability between samples with manganese chloride; this may again be due to electrostatic interactions which would depend on matrix condition.
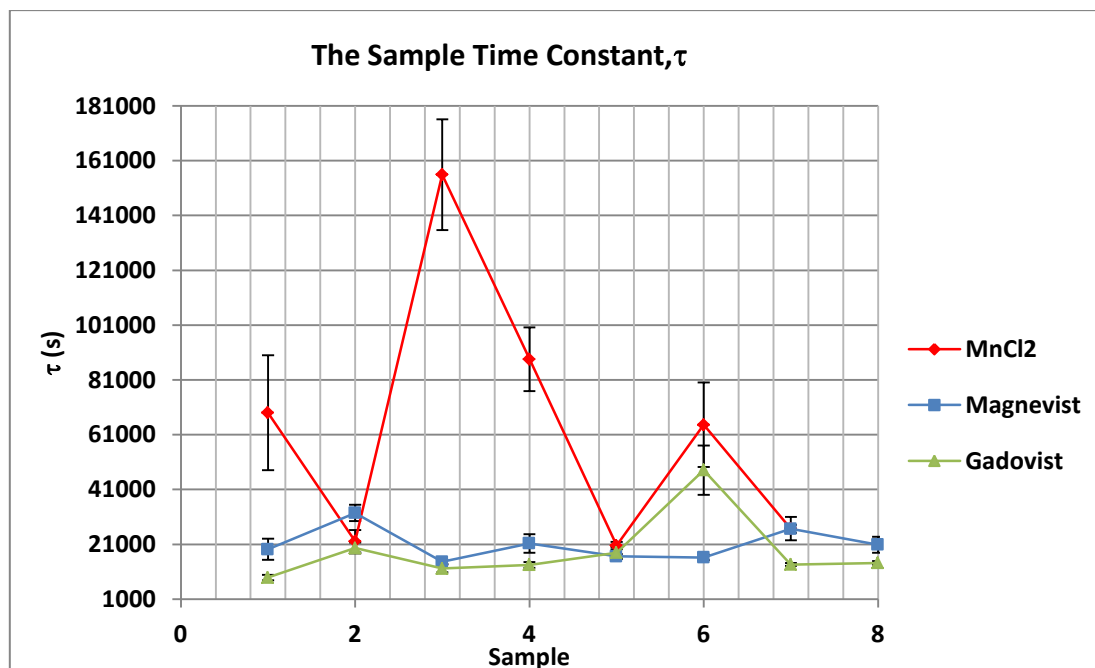
Figure 134**: The value of the time constant, τ for each of the samples; error bars are standard error. These are unnormalised; time constants are dependent on the distance travelled, however, it does give some indication that manganese will have the longest time constant.**

233
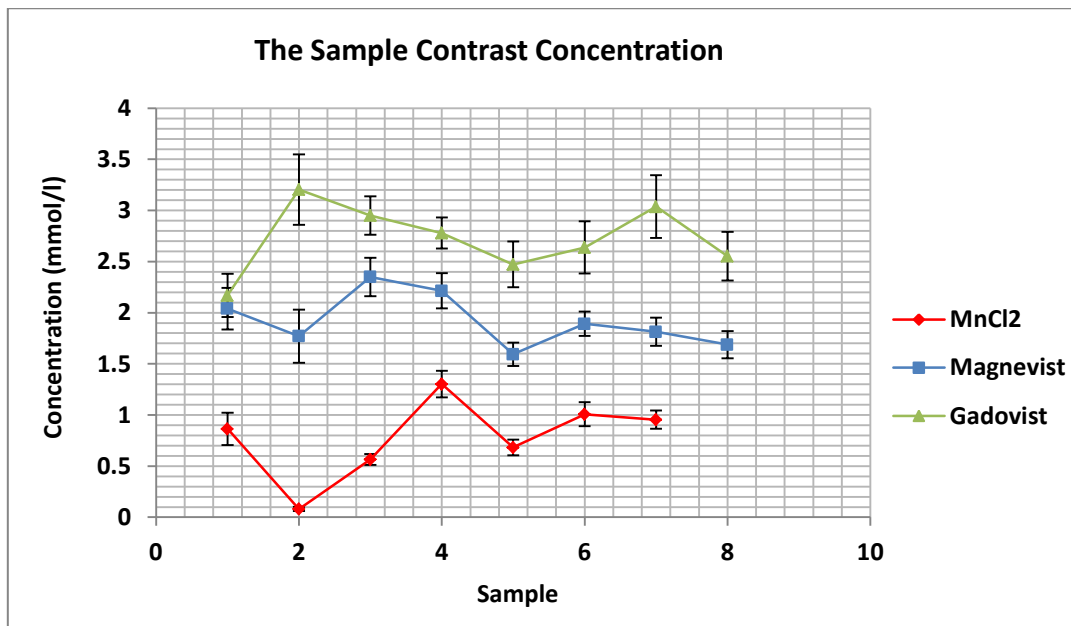
Figure 135: The value of the contrast concentration for each of the samples; error bars are standard error.

Figure 135 shows the raw and unnormalised data for concentration of contrast agent. Concentration in the tissue has a linear dependence on the concentration of the initial bathing solution; the Gadovist bathing solution is at the highest initial concentration and manganese chloride is the lowest. This explains Gadovist having the highest overall concentration. Manganese chloride shows the largest range between samples, a range of 1.3 mmol/l. It is likely, as with the time constant, matrix composition differences between samples impact on the manganese ion's transport.

Figure 136 below shows the average time constant, τ for each of the 3 contrast agents in the 13 ROIs.
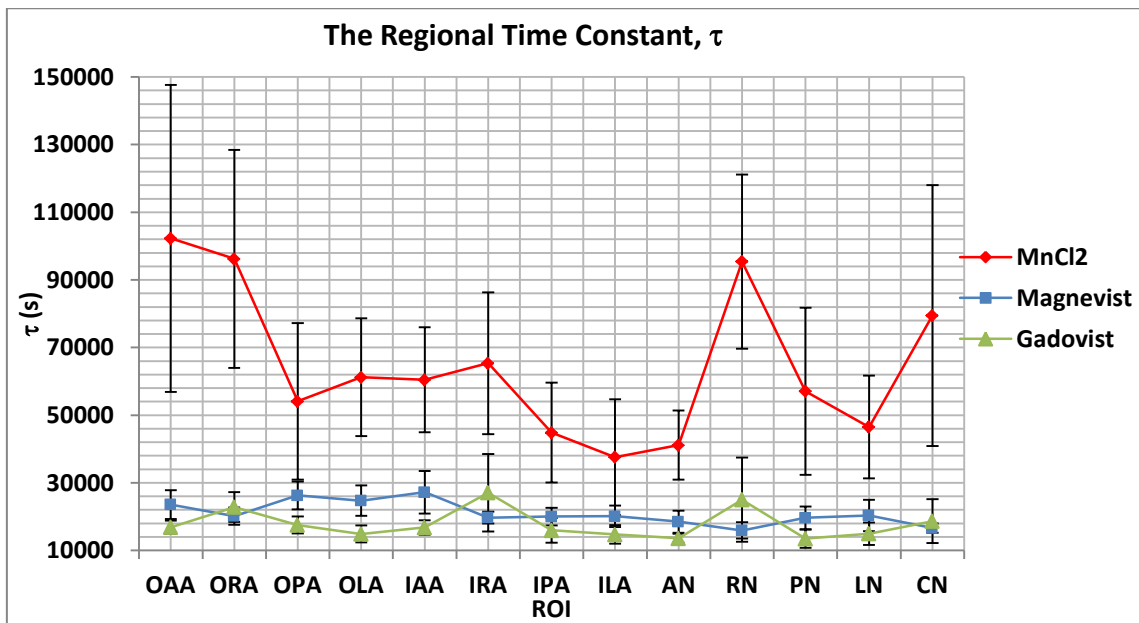
Figure 136: An illustration of the average time constant for each of the 13 ROIs in the contrast agents manganese chloride, Magnevist and Gadovist. The region abbreviations are those shown in Figure 129. The regions are arranged in a spiral starting at the outer anterior surface and moving in a clockwise direction to finish in the central nucleus. The error bars are the standard error. These are not normalised to a standard size of disc.

Dividing the sample into regions shows that the manganese chloride in particular has variation in time constant between the regions; with the anterior aspect and the central nucleus having the longest time constants. The nucleus' negative fixed charge density will affect the transport of the manganese ion; this may well indicate that the central portion of the nucleus has a higher fixed charged density than the periphery of the nucleus. The median caudal artery runs along the anterior aspect of the disc and it may be the case that structurally the anterior annulus is modified to take advantage of this. The error bars on the manganese are large; the curve fit for these samples is good and even though there is a large range of values we would not exclude these but suggest they are a variance which occurs in small charged ions, possibly due to differences in matrix composition both between regions and samples.

The average concentration of contrast agent in each of the 3 contrast agents is calculated for each of the 13 regions and displayed in Figure 137 below. From the outside to the centre of the disc a steady increase in concentration is shown for all 3 contrast agents. This is to be expected in the case of manganese chloride as the fixed charge density of the nucleus attracts the positive ion. It is not expected the Magnevist would behave in this way; it would have been more likely to be repelled by the nucleus. It is unclear why it exhibits this behaviour.
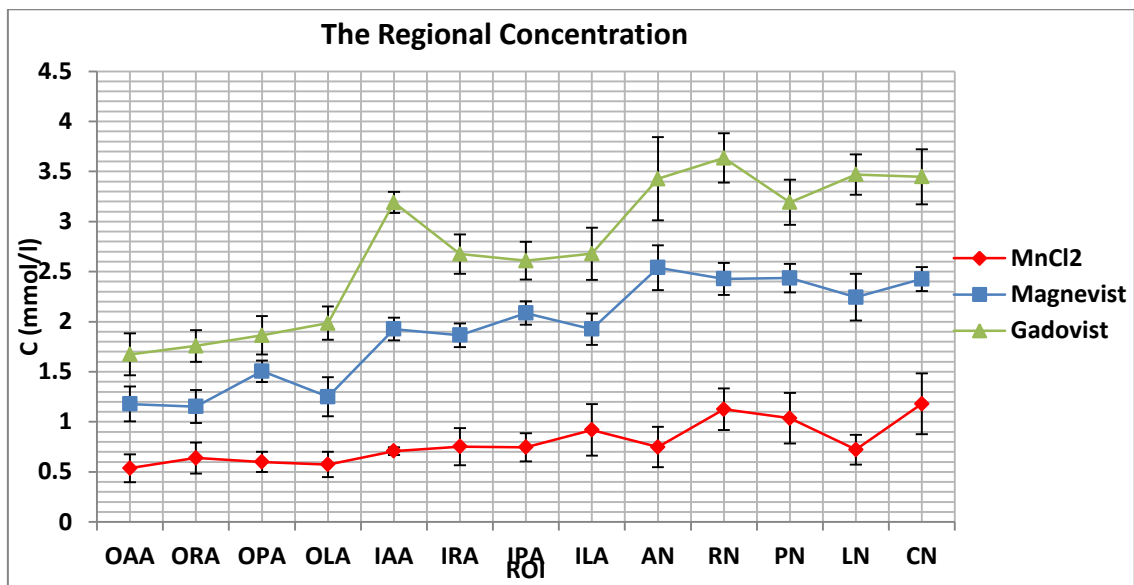
Figure 137: An illustration of the average concentration of each of the three contrast agents in each of the 13 ROIs. The region abbreviations are those from Figure 129. The regions are arranged in the form of a spiral starting at the outer anterior region moving in a clockwise direction to finish in the central nucleus. The error bars are the standard error. Concentration has a linear relationship with the initial concentration; the concentrations are dissimilar initially, therefore, this graph represents results which are not normalised.

The experimental data is based on an excised disc. Due to the orientation of the disc in the cell, diffusion will predominantly occur from the superior and inferior surfaces. The slice from the disc examined is the central slice; to accurately compare the time constant between samples the thickness of the samples must be considered. Sample 1 is 9 mm thick; all other discs are normalised to the thickness of this sample.

$$\tau_n = \tau \times \left(\frac{\mathcal{L}_{ref}}{\mathcal{L}}\right)^2 \quad \text{Equation 26}$$

Equation 26 illustrates the normalised time constant, τ_n, which is calculated by using a normalisation coefficient which is the ratio of the thickness of sample 1, L_{ref}, and the thickness of the sample in question, L. This coefficient is multiplied by the time constant, τ, of the sample being normalised. In principle there is some uncertainty associated with this normalisation, since the thickness L of an excised disc is not expected to be constant throughout – in practice the thickness, as measured on the MRI scans, was surprisingly constant in almost all cases.

Normalised time constants are plotted in Figure 138. (It appears that the $MnCl_2$ data have greater variability, but this is largely due to $MnCl_2$ values being higher-the percentage variability is similar for all three data sets.)
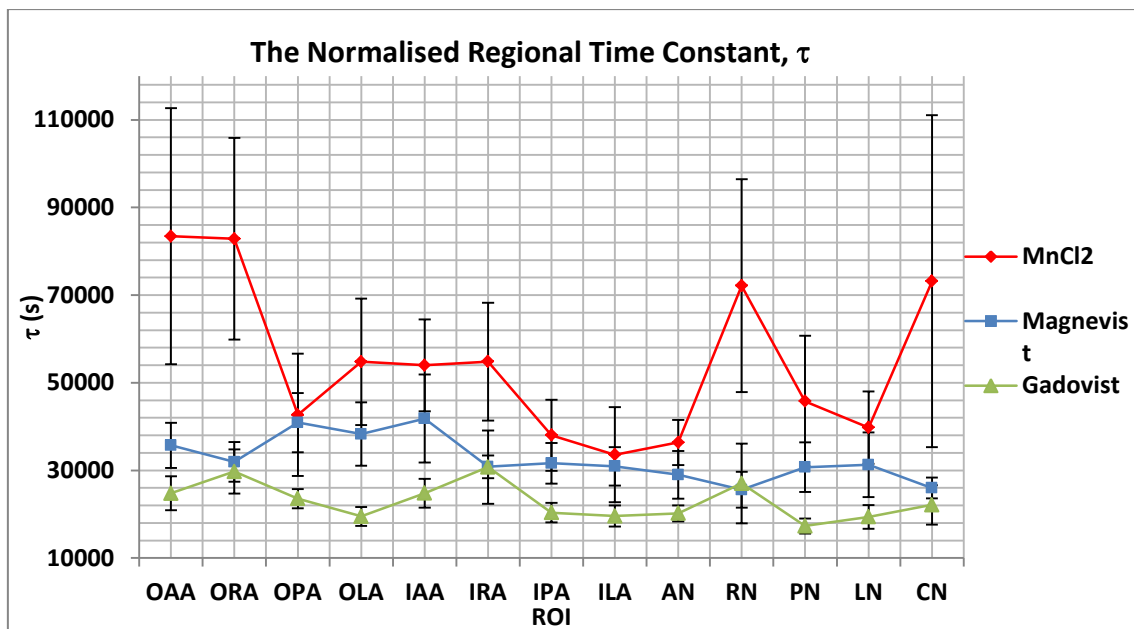
Figure 138: The average values for the individual regions have been normalised to a reference intervertebral disc thickness of 9 mm. The ROIs form a spiral from the outer Anterior Annulus in a clockwise direction finishing at the Central Nucleus; Abbreviations of ROIs relate to those demonstrated in Figure 129. The error bars are the standard error. After the normalisation process, it can be seen that manganese chloride, in this particular set of samples, has the longest time constant. Gadovist is quickest at diffusion.

237

The concentrations of the contrast agents need to be normalised to allow comparison between samples. The assumed mathematics as previously described is linear; if the initial concentration is doubled then all the subsequent concentrations and rates also double while the time constant, τ stays the same. To normalise the concentrations observed in the tissue, we can work in terms of the ratio of the equilibrium concentrations (C_{nratio}); this is the ratio of the asymptotic concentration (C_{tissue}) observed in the tissue to the initial concentration in the bathing solution (C_{peg}). This parameter is close to what is referred to in most of the disc literature as the partition coefficient.

$$C_{nratio} = \frac{C_{tissue}}{C_{peg}} \quad \text{Equation 27}$$
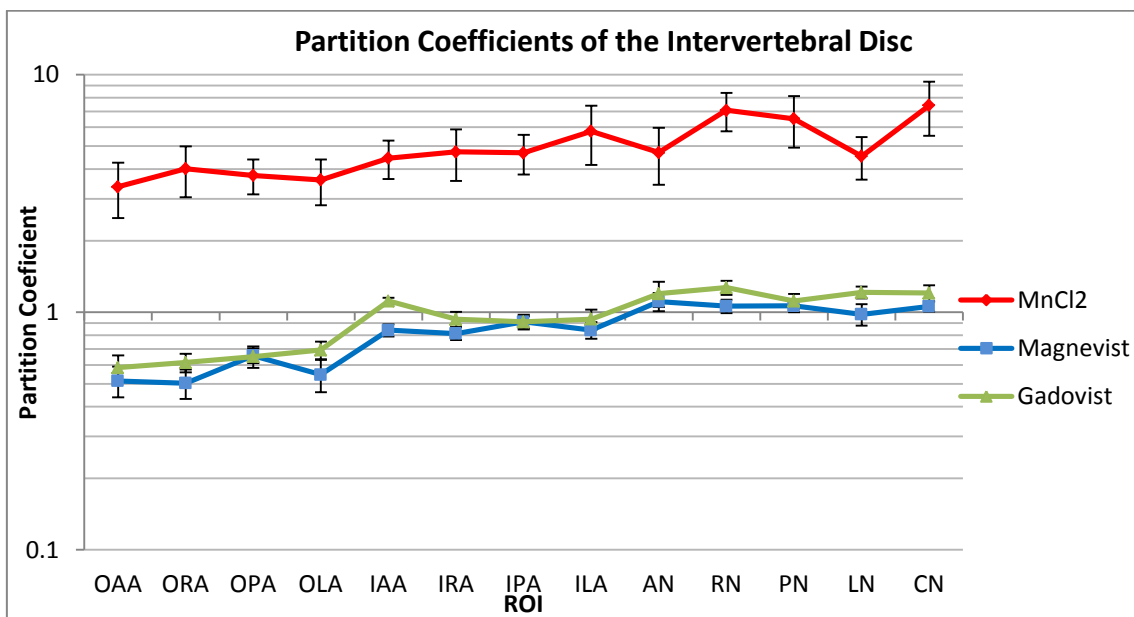
Figure 139: The partition coefficients, (the fractional concentration of contrast agent in the tissue compared to the initial concentration in the bathing solution), in the 13 ROIs. The regions are orientated starting at the Outer Anterior Annulus and rotating in a clockwise direction finishing at the Central Nucleus. A logarithmic scale is used to enable the Magnevist and Gadovist to be clearly distinguished. The error bars are the standard error. It can be seen that manganese has a distribution where its partiotion coefficient is above 7 in the central nucleus. Magnevist and Gadovist have similar partition coefficients which are close to unity or below.

Figure 139 illustrates the partition coefficients for the 3 contrast agent tracers. Gadovist and Magnevist for all regions have partition coefficients which are less than or close to 1. Once normalised there is very little difference in the partition coefficient of Magnevist and Gadovist within similar regions. The outer annular regions have the lowest partition coefficients at approximately 0.5. The manganese chloride has a partition coefficient which is much greater than 1; this is consistent with the expected electrostatic interaction with the negatively charged proteoglycans particularly in the nucleus.

The diffusion coefficient, α, can be determined using Equation 10. This quite clearly illustrates that Gadovist is transported more effectively. We have already discussed the impact on charged solutes by the fixed charge density of the matrix; from this data we may conclude that the size and shape of small to medium sized ions and molecules (in comparison to proteins) has less of an impact on transport than charge.
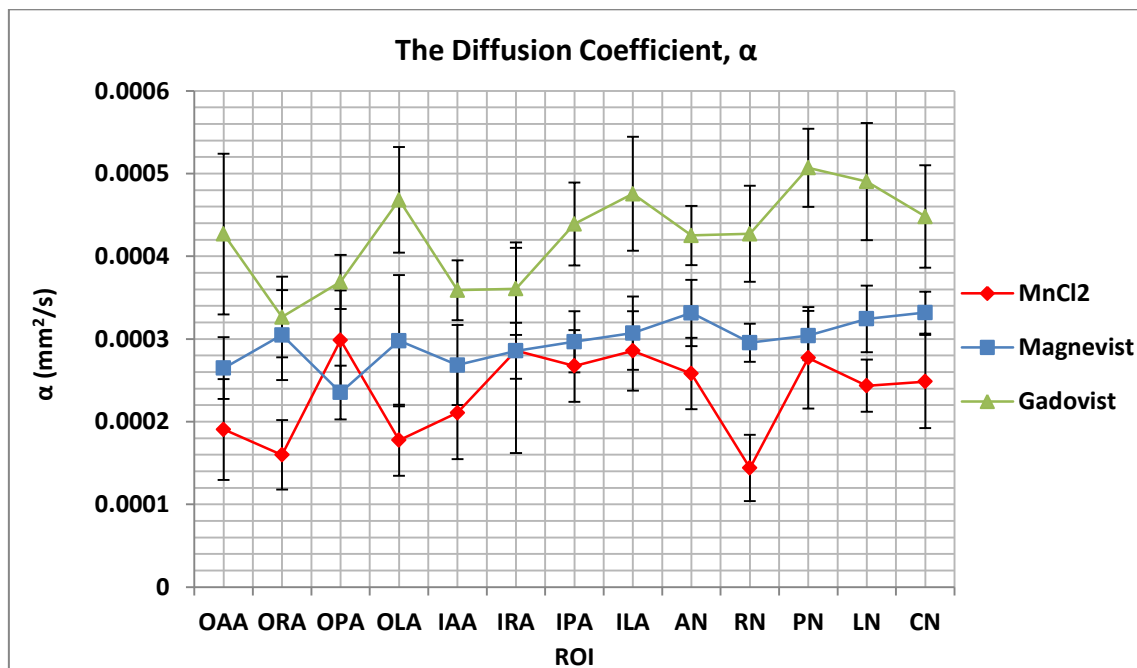
Figure 140**: The diffusion coefficient for the 13 ROIs. The regions are arranged in a clockwise spiral starting at the outer anterior annulus. The error bars are the standard error. It can be seen due to the long time constant already established for manganese chloride its diffusion rate is very slow.**

An Analysis of Variance (ANOVA) test was performed on the normalised time constant, τ data to determine if the differences demonstrated in Figure 138 were statistically significant. An alpha value of 0.05 was used to determine significance. A p-value of 0.013 (to 3 s.f.) was calculated. This indicates a statistical difference between groups not explained by a Type 1 or sampling error. The F-statistic gave a value of 5.47 (to 3 s.f.), with an F-critical value of 3.49 (to 3 s.f.). Thus, the differences in time constant are significant.

The three 'right' regions in Figure 138 show lower time constants for Magnevist and higher time constants for Gadovist. However, a comparison over all thirteen regions shows no evidence of a negative correlation overall- the effect in 'right' regions is therefore likely to be from chance.

An ANOVA test was also performed on the partition coefficient; the data illustrated in Figure 139. An alpha value of 0.05 was used to determine significance. A p-value of 6.66×10^{-06} was calculated. This p-value is considerably smaller than the alpha value illustrating a significant difference between the 3 contrast agents. The F-statistic gave a value of 22.9 (to 3 s.f.), with an F-critical value of 3.49 (to 3 s.f.). Figure 139 shows that manganese chloride is very different to Magnevist and Gadovist. ANOVAs cannot tell us where the actual difference is, therefore, it may simply be due to the manganese chloride.

To determine if there is a statistical difference between the time constants and partition coefficients of Magnevist and Gadovist, a two-sample t-test assuming unequal variances was undertaken between pairings of these contrast agents to determine where differences occurred.

Considering the time constant first. A t-test performed between manganese and Magnevist gave a p-value of 0.130 (to 3 s.f.). The t-statistic has a value of 1.71 (to 3 s.f.), with an t-critical value of 2.36 (to 3 s.f.); the smaller t-statistic (than the t-critical value) means that, statistically they have no significant difference. A t-test performed between manganese and Gadovist gave a p-value of 0.03 (to 3 s.f.). The t-statistic has a value of 2.65 (to 3 s.f.), with a t-critical value of 2.36 (to 3 s.f.). Statistically, there is a difference in the time constants of these two contrast agents. A t-test performed between Magnevist and Gadovist gave a p-value of 0.05 (to 3 s.f.). The t-statistic has a value of 2.16 (to 3 s.f.), with a t-critical value of 2.16 (to 3 s. F.). Statistically, there is no difference in the time constants of these two contrast agents.

Consider next the partition coefficient. A t-test performed between manganese and Magnevist gave a p-value of 0.004 (to 3 s.f.). The t-statistic has a value of 4.52 (to 3 s.f.), with a t-critical value of 2.45 (to 3 s.f.). This shows there is a statistical difference between these two contrast agents. A t-test performed between manganese and Gadovist gave a p-value of 0.07 (to 3 s.f.). The t-statistic has a value of 4.39 (to 3 s.f.), with a t-critical value of 2.45 (to 3 s.f.). This shows there is a statistical difference between these two contrast agents. A t-test performed between Gadovist and Magnevist gave a p-value of 0.070 (to 3 s.f.). The t-statistic has a value of -1.96 (to 3 s.f.), with a t-critical value of 2.14 (to 3 s.f.). There is shown to be no statistical difference between these two contrast agents.

The relationship between the normalised time constant τ and the partition coefficients with the age of the horses was investigated for all 3 of the contrast agents.
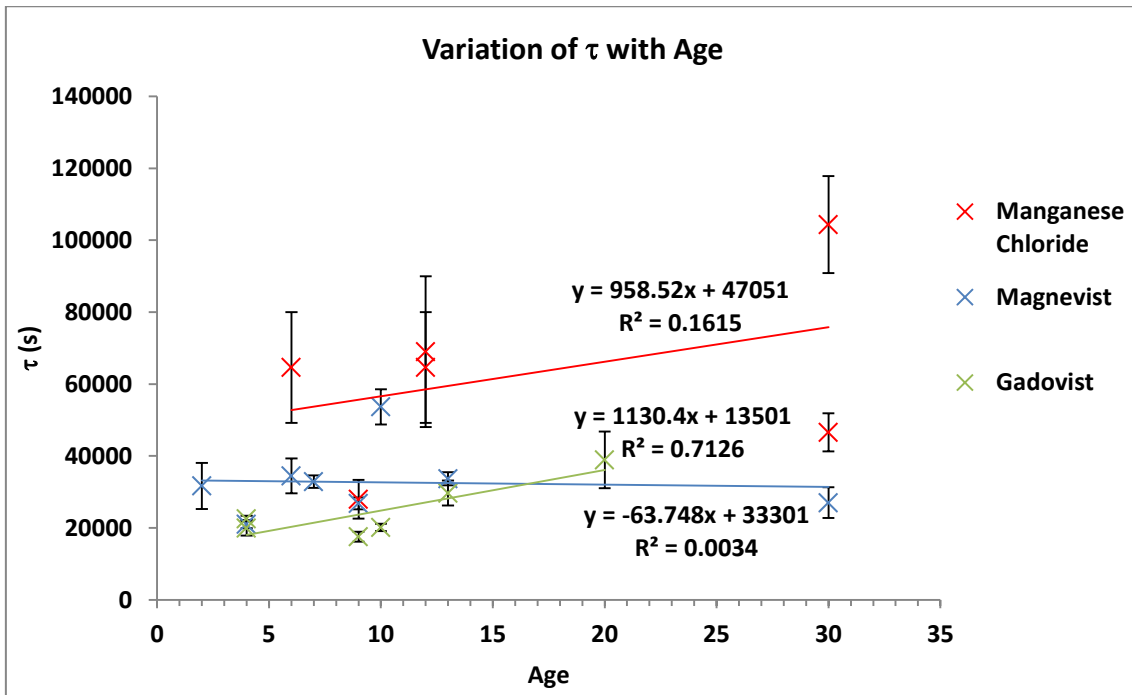
Figure 141: An illustration of how τ changes as a result of the age of the sample. Where multiple discs have been used within the same sample for the same contrast agent the value of τ is averaged to minimise the effect of a deviant sample. The error bars are the standard error.

Figure 141 above visually shows that there appears to be no relationship between the time constant, τ and the age of the sample for manganese chloride and Magnevist. However, Gadovist does show a positive correlation between τ and the age of the sample, the R^2 value of the trendline is 0.7126. This was further investigated by using the CORREL function in Excel to calculate a correlation coefficient; this function is the same as Pearson's correlation coefficient. The correlation coefficients are: manganese chloride 0.402, Magnevist -0.058 and Gadovist 0.844. The correlation coefficients reinforce Figure 141, confirming the link between the time constant for Gadovist and the age of the samples used. The correlation coefficient does show a weak correlation between the time constant for manganese chloride and the age of the sample. The positive nature of the correlation coefficients for manganese

chloride and Gadovist shows that as the age of the sample increases the contrast agent takes longer to diffuse into the tissue regions.

The time constant, τ of the annulus and nucleus of the samples was investigated and shown below in Figure 142.
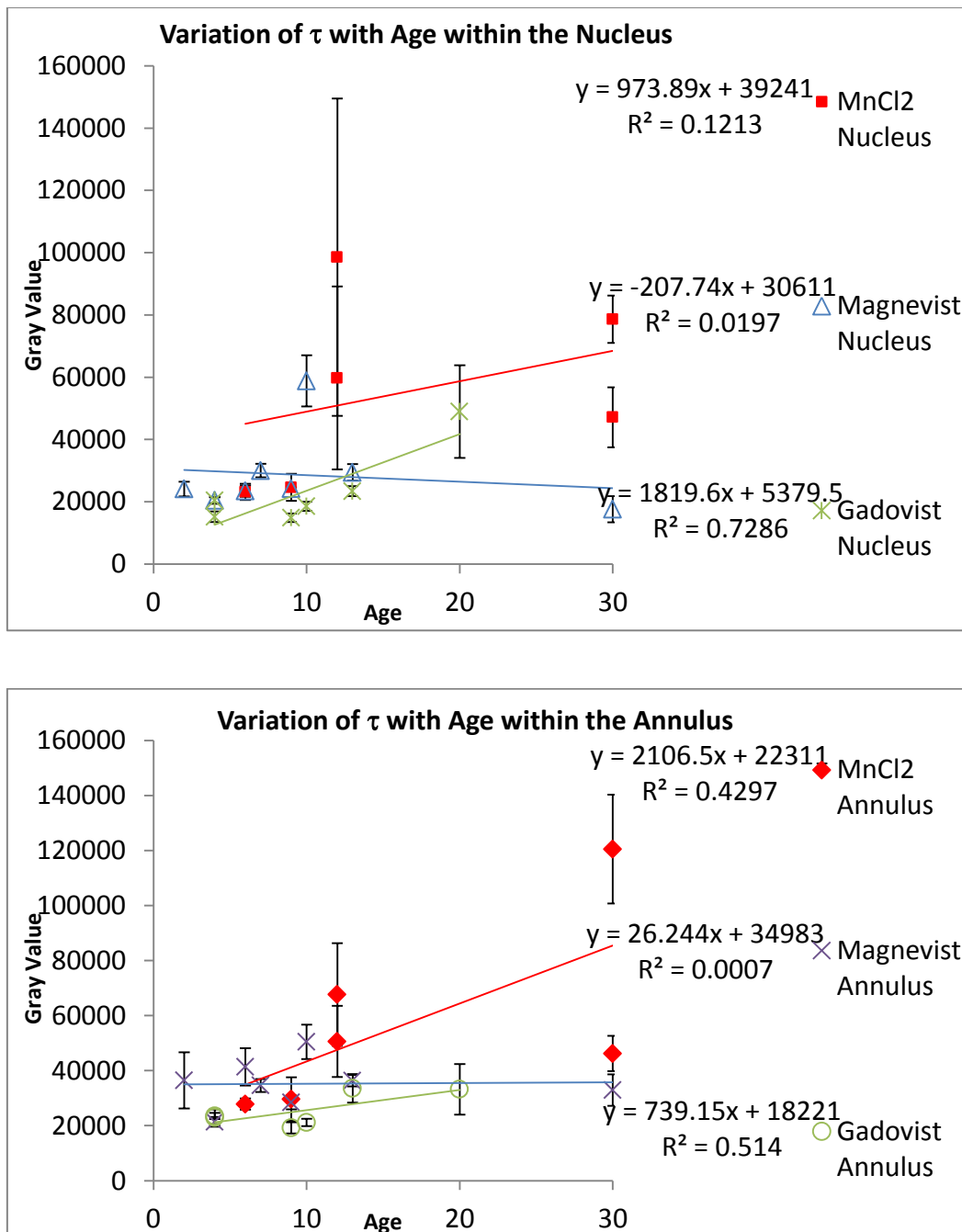
Figure 142: Variation of the time constant of the annulus and nucleus for the three contrast agents. The error bars are the standard error. In the nuclear area, Gadovist has a strong positive correlation with age. There appears to be no correlation between manganese and Magnevist for the nucleus area. In the annular area, Gadovist and manganese have a positive correlation with age.

243

Figure 142 shows that the rate of transport of Gadovist decreases particularly in the nucleus as the age of the disc increases. Manganese chloride shows a weak correlation particularly with the disc annulus. Magnevist shows no correlation between age and transport. Using EXCEL correlation coefficients were obtained: manganese chloride had a correlation of 0.34 with the nucleus and 0.66 with the annulus, Magnevist has a correlation of -0.14 with the nucleus and 0.03 with the annulus, and Gadovist has a correlation of 0.85 with the nucleus and 0.72 with the annulus.

The same process was undertaken to investigate the partition coefficient and its relationship with the age of the sample.
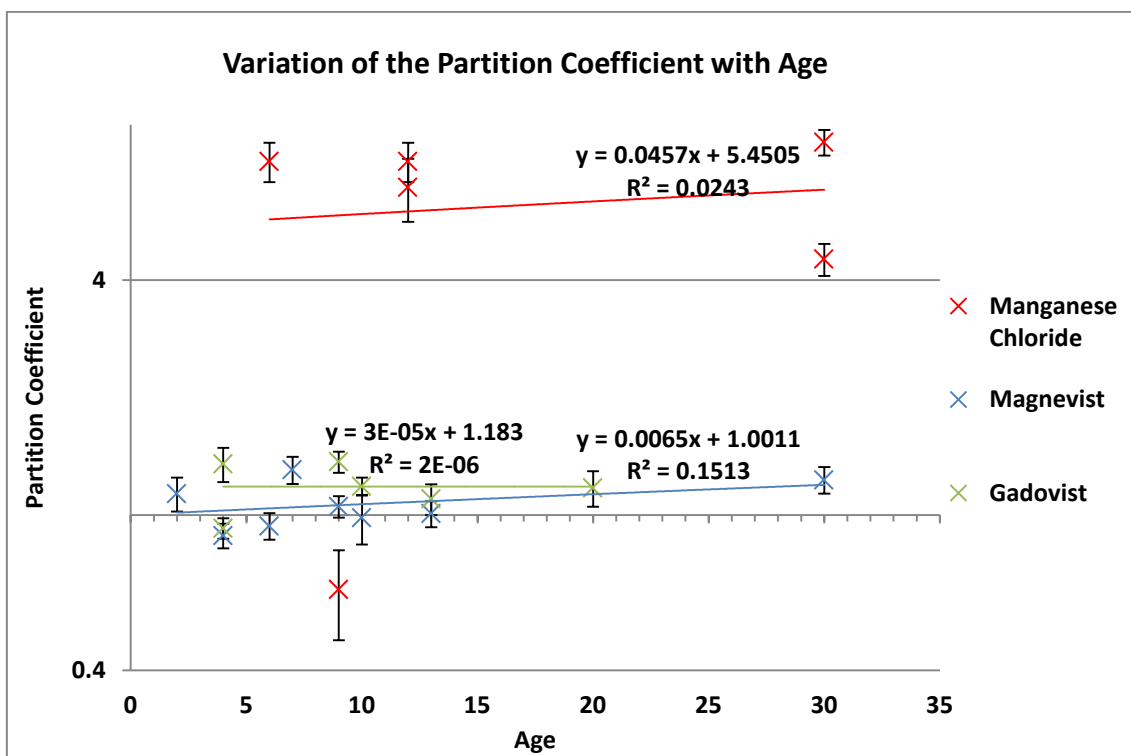
Figure 143: Correlation between partition coefficient and age. Where multiple discs have been used from the same sample for the same contrast agent, these values have been averaged to minimise the effects of a deviant sample. The error bars are the standard error. There does not seem to be any correlation between partition coefficient and age.

Figure 143 shows that there appears to be no correlation between partition coefficient and age. This was confirmed by the calculation of correlation coefficients: manganese chloride 0.156, Magnevist 0.389 and Gadovist 0.001; only for Magnevist is this weakly significant.

To extend the investigation of the partition coefficient, the samples were split into their constituent nucleus and annulus, shown below in Figure 144.
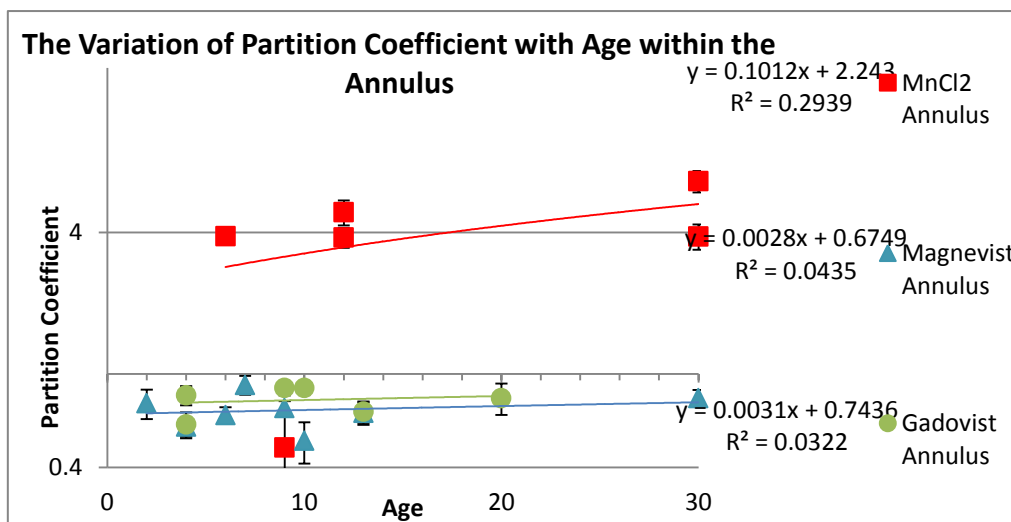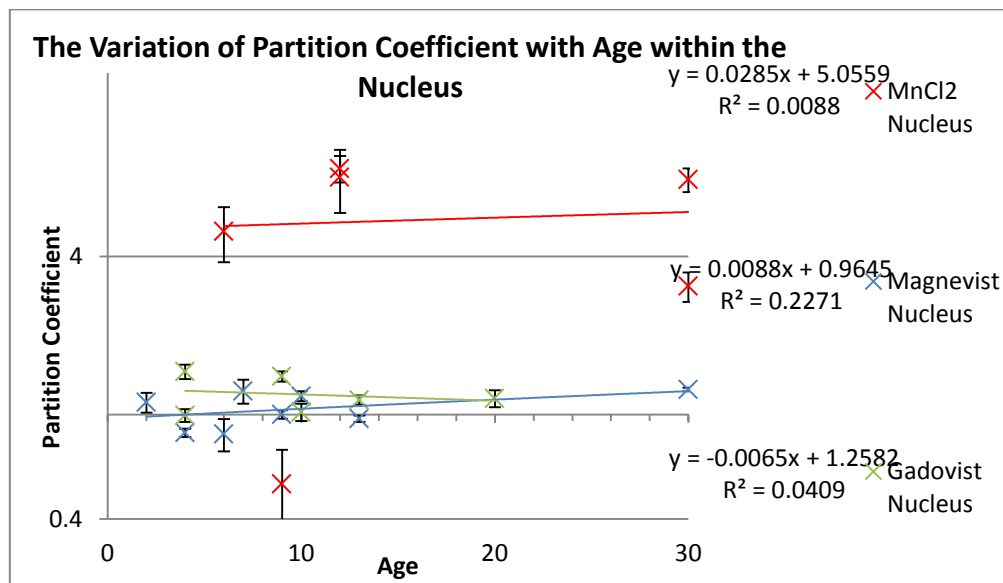
Figure 144: The relationship of the transport of the 3 tracers in the annulus and nucleus with the age of the sample. The error bars are the standard error. There is only a limited correlation between Magnevist and age in the nuclear area. There is no correlation between manganese and Gadovist and age in the nuclear area. There is only a limited correlation between manganese and age in the annular area. There is no correlation between Magnevist and Gadovist.

Correlation coefficients were determined for the annulus and nucleus and age for the 3 tracers: manganese chloride has correlation coefficients of -0.12 for the nucleus and 0.43 for the annulus, Magnevist has correlation coefficients of o.48 for the nucleus and 0.14 for the annulus, Gadovist has correlation coefficients of -0.2 for the nucleus and 0.18 for the annulus. Separating the samples into annulus and nucleus shows a stronger correlation for manganese chloride and the annulus and Magnevist shows a stronger correlation between age of the sample and its transport in the nucleus.

4.5 Discussion

The distribution of a charged ion such as $MnCl_2$ within the disc is governed by the Gibbs-Donnan relationship introduced in Chapter 1. Due to the density of fixed charges in the disc an electric potential arising between the contrast/PEG solution and the disc is called the 'Donnan Potential'.

Consider first the $MnCl_2$ contrast agent. This is a salt which dissociates in solution to form two ions, Cl_2^- and Mn^{2+}. The Cl_2^- is excluded from the tissue but the manganese ion is attracted into the tissue.

The MR signal is sensitive to the presence of Mn^{2+} ions; where more of them accumulate the brighter a T_1 weighted image will be due to the shortening of the longitudinal relaxation time. The areas of the disc which have greater concentrations of proteoglycans, that is, the nucleus will attract more Mn^{2+} ions resulting in this area being brighter. In fact, the results indicate that in all areas there is greater concentration of Mn^{2+}, but this is particularly true of the central nucleus which has almost 6 times the concentration when compared to the contrast solution.

The same explanation can be used to describe the amounts of Magnevist and Gadovist within the tissue. For both these contrast agents more remains in the contrast solution than diffuses into the tissue. Magnevist dissociates into an ion with a 2- charge and its behaviour is the reverse of the manganese ion. Gadovist is a neutral molecule unaffected in terms of charge by the negatively charged proteoglycans; however, Figure 139 shows little difference in partition coefficient between Gadovist and Magnevist. This may be because charge related effects are counteracted by the effects of molecular size and structure. It has been shown that charge and solubility consistently correlate with concentration, (Bar-Even, et al., 2011).Due to the pore pressure provided by the proteoglycans, size and shape of the molecule affect its transport. Gadovist is larger than manganese chloride and Magnevist and it has a ring structure. It showed the lowest partition coefficient in most regions compared to manganese chloride and Magnevist. The variation in time constant, τ with contrast agent is more difficult to explain. τ is a measure of the diffusivity of the solute. Manganese has the longer time constant for all regions, even though it is likely to be attracted to the negative charge of the disc tissue. This may be due to its high mobility being quite small; the time taken for equilibrium is increased as the Mn^{2+} ion interacts with every proteoglycan molecule it comes into contact with. Gadovist has the shortest time constant. Although it is a medium sized molecule, it is ring shaped and neutral, both will reduce its mobility. In fact, if the statistical tests are considered there is only a difference between manganese and Gadovist in terms of the time constant; this gives some indication that molecular size/shape affects transport more than electrostatic charge. This has interesting implications for the transport of metabolites with those metabolites which are charged taking longer to diffuse within the disc tissue; important ions

247

such as nicotinamide adenine dinucleotide, carrying a single positive charge. Another important application is potential drug delivery; although neutral drug transporters may transport more quickly, their final concentration will be lower when compared to a positive transporter.

It has been found to take more than 18 hours to achieve equilibrium for these small molecules, so a drug or contrast agent would need to be kept at a uniform concentration in the blood for this time to determine partition coefficients and to successfully deliver antibiotics and drugs in sufficient quantities. While in vivo, the presence of the endplate may slow transport down, cyclic loading may speed it up. It may be possible to use tracers such as manganese to measure fixed charge density proteoglycan concentration in vivo; a divalent cation would be more sensitive compared to sodium imaging.

The long time constants observed can be expressed in terms of apparent diffusion coefficients of around 3×10^{-4} mm^2 s^{-1}. In the range of values reported for tissues such as cartilage, (Antoniou, 2004).

In chapter 1 it has been discussed how age may affect matrix synthesis and ultimately proteoglycan concentration. These present results show that the time constant for Gadovist was strongly influenced by the age of the sample and the time constant for manganese chloride weakly influenced by age. This may be due to the diminished proteoglycan content for two different reasons. Less proteoglycans within the tissue reduces the electric potential between the tissue and contrast solution reducing the attraction of the manganese ion. Less proteoglycans also lead to a reduction in pore pressure within the tissue which may inhibit the movement of the hydrophilic manganese, but enable Gadovist to move more freely resulting in equilibrium taking longer. It is surprising that this

does not appear to equally affect Magnevist; Magnevist is larger than manganese, however it is also hydrophilic, lack of proteoglycans will reduce hydration meaning Magnevist does not have increased transport.

The concentration of manganese and Magnevist is shown to weakly correlate with age. This is likely to be matrix related as the concentration of Gadovist seems unaffected. As previously described solubility and charge correlates strongly with concentration. A decrease in proteoglycan within the matrix also leads to decreased water content, therefore the soluble properties of Manganese and Magnevist may influence their asymptotic concentration, although it is surprising that their concentration both increase.

5 Discussion

5.1 Introduction

In this thesis I have investigated the anatomy of the equine intervertebral disc on a macroscopic and microscopic level. The surrounding vasculature and patterns of diffusion within the intervertebral disc have also been studied. As a conclusion to this thesis, it is important to link the anatomy and patterns of diffusion and this is done in the following section to. In this chapter I will discuss limitations which have impacted on the experimental work within this thesis. Finally I will then discuss how this work may be taken forward in the future.

5.2 Overview

The predominant vessel supplying nutrition to the equine tail is the median caudal artery positioned on the anterior aspect of the vertebral bodies. The diameter of this vessel is between 5 and 6 mm. In humans there is a similar vascular construction with the aorta in the lumbar spine branching into a pair of arteries in the front of each of the vertebrae (Ratcliffe, 1980).. In humans the aorta is larger than the median caudal artery. The normal diameter of the abdominal aorta is regarded to be less than 3 cm; this normal range is adjusted for age, sex and physical activity (Erbel & Eggebrecht, 2006). In the human lumbar region there are 1 or 2 anterior radicular arteries; these have a diameter of 0.2 mm to 0.8 mm. One in particular, the anterior radicularis magna is 1 to 1.3 mm and supplies the lumbar cord enlargement (Mai & Paxinos, 2012).In the particular samples studied in this thesis, (the barium sulphate and barium sulphate/Evans blue perfused samples), the radicular artery was seen to be comparable to the human radicular artery at 0.24 mm. In humans, the

basivertebral vein extends through openings in the sides and front of the vertebral bodies joining with the anterior external vertebral plexus. The equine tail sample distinctly shows the basivertebral vein exiting the core of the vertebral body and joining the tortuous venous plexus. There is evidence of a vascular network in the horse which joins adjacent vertebral bodies together externally; these branches come from the equatorial sub-radicular artery. This is a similar vascular construction to that seen in the human spine (Ratcliffe, 1980). The experiments performed with barium sulphate have indicated a large network of periosteal arteries anatomising over the surface of the vertebral bodies penetrating the vertebral bodies via small channels. Human periosteal arteries similarly supply nutrients via Volkmann's canals (Tortora & Grabowski, 2003).

The vascular supply to the equine intervertebral disc itself has been shown in this thesis to be via two routes; small vessels which penetrate a short way into the outer annulus and vessels in the vertebral endplate. The disc itself is largely avascular with the vessels which penetrate the outer annulus itself doing so by 1 to 2 mm. There is consensus in the literature that in humans, vessel ingrowth in normal individuals is confined to the outer annulus, although the extent is not clear, (Nerlich, et al., 2007). The most likely nutritional route for the nucleus of the disc is via the vertebral endplate. This is evident in the structure of the vessel terminations which have been highlighted in this thesis. The vessels terminate at the level of the cartilage endplate; they do penetrate the subchondral area of the vertebral body. There is a distinct variability of these vessels along the endplate. At the area of the endplate adjacent to the nucleus the density of terminations is larger and distinctly spherical. These discoid vessels then branch into a series of tiny vessels which go to the edge, but do

not penetrate, the cartilage endplate. At the area next to the annulus and in particular the outer annulus there is an absence of large spherical terminations; the vessels terminated in smaller buds. There are also none of the tiny vessels alongside the cartilage endplate. The thickness of the endplate itself is variable along its length from 0.16 mm to 0.33 mm; the widest part was adjacent to the nucleus pulposus. In humans by adulthood, the endplate is less than 1 mm thick (Urban & Winlove, 2007). This variability in vessels at the endplate has been seen in other species, such as canine and importantly humans. The density of capillary terminations in humans was also seen to be greatest adjacent to the nucleus. Endplate cartilage damage has been seen to cause changes in diffusion (Rajasekaran, 2004).

Physiologically the structure of these vascular routes is important in facilitating the movement of nutritional solutes into the disc and the removal of metabolites. Cells within the nucleus in humans can find themselves up to 8 mm from the nearest vessel (Ferguson, et al., 2004).The equine disc, although smaller, still has to maintain a viable nutritional route. The greater density of capillary terminations adjacent to the nucleus will aid diffusion into the very centre of the disc. This route will bypass the annulus, whose small pore structure stearically excludes the larger molecules. The fixed charge density of the nucleus and annulus is different; the nucleus has a high negative fixed charge density due to the highly sulphated proteoglycans. This will influence the diffusion and distribution of various charged solutes.

The equine intervertebral disc is a good model for the human disc. Its structure is similar; consisting of a nucleus and annulus. The equine disc, although smaller than the human lumbar disc will still enable a scaling of data collected

for comparison. Similarly to the human disc, the annulus is highly ordered with bundles of collagen fibres arranged at angles of approximately 45° to the vertebral body (Urban, 1990). An important difference between the species is the width of the lamellae and their number. Equines have thicker and fewer lamellae. Physiologically, the lamellae help the nucleus retain its shape and spread load across the disc. It is not clear that having fewer but thicker lamellae would hinder this important role; the movement required in the tail is different to that in the lumbar region of the spine. In the equine species, the range of lamellar width is greater when compared with humans. Values of lamellar width were similar when calculated from histological samples or MRI images. In humans lamellar width are seen to be between 200 and 400 microns (Takeda, 1975), whereas the equine lamellae are between 140 and 1110 microns. Anteriorly there were often 1 or 2 more lamellae than posteriorly; therefore, there is evidence that the lamellae are not continuous. Physiologically this may be due to the requirements of motion of the tail.

The shape and size of the equine caudal intervertebral disc when compared to the human lumbar disc is quite different. Human discs are distinctly 'kidney' shape whilst the equine disc is slightly oval. Both discs have a longer axis; in the humans it is the lateral axis, however, equines appear to show no preference in the orientation of the long axis, either laterally or anteroposteriorly. Crucially, the intervertebral discs in both species mimic the shape of the flat surface of the vertebral bodies to which the discs are attached. The caudal vertebral bodies are rod shaped. The thickness of the intervertebral disc and overall dimensions are different between horse and human; the human lumbar disc is 40 mm in diameter anteroposteriorly and 7 to 10 mm thick, the equine disc is between 10 and 21 mm anteroposteriorly and has a variable thickness

due to its concave surfaces between 1.35 and 3.83 mm at its minimum, and between 4.47 and 11.8 mm at its edges.

Histological samples illustrated that the equine disc contained a great deal of collagen, even in its nucleus, although the collagen fibres were finer in the nucleus than the annulus. The lamellae appeared as distinct rings separated by thinner rings containing elastin. Within the rings themselves, the collagen fibres appeared well ordered providing a structural mesh. This is much the same as the described microscopy of the human disc (Happey, 1980). The nucleus of the equine disc also contains a great deal of collagen. Contrary to current literature the finer collagen fibres of the nucleus did appear to have some local order when viewed under polarised light.

The three contrast agents chosen for the purposes of studying diffusion were complementary as they were different in size and charge structure. Diffusion occurred in the cell employed in these investigations in the same direction as diffusion would occur in vivo from the vertebral endplate. Time constants for the regions were longer than current literature suggests. The longest time constant experienced was for the positively charged solute manganese in the region of the outer anterior annulus of the order of 22 hours. The shortest time constant experienced was 5 ½ hours in the central nucleus region for the neutral molecule Gadovist. Overall, the neutral molecule attained equilibrium faster for all regions when compared to the positive ion; the negative ion (Magnevist) was between the two. This may suggest that molecular size and shape is more important than electrostatic charge in determining solute transport. The 13 regions do show variation as discussed in chapter 1 which supports the literature (Leddy, et al., 2006). This has serious implications for clinical MR

imaging when using contrast; the type of contrast used will affect how long equilibrium between the subject's disc and surroundings will need to be maintained. This will have implications for accurately detecting pathologies and degeneration. An important consideration is using certain molecules and ions as carriers for drug delivery; the time constant data has shown wide variations in the time for this to occur which may affect the success of the treatment. The ability for a drug to successfully reach its destination depending on its charge needs also to be considered. These considerations are also relevant to problems such as antibiotic delivery before/during or after surgery.

Values obtained for the partition coefficient of the tracers used have given insight into the balance of nutrients within the disc environment. The partition coefficient of the positive ion was greatest in the negatively charged nucleus with a value of almost 6. The negative ion produced the lowest partition coefficients at little over 0.5 in three regions including the central nucleus. In the previous paragraph the long time constant of the positive ion was noted, however, its advantage is that at equilibrium much of the ion distributes itself within the disc. This again will be an important consideration when delivering drugs or using chemical carriers.

The final property investigated was the diffusion coefficient. Overall the neutral molecule had the highest diffusion coefficient and the positive ion the lowest. There are two peaks in the diffusion coefficient of the positive ion, both on the left side of the nucleus. Physiologically, it was noted on the MRA images that the vertebral bodies appeared well perfused laterally which may account for these peaks.

The longer time constant and diffusion coefficient of the positive ion may be due to increased electrostatic interactions between the ion and the proteoglycans.

It has been noted in the literature that age related degeneration may cause matrix related changes; for example, a change in proteoglycan synthesis (Patel, 2005). The positive ion and neutral molecule take longer to diffuse as age increases. It is unclear why the neutral molecule shows a relationship, however, it may be a change in hydration which affects convection within the disc. Manganese is hydrophilic; lack of proteoglycans may reduce water content in the disc and hence movement of manganese.

The concentration of the negative ion, Magnevist, increases with age. This again may be related to a change in matrix composition; less proteoglycans present will reduce the negative fixed charge density within the nucleus allowing more Magnevist to be present.

5.3 Limitations

The anatomy studies are based 3 samples imaged with x-ray, 2 samples imaged with contrast enhanced MRI and 20 samples imaged with MRI. The diffusion studies are based on 23 samples. This sample number may have an impact when drawing conclusions about age related changes, as some samples have more than one disc used reducing the data available. However, considering the curve fits, which are good, suggests the samples are not atypical. The ANOVA and t-tests show clear differences between the contrast agents which would be unlikely to be seen if samples were not displaying their true properties. However, the behaviours of Gadovist and Magnevist are similar suggesting that charge related effects are counteracted by the effects of molecular size and structure. It would be an improvement to use a wider range

of T_1 contrast agents, for example, including Vasovist (Gadofosveset trisodium) and Gadoteridol. Vasovist has a 3- charge, and is a ring structure with a molecular mass of 975.88 g/mol. Gadoteridol is a neutral ring structure with a molecular mass of 558.68 g/mol. This might allow the effects of charge, molecular size and molecular structure to be separated out.

In vivo diffusion occurs via two routes, the annulus and the vertebral endplate. In the experiment using the diffusion cell there is no endplate present. The endplate may cause some natural delay, however, once the solute has passed this point transport through the disc should be similar. In the present experiment the disc was unloaded and there was no natural movement, which would normally cause water to be moved in and out of the disc and this may affect the transport of some solutes. It would be straightforward to adapt either the diffusion cell or the perfused tail to subject the disc to time varying loads to test this possibility.

The experimental set-up requires the contrast solution to be syringed into each half of the dialysis cell separately. This results in one half being filled sooner than the other. It has been shown in diffusion theory that initially there is a lag. Also, the time constant and concentration are based on equilibrium values which will mean the time delay should not affect the final results.

An overall limitation was the lack of available data about breed of the various horses, and other aspects of their life histories. This should be remedied if possible in future work. Similarly, individual discs are categorised by age in the diffusion studies (chapter 4)-it would be an improvement to also categorise by degeneration states. (perhaps using a wider range of anatomical MR scans; this was not possible in the present study due to lack of time.)

5.4 Further Work

The work presented in this thesis has investigated in detail three important parameters (time constant, concentration and diffusion coefficient) for three tracers in the nucleus and annulus. There have been some previous studies but this work has looked at 13 regions in a detailed manner in a species which has not been studied at this level previously. Diffusion has been tracked over an extended period of time until equilibrium has been reached which is novel. To consolidate the data presented it is important to relate the time-intensity curves to matrix composition. For each sample investigated, detailed histology and matrix analysis should in future accompany the time-intensity curves. This will enable relationships and conclusions to be drawn about the effect of the matrix on diffusion of solutes of varying molecular weight and electrostatic charge.

The next stage of this process will be to link intensity (gray value) with a level of hydration or degeneration. This will enable a standard conversion chart to be produced that will enable the level of matrix degeneration to be determined non-invasively with MRI. The sequences used would need to be adapted to typical clinical sequences.

These methods could then be introduced into the clinical environment. Initially this will have to accompany standard surgical procedures and treatments. The development of a scan protocol which could be undertaken during normal patient scanning and comparison of intensity with the observed condition of the disc will eventually enable hydration to be directly determined from these intensity curves influencing patient treatment without unnecessary invasive surgery being undertaken.

Appendix 1

```
===              DATA          DESCRIPTION              FILE

========================================================

#

# CAUTION - Investigational device.

# Limited by Federal Law to investigational use.

#

# Dataset name: H:\S3G\PH_05_sample_3G_anatomy_CLEAR_5_1

#

# CLINICAL TRYOUT          Research image export tool     V4.2

#

#              ===              GENERAL              INFORMATION

========================================================

#

.    Patient name              :  PH_05_sample_3G

.    Examination name              :   none

.    Protocol name              :   anatomy CLEAR

.    Examination date/time              :   2009.07.08 / 13:22:45

.    Series Type              :  Image   MRSERIES

.    Acquisition nr              :  5
```

. Reconstruction nr : 1

. Scan Duration [sec] : 1.54e+003

. Max. number of cardiac phases : 1

. Max. number of echoes : 1

. Max. number of slices/locations : 20

. Max. number of dynamics : 1

. Max. number of mixes : 1

. Patient position : Head First Supine

. Preparation direction : Right-Left

. Technique : FFE

. Scan resolution (x, y) : 576 576

. Scan mode : 3D

. Repetition time [ms] : 33.000

. FOV (ap,fh,rl) [mm] : 60.000 20.000 60.000

. Water Fat shift [pixels] : 3.004

. Angulation midslice(ap,fh,rl)[degr]: 0.000 0.000 0.000

. Off Centre midslice(ap,fh,rl) [mm] : -95.403 9.429 36.429

. Flow compensation <0=no 1=yes> ? : 0

. Presaturation <0=no 1=yes> ? : 0

.   Phase encoding velocity [cm/sec]   :   0.000000 0.000000 0.000000

.   MTC   <0=no 1=yes> ?   :   0

.   SPIR   <0=no 1=yes> ?   :   0

.   EPI factor   <0,1=no EPI>   :   1

.   Dynamic scan   <0=no 1=yes> ?   :   0

.   Diffusion   <0=no 1=yes> ?   :   0

.   Diffusion echo time [ms]   :   0.0000

.   Max. number of diffusion values   :   1

.   Max. number of gradient orients   :   1

.   Number of label types   <0=no ASL> :   0

#

===   PIXEL   VALUES

==
=

PV = pixel value in REC file, FP = floating point value, DV = displayed value

on console

RS = rescale slope,   RI = rescale intercept,   SS = scale slope

DV = PV * RS + RI   FP = DV / (RS * SS)

#

=== IMAGE INFORMATION DEFINITION

===

The rest of this file contains ONE line per image, this line contains the following information:

#

slice number   (integer)

echo number   (integer)

dynamic scan number   (integer)

cardiac phase number   (integer)

image_type_mr   (integer)

scanning sequence   (integer)

index in REC file (in images)   (integer)

image pixel size (in bits)   (integer)

scan percentage   (integer)

recon resolution (x y)   (2*integer)

rescale intercept   (float)

rescale slope   (float)

scale slope   (float)

window center   (integer)

window width   (integer)

image angulation (ap,fh,rl in degrees) (3*float)

image offcentre (ap,fh,rl in mm)   (3*float)

slice thickness (in mm)   (float)

slice gap (in mm)   (float)

image_display_orientation   (integer)

slice orientation (TRA/SAG/COR)   (integer)

fmri_status_indication   (integer)

image_type_ed_es (end diast/end syst)   (integer)

pixel spacing (x,y) (in mm)   (2*float)

echo_time   (float)

dyn_scan_begin_time   (float)

trigger_time   (float)

diffusion_b_factor   (float)

number of averages   (integer)

image_flip_angle (in degrees)   (float)

cardiac frequency   (bpm)   (integer)

minimum RR-interval (in ms)   (integer)

maximum RR-interval (in ms)   (integer)

TURBO factor <0=no turbo>   (integer)

Inversion delay (in ms)   (float)

diffusion b value number   (imagekey!) (integer)

gradient orientation number (imagekey!) (integer)

contrast type   (string)

diffusion anisotropy type   (string)

diffusion (ap, fh, rl)   (3*float)

label type (ASL)   (imagekey!) (integer)

#

===   IMAGE   INFORMATION

===

sl ec dyn ph ty   idx pix scan% rec size   (re)scale   window
angulation   offcentre   thick gap info   spacing   echo   dtime
ttime   diff avg flip   freq   RR-int turbo delay b grad cont anis   diffusion
L.ty

 1 1   1 1 0 2   0 16   78 576 576   0.00000 30.34603 5.17723e-004
994 1728 0.00   0.00   0.00 -95.40   -0.07   36.43 1.000 0.000 0 1 0 2 0.104
0.104 11.00   0.00   0.00   0.00 4 30.00   0   0   0   1 0.0 1 1   7   0
0.000   0.000   0.000 1

 2 1   1 1 0 2   1 16   78 576 576   0.00000 30.34603 5.17723e-004
1021 1776 0.00   0.00   0.00 -95.40   0.93   36.43 1.000 0.000 0 1 0 2

0.104 0.104 11.00   0.00   0.00   0.00   4 30.00   0   0   0   1 0.0 1 1

7   0 0.000   0.000   0.000 1

 3 1   1 1 0 2   2 16   78 576 576   0.00000 30.34603 5.17723e-004

1080 1877 0.00   0.00   0.00 -95.40   1.93   36.43 1.000 0.000 0 1 0 2

0.104 0.104 11.00   0.00   0.00   0.00   4 30.00   0   0   0   1 0.0 1 1

7   0 0.000   0.000   0.000 1

 4 1   1 1 0 2   3 16   78 576 576   0.00000 30.34603 5.17723e-004

1093 1899 0.00   0.00   0.00 -95.40   2.93   36.43 1.000 0.000 0 1 0 2

0.104 0.104 11.00   0.00   0.00   0.00   4 30.00   0   0   0   1 0.0 1 1

7   0 0.000   0.000   0.000 1

 5 1   1 1 0 2   4 16   78 576 576   0.00000 30.34603 5.17723e-004

1081 1879 0.00   0.00   0.00 -95.40   3.93   36.43 1.000 0.000 0 1 0 2

0.104 0.104 11.00   0.00   0.00   0.00   4 30.00   0   0   0   1 0.0 1 1

7   0 0.000   0.000   0.000 1

 6 1   1 1 0 2   5 16   78 576 576   0.00000 30.34603 5.17723e-004

1075 1869 0.00   0.00   0.00 -95.40   4.93   36.43 1.000 0.000 0 1 0 2

0.104 0.104 11.00   0.00   0.00   0.00   4 30.00   0   0   0   1 0.0 1 1

7   0 0.000   0.000   0.000 1

 7 1   1 1 0 2   6 16   78 576 576   0.00000 30.34603 5.17723e-004

1071 1862 0.00   0.00   0.00 -95.40   5.93   36.43 1.000 0.000 0 1 0 2

0.104 0.104 11.00   0.00   0.00   0.00   4 30.00   0   0   0   1 0.0 1 1

7   0 0.000   0.000   0.000 1

 8 1   1 1 0 2   7 16   78 576 576   0.00000 30.34603 5.17723e-004

1068 1856 0.00   0.00   0.00 -95.40   6.93   36.43 1.000 0.000 0 1 0 2

0.104 0.104 11.00   0.00   0.00   0.00   4 30.00   0   0   0   1 0.0 1 1

7   0 0.000   0.000   0.000 1

 9 1   1 1 0 2   8 16   78 576 576   0.00000 30.34603 5.17723e-004

1082 1881 0.00   0.00   0.00 -95.40   7.93   36.43 1.000 0.000 0 1 0 2

0.104 0.104 11.00   0.00   0.00   0.00   4 30.00   0   0   0   1 0.0 1 1

7   0 0.000   0.000   0.000 1

 10 1   1 1 0 2   9 16   78 576 576   0.00000 30.34603 5.17723e-004

1074 1867 0.00   0.00   0.00 -95.40   8.93   36.43 1.000 0.000 0 1 0 2

0.104 0.104 11.00   0.00   0.00   0.00   4 30.00   0   0   0   1 0.0 1 1

7   0 0.000   0.000   0.000 1

 11 1   1 1 0 2   10 16   78 576 576   0.00000 30.34603 5.17723e-004

1070 1860 0.00   0.00   0.00 -95.40   9.93   36.43 1.000 0.000 0 1 0 2

0.104 0.104 11.00   0.00   0.00   0.00   4 30.00   0   0   0   1 0.0 1 1

7   0 0.000   0.000   0.000 1

 12 1   1 1 0 2   11 16   78 576 576   0.00000 30.34603 5.17723e-004

1067 1855 0.00   0.00   0.00 -95.40   10.93   36.43 1.000 0.000 0 1 0 2

0.104 0.104 11.00   0.00   0.00   0.00   4 30.00   0   0   0   1 0.0 1 1

7   0 0.000   0.000   0.000 1

 13 1   1 1 0 2   12 16   78 576 576   0.00000 30.34603 5.17723e-004

1042 1812 0.00   0.00   0.00 -95.40   11.93   36.43 1.000 0.000 0 1 0 2

0.104 0.104 11.00   0.00   0.00   0.00   4 30.00   0   0   0   1 0.0 1 1

7   0 0.000   0.000   0.000 1

 14 1   1 1 0 2   13 16   78 576 576   0.00000 30.34603 5.17723e-004

1007 1751 0.00   0.00   0.00 -95.40   12.93   36.43 1.000 0.000 0 1 0 2

0.104 0.104 11.00   0.00   0.00   0.00 4 30.00   0   0   0   1 0.0 1 1

7   0 0.000   0.000   0.000 1

 15 1   1 1 0 2   14 16   78 576 576   0.00000 30.34603 5.17723e-004

970 1685 0.00 0.00 0.00 -95.40 13.93 36.43 1.000 0.000 0 1 0 2 0.104

0.104 11.00   0.00   0.00   0.00 4 30.00   0   0   0   1 0.0 1 1   7   0

0.000   0.000   0.000 1

 16 1   1 1 0 2   15 16   78 576 576   0.00000 30.34603 5.17723e-004

960 1669 0.00 0.00 0.00 -95.40 14.93 36.43 1.000 0.000 0 1 0 2 0.104

0.104 11.00   0.00   0.00   0.00 4 30.00   0   0   0   1 0.0 1 1   7   0

0.000   0.000   0.000 1

 17 1   1 1 0 2   16 16   78 576 576   0.00000 30.34603 5.17723e-004

952 1655 0.00 0.00 0.00 -95.40 15.93 36.43 1.000 0.000 0 1 0 2 0.104

0.104 11.00   0.00   0.00   0.00 4 30.00   0   0   0   1 0.0 1 1   7   0

0.000   0.000   0.000 1

 18 1   1 1 0 2   17 16   78 576 576   0.00000 30.34603 5.17723e-004

951 1652 0.00 0.00 0.00 -95.40 16.93 36.43 1.000 0.000 0 1 0 2 0.104

0.104 11.00   0.00   0.00   0.00 4 30.00   0   0   0   1 0.0 1 1   7   0

0.000   0.000   0.000 1

 19 1   1 1 0 2   18 16   78 576 576   0.00000 30.34603 5.17723e-004

966 1680 0.00 0.00 0.00 -95.40 17.93 36.43 1.000 0.000 0 1 0 2 0.104

0.104 11.00   0.00   0.00   0.00 4 30.00   0   0   0   1 0.0 1 1   7   0

0.000   0.000   0.000 1

 20 1   1 1 0 2   19 16   78 576 576   0.00000 30.34603 5.17723e-004

953 1656 0.00 0.00 0.00 -95.40 18.93 36.43 1.000 0.000 0 1 0 2 0.104

0.104 11.00   0.00   0.00   0.00 4 30.00   0   0   0   1 0.0 1 1   7   0

0.000   0.000   0.000 1

=== END OF DATA DESCRIPTION FILE

==

References

Adams, M. A. & Hutton, W. C., 1983. The Effect of Posture on the Fluid Content of Lumbar Intervertebral Discs. *Spine,* Volume 6, pp. 665-671.

Adams, P., Eyre, D. & Muir, H., 1977. Biochemical Aspects of Development and Ageing of Human Lumbar Intervertebral Discs. *Rheumatol Rehab,* Volume 16, pp. 22-29.

Akansel, G., Haughton, V. M., Papke, A. & Censky, S., 1997. Diffusion into Human Intervertebral Disks Studied with MR and Gadoteridol. *American Journal of Neuroradiology,* Volume 18, pp. 443-445.

Alini, M. et al., 2008. Are Animal Models Useful for Studying Human Disc Disorders/Degeneration?. *Eur Spine Journal,* pp. 2-19.

Anderson, W., Harthill, J., James, W. & Montgomery, D., 1980. Barium Sulphate Preparations for use in Double Contrast Examination of the Upper Gastrointestinal Tract. *British Journal of Radiology,* 53(636), pp. 1150-9.

Antoniou, J., 2004. Apparent Diffusion Coefficient of Intervertebral Discs Related to Matrix Composition and Integrity. *Magnetic Resonance Imaging,* Volume 22, pp. 963-972.

Antoniou, J. et al., 2013. Analysis of Quantitative Magnetic Resonance Imaging and Biomechanical Parameters on Human Discs with Different Grades of Degeneration. *Journal of Magnetic Resonance Imaging,* 38(6), pp. 1402-1414.

Arun, R. et al., 2009. What Influence does Sustained Mechanical Load have on Diffusion in the Intervertebral Disc? An In Vivo Study using Serial Post Contrast Magnetic Resonance Imaging. *Spine,* Volume 34, pp. 2324-2337.

Bammer, R., 2003. Line Scan Diffusion Imaging of the Spine. *American Journal of Neuroradiology,* Volume 24, pp. 5-12.

Bancroft, J. & Gamble, M., 2002. *Theory and Practice of Histological Techniques.* 5th ed. London: Churchill Livingstone.

Bar-Even, A. et al., 2011. Hydrophobicity and Charge Shape Cellular Metabolite Concentrations. *Computational Biology,* 7(10).

Bartleby.com, 2008. *The Veins of the Upper Extremity and Thorax.* [Online]
Available at: www.bartleby.com/107/172.html
[Accessed 16 February 2008].

Bashir, A., Gray, M. L., Hartke, J. & Burstein, D., 1999. Nondestructive Imaging of Human Cartilage Glycosaminoglycan Concentration by MRI. *Magnetic Resonance in Medicine,* Volume 41, pp. 857-865.

Bayer Healthcare Pharmaceuticals, 2012. *Magnevist (a brand of gadopentetate dimeglumine) Injection.* [Online]
Available at:
http://labeling.bayerhealthcare.com/html/products/pi/Magnevist_PI.pdf
[Accessed 17 May 2013].

Bayer Inc., 2007. *Product Monograph Vasovist,* Toronto: BayerInc..

Bayer New Zealand Limited, 2013. *Data sheet Gadovist.* [Online]
Available at: http://www.medsafe.govt.nz/profs/datasheet/g/Gadovistinj.pdf
[Accessed 17 May 2013].

Beard, H. K. & Stevens, R. L., 1980. Biochemical Changes in the Intervertebral Disc. In: J. M. I. V, ed. *The Lumbar Sppine and Backache.* London: Pitman, pp. 407-436.

Benneker, L. et al., 2005. Vertebral Endplate Marrow Contact Channel Occlusions and Intervertebral Disc Degeneration. *Spine,* 30(2), pp. 167-173.

Bergknut, N. et al., 2013. Intervertebral Disc Disease in Dogs-Part 1: A New Histological Grading Scheme for Classification of Intervertebral Disc Degeneration in Dogs. *The Veterinary Journal,* Volume 195, pp. 156-163.

Bernardino, M. E. et al., 1994. Safety and Optimum Concentration of a Manganese Chloride-Based Oral MR Contrast Agent. *Journal of Magnetic Resonance Imaging,* 4(6), pp. 872-6.

Best, B. A. et al., 1994. Compressive Mechanical Properties of the Human Anulus Fibrosus and their Relationship to Biochemical Composition. *Spine,* 19(2), pp. 212-221.

Bogduk, N., 2001. *Clinical Anatomy of Lumbar Spine and Sacrum.* London: Harcourt.

Borthakur, A. et al., 2000. Sensitivity of MRI to Proteoglycan Depletion in Cartilage: Comparison of Sodium and Proton MRI. *Osteoarthritis and Cartilage,* 8(4), pp. 288-293.

Brickley-Parsons & Gumcher, 1984. cited in Urban, J. P. et al. (2000) The Nucleus of the Intervertebral Disc from Development to degeneration. *American Zoologist,* 40(1), pp. 53-61.

Brodin, 1955. *cited in Stockwell, R. (1979) Biology of cartilage cells.* Cambridge: cambridge University Press.

Brown, S. et al., 2012. A Comparative Evaluation of the Small Leucine-Rich Proteoglycans of Pathological Human Intervertebral Discs. *European Spine Journal,* 21(2), pp. 154-159.

Buckwalter, J. A., 1995. Aging and Degeneration of the Human Intervertebral Disc. *Spine,* 20(11), pp. 1307-1314.

Buckwalter, J. A., Pedrini-Mille, A., Pedrini, V. & Tudisco, C., 1985. Proteoglycans of Human Infant Intervertebral Disc. Electron Microscope and Biochemical Studies. *J Bone Joint Surg,* 67(2), pp. 284-94.

Budras, K. D., 2001. *Anatomy of the Horse an Illustrated Text.* Germany: Schlutersche Hanover.

Bushell, G. R., Ghosh, P., Taylor, T. F. & Akeson, W. H., 1977. Proteoglycan Chemistry of the Intervertebral Disks. *Clin Orthop Relat Res,* Volume 129, pp. 115-23.

Bydder, G. M. et al., 2001. *Visualization of Solute Transport into and within Lumbar Intervertebral Disks using Delayed High Dose Gadodiamide-Enhanced MR Imaging.* s.l., American Society of Neuroradiology.

Bydder, M., Rahal, A., Fullerton, G. & Bydder, G., 2007. The Magic Angle Effect: a Source of Artifact, Determinant of Image Contrast, and Technique for Imaging. *Journal of Magnetic Resonance Imaging,* 25(2), pp. 290-300.

Caretto, L., 2009. *Solution of the Diffusion Equation.* [Online]

Available at: http://www.csun.edu/~lcaretto/me501b/diffusion.doc.

[Accessed 23 July 2013].

Carlton, R. & Adler, A., 2013. *Radiographic Imaging Concepts and Principles.* 5th ed. USA: Delmar Cengage.

Cassinelli, E. H., Hall, R. A. & Kang, 2001. Biochemistry of intervertebral disc degeneration and the potential for gene therapy applications. *The Spine Journal,* 1(3), pp. 205-214.

Clouet, J. et al., 2011. Characterization of the Age-Dependent Intervertebral Disc Changes in Rabbit by Correlation Between MRI, Histology and Gene Expression. *BMC Musculoskeletal Disorders,* 12(147).

Coventry, M. B., Ghormley, R. K. & Kemohan, J. W., 1945. The Intervertebral disc: its Microscopic Anatomy and pathology. Part 1. Anatomy, Development and Physiology. *J Bone Joint Surg,* Volume 27, pp. 105-112.

Crock, H. & Goldwasser, M., 1984. Anatomic Studies of the Circulation in the Region of the Vertebral End-Plate in Adult Greyhound Dogs. *The Spine Journal,* 9(7), pp. 702-706.

Crock, H. V. & Yoshizawa, H., 1976. The Blood Supply of the Lumbar Vertebral Column. *Clinical Orthopaedics and Related Research*, March-April.

Crock, H. V., Yoshizawa, H. & Kame, S. K., 1973. Observations on the Venous Drainage of the Human Vertebral Body. *The Journal of Bone and Joint Surgery,* 55(3), pp. 528-533.

Damadian, R., 1971. Tumor Detection by Nuclear Magnetic Resonance. *Science,* 171(3976), pp. 1151-1153.

Department of Health, 2007. *The Ionising Radiation (Medical Exposure) Regulations 2000.* [Online]
Available at:
http://webarchive.nationalarchives.gov.uk/+/www.dh.gov.uk/en/publicationsandstatistics/publications/publicationspolicyandguidance/dh_4007957
[Accessed 8 April 2013].

Drasin, G. F., Daffner, R. H., Sexton, R. F. & Cheatham, W. C., 1976. Epidural Venography: Diagnosis of Herniated Intervertebral Discs and Other Disease of the Epidural Space. *American Journal of Roentgenology,* 126(5), pp. 1010-1016.

Dunn, J. F., Foniok, T. & Matyas, J. R., 2006. Magic Angle MR Microscopy and T2 Quantification of Intervertebral Discs Highlights the 3-Dimensional Collagen Structure. *Proc. Intl. Soc. Mag. Reson. Med. ,* Volume 14, p. 1712.

Erbel, R. & Eggebrecht, H., 2006. Aortic Dimensions and the Risk of Dissection. *Heart,* 92(1), pp. 137-142.

Eyre, D. & Muir, H., 1976. Types I and II Collagens in Intervertebral Disc. *Biochem. J.,* Volume 157, pp. 267-270.

Fawcett, D. & Jensh, R., 2002. *Bloom and Fawcett's Concise Histology.* London: Oxford University Press.

Ferguson, S. J., Ito, K. & Nolte, L. P., 2004. Fluid flow and convective transport of solutes within the intervertebral disc. *The Journal of Biomechanics,* 37(2), pp. 213-221.

Flower, M. A., 2012. *Webb's Physics of Medical Imaging.* 2nd ed. New York: Taylor and Francis.

Freemont, T., 2001. Degeneration of intervertebral discs: current understanding of cellular and molecular events, and implications for novel therapies. *Expert reviews in molecular medicine*, pp. 1-10.

Frijins, A., 2005. *Centre for Analysis, Scientific Computing and Applications.* [Online]
Available at: www.win.the.nv.../previousprojects/frijins.html
[Accessed 2 february 2008].

Galbusera, F., Brayda-Bruno, M. & Wilke, H., accepted June 2014. Is Post Contrast MRI a Valuable Method for the Study of the Nutrition of the Intervertebral Disc?. *Journal of Biomechanics.*

Garroway, A. N., Grannell, P. K. & Mansfield, P., 1974. Image Formation in NMR by a Selective Irradiative Process. *J. Phys. C:Solid State Phys,* Volume 7, pp. 451-462.

Gartner, L. & Hiatt, J., 1997. *Colour Textbook of Histology.* Philadelphia: W.B.Saunders Company.

Gillis, A. M., Samosky, J. T., Gray, M. L. & Burstein, D., 2000. Effect of Charge on Transport and Distribution of Contrast Agents in Cartilage. *Proc. Intl. Soc. Mag. Reson. Med.,* Volume 8.

Graham, D., Cloke, P. & Vosper, M., 2012. *Principles and Applications of Radiological Physics.* London: Elsevier.

Gray, M. L., Burstein, D., Lesperance, L. M. & Gehrke, L., 1995. Magnetization Transfer in Cartilage and its Constituent Macromolecules. *Magnetic Resonance in Medicine,* 34(3), pp. 319-325.

Grodzinsky, A. J. & Urban, J. P., 1995. Physical Regulation of Metabolism in Cartilaginous Tissues: Relation to Extracellular Forces and Flows. In: R. K. Reed, et al. eds. *Interstitium Connective Tissue and Lymphatics.* London: Portland Press, pp. 67-84.

Gruber, H. E., Ingram, J. & Hanley Jr, E. N., 2002. An Improved Staining method for Intervertebral Disc Tissue. *Biotechnic and Histochemistry,* 77(2), pp. 81-83.

Grunhagen, T. et al., 2006. Nutirient Supply and Intervertebral Disc Metabolism. *The Journal of Bone and Joint Surgery,* 88(2), pp. 30-35.

GU, W. Y., Lai, W. M. & Mow, V. C., 1998. A Mixture Theory for Charged-Hydrated Soft Tissues Containing Multi-electrolytes: Passive Transport and Swelling Behaviours. *Journal of Biomechanical Engineering,* Volume 120, pp. 169-80.

Happey, 1980. cited in Urban J. P. (1990) Solute Transport in Articular cartilage and the Intervertebral Dics. In: D. Hukins, ed. *Connective Tissue Matrix, Part 2.* London: Macmillan Press, pp. 44-65.

Hardingham, T. E. & Fosang, A. J., 1992. Proteoglycans: Many Forms and Many Functions. *FASEB J,* Volume 6, pp. 861-870.

Hasue, M., Kikuchi, S., Sakuyama, Y. & Ito, T., 1983. Anatomic Study of the Interrelation between Lumbosacral Nerve Roots and their Surrounding Tissues. *Spine,* 8(1), pp. 50-8.

Heinegard, D. & Oldberg, A., 1989. Structure and Biology of Cartilage and Bone Matrix Noncollagenous Macromolecules. *FASEB J,* pp. 2042-2051.

Henkelman, R. M., Stanisz, G. J. & Graham, S. J., 2001. Magnetization Transfer in MRI: A Review. *NMR in Biomedicine,* Volume 14, pp. 57-64.

Hickey, D. S., Aspden, R. M., Sivewright, G. J. & J, P. D., 1990. MR Imaging of Connective Tissue Degeneration. In: *Connective Tissue Matrix.* London: Macmillan, pp. 229-243.

Hirokazu, I. e. a., 1997. Proteoglycan Synthesis in the Intervertebral Disk Nucleus: the Role of Extracellular Osmolality. *The American Physiological Society,* pp. 1499-1506.

Hirsch, C. & Nachemson, A., 1954. New Observations on Mechanical Behaviour of Lumbar Discs. *Acta Orthop Scandinav,* Volume 23, pp. 254-283.

Holm, S. et al., 1981. Nutrition of the Intervertebral Disc: Solute Transport and Metabolism. *Connect Tiss Res,* 8(2), pp. 101-119.

Holm, S. & Nachemson, A., 1983. variations in the Nutrition of the Canine Intervertebral Disc Induced by Motion. *Spine,* Volume 8, pp. 866-874.

Hukins, 1984. cited in Urban, J. P. et al. (2000) The Nucleus of the Intervertebral Disc from Development to Degeneration. *American Zoologist,* 40(1), pp. 53-61.

Ibrahim, M. A., Haughton, V. M. & Hyde, J. S., 1994. Enhancement of Intervertebral Disks with Gadolinium Complexes: Comparison of an Ionic and Non-ionic Medium in an Animal Model. *American Journal of Neuroradiology,* Volume 15, pp. 1907-1910.

Ibrahim, M. A., Haughton, V. M. & Hyde, J. S., 1994. Enhancement of Normal Intervertebral Disk with Gadolinium Complexes: Comparison of an Ionic and a Nonionic Medium. *AJNR Am J Neuroradiol,* Volume 15, pp. 1907-1910.

Ibrahim, M. A., Haughton, V. M. & Hyde, J. S., 1995. Effect of Disc Maturation on Diffusion of Low Molecular Weight Gadolinium Complexes: an Experimental Study in Rabbits. *American Journal of Radiology,* Volume 16, pp. 1307-1311.

Ibrahim, M. A., Jesmanowicz, A. & Hyde, J. S., 1994. Contrast Enhancement of Normal Intervertebral Disks: Time and Dose Dependence. *American Journal of Neuroradiology,* Volume 15, pp. 419-423.

Inknen, 1999. cited in Yu, J. et al. (2002) Elastic Fibre Organisation in the Intervertebral Discs of the Bovine Tail. *Journal of Anatomy,* 202(2), p. 253.

Inoue & Takeda, 1975. cited in Urban, J. P. (1990) Solute transport in articular cartilage and the intervertebral disc. In: H. D, ed. *Connective tissue matrix, part 2.* London: Macmillan Press, pp. 44-65.

Jackson, A. R., Yao, H., Brown, M. D. & Gu, W. Y., 2006. Anisotropic Diffusivity in Intervertebral Disc: Electrical Conductivity Approach. *Spine,* Volume 31, pp. 2783-9.

Johnson, E. F., Berryman, H., Mitchell, R. & Wood, W. B., 1985. Elastic Fibres in the Anulus Fibrosus of the Adult Human Lumbar Intervertebral Disc. A Preliminary Report. *J Anat.,* Volume 143, pp. 57-63.

Johnson, E. F. et al., 1982. The Distribution and Arrangement of Elastic Fibres in the Intervertebral Disc of the Adult Human. *J Anat.,* Volume 135, pp. 301-309.

Kiani, C. et al., 2002. Structure and Function of Aggrecan. *Celll Research,* 12(1), pp. 19-32.

Kim, D. K. et al., 1993. Analysis of Water-Macromolecule Proton Magnetization Transfer in Articular Cartilage. *Magnetic Resonance in Medicine,* Volume 29, pp. 211-215.

Kuettner, K. E., 1994. Cartilage Integrity and Homeostasis. In: J. H. Klippel & P. A. Dieppe, eds. *Rhematology.* St. Louis: Mosby, pp. 7.6.1-7.6.16.

Lampidis, T. J. et al., 1989. Relevance of the Chemical Charge of Rhodamine Dyes to Multiple Drug Resistance. *Biochemical Pharmacology,* 38(23), pp. 4267-71.

Laurent, D. et al., 2003. In Vivo Assessment of Macromolecular Content in Articular Cartilage of the Goat Knee. *Magnetic Resonance in Medicine,* Volume 49, pp. 1037-1046.

Lauterbur, P. C., 1973. Image Formation by Induced Local Interactions: Examples Emplying Nuclear Magnetic Resonance. *Nature,* Volume 242, pp. 190-191.

Leddy, H. A., Haider, M. A. & Guilak, F., 2006. Diffusional Anisotropy in Collagenous Tissues: Fluorescence Imaging of Continuous Point Photobleaching. *Biophys J,* Volume 91, pp. 311-6.

Leo, A., Hansch, C. & Elkins, D., 1971. Partition Coefficients and their Uses. *Chemical Reviews,* 71(6), pp. 525-616.

Maciver, D. & Letts, R., 1968. Intraosseous Vertebral Venography as a Diagnostic Aid in Intervertebral Disc Disease. *The Canadian Journal of Surgery,* Volume 11, pp. 160-165.

Mai, J. & Paxinos, G., 2012. *The Human Nervous System.* 3rd ed. San Francisco: Elsevier.

Mansfield, P., 1977. Multi-planar Image Formation using NMR Spin Echoes. *J.Phys. C: Solid State Phys,* Volume 10, pp. 55-58.

Maroudas, A., 1970. Distribution and Diffusion of Solutes in Articular Cartilage. *Biophys J,* Volume 10, pp. 365-79.

Maroudas, A., 1976. Transport of Solutes Through Cartilage: Permeability to Large Molecules. *J. Anat.,* Volume 122, pp. 335-47.

Maroudas, A., 1978. Biophysical Chemistry of Cartilaginous Tissues with Special Reference to Solute and Fluid Transport. *Biorheology,* Volume 15, pp. 203-21.

Maroudas, A., 1988. Nutrition and Metabolism of the Intervertebral Disc. In: P. Ghosh, ed. *The Biology of the Intervertebral Disc.* Boca Raton: CRC Press, pp. 1-37.

Maroudas, A., Stockwell, R. A., Nachemson, A. & Urban, J., 1975. Factors Involved in the Nutrition of the Human Lumbar Intervertebral Disc: Cellularity and Diffusion of Glucose in Vitro. *J Anat.,* Volume 120, pp. 113-130.

McCausland Center for Brain Imaging, n.d. *Chris Rorden Research.* [Online] Available at: http://www.mccauslandcenter.sc.edu/mricro/ [Accessed 16 July 2013].

McRobbie, D. W., Moore, E., Graves, M. & Prince, M., 2007. *MRI from Picture to Proton.* 2nd ed. Cambridge: Cambridge University Press.

MedlinePlus, 2013. *Heparin Injection.* [Online]
Available at: http://www.nlm.nih.gov/medlineplus/druginfo/meds/a682826.html
[Accessed 30 April 2013].

Miller, J. A., Schmatz, C. & Schultz, A. B., 1988. Lumbar Disc Degeneration: Correlation with Age, Sex and Spine Levelin 600 Autopsy Specimens. *Spine,* Volume 13, pp. 173-178.

Miller, K. e. a., 2004. Steady-State Diffusion-Weighted Imaging of In Vivo Knee cartilage. *Magnetic Resonance in Medicine,* Volume 51, pp. 394-398.

Moore, R., 2006. The Vertebral Endplate: Disc Degeneration, Disc Regeneration. *Eur Spine J,* Volume 15, pp. 8333-8337.

MR-Technology Information Portal, 2013. *Fast Field Echo.* [Online]
Available at: http://www.mr-
tip.com/serv1.php?type=db1&dbs=Fast%20Field%20Echo
[Accessed 30 April 2013].

MR-Technology, 2008. *Vasovist.* [Online]
Available at: http://www.mr-tip.com/serv1.php?type=db1&dbs=Vasovost
[Accessed 3 June 2008].

Murphy, D. & Davidson, M., 2013. *Fundamentals of Light Microscopy and Electronic Imaging.* 2nd ed. New Jersey: John Wiley and Sons, Inc..

Nachemson, A., 1960. Lumbar Intradiscal Pressure: Experimental Studies on Post-Mortem Material. *Acta Orthopaed Scand Suppl,* Volume 43, pp. 1-104.

Nachemson, A., 1981. Disc Pressure Measurements. *Spine,* 6(1).

Nachemson, A., Lewin, T., Maroudas, A. & Freeman, M., 1970. In Vitro Diffusion of Dye Through the End-Plates and Annulus Fibrosus of Human Lumbar Intervertebral Discs. *Acta Orthop Scand,* Volume 41, pp. 589-607.

Nerlich, A., Schaff, R., Walchli, B. & Boos, N., 2007. Temporo-spatial Distribution of Blood Vessels in Human Intervertebral Discs. *European Spine Journal,* 16(4), pp. 547-555.

Nguyen-minh, C. et al., 1998. Measuring Diffusion of Solutes into Intervertebral Disks with MR Imaging and Paramagnetic Contrast Medium. *American Journal of Neuroradiology,* Volume 19, pp. 1781-1784.

Niesen, K., 2003. The Effects of Heparin Versus Normal Saline for Maintenance of Peripheral Intravenous Locks in Pregnant Women. *Journal of Obstetric, gynecologic and Neonatal Nursing,* 32(4), pp. 503-508.

Niinimaki, J. et al., 2008. Association between Visual Degeneration of Intervertebral Discs and the Apparent Diffusion Coefficient. *Magnetic Resonance Imaging,* 27(5), pp. 641-7.

Niinimaki, J. L. et al., 2006. In Vivo Quantification of Delayed Gadolinium Enhancement in the Nucleus Pulposus of Human Intervertebral Disc. *Journal of Magnetic Resonance Imaging,* Volume 24, pp. 796-800.

Niu, G. et al., 2011. Apparent Diffusion Coefficient in Normal and Abnormal Pattern of Intervertebral Lumbar Discs: Initial Experience. *J Biomed Res,* 25(3), pp. 197-203.

Ohshima, H. & Urban, J. P. G., 1992. The Effect of Lactate and pH on Proteoglycan and Protein Synthesis Rates in the Intervertebral Disc. *Spine,* Volume 17, pp. 1079-1082.

Oklahoma, U. o., 2008. *Vertebral Arteries.* [Online]

Available at: www.sanjoaquinhospital.org/education/cne/lumb....

[Accessed 17 February 2008].

OpenLearn LabSpace, n.d. *Imaging in Medicine.* [Online]

Available at: http://labspace.open.ac.uk/mod/resource/view.php?id=417927

[Accessed 21 March 2013].

OrthoIndy, C. O. C., 2007. *What makes up a healthy spine?.* [Online]

Available at: http://www.indyspinemd.com/Normal/index.asp.

[Accessed 6 July 2012].

Paajanen, H. et al., 1994. Magnetization Transfer Imaging of Lumbar Disc Degeneration: Correlation of Relaxation Parameters with Biochemistry. *Spine,* 19(24).

Patel, R., 2005. *Lumbar Degenerative Disc Disease.* [Online]

Available at: www.emedicine.com/pmr/TOPIC67.HTM

[Accessed 18 January 2008].

Patel, R., 2010. *Lumbar Degenerative Disk Disease.* [Online]

Available at: www.emedicine.com/pmr/TOPIC67.HTM

[Accessed 6 August 2012].

Peprotech, 2005. *Cartilage Related Cytokines and Osteoarthritis.* [Online]

Available at: www.peprotech.com/content/focusarticles.htm?id=72

[Accessed 1 February 2008].

Perlewitz, T. J. et al., 1997. Effect of MolecularWeight on the Diffusion of Contrast Media into Cartilage. *Spine,* 22(23), pp. 2707-2710.

Pezowicz, C., Robertson, P. & Broom, N., 2005. Intralamellar Relationships within the Collagenous Architecture of the Annulus Fibrosus Imaged in its Fully Hydrated State. *J. Anat.,* Volume 207, pp. 299-312.

Physicians, I. M. A. o., 2006. *Manipulation Under Anesthesia: Pathomechanics.* [Online]
Available at: www.muaphsicians.com
[Accessed 10 February 2013].

Prescher, A., 1998. Anatomy and Pathology of the Ageing Spine. *European Journal of Radiology,* 27(3), pp. 181-195.

Quinn, T. M., Kocian, P. & Meister, J. J., 2000. Static Compression is Associated with Decreased Diffusivity of Dextrans in Cartilage Explants. *Arch Biochem Biophys,* Volume 384, pp. 327-34.

Radsource LLC, 2009. *MRI Web Clinic - Spine Nomenclature.* [Online]
Available at: www.radsource.us/clinic/0804
[Accessed 11 February 2013].

Rajasekaran, S., 2004. A Study of Diffusion in Human Lumbar Discs: A Serial Magnetic Resonance Imaging Study Documenting the Influence of the Endplate on Diffusion in Normal and degenerate Discs. *The Spine Journal,* 29(3), pp. 2654-2667.

Rajasekaran, S. et al., 2008. Pharmacological Enhancement of Disc Diffusion and Differentiation of Healthy, Ageing and Degenerated Discs; Results from In-

Vivo Serial Post-Contrast MRI Studies in 365 Human Lumbar Discs. *European Spine Journal,* May, 17(5), pp. 626-643.

Rajasekaran, S. et al., 2010. A Study of the Effects of In Vivo Mechanical Force on Human Lumbar Discs with Scoliotic Disc as a Biological Model: Results from Serial Post Contrast Diffusion Studies, Histopathology and Biochemical Analysis of Twenty-One Human Lumbar Discs. *Spine,* October, 35(21), pp. 1930-1943.

Ratcliffe, J. F., 1980. The Arterial Anatomy of the Adult Human Lumbar Vertebral Body: a Microarteriographic Study. *J. Anat.,* 131(1), pp. 57-79.

Reddy, R. et al., 1998. Sodium MRI of Human Articular Cartilage in vivo. *Magnetic Resonance in Medicine,* 39(5), pp. 697-701.

Roberts, S., Menage, J. & Urban, J., 1989. Biochemical and Structural Properties of the Cartilage End-Plate and its Relation to the Intervertebral Disc. *Spine,* Volume 14, pp. 166-174.

Roberts, S., Urban, J. P., Evans, H. & Eisenstein, S., 1996. Transport Properties of the Human Cartilage Endplate in Relation to its Composition and Calcification. *Spine,* 21(4), pp. 415-420.

Robinson, J. R., 1971. Control of Water Content of Non-Metabolizing Kidney Slices by Sodium Chloride and Polyethylene Glycol (PEG 6000). *Journal of Physiology,* 213(1), pp. 227-34.

Rohlf, J. W., 1994. *Modern Physics from a to ZO.* s.l.:Wiley.

Roura, P., Fort, J. & Saurina, J., 2000. How Long Does it Take to Boil an Egg? A Simple Approach to the Energy Transfer Equation. *Eur. J. Phys,* pp. 95-100.

Rutges, J. P. H. J. et al., 2013. A Validated New Histological Classification for Intervertebral Disc Degeneration. *Osteoarthritis and cartilage,* Volume 21, pp. 2039-2047.

Sato, K., Kikuchi, S. & Yonezawa, T., 1999. In Vivo Intradiscal Pressure Measurement in Healthy Individuals and in Patients with Ongoing Back Problems. *Spine,* 24(23).

Schollum, M., Robertson, P. A. & Broom, N., 2009. A Microstructural Investigation of Intervertebral Disc lamellar connectivity: detailed analysis of the Translamellar Bridges. *J. Anat.,* 214(6), pp. 805-816.

Shanker, H., Scarlett, J. A. & Abram, S., 2009. Anatomy and pathophysiology of intervertebral disc disease. *Techniques in Regional Anethesia and Pain Management,* 13(2), pp. 67-75.

Sigma-Aldrich, 2013. *Evans blue.* [Online]
Available at:
http://www.sigmaaldrich.com/catalog/product/sigma/e2129?lang=en&region=GB

[Accessed 22 April 2013].

Sigma-Aldrich, 2013. *Manganese (II) Chloride Tetrahydrate.* [Online]
Available at:
http://www.sigmaaldrich.com/catalog/product/sial/m8054?lang=en&region=GB
[Accessed 17 May 2013].

Sivan, S. S. et al., 2013. Biochemical Composition and Turnover of the Extracellular Matrix of the Normal and Degenerate Intervertebral Disc. *European Spine Journal.*

Spine Bioengineering Laboratory, n.d. *Researching Intervertebral Disc Mechanobiology.* [Online]

Available at: http://www.emba.uvm.edu/~jiatridi/research/research.html

[Accessed 21 July 2013].

Stairmand, J. W., Holm, S. & Urban, J. P., 1991. Factors Influencing Oxygen Concentration Gradients in the Intervertebral Disc: a Theoretical Analysis. *Spine,* Volume 16, pp. 444-449.

Stockwell, R., 1979. *Biology of Cartilage Cells.* Cambridge: Cambridge University Press.

Szimai, 1970. cited in Yu, J. et al. (2002) Elastic Fibre Organisation in the Intervertebral Discs of the Bovine Tail. *Journal of Anatomy,* 202(2), p. 253.

Takeda, 1975. cited in Yu, J. et al. (2002) Elastic Fibre Organisation in the Intervertebral Discs of the Bovine Tail. *Journal of Anatomy,* 202(2), p. 253.

Tak-Man Cheung, J., Zhang, M. & Hung-Kay Chow, D. H. K., 2003. Biomechanical responses of the intervertebral joints to static and vibrational loading: a finite element study. *Clinical Biomechanics,* 18(9), pp. 790-799.

TdB Consultancy, 2010. *FITC-Dextran-TdB cons Dextran Derivatives.* [Online]

Available at: http://www.tdbcons.se/tdbcons2/attachment/fitcdextran2.pdf

[Accessed 16 May 2013].

Tikall, 2013. *Horse Skeleton.* [Online]

Available at: www.tikall.deviantart.com/art/Horse-Skeleton-272659715

[Accessed 15 February 2013].

Toffanin, R., 2001. Proteoglycan Depletion and Magnetic Resonance Parameters of Articular Cartilage. *Archives of Biochemistry and Biophysics,* 390(2), pp. 235-242.

Tortora, G. & Grabowski, S., 2003. *Principles of Anatomy and Physiology.* 12th ed. London: Wiley.

University of Exeter, 2013a. *Introduction to x-ray imaging,Clinical Imaging 1 PAM1017. [Lecture Notes].* Exeter: University of Exeter.

University of Exeter, n.d. *Exeter MR Research Centre.* [Online]
Available at: http://centres.exeter.ac.uk/pmrrc/
[Accessed 24 April 2013].

Urban, J. P., 1990. Solute transport in articular cartilage and the intervertebral disc. In: D. Hukins, ed. *Connective tissue matrix, part 2.* London: Macmillan Press, pp. 44-65.

Urban, J. P., 2002. The role of the physiochemical environment in determining disc cell behaviour. *Biochemical Society Transactions,* 30(6), pp. 858-864.

Urban, J. P., Holm, S. & Maroudas, A., 1978. Diffusion of Small Solutes into the Intervertebral Disc: as In Vivo Study. *Biorheology,* Volume 15, pp. 203-21.

Urban, J. P., Holm, S., Maroudas, A. & Nachemson, A., 1982. Nutrition of the Intervertebral Disc: Effect of Fluid Flow on Solute Transport. *Clin Orthop,* Volume 170, pp. 296-302.

Urban, J. P. & Maroudas, 1979. cited in Urban, J. P. (1990) Solute Transport in Articular Cartilage and the Intervertebral Disc. In: D. Hukins, ed. *Connective Tissue Matrix, part 2.* London: Macmillan Press, pp. 44-65.

288

Urban, J. P. & Maroudas, A., 1980. The Chemistry of the Intervertebral Disc in Relation to its Physiological Function. *Clin Rheum Dis,* Volume 6, pp. 51-76.

Urban, J. P. & Roberts, S., 2003. Degeneration of the intervertebral disc. *Arthritis Res The,* Volume 5, pp. 120-130.

Urban, J. P., Roberts, S. & Ralphs, J. R., 2000. The Nucleus of the Intervertebral Disc from Development to Degeneration. *American Zoologist,* 40(1), pp. 53-61.

Urban, J. P. & Winlove, C. P., 2007. Intervertebral disc pathophysiology-The pathophysiology of the intervertebral disc and the challenges for MRI. *The Journal of Magnetic Resonance Imaging,* 25(2), pp. 419-432.

Van Der Meulen, P., Groen, J. P., Tinus, A. M. C. & Bruntink, G., 1988. Fast Field Echo Imaging: An Overview and Contrast Calculations. *Magnetic Resonance Imaging,* Volume 6, pp. 355-368.

Vertcal Health LLC, 2013. *Degenerative Disc Disease Center.* [Online] Available at: www.spineuniverse.com/conditions/degenerative-disc-disease [Accessed 11 February 2013].

Viidik, 1973. cited in Yu, J. et al. (2002) Elastic Fibre Organisation in the Intervertebral Discs of the Bovine Tail. *Journal of Anatomy,* 202(2), p. 253.

Wade, K., Robertson, P. & Broom, N., 2011. A fresh look at the Nucleus-Endplate Region: NewEvidence for Significant Structural Integration. *Eur Spine J,* Volume 20, pp. 1225-1232.

Weber, I. T., Harrison, R. W. & Iozzo, V., 1996. Model Structure of Decorin and Implications for Collagen Fibrillogenesis. *The Journal of Biological Chemistry,* 271(50), pp. 31767-31770.

White, A., Handler, P. & Smith, E. L., 1968. *Principles of Biochemistry.* 4th ed. New York: McGraw-Hill.

Williams, A. et al., 2007. Suitability of T!Gd as the "dGEMRIC Index" at 1.5T and 3.0T. *Magnetic Resonance in Medicine,* Volume 58, pp. 830-834.

Wuertz, K. et al., 2007. Influence of Extracellular Osmolarity and Mechanical Stimulation on Gene Expression of Intervertebral Disc Cells. *Journal of Orthopaedic Research,* 25(11), pp. 1513-22.

Young, B. & Heath, J. W., 2000. *Wheater's Functional Histology.* 4th ed. USA: Harcourt.

Yu, J., 2002. Elastic Fibre Organisation in the Intervertebral Discs of the Bovine Tail. *Journal of Anatomy,* 202(2), p. 253.